

A7-E800785

6

ADA 132116

SYMPOSIUM PROCEEDINGS  
Part 2

THE INTERACTION OF  
NON-NUCLEAR MUNITIONS  
WITH STRUCTURES

U.S. AIR FORCE ACADEMY, COLORADO  
MAY 10-13, 1983

DTIC FILE COPY

DISTRIBUTION STATEMENT A  
Approved for public release  
Distribution Unlimited

DTIC  
ELECTE  
SEP 1 1983  
S D  
B

83 08 19 09 4

## COMPONENT PART NOTICE

THIS PAPER IS A COMPONENT PART OF THE FOLLOWING COMPILATION REPORT:

(TITLE): The Interaction of Non-Nuclear Munitions with Structures: Symposium Proceedings  
Held at U.S. Air Force Academy, Colorado on May 10-13 1983 Part 2.

(SOURCE): Florida Univ., Eglin AFB. Graduate Engineering Center.

TO ORDER THE COMPLETE COMPILATION REPORT USE AD-A132 116.

THE COMPONENT PART IS PROVIDED HERE TO ALLOW USERS ACCESS TO INDIVIDUALLY AUTHORED SECTIONS OF PROCEEDINGS, ANNALS, SYMPOSIA, ETC. HOWEVER, THE COMPONENT SHOULD BE CONSIDERED WITHIN THE CONTEXT OF THE OVERALL COMPILATION REPORT AND NOT AS A STAND-ALONE TECHNICAL REPORT.

THE FOLLOWING COMPONENT PART NUMBERS COMPRISE THE COMPILATION REPORT:

AD#:	TITLE:
AD-P001 749	Has a Decade Made a Difference?
AD-P001 750	Some Considerations in the Analysis and Prediction of Ground Shock from Buried Conventional Explosions.
AD-P001 751	Centrifugal Modeling Techniques.
AD-P001 752	Impact and Penetration of Layered Pavement Systems.
AD-P001 753	Concrete Penetration and Ricochet Testing of Two Projectile Types with Two Nose Shapes.
AD-P001 754	Interaction of High Velocity Aluminum Shaped Charge Jets with Finite Steel and Concrete Targets.
AD-P001 755	Penetration Equation from Steel Aluminum, and Titanium Plates by Deforming Projectiles at Obliquity.
AD-P001 756	Plain Concrete Loaded at High Strain Rates.
AD-P001 757	Laboratory Test Facilities for Static and Dynamic Loading of Concrete Structures.
AD-P001 758	Blast Induced Soil Liquefaction.
AD-P001 759	Soil Characterization for Non-Destructive in Situ Testing.
AD-P001 760	Soil Model Evaluation Under Dynamic Loadings.
AD-P001 761	Constitutive Models for Saturated Soils.
AD-P001 762	The Response of Reinforced Concrete Structures Under Impulsive Loading.
AD-P001 763	A Review of the 1983 Revision of TM 5-855-1. "Fundamentals of Protective Design" (Non-Nuclear).
AD-P001 764	Model Law for Concrete Structure Under Dynamic Loads.
AD-P001 765	Response of Drag-Sensitive, Steel-Framed, Industrial-Type Structures to Airblast Loading.

### DISTRIBUTION STATEMENT A

Approved for public release;  
Distribution Unlimited

Accession For	
NTIS	CRAI
DTIC	TAH
Unannounced	<input type="checkbox"/>
Justification	
By	
Distribution/	
Availability Codes	
Dist	Avail and/or
A	Special

COMPONENT PART NOTICE (CON'T)

AD#:	TITLE:
AD-P001 766	Response of Buried Concrete Structures to Buried High Explosive Charges: A Review in Similitude Format.
AD-P001 767	The Measurement of Blast-Induced Motion of Structures Using a Doppler Radar.
AD-P001 768	High Explosive Testing of Hardened Aircraft Shelters.
AD-P001 769	A Statistical Approach to Conventional Weapons Experimentation.
AD-P001 770	Blast Response Tests of Aboveground Reinforced Concrete Box Structures.
AD-P001 771	Concrete Bridges Subjected to Impulsive Loading from Fuel-Air Explosives.
AD-P001 772	The AFWL Chebs (Conventional High Explosive Blast and Shock) Test Series.
AD-P001 773	The Behavior of Mounded Horizontal Cylinders in a Conventional Weapon Environment.

**SYMPOSIUM PROCEEDINGS**

**Part 2**

**THE INTERACTION OF  
NON-NUCLEAR MUNITIONS  
WITH STRUCTURES**

**U.S. AIR FORCE ACADEMY, COLORADO  
MAY 10-13, 1983**



This document represents Part 2 of the proceedings of a symposium "The Interaction of Non-Nuclear Munitions with Structures", U S Air Force Academy, Colorado, May 10-13, 1983. The symposium was sponsored by the following U S Air Force agencies:

**Armament Laboratory**  
Eglin AFB, FL

**Engineering & Services Laboratory**  
Tyndall AFB, FL

**Office of Scientific Research**  
Bolling AFB, DC

**Weapons Laboratory**  
Kirtland AFB, NM

The symposium was coordinated through the University of Florida Graduate Engineering Center, Eglin AFB, FL, under USAF Contract No. F08635-81-C-0302. Dr. C. A. Ross served as the symposium coordinator.

All the manuscripts in this document have been approved for public release either by the author or the cognizant federal agency.

See the first part of the proceedings for additional papers.

This document was produced at a total cost of \$0,000.00 or \$0.00 per copy.

Accession For	
NTIS GRA&I	<input checked="checked" type="checkbox"/>
DTIC TAB	<input type="checkbox"/>
Unannounced	<input type="checkbox"/>
Justification	
By _____	
Distribution/ _____	
Availability Codes	
Dist	Avail and/or Special
A	



# TABLE OF CONTENTS

## Part 2

### KEYNOTE SPEECHES

#### HAS A DECADE MADE A DIFFERENCE?

J. D. Haltiwanger, *University of Illinois*

#### SOME CONSIDERATIONS IN THE ANALYSIS AND PREDICTION OF GROUND SHOCK FROM BURIED CONVENTIONAL EXPLOSIONS

C. J. Higgins, *Applied Research Associates Inc*

### CENTRIFUGE MODELING

#### CENTRIFUGAL MODELING TECHNIQUES

P. L. Rosengren, Jr., *USAF Engineering & Services Lab*

#### IMPACT AND PENETRATION OF CONCRETE AND ROCK

#### IMPACT AND PENETRATION OF LAYERED PAVEMENT SYSTEMS

T. E. Bretz, Jr., *USAF Engineering & Services Lab*, and  
P. T. Nash, *Southwest Research Institute*

#### CONCRETE PENETRATION AND RICOCHET TESTING OF TWO PROJECTILE TYPES WITH TWO NOSE SHAPES

R. D. Szczepanski, *Orlando Technology, Inc.*, and J. A. Collins, *USAF Armament Lab*

#### IMPACT AND PENETRATION OF EXPLOSIVES AND SHAPED CHARGES

#### INTERACTION OF HIGH VELOCITY ALUMINUM SHAPED CHARGE JETS WITH FINITE STEEL AND CONCRETE TARGETS

D. K. Davison, *Physics International Company*

### IMPACT AND PENETRATION MODELS

#### PENETRATION EQUATION FROM STEEL, ALUMINUM, AND TITANIUM PLATES BY DEFORMING PROJECTILES AT OBLIQUITY

J. S. O'Brasky and T. N. Smith, *Naval Surface Weapons Center*

### MATERIAL RESPONSE

#### PLAIN CONCRETE LOADED AT HIGH STRAIN RATES

R. G. Galloway, *USAF Weapons Lab*

#### LABORATORY TEST FACILITIES FOR STATIC AND DYNAMIC LOADING OF CONCRETE STRUCTURES

W. J. Carter, *TerraTek Engineering*

### SOIL LIQUEFACTION

#### BLAST INDUCED SOIL LIQUEFACTION

W. A. Charlie, G. E. Jeyera, S. R. Abt and H. D. Patrone, *Colorado State University*

### SOIL MODELS

#### SOIL CHARACTERIZATION FOR NON-DESTRUCTIVE IN SITU TESTING

K. Arulanandan, A. Anandarajah and N. J. Meegoda, *University of California*

#### SOIL MODEL EVALUATION UNDER DYNAMIC LOADINGS

W. C. Dass and J. L. Bratton, *Applied Research Associates, Inc*

#### CONSTITUTIVE MODELS FOR SATURATED SOILS

R. S. Sandhu, *Ohio State University*

### STRUCTURAL ANALYSIS

#### THE RESPONSE OF REINFORCED CONCRETE STRUCTURES UNDER IMPULSIVE LOADING

W. A. Mihave, and J. Isenberg, *Weidinger Associates*

### STRUCTURAL DESIGN

#### A REVIEW OF THE 1983 REVISION OF TM 5-855-1, "FUNDAMENTALS OF PROTECTIVE DESIGN" (NON-NUCLEAR)

S. A. Kiger and J. P. Balsara, *USAE Waterways Experiment Station*

### STRUCTURAL RESPONSE

#### MODEL LAW FOR CONCRETE STRUCTURE UNDER DYNAMIC LOADS

H. R. Fuehrer, *Martin Marietta Corporation*

#### RESPONSE OF DRAG-SENSITIVE, STEEL-FRAMED, INDUSTRIAL-TYPE STRUCTURES TO AIRBLAST LOADING

H. S. Levine and E. M. R. Weidinger Associates

**RESPONSE OF BURIED CONCRETE STRUCTURES  
TO BURIED HIGH EXPLOSIVE CHARGES: A  
REVIEW IN SIMILITUDE FORMAT**

J S O'Brasky, *Naval Surface Weapons Center*

110

**STRUCTURAL TESTS**

**THE MEASUREMENT OF BLAST-INDUCED MOTION  
OF STRUCTURES USING A DOPPLER RADAR**

R K. Bailey, M Brook and J J. Forster, *New Mexico Tech*

116

**HIGH EXPLOSIVE TESTING OF HARDENED  
AIRCRAFT SHELTERS**

R R Bousek, *Defense Nuclear Agency*

122

**A STATISTICAL APPROACH TO CONVENTIONAL  
WEAPONS EXPERIMENTATION**

J M Carsor, *University of New Mexico*

128

**BLAST RESPONSE TESTS OF ABOVEGROUND  
REINFORCED CONCRETE BOX STRUCTURES**

D. R. Coltharp, *U S Army Engineer Waterways Experiment  
Station*

133

**CONCRETE BRIDGES SUBJECTED TO IMPULSIVE  
LOADING FROM FUEL-AIR EXPLOSIVES**

B Hobbs, *The University of Sheffield, United Kingdom*

139

**THE AFWL CHEBS (CONVENTIONAL HIGH  
EXPLOSIVE BLAST AND SHOCK) TEST SERIES**

D Morrison, *University of New Mexico*

145

**THE BEHAVIOR OF MOUNDED HORIZONTAL  
CYLINDERS IN A CONVENTIONAL-WEAPON  
ENVIRONMENT**

S R Whitehouse, *USAF Weapons Lab*

148

# APPENDIX A: PAPERS APPEARING IN PART 1.

## GROUND SHOCK AND LOADS

### GROUND SHOCK FROM PENETRATING CONVENTIONAL WEAPONS

J. L. Drake and C. D. Little, Jr., *U.S. Army Engineer Waterways Exp. Station*

### CALCULATIONAL EVALUATION OF THE INCLUSION EFFECTS ON STRESS GAGE MEASUREMENTS IN ROCK AND SOIL

A. L. Florence, D. D. Keough and R. Mak, *SRI International*

### FREE-FIELD GROUND SHOCK PRESSURES FROM BURIED DETONATIONS IN SATURATED AND UNSATURATED SOILS

P. S. Westine and G. J. Friesenhahn, *Southwest Research Institute*

## IMPACT AND PENETRATION OF CONCRETE AND ROCK

### HIGH VELOCITY PENETRATION INTO FIBRE-REINFORCED CONCRETE MATERIALS - PROTECTION OF BUILDINGS

W. F. Anderson, A. J. Watson and P. J. Armstrong, *University of Sheffield, United Kingdom*

### ANALYTICAL AND EXPERIMENTAL STUDIES ON PENETRATION INTO GEOLOGICAL TARGETS

M. J. Forrestal, D. B. Longcope and L. M. Lee, *Sandia National Laboratories*

### PENETRATION BEHAVIOR OF HIGHLY DEFORMABLE PROJECTILES IN CONCRETE SLABS

M. Hulsewig, E. Schneider and A. J. Stilp, *Ernst-Mach-Institut, F.R. Germany*

## IMPACT AND PENETRATION OF EXPLOSIVES AND SHAPED CHARGES

### RAPID RUNWAY CUTTING WITH SHAPED CHARGES

C. E. Joachim, *USAE Waterways Experiment Station*

### MODELING THE BURN-TO-VIOLENT REACTION TO SIMULATE IMPACT-DAMAGED GP WARHEADS

H. Krier, M. Dahm and P. B. Butler, *University of Illinois*

### PREDICTING RESPONSE OF MUNITIONS TO MASSIVE SECONDARY FRAGMENT IMPACT: A PROPOSED ANALYTICAL METHOD

H. Napadensky, A. Longinow, E. Hahn and E. Swider, *IIT Research Institute*

## MATERIAL MODELS

### MICROPLANE MODEL FOR FRACTURE ANALYSIS OF CONCRETE STRUCTURES

Z. P. Bazant and B. H. Oh, *Northwestern University*

### A PLASTIC FRACTURE MODEL FOR CONCRETE MATERIALS

W. F. Chen and T. Y. Chang, *Purdue University*

### THE EFFECTS OF CURING AND AGING ON THE TRIAXIAL PROPERTIES OF CONCRETE IN UNDERGROUND STRUCTURES

M. M. Hightower, *Sandia National Laboratories*

### STRENGTH CRITERIA FOR ANISOTROPIC MATERIALS

C. L. D. Huang and H. S. Walker, *Kansas State University*

### CONSTITUTIVE PROPERTIES OF STEEL FIBER REINFORCED CONCRETE IN MULTIAXIAL LOADING

H.-Y. Ko, R. W. Meier, D. E. Egging, S. Sture and C. C. Feng, *University of Colorado*

### A SIMPLIFIED VISCOPLASTIC THEORY FOR FRICTIONAL MATERIALS

H. L. Schreyer and J. E. Bean, *University of New Mexico*

### CONSTITUTIVE RELATIONS OF CONCRETE SUBJECTED TO A VARYING STRAIN RATE

S. P. Shah, *Northwestern University Technological Institute*

## MATERIAL RESPONSE

### ROCK/ELASTOMER COMPOSITES AS IMPACT RESISTANCE MATERIALS

W. F. Anderson, A. J. Watson, M. R. Johnson and G. J. McNeil, *University of Sheffield, United Kingdom*

### BEHAVIOR OF FIBER REINFORCED CONCRETE SLABS UNDER IMPACT LOADING

M. Hulsewig, E. Schneider and A. J. Stilp, *Ernst-Mach-Institut, F.R. Germany*

### EXPERIMENTAL MODELING OF STRENGTH AND DEFORMATION BEHAVIOR OF CONCRETE IN DIRECT SHEAR

S. Sture, *University of Colorado*

### FINITE ELEMENT ANALYSIS OF CONCRETE FAILURE IN SHEAR

J. Christensen and K. J. Willam, *University of Colorado*

## SOIL LIQUEFACTION

### SHAKING TABLE TESTS TO EVALUATE THE LIQUEFACTION POTENTIAL OF NEAR SURFACE SATURATED SAND DEPOSITS

S. F. Mason and W. E. Wolfe, *Ohio State University*

## STRUCTURAL ANALYSIS

### ANALYSIS OF BURIED REINFORCED CONCRETE ARCH STRUCTURES UNDER DYNAMIC LOADS

H. E. Auld and W. C. Dass, *Applied Research Assoc., Inc.*

### THE USE OF COMPENDIA, DESIGN MANUALS, AND REFERENCE TEXTS IN PREDICTION OF NONNUCLEAR WEAPONS EFFECTS

W. E. Baker, *Southwest Research Institute*

### ANALYSIS OF CONTAINMENT RINGS FOR FLYWHEEL BURST PROTECTION

C. W. Bert, *University of Oklahoma*

### A RATIONAL APPROACH TO THE ANALYSIS OF STRUCTURES SUBJECTED TO UNDERGROUND BLASTS

S. F. Borg, *Stevens Institute of Technology*

### EXTREME DYNAMIC LOADING EFFECTS ON STEEL AND CONCRETE SHELL STRUCTURES

Y. Crutzen, *Control Data Italia, Italy*

### FRACTURE DIAGNOSIS IN STRUCTURES USING CIRCUIT-ANALOGY

M. Akgun, F. D. Ju and T. L. Paez, *University of New Mexico*

### DYNAMIC LOADING: MORE THAN JUST A DYNAMIC LOAD FACTOR

W. Karthaus and J. W. Leussink, *Prins Maurits Laboratory TNO, The Netherlands*

### THE EFFECTS OF INDIRECT-FIRE MUNITIONS ON FRAMED STRUCTURES

B. L. Morris and P. H. Zabel, *Southwest Research Institute*

### MODELS FOR DAMAGE DIAGNOSIS IN SDF STRUCTURES

M.-G.-L. Wang, T. L. Paez and F. D. Ju, *University of New Mexico*

## STRUCTURAL DESIGN

### TODAY'S CONSTRAINTS DRIVE AMMO MAGAZINES UNDERGROUND

W. A. Keenan and J. E. Tancreto, *Naval Civil Engineering Laboratory*

### SWEDISH DESIGN MANUAL FOR PROTECTIVE STRUCTURES

B. E. Vretblad and G. B. Svædbjork, *Royal Swedish Fortifications Administration, Sweden*

### DESIGN OF UNDERGROUND SHELTERS INCLUDING SOIL-STRUCTURE INTERACTION EFFECTS

F. S. Wong and P. Weidlinger, *Weidlinger Associates*

## STRUCTURAL RESPONSE

### GAS PRESSURE LOADS FROM EXPLOSIONS WITHIN VENTED AND UNVENTED STRUCTURES

W. E. Baker, J. C. Hokanson, E. D. Esparza and N. R. Sandoval, *Southwest Research Institute*

### STRUCTURAL RESPONSE OF RC-MEMBERS IN CASE OF IMPULSIVE LOADING: FAILURE ANALYSIS IN BENDING AND SHEAR

C. van der Veen and J. Blaauwendraad, *Rijkswaterstaat Bouwresearch, The Netherlands*

### COMPARISON OF PREDICTIVE METHODS FOR STRUCTURAL RESPONSE TO HE BLAST LOADS

W. Char and M. M. Dembo, *U.S. Army Engineering Div. Huntsville*

### RESPONSE OF A LINEAR STRUCTURE TO AN EXPONENTIAL PRESSURE PULSE

F. D. Hains, *Naval Surface Weapons Center*

### THE USE OF STEEL FIBER REINFORCED CONCRETE IN CONTAINMENT AND EXPLOSIVE-RESISTANT STRUCTURES

C. H. Henager, *Battelle Northwest*

### SIMULATION OF PRESSURE WAVES AND THEIR EFFECTS ON LOADED OBJECTS, PART I: OUTLINING THE PROBLEM, DESCRIPTION OF THE SIMULATION DEVICE

G. Hoffmann and K. Behrens, *Fraunhofer-Institut für Kurzzeltdynamik, F.R. Germany*

### SIMULATION OF PRESSURE WAVES AND THEIR EFFECTS ON LOADED OBJECTS, PART II: EXPERIMENTS AND CALCULATIONS, DESTRUCTION CURVES

K. Behrens and G. Hoffman, *Fraunhofer-Institut für Kurzzeltdynamik, F.R. Germany*

### RESPONSE OF STRUCTURES TO DETONATIONS IN SAND

B. E. Vretblad, *Royal Swedish Fortifications Administration, Sweden*

## STRUCTURAL TESTS

### EFFECTS OF BARE AND CASED EXPLOSIVES CHARGES ON REINFORCED CONCRETE WALLS

H. Hader, *Ernst Basler & Partners, Switzerland*

### TESTS AND EVALUATIONS OF CLOSE-IN DETONATIONS

M. Kropatscheck, *Federal Armed Forces Institute for Operational Analysis and Exercises, F.R. Germany*

## APPENDIX B: LIST OF ATTENDEES

Ahmed Abou-Sayed  
Terra Tek International  
400 Wakara Way  
Salt Lake City, Utah 08108

Mehmet Akgun  
Department of Mechanical Engineering  
University of New Mexico  
Albuquerque, New Mexico 87131

John J. Allen  
AFOSR/NA  
Bolling AFB, DC 20332

W. F. Anderson  
Dept. of Civil & Structural Engineering  
University of Sheffield  
Mappin Street  
Sheffield S1 3JD  
United Kingdom

K. Arulanandan  
Department of Civil Engineering  
University of California, Davis  
Davis, California 95616

Bertil Arvidsson  
Bofors Ordnance  
R&D Department  
Box 500  
S-691 80 Bofors  
Sweden

Harry E. Auld  
Applied Research Assoc., Inc.  
2101 San Pedro Blvd., N.E.  
Suite A  
Albuquerque, New Mexico 07112

Ronald L. Bagley  
USAFA/DFEM  
U.S. Air Force Academy  
Colorado Springs, Colorado 80840

Richard K. Bailey  
New Mexico Tech/Tera  
Campus Station  
Socorro, New Mexico 87801

Shirley Bailey  
New Mexico Institute of Mining &  
Technology  
Socorro, New Mexico 87801

Charles F. Baker  
Code L-799  
Lawrence Livermore Laboratory  
P.O. Box 5506  
Livermore, California 94550

Wilfred E. Baker  
Southwest Research Institute  
6220 Culebra Road  
San Antonio, Texas 78284

Per A. Bakkejord  
INGENIOR P A BAKKEJORD A/S  
P.O. Box 45  
1321 Stabekk  
Norway

Steve Barnes  
60th ABG/DEEE  
Travis AFB, California 94535

T. Michael Baseheart  
Civil Engineering  
Mail oc. # 71  
University of Cincinnati  
Cincinnati, Ohio 45221

Zdenek P. Bazant  
Civil Engineering  
Center for Concrete & Geomaterials  
Northwestern University  
Evanston, Illinois 60201

Karsten Behrens  
Fraunhofer-Institut fur Kurzzeiddynamik  
ERNST-MACH-Institut  
Eckerstr. 4  
7800 Freiburg  
F.R. Germany

Ted Belytschko  
Department of Civil Engineering  
Northwestern University  
Evanston, Illinois 60201

David Bennett  
BEI Defense Systems Company  
P.O. Box 917  
Camden, Arkansas 71701

Andreas Bienz  
Ernst Basler & Partners  
Consulting Engineers & Planners  
P.O. Box, CH-8029 Zurich  
Switzerland

John Blaauwendraad  
Rijkswaterstaat Bouwresearch  
Postbus 20000  
3502 LA Utrecht  
The Netherlands

S. F. Borg  
Civil Engineering  
Stevens Institute of Technology  
Hoboken, New Jersey 07030

Ronald R. Bousek  
Defense Nuclear Agency/FCTT  
Kirtland AFB, New Mexico 87115

Steven C. Boyce  
DFCE  
U.S. Air Force Academy  
Colorado 80840

Robert E. Boyer  
Commander  
341st Civil Engineering Squadron  
Malstrom AFB, Montana 59402

Jimmie L. Bratton  
Applied Research Assoc., Inc.  
2101 San Pedro Blvd., N.E.  
Suite A  
Albuquerque, New Mexico 07112

Tom E. Bretz, Jr.  
Alternate Surfaces  
AFESC/RDCR  
Tyndall AFB, Florida 32403

William Brown  
Division 5533  
Sandia National Laboratories  
Albuquerque, New Mexico 87185

Walt Buchholtz  
Rsh Structural Engineer  
AFESC/RDCS  
Tyndall AFB, Florida 32403

Edward H. Bultmann, Jr.  
The BDM Corporation  
1801 Randolph Road, S.E.  
Albuquerque, New Mexico 87106

Timothy C. Campbell  
U.S. Army Corps of Engineers  
6014 USPO and Court House  
Omaha, Nebraska 68102

Donald L. Carew  
HQ ADTAC/SEW  
Langley AFB, Virginia 23665

Brock A. Carpenter  
Lockheed Missiles & Space Co., Inc.  
P.O. Box 504, 0/55-50, Bldg. 592  
Sunnyvale, California 94086

Jim M. Carson  
Campus P.O. Box 25  
Albuquerque, New Mexico 87131

W. O. Carter  
Department of Civil Engineering  
Utah State University  
Logan, Utah 84321

William J. Carter  
Terra Tek Engineering  
400 Wakara Way  
Salt Lake City, Utah 84108

T. Y. Chang  
University of Akron  
Akron, Ohio 44304

Washington Char  
U S Army Engineer Div. Huntsville  
P.O. Box 1600  
Huntsville, Alabama 35807

Wayne A. Charlie  
Department of Civil Engineering  
Colorado State University  
Fort Collins, Colorado 80523

Major Stoney P. Chisolm  
HQ USAF EUROPS/DEXX  
Ramstein AB, Germany  
APO, New York 09012

Lily C. Clouston  
University of Florida  
Eglin Graduate Center  
P.O. Box 1918  
Eglin AFB, Florida 32542

John A. Collins  
AFA7 /DLYW  
Eglin AFB, Florida 32542

David R. Coltharp  
USAE Waterways Experiment Station  
P.O. Box 631  
Vicksburg, Mississippi 39180

Malcolm J. G. Connell  
Lunar House/Room 1713  
40 Wellesley Road  
Croydon CR9 2EL  
United Kingdom

Roger D. Crowson  
U.S. Army Engineer Division—Europe  
EUDED-TA  
APO, New York 09757

Yves Crutzen  
Control Data Italia S.P.A.  
20090 SEGRATE (Ni)  
Palazzo Bernini-Centro Direzionale  
di Milano 2  
Italy

Martin Dahm  
#302 1106 S Euclid Street  
Champaign, Illinois 61820

Chris Dalton  
Division Supervisor  
Sandia National Laboratories  
Albuquerque, New Mexico 87185

William C. Dass  
Applied Research Associates, Inc.  
2101 San Pedro Blvd., N.E., Suite A  
Albuquerque, New Mexico 87110

David K. Davison  
Physics International Company  
2700 Merced Street  
San Leandro, California 94577

John O. Dow  
Assistant Professor  
Civil Engineering  
University of Colorado  
Boulder, Colorado 80302

James L. Drake  
USAE Waterways Experiment Station  
P.O. Box 631  
Vicksburg, Mississippi 39180

Reuben Eytan  
EBD International LTD  
44 Ugant Street  
69016 Tel Aviv  
Israel

Chuan C. Feng  
Professor of Engineering  
University of Colorado  
Campus Box 428  
Boulder, Colorado 80309

A. L. Florence  
SRI International  
Menlo Park, California 94025

Jesus Flores  
AFATL/DLJW  
Eglin AFB, Florida 32542

Michael J. Forrestal  
Exploratory Systems I  
Division 1621  
Sandia National Laboratories  
Albuquerque, New Mexico 87185

James J. Forster  
New Mexico Tech/Tera  
Campus Station  
Socorro, New Mexico 87801

John Foster  
Naval Surface Weapons Center—G31  
Dahlgren, Virginia 22448

Hans R. Fuehrer  
Martin Marietta Corporation  
P.O. Box 5837, MP-109  
Orlando, Florida 32855

Thomas Fultz  
Engineer Technician  
DFEM/I/SAFA  
Colorado Springs, Colorado 80840

Rodney G. Galloway  
AFWL/NTESR  
Kirtland AFB, New Mexico 87117

Ferdinand Glaser, Dipl. Ing.  
Bauberrat  
AFB KG IV  
Erprobungsstelle 91 d Bw  
4470 Meppen  
F.R. Germany

Don Gross  
MZ-21-1015  
General Dynamics Convair  
P.O. Box 80847  
San Diego, California 92138

Arthur Gurson  
AVCO Systems Division  
201 Lowell Street  
Wilmington, Massachusetts 01887

Hansjoerg Hader  
Ernst Basler & Partners  
Consulting Engineers  
P.O. Box, CH-8029  
Zurich  
Switzerland

Franklin D. Hains  
Naval Surface Weapons Center  
White Oak  
Silver Spring, Maryland 20910

J. D. Haltiwanger  
Newmark Civil Engineering Laboratory  
University of Illinois  
208 North Romine Street  
Urbana, Illinois 61801

Robert J. Hampson  
Air Force Weapons Laboratory  
AFWL/NTE  
Kirtland AFB, New Mexico 87117

Ralf H. Hansen  
Landa Division  
7010 Shape/Mons  
Belgium

John R. Hayes, Jr.  
AD/YQT  
Eglin AFB, Florida 32542

William R. Heincker  
Department Engineering Mechanics  
USAF Academy, Colorado 80840

Charles H. Henager  
Applied Mechanics & Structures Section  
Battelle Northwest  
P O Box 999  
Richland, Washington 99352

Cornelius J. Higgins  
Applied Research Associates, Inc  
2101 San Pedro Blvd, N E  
Suite A  
Albuquerque, New Mexico 87110

Mike Hightower  
Sandia National Laboratories  
Division 1621  
Albuquerque, New Mexico 87185

Thomas J. Hilferty  
Air Force Engineering & Services Center  
Tyndall AFB, Florida 32403

William V. Hill  
Black & Veatch Consulting Engineers  
P O. Box 8405  
Kansas City, Missouri 64114

Gunter Hoffman  
Fraunhofer-Institut für Kurzzeitdynamik  
ERNST-MACH-Institut  
Eckerstr 4  
7800 Freiburg  
F R Germany

Chester Hoggatt  
Denver Research Institute  
University of Denver  
P O. Box 10127  
Denver, Colorado 80010

James R. Holder  
AFATL/DLYV  
Eglin AFB, Florida 32542

Robin Houlston  
Defense Research Establishment Suffield  
Ralston, Alberta  
Canada

Jeremy Isenberg  
Weidlinger Associates  
3000 Sand Hill Road, 4-155  
Menlo Park, California 94025

Edward C. Jackett  
Box 1925  
Eglin AFB, Florida 32542

Ernst H. Jaeger AG1007  
Messerschmitt Bolkow Blohm  
Postfach  
D-8898 Schrobenuhausen  
F.R. Germany

Charles E. Joachim  
IJSAE Waterways Experiment Station  
P.O. Box 631  
Vicksburg, Mississippi 39180

Frederick D. Ju  
Department of Mechanical Engineering  
University of New Mexico  
Albuquerque, New Mexico 87131

Ir. W. Karthaus  
Prins Maurits Laboratory TNO  
P O. Box 45  
2280 AA Rijswijk  
The Netherlands  
015-13 87 77

W. A. Keenan  
Naval Civil Engineering Laboratory  
Port Hueneme, California 93043

Allen E. Kelly  
School of Civil Engineering  
Oklahoma State University  
Stillwater, Oklahoma 74078

S. A. Kiger  
USAE Waterways Experiment Station  
Corps of Engineers  
P.O. Box 631  
Vicksburg, Mississippi 39180

C. Y. King  
Code L-799  
Lawrence Livermore Laboratory  
P.O. Box 5506  
Livermore, California 94550

Timothy Knight  
U S. Army Corps of Engineers  
6014 USPO & Court House  
Omaha, Nebraska 68102

Hon-Yim Ko  
Civil, Environmental & Architectural  
Engineering  
Campus Box 428  
University of Colorado, Boulder  
Boulder, Colorado 80809

Christian A. Kot  
Components Technical Division - 335  
Argonne National Laboratory  
9700 S. Cass Avenue  
Argonne, Illinois 60439

Rolf-Helmut Kraus  
Bundesamt für Wehrtechnik  
und Beschaffung  
Rauental Postfach 7360  
D5400 Koblenz 1  
F R. Germany

Herman Kner  
144 MED, 1206 W. Green Street  
University of Illinois  
Urbana, Illinois 61801

Martin Kropatschek  
Federal Armed Forces Institute  
for Operational  
Analysis and Exercises  
Amt für Studien und Übungen  
der Bundeswehr  
Friedrich-Ebert-Str 72  
5060 Bergisch Gladbach 1  
F R. Germany

Mr. Rene LaRose  
Armament Division  
Defense Research Est  
Valcartier  
P.O. Box 8800  
Courscellette B Q.  
Postal Code GOA/IRO  
Canada

Russell Lechliders  
AFIS, INT  
Bolling AFB, 20332

Larry M. Lee  
Ktech Corporation  
901 Pennsylvania NE  
Albuquerque, New Mexico 87110

Howard S. Levine  
Weidlinger Associates  
3000 Sand Hill Road, 4-155  
Menlo Park, California 94025

Charles Lindberg  
Lindbergh & Associates  
2175 Ashley Phosphate Road  
Suite G  
Charleston, South Carolina 29405

Norman Lipner  
TRW Defense Systems Group  
One Space Park  
Redondo Beach, California 90278

A. Longinow  
Illinois Institute of Technology  
10 West 35th Street  
Chicago, Illinois 60616



Donald G. Madsen  
Honeywell Inc.  
Twin City Army Ammunition Plant  
New Brighton, Minnesota 55112

Larry Malvern  
Department of Engineering Sciences  
University of Florida  
Gainesville, Florida 32611

Ronald L. Mann  
General Electric Company  
Building 5, Room F4 Court Street  
Syracuse, New York 13221

William P. Martin  
112 Rub Royal  
Slidell, Louisiana 70458

Andrew E. Mathew  
Rex, Thompson & Partners, Newnham  
West Street  
Farnham,  
Surrey  
England

Ralph L. McGuire  
AFATL/DLYV  
Eglin AFB, Florida 32542

William A. Millavec  
Senior Research Engineer  
Weidinger Associates  
3000 Sand Hill Road  
Building 4/Site 155  
Menlo Park, California 95025

Tom Miller  
USAF  
Ramstein AFB, Germany  
APO, New York 09012

Paul E. Minto  
USAF Weapons Laboratory  
Civil Engineering Research Div/NTESA  
Kirtland AFB, New Mexico 87117

Bruce L. Morris  
Southwest Research Institute  
P.O. Drawer 28510  
San Antonio, Texas 78284

Dennis Morrison  
Campus P.O. Box 25  
Albuquerque, New Mexico 87131

R. A. Muldoon  
Mechanical Engineer  
AMMRC  
Arsenal Street  
Watertown, Massachusetts 02172

Phillip T. Nash  
Southwest Research Institute  
P.O. Drawer 28510  
San Antonio, Texas 78284

James S. O'Brasky  
Naval Surface Weapons Center  
Code G31  
Dahlgren, Virginia 22448

Thomas L. Paez  
Department of Civil Engineering  
University of New Mexico  
Albuquerque, New Mexico 87131

Hermann Fahl  
NATO-International Staff  
Airfield Section  
NATO Headquarters  
1010 Brussels  
Belgium

A. G. Papp  
Mason & Hanger, Silas Mason Co., Inc.  
P.O. Box 30020  
Amarillo, Texas 79177

H. R. Perry  
Mechanical Engineer  
NSWSES, Code 6303  
Port Hueneme, California 93043

M. A. Plamondon  
AFWL/NTE  
Kirtland AFB, New Mexico 87117

Myron Plooster  
Denver Research Institute  
University of Denver  
P.O. Box 10127  
Denver, Colorado 80010

John C. Pulos  
NKF Engineering Associates, Inc.  
8150 Leesburg Pike  
Vienna, Virginia 22180

Rex N. Randolph  
Naval Weapons Center  
Code 3917  
China Lake, California 93555

P. Riedel  
WHQ Section, NATO Headquarter  
Brussels  
Belgium

Greg Riggs  
DFCE  
U.S. Air Force Academy,  
Colorado 80840

Paul L. Rosengren, Jr  
AFESC/RDCS  
Tyndall AFB, Florida 32403

C. Allen Ross  
University of Florida  
Eglin Graduate Center  
P.O. Box 1918  
Eglin AFB, Florida 32542

Ranbir S. Sandhu  
Ohio State University  
2070 Neil Avenue  
Columbus, Ohio 43210

Robert Schilling  
Bundesminister der Verteidigung  
5300 Bonn 1; Postfach 1328  
F.R. Germany

Dorman Schmidt  
Engineer Technician  
DFEM/USAF  
Colorado Springs, Colorado 80840

Eberhard Schnieder  
Ernst-Mach-Institut  
Eckerstrasse 4  
7800 Freiburg 1. Br.  
F.R. Germany

Howard L. Schreyer  
New Mexico Engineering Research Institute  
University of New Mexico  
Campus P.O. Box 25  
Albuquerque, New Mexico 87131

Surendra P. Shah  
Civil Engineering  
Northwestern University Tech. Institute  
Evanston, Illinois 60201

Robert L. Sierakowski  
Department of Engineering Sciences  
College of Engineering  
University of Florida  
Gainesville, Florida 32611

Joseph A. Smith  
AFATL/DLJW  
Eglin AFB, Florida 32542

Kim B. Sorenson  
Sandia National Laboratories  
P.O. Box 5800  
Organization 3632  
Albuquerque, New Mexico 87185

Ervell A. Staab  
U.S. Army Corps of Engineers  
Missouri River Division  
Box 103 DTS  
Omaha, Nebraska 68101

D O Swint  
Department of Civil Engineering  
USAF Academy  
Colorado Springs, Colorado 80840

Richard D. Szczepanski  
Orlando Technology, Inc  
P.O. Box 855  
Shalimar, Florida 32579

Wendell D Thomas  
262 Georgia Avenue  
Valparaiso, Florida 32580

Norris O. Thompson, Jr  
3460 TecIG/TTMTD-S  
Lowry AFB, Colorado 80230

Paul Thompson  
AFESC/RDC  
Tyndall AFB, Florida 32403

Fred Torgerson  
Operations Research Analyst  
HQ PACAF/OA  
Hickam AFB, Hawaii 96853

George E. Veyera  
Department of Civil Engineering  
Colorado State University  
Ft Collins, Colorado 80523

William C. Vogt  
Deputy, Targeting Concepts  
and Applications Division  
AFIS/INTA  
Bolling AFB, DC 20332

Rudolph H Volin  
Code 5804  
U.S Naval Research Laboratory  
Washington, DC 20375

Frhr von Oer  
Brigadier General  
Federal Armed Forces Institute  
for Operational Analysis and Exercises  
Amt fur Studien und Ubungen der Bundes  
Friedrich-Ebert-Str. 72  
5060 Bergisch Gladbach 1  
F R. Germany

Bengt E. Vretblad  
Royal Swedish Fortifications Administration  
S-63189 Eskilstuna  
Sweden

Neal Ware  
U S. Army Human Engineering Laboratory  
Building 459, DRXHE-CC  
Aberdeen Proving Ground,  
Maryland 21005

George W. Watt  
AFIT/ENY  
Wright-Patterson AFB, Ohio 45433

Bill G Watters  
Bolt Beranek and Newman Inc  
70 Fawcett Street  
Cambridge, Massachusetts 02238

Gale Weeding  
Denver Research Institute  
University of Denver  
P.O. Box 10127  
Denver, Colorado 80208

Brad Weich  
Goodyear Aerospace Corporation  
1210 Massillon Road  
Akron, Ohio 44315

Paul Weidinger  
Weidinger Associates  
333 7th Avenue  
New York, New York 10001

Peter S Westine  
Southwest Research Institute  
P O. Box 28510  
San Antonio, Texas 78284

Stephen R. Whitehouse  
AFWL/NTES  
Kirtland AFB, New Mexico 87117

Kaspar J Willam  
Campus Box 428  
University of Colorado  
Boulder, Colorado 80309

William E Wolfe  
Ohio State University  
Columbus, Ohio 43210

Felix S Wong  
Weidinger Associates  
3000 San Hill Road, 4-155  
Menlo Park, California 94025

Michael K W Wong  
AFWL/NTESA  
Kirtland AFB, New Mexico 87109

Clifton D Wright, Jr  
Major General  
Director of Engineering and Services  
HQ USAF/LEE  
Washington, DC 20330

Jerry Yatteau  
Denver Research Institute  
P.O. Box 10127  
Denver, Colorado 80208

## AUTHOR INDEX

### Part 2

Abt, S R., 62  
Anandarajah, A., 69  
Arulanandan, K., 69  
Bailey, R. K., 116  
Balsara, J. P., 91  
Bousek, R. R., 122  
Bratton, J. L., 76  
Bretz, T. E., Jr., 29  
Brook, M., 116

Carson, J. M., 128  
Carter, W. J., 59  
Charlie, W. A., 62  
Collins, J. A., 35  
Coltharp, D. R., 133

Dass, W. C., 76  
Davison, D. K., 43

Forster, J. J., 116  
Fuehrer, H. R., 97

Galloway, R. G., 53

Haltiwanger, J. D., 1  
Higgins, C. J., 5  
Hobbs, B., 139

Isenberg, J., 88

Kiger, S. A., 94

Levine, H. S., 103

Meegoda, N. J., 69  
Millavec, W. A., 88  
Morrison, D., 145

Nash, P. T., 29

O'Brasky, J. S., 48, 110

Patrone, H. D., 62

Raney, E. M., 103  
Rosengren, P. L., Jr., 25

Sandhu, R. S., 82  
Smith, T. N., 48  
Szczepanski, R. D., 35

Veyera, G. E., 62

Whitehouse, S. R., 148

AD P 001749

HAS A DECADE MADE A DIFFERENCE?

J. D. Hiltiwanger

University of Illinois  
Urbana-Champaign

Last November I received a letter from Allen Ross, the coordinator of this symposium, describing the plans that were being made for the symposium and inviting me to speak at this, the opening session of it. The program certainly sounded like an interesting one, and, in a weak moment, when May 10, 1983 seemed to be a long way in the future, I accepted his invitation.

But I must confess to some uncertainty as to the extent to which my background will permit me to contribute usefully to the subject being addressed by this symposium. After all, while I have been rather closely involved over the years with problems related to the behavior of structures when subjected to the effects of nuclear weapons, and with the development of procedures and criteria for the design of structures to resist nuclear weapons' effects, I have had rather limited and somewhat indirect experience in regard to the response of structures to the effects of conventional weapons. However, upon reflection, it did seem possible that the problems and questions being addressed here this week might be placed in useful perspective if someone were to address them, in very general terms, against a background of the concepts and the experimental and analytical methodologies that have been developed in recent years in an effort to understand the response of structures to the effects of nuclear weapons.

To place the questions and problems that are being addressed here in perspective, we should remember that the most recent publications that attempt to define the state-of-the-art in this area are the Department of the Army TM5-855-1 (Fundamentals of Protective Design, Non-Nuclear), which is now being revised, but which was published in 1965, and AFWL-TR-70-127 (Protection from Non-Nuclear Weapons), which was published by the Air Force Weapons Laboratory in 1971. There is, additionally, a tri-service report entitled "Structures to Resist the Effects of Accidental Explosions" dated 1969, which also holds some interest for us. The youngest of these documents is now 12 years old, and the research data upon which they relied were generally much older, except to the extent that research into the behavior of structures under nuclear weapons' effects was extrapolated for applicability to the behavior of structures under conventional weapons' effects.

In preparation for this symposium, and to increase my familiarity with the state-of-the-art as published in the area of protective design for non-nuclear effects, I spent a substantial amount of time studying the documents noted above. As I studied those documents, I was struck by several factors, probably the most significant of which was that the design of structures to resist conventional weapons' effects is significantly more complex than is the design of structures to withstand the effects of nuclear weapons. In the case of nuclear weapons' effects, there are, really, only three problems that face the designer of a protective structure. These problems can be identified, in general terms, as follows:

- (1) Define the free-field, blast-induced environment in which the structure will exist;
- (2) Define the time-dependent and spatially distributed forces and motions that are imposed by this environment on the structure;
- (3) Compute the response of the structure to these blast-imposed excitations.

As those of you who have been involved in protective construction for nuclear effects will agree, this is a bit of an oversimplification, not in the statement itself, but in the implications of it. In most cases, there exists within each of these three steps in the study process some very big questions to which we still have very poor answers, despite the decades of research and study that have gone into them. For example, we are still unable to predict the free-field, blast-induced environment with confidence, under other than the most ideal of circumstances. Illustrative of this is the fact that we are still able to plot free-field overpressure and dynamic pressure-time functions with confidence only when the blast is propagated over an ideal surface. If we introduce dust and moisture into the air, or propagate the blast across an irregular surface with obstructions on it, we are in trouble.

And even if we do define the free-field, blast-induced environment with confidence, it is no mean trick to develop from these "known" free-field effects, the forces and/or motions that they impose on a structure which they envelope. Among the early problems of nuclear protective construction with which I was associated back in the mid-fifties (almost 30 years ago) was the behavior of

typical mill buildings to nuclear air blast loadings. To this end, we tested such structures in full-scale and in small-scale models, and we developed simple analytical models in an effort to replicate analytically the results that were observed in the tests. But what many of you may not know is that this work continues to this day. Within the last two years, there have been more tests and more analyses in a continuing (or, in this case, more correctly, a renewed) effort to define, in time and in spatial distribution, the forces produced by the air blast on the structure.

Similarly, back in the mid-fifties, my colleagues and I were interested in the behavior of shallow buried, reinforced concrete box-type structures. And we tested some and we analyzed them. And on this basis we evolved failure criteria and design procedures for such structures. But within the last two years, under a program funded by DNA and conducted experimentally by the Waterways Experiment Station, with analytical support from other laboratories, it has been shown that our earlier work in this regard was totally inadequate. The interaction between the structure and the soil around it is much more complex than was earlier assumed, and such shallow buried structures are, generally, much more resistant to nuclear blast effects than they were earlier thought to be.

And the illustrations of the problems that persist in our efforts to learn how to design structures to resist nuclear weapons' effects could be continued. It takes very little imagination to recognize the problems that are associated with the design of an above-ground arched structure, or of the same structure partially buried or mounded, or of a minuteman silo. But despite the complexity of the problem, in each case, the total problem can be reduced to the three components that I identified earlier --

- (a) Definition of the free-field, blast-induced environment.
- (b) Definition of the forces and/or motions imposed by this environment on the structure.
- (c) Computation of the response of the structure to these blast-imposed excitations.

In the case of conventional weapons, it seems to me that the problems are far more complex. To be sure, the design of a structure to withstand the effects of conventional weapons can be reduced to the same three problem components, but for conventional weapons each of these three primary problem components contains a subset of clearly distinguishable problems.

For example, for a nuclear protective structure designer, the threat is rather completely defined by specification of the weapon yield, its height-of-burst, and the ground range and depth-of-burial (if any) of the target structure. Within the limits of currently available technology, this should permit us to define the blast-induced environment around the structure, estimate the forces and/or motions thus imposed on the struc-

ture, and then to analyze the structure. Clearly, this scenario presumes that the structure of interest is also defined, as are the properties of its materials and of those materials which are around it.

But for a protective structure to resist conventional weapons' effects, the problem is not nearly so simply put--even acknowledging an oversimplification in the preceding statement descriptive of the nuclear case. For the nuclear case, at least as far as the structural designer is concerned, there is only one weapon of interest. But "conventional weapons" includes a host of different types, which produce different environments around and responses of a structure. Reference to the previously cited most current reference manuals on this subject identifies a number of different weapons of potential interest, a partial list of which would include:

Projectiles: Armor Piercing Solid Shot  
 Armor Piercing with Bursting Charge  
 Armor Piercing, Capped, with Bursting Charge  
 High Explosive Shell

each of which come in an assortment of sizes and with a variety of delivery systems.

And, then, we have bombs of several different types: General Purpose, Semi-Armor Piercing, Armor Piercing, and Fragmentation, each of which also comes in a variety of sizes and charge weights, and high explosive content.

Each of these weapon types poses its own unique set of problems for the engineer who would design a structure to resist its effects. For penetrating weapons, the depth of penetration is a function of the weapon characteristics (its weight, shape, resistance, fuzing, incident velocity, angle of incidence, and angle of yaw), and the properties of the target material (its strength, density, porosity, ductility, and thickness). And associated with weapon penetration, we must be concerned also with front face cratering and rear face scabbing under conditions of partial penetration or ricochet, which are also functions of the type of weapon, its velocity and angle of impact, and of the thickness and properties of the slab surface being impacted. Clearly, these are factors which must be considered when designing to resist conventional effects, but which are of little or no concern to the nuclear protection designer.

Even the blast effects, as opposed to impact and penetration effects, are more complex for conventional weapons than for nuclear weapons, because of the diversity of explosive types, the size, shape and strength of casings, the orientation of the weapon with respect to the surface being loaded and indeed, the location of the point of detonation with respect to the ground surface, either above or below it. All of these factors influence the variation of blast-induced pressure with time, as functions of distance from the point

of detonation. The blast loading problem is further complicated for conventional weapons by virtue of the fact that the dimensions of the loaded structure are frequently of the same order as are the distances from the structure to the point of detonation. As a consequence, the dynamic force applied to the structure by the blast varies not only in time, but also spatially over and around the structure. The same problem exists when a structure is loaded by a nuclear blast, but in this case the dimensions of the structure are, generally, sufficiently small relative to its distance from the point of detonation that, for free-field effect determination, the structure can be considered a point target. Such is clearly not the case for conventional weapon effects.

And associated with this greater non-uniformity of blast-induced loading on the structure, relative to the situation that prevails under nuclear effects, is a correspondingly greater uncertainty or variation in the possible or probable failure modes of structural response that must be investigated. Under nuclear blast, failure usually manifests itself as excessive deformation in a readily definable mode, generally the fundamental mode, of a critical element (a wall or roof) of the structure. The non-uniformity of the loading imposed by the blast pressures from conventional weapons will excite more complex responses. As a consequence, one must anticipate the possibility not only of dominant response, up to and including failure, in the fundamental modes of the loaded walls or other external structural elements, but also of severe localized deformations, including the possibility of localized penetrations, in regions of intense blast-induced pressure.

If the comparisons just drawn leave us a bit discouraged, then they have had the desired effect. A decade of neglect, albeit benign, has made a difference. While we have worked with reasonable diligence during the last decade to improve our ability to design structures to resist the effects of nuclear weapons, we have made relatively little progress in the realm of structural design for conventional weapons' effects.

To be sure, within the last decade there has been a substantial amount of research that is directly applicable to protective design for conventional weapons' effects, but the effort in this regard has been rather fragmented. And some of the recent research to improve our ability to design protective structures for nuclear effects finds applicability also in the realm of protective design for conventional effects. But because of the differences in the problems that are faced in these two cases, as illustrated earlier, technology transfer between them is not as great as one might expect, or hope.

Consequently, it is important (Perhaps I should say "imperative".) that we concentrate our attention again on the effects of conventional weapons. Where recent data exist, we should translate those data into conveniently usable

design criteria and procedures. And where adequate data do not exist, we should undertake the research needed to obtain them. Fortunately, despite my earlier rather gloomy comparisons, there does now exist a significant amount of comparatively recent, directly applicable research data, as well as the potential for substantive technology transfer from the nuclear protection arena. But to compensate for the slow rate of progress during the last decade, we need now to redouble our efforts to develop new and improved methods of providing the needed protection to the effects of conventional weapons.

I feel this now much more strongly than I did even a few weeks ago. It was my privilege, then, to visit a number of our air bases in Europe as a member of an ad hoc committee of the Air Force Science Advisory Board. This committee was established last Fall to give guidance to Gen. Wright's shop--the Engineering and Services Division--in regard to the research that is needed to improve the ability of his people to provide the services that are desired and expected of them. And the primary job that is expected of them in wartime is the provision of an operational base from which aircraft may be launched and to which those aircraft may return, and be launched again, and again, and again. To do this, we must provide adequate protection for both sensitive equipment and operational personnel. And, at the moment, this is not being done to the extent that it should be done.

The personnel in the field feel very strongly about this, and I think that you and I would share their sense of urgency if we were to trade places with them. May I share with you a shopping list, as it were, of research requirements in the area of protective construction that was developed recently by Air Force Civil Engineers now stationed in Europe. This list was prepared by Maj. Bartel and Maj. Chisholm, both of whom are now stationed at Ramstein Air Base in West Germany. A sampling of their requests would include but would certainly not be limited to the study of:

- (1) Precast modular protective structures - i.e., the AMF-80 (French sewer pipe) -  
Advantages: Rapid fielding  
Natural camouflage by berming  
Quality control
- (2) Improved antipenetration systems - possibly rock rubble over reinforced concrete to improve the probability of reducing the effectiveness of the weapon or, perhaps, even destroying it.
- (3) An enhanced conventional weapons' effects program - To obtain better definitions of blast, shock and fragment loads on protective structures.
- (4) Tests of semi-hardened walls.
- (5) Modular concrete revetments.
- (6) Effects of earth berms on the hardness of structures.
- (7) Design criteria for blast valves.
- (8) Design guidance for shock isolation of

- internal equipment. And finally,  
(9) Publication of a revised and updated Protective Construction Manual.

Clearly, this is but a sample of the problems that need to be addressed as we renew our research and development program in the area of protective construction for conventional weapons' effects. And I am heartened in this regard as I review the program of the symposium that we are convening here this morning. It addresses not only the specific and immediate problems posed by Majors Bartel and Chisholm from their unenviable vantage point of vulnerability in Europe, but much, much more. It is, indeed, a comprehensive program that embraces the full spectrum of problems that confront us. It represents impressively the recently reawakened interest in protective construction to resist the effects of conventional weapons and it brings to bear on these problems the technologies of a multiplicity of disciplines. It does, indeed, provide a strong springboard for the further development of protective construction technology. Let us hope that the impetus provided by this symposium will not be lost, but that the work here begun will be continued. We can ill-afford another decade of relative inactivity in this very important aspect of our nation's military preparedness.



AD P001750

# SOME CONSIDERATIONS IN THE ANALYSIS AND PREDICTION OF GROUND SHOCK FROM BURIED CONVENTIONAL EXPLOSIONS

Cornelius J. Higgins

Applied Research Associates, Inc., Albuquerque, New Mexico

## ABSTRACT

This paper discusses several topics associated with the analysis and prediction of ground shock from buried conventional explosions. The paper is not intended to provide detailed equations for ground shock predictions. Other papers in this conference provide such information. Rather, this paper is intended to address topics associated with general methodology and uncertainty. As a background for discussion, the first part of the paper lists and briefly discusses the major parameters which govern the ground shock. Some of the parameters are treated in more detail in later sections of the paper. The second and main part of the paper treats scaling. It attempts to put the usefulness of dimensional analysis, scaling and theoretical calculations in perspective. The third portion of the paper discusses the characteristics of a limited data set with respect to material properties and depth of burst factors. Some brief comments about soil-structure interactions and loads on structures are made in a fourth part. Finally, research needs to enable improvement in conventional ground shock and soil-structure interaction technology are mentioned.

## PARAMETERS INFLUENCING GROUND SHOCK

The term ground shock as used here includes all of the stresses and motions induced in the ground as a result of an explosion. The stresses are most important from a structure survivability viewpoint while the motions affect the response of structure contents (equipment and people). Particle velocity is also important as an indirect measurement of stress.

In general, structures are designed to resist a very near hit by a conventional weapon. As a result scaled ranges of interest are in the range of  $0.5 \text{ ft/lb}^{1/3}$  to  $1.5 \text{ ft/lb}^{1/3}$  (4 to 12 ft for a 500 lb bomb). Under this condition the ground shock very close-in to the detonation is important. Figure 1 illustrates two of several potential conditions under which close-in ground shock

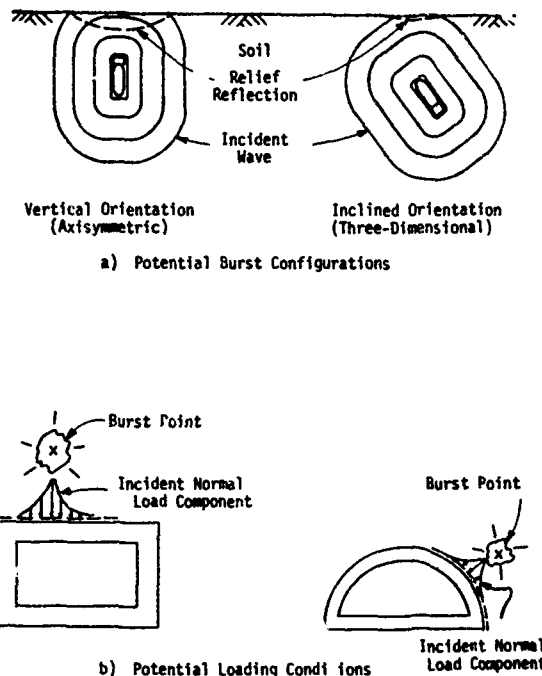


Figure 1. Some Potential Burst and Loading Conditions for Conventional Weapons

parameters must be characterized. Several factors can be observed. First, it is apparent that the wave contours near to the source are not spherical. Hence, the stress conditions at the wavefront are nonuniform. Second, because of the nearness of the free-surface, relief waves are initiated shortly after detonation. The amplitude and arrival time of these waves at some point are dependent upon the depth of burial. Third, it is likely that the weapon will be oriented in some inclined position with respect to the free surface and the structure. Hence, the problem is inherently three-dimensional.



A full list of parameters influencing the ground shock includes:

- Weapon Shape
- Case Properties
- Explosive Type and Amount
- Depth of Burial
- Geologic Material Properties
- Layering

The following paragraphs briefly describe the importance of each parameter. The layering category includes the burster slab problem as a subset. This topic is not covered here but is discussed by others in this conference.

Conventional weapons, for aerodynamic stability, penetration and other reasons, are normally not perfectly spherical. Rather, they are more cylindrical or cigar shaped. In the close-in region this shape will have an influence on the ground shock characteristics but the amount of influence is uncertain. It is often assumed that detailed shape effects cannot be detected at distances from the explosions which are large compared with the explosive dimensions. However, there is some evidence that, although attenuation rates at large distances are spherical, the actual amplitude of ground shock is different from spherical. Figure 2 compares ground shock measurements from three explosions of 40 tons of ammonium nitrate slurry. One explosion (DIPIA) was concentrated while the other two were in rectangular vertical arrays of different sizes. The data indicate that ground shock amplitudes from the arrays in a direction perpendicular to the array are reduced in the close-in region but more intense at greater ranges. It appears that the distribution of explosive has an influence on

ground shock in both the near and far regions but this effect has not been thoroughly evaluated.

In the ground, as opposed to in the air, the effect of the case is thought to be small because all of the energy transmitted to the case is ultimately coupled into the ground. It is possible that the mass, stiffness and strength of some cases might serve to contain the explosion to some extent and thereby stretch the stress wave leading to a somewhat reduced pressure for a given impulse. The high impedance of the case might also serve to alter the boundary condition at the explosive/soil interface.

The amount of explosive simply determines the range to which ground shock effects of a given level will propagate in a given material. Explosive type is important because it determines the initial conditions in the explosion. Explosive parameters of importance include detonation pressure, detonation speed, initial density, initial specific energy and ratio of specific heats. In general, equivalencies between explosives have been determined on the basis of initial specific energy and, sometimes, on the basis of measured effects. This latter method is a good method if adequate measurements are available but specific energy alone is unsatisfactory. As will be shown later, all the other explosive parameters are also important.

Burial improves coupling and, therefore, increases the range to which ground shock levels of a given amount persist. Coupling factors have been developed by various investigators for different parameters (e.g. pressure, impulse,

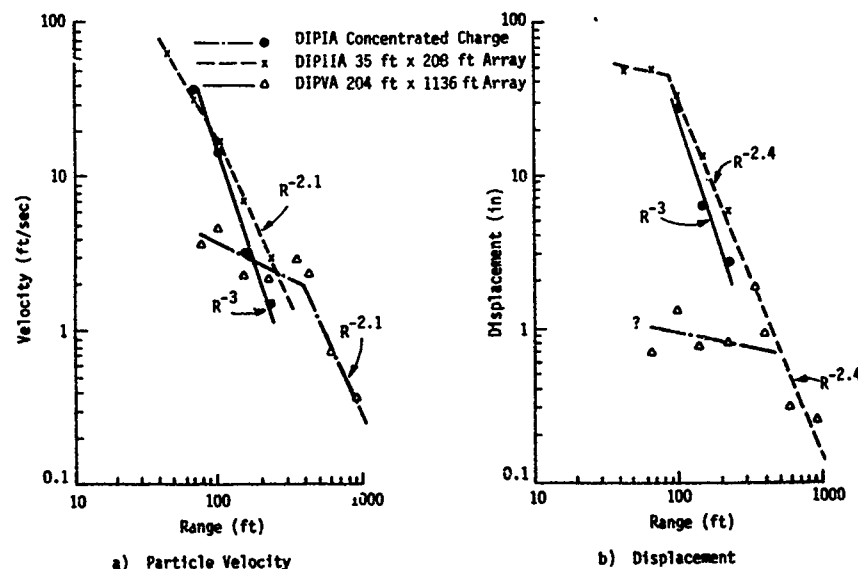


Figure 2. Illustration of Effect of Charge Shape on Ground Shock

velocity, displacements). For example, Lampson (Ref. 1) suggests a single coupling factor for all parameters. The factor achieves a maximum at a scaled depth of burst of  $2.0 \text{ ft/lb}^{1/3}$  and even diminishes for greater depths. There are several concerns with this relationship. First, one would expect the coupling to achieve a maximum at some depth and then remain at that maximum rather than decrease. Second, it is expected that maximum coupling for some parameters (e.g. stress, velocity, acceleration) would be achieved at a more shallow depth than parameters which are integrated quantities (e.g. impulse, displacement). Figure 1 illustrates the effects of the free surface. A major relief wave, which results from the free surface reflection, penetrates back into the ground and erodes the back end of the initial pulse. Beyond some depth, the relief wave arrives too late to affect the peak parameters. At more shallow depths, it has an effect but the parameters which occur close to the wavefront are affected last. Also, it is apparent that positions beneath the explosion are affected less than positions to the sides of the explosive which are nearer to the free surface.

Material properties of importance include constrained modulus, hysteretic compaction, shear stiffness and strength. As will be illustrated in a later discussion, it is becoming apparent that a multi-phase model of the air, water, and grain matrix may be necessary for modeling wet material. Grain matrix models which include coupling of volumetric and deviatoric strain will be necessary to predict multi-phase response. Geologic layering in the vicinity of the burst can intensify the ground shock due to reflection. This can be important if a near-surface water table is present.

Figure 1 also illustrates some of the complexities associated with the interaction of the free-field waves with structures. Generalized incident normal loads are shown. The word "incident" is used here because the actual load experienced by the structure is dependent upon complex soil-structure interaction. Three important points must be made. First, the loading is nonuniform both in time and space. This results from the relative smallness and nearness of the source with respect to the structure, as well as the geometry of the structure in the case of the arch. Second, the load is generally asymmetric with respect to the structure leading to important three-dimensional effects. Third, although not illustrated, there are strong shear load components with respect to the structures. These result from the large spatial load gradients. The time history of the load has not been shown although it is known to be highly transient in nature. All of these conditions combine to complicate analysis and prediction of soil-structure interaction and the resulting actual loads experienced by the structures.

Some comments on soil-structure interaction are given in a later paragraph.

#### DIMENSIONAL ANALYSIS AND SCALING

The subject of scaling continually arises as various investigators attempt to analyze and collapse the results of experiments and to use these results to predict new conditions. Cube root of yield scaling is well known and reasonably accurate so long as yield variations are within about an order of magnitude (i.e., gravity effects are small). Scaling to account for material properties however has not been successful. This section reviews dimensional analysis and scaling concepts in an attempt to reveal the usefulness and shortcomings of scaling as well as provide some insight into observed behavior.

The need for scaling derives from the fact that the phenomena involving explosive sources in inelastic media are so complex that mathematical formulation of closed form solutions is extremely difficult. As a result, it is common practice to evaluate the phenomena experimentally or numerically and develop empirical relations from measured or calculated response data. The main quantitative relations are derived from data but calculations are useful in providing qualitative guides to behavior.

Whether a theoretical or an experimental approach is taken to a problem, the initial steps in the analysis must be; first, a qualitative evaluation of the phenomena and, second, identification of the important physical parameters which control the phenomena. The two approaches depart at this point. The theoretical approach attempts to develop a mathematical model for the problem which will lead to the mathematical relations between the parameters, while the experimental approach attempts to establish the relations by means of experiments in which the governing parameters are varied in a reasonable way.

Experiments are expensive, and it is important to keep the experiment size and the number of parameter variations to a minimum. Further, it is important to have a uniform guide for "scaling" and evaluating experimental results from different experiments so that empirical relations among the parameters can be developed. Dimensional analysis is a very useful tool in meeting these requirements. The fundamentals of dimensional analysis are described in a number of references (e.g. Refs. 2 and 3). Some of the basic results are reviewed here and used to develop consistent scaling parameters for various high explosive configurations.

Dimensional analysis is based upon the fact that most of the parameters that are dealt with in physical sciences depend in magnitude upon the scale used to measure them. Such parameters

are called dimensional quantities. Non-dimensional quantities are independent of the system of measurement. The establishment of units for three physical quantities is ordinarily enough to define the units for any other physical quantity. Mass, length and time or force, length and time are convenient units usually selected and they are called fundamental or primary units. In thermodynamic problems a fourth unit, perhaps temperature, is also necessary. Other units, for example velocity, may be derived from the fundamental units and these are called derived or secondary units. If force, length and time are selected as fundamental units, the associated dimensions can be written:

$$\text{dimension of force} \stackrel{d}{=} [F]$$

$$\text{dimension of length} \stackrel{d}{=} [L]$$

$$\text{dimension of time} \stackrel{d}{=} [T]$$

where  $\stackrel{d}{=}$  indicates dimensional equivalence and the brackets  $[\ ]$  indicate the dimensions of the quantity. The dimensions of any physical quantity can be written as a monomial power of the three fundamental units or

$$\text{dimensions of a quantity} \stackrel{d}{=} [F]^a [L]^b [T]^c$$

where  $a$ ,  $b$ , and  $c$  are exponents. If the quantity is dimensionless then  $a = b = c = 0$ .

Physical laws are function relations between the parameters which define the phenomena. Since the phenomena are independent of the system of measurement, the functional relations must be independent of the systems of measurement. Hence, if the relation between the physical parameters governing a particular phenomena is

$$f(A_1, A_2, A_3, \dots, A_n) = 0 \quad (1)$$

then

$$[A_1]^a [A_2]^b \dots [A_n]^c \stackrel{d}{=} [F]^0 [L]^0 [T]^0 \quad (2)$$

Equation 2 is a statement of dimensional homogeneity and states that the most general term in equation 1 must be dimensionless.

Since the functional relation must be independent of the system of units, equation 1 can be written as

$$f(\pi_1, \pi_2, \pi_3, \dots, \pi_m) = 0 \quad (3)$$

where  $\pi_1, \pi_2, \dots, \pi_m$  are dimensionless quantities and are functions of the original parameters. Buckingham's Pi theorem (Ref. 4) states that if equation 1 is complete, the  $\pi$  terms of equation 3 are independent products of

the original parameters  $A_1$  through  $A_n$ , are dimensionless in the fundamental dimensions, and that the number of terms in the solution  $m$ , is less than the original number of terms,  $n$ , by a factor,  $k$ , where  $k$  usually equals the number of fundamental dimensions, i.e.,  $m = n - k$ . A proof for the theorem is given in reference 2.

If the number of fundamental dimensions is 3 (e.g. F, L, T) then the general relation (Eq. 3) usually contains 3 terms less than the original relation (Eq. 1). This simplification, as well as the formulation of the non-dimensional  $\pi$  terms, are the main advantage which dimensional analysis lends to the analysis of a physical problem. If the number of fundamental dimensions equals the number of physical parameters with independent dimensions which govern a phenomena, then the relations will be completely determined to within constant factor by dimensional analysis (Ref. 2). In the most general case, however, dimensional analysis does not yield the functional relation. It must be determined from experiments.

In formulating a dimensional analysis, it is necessary to include all the parameters which may control the phenomena even if they are constant. The derivation of the dimensionless  $\pi$ -terms may then be determined in any number of ways. Inspection is one approach, but the use of the statement of dimensional homogeneity (Eq. 2) provides a systematic approach.

One of the first to use dimensional analysis to include material properties in scaling terms was Hendron (Ref. 5). He considered the case of a spherical explosion in a homogeneous elastic soil. The parameters listed in Table 1 were considered important in governing the phenomena. Dimensions of force, length and time are taken as fundamental.

Table 1

Some Parameters Determining Explosion Phenomena from a Spherical Source in an Elastic Soil

Parameter	Symbol	Dimensions
1. Dependent		
Peak Soil Stress	$\sigma$	$F/L^2$
Peak Particle Acceleration	$a$	$L/T^2$
Peak Particle Velocity	$v$	$L/T$
Peak Displacement	$d$	$L$
Various Characteristic Times	$t$	$T$
2. Independent		
Explosive Energy	$E_0$	$FL$
Range	$R$	$L$
Soil Density	$\rho$	$FT^2/L$
Dilatational Wave Speed	$C$	$L/T$
Poisson's Ratio	$\nu$	---

The equations relating the dependent and independent parameters are

$$\begin{aligned}\sigma &= f_1(E_0, R, \rho, C, v) & (a) \\ a &= f_2(E_0, R, \rho, C, v) & (b) \\ v &= f_3(E_0, R, \rho, C, v) & (c) \quad (4) \\ d &= f_4(E_0, R, \rho, C, v) & (d) \\ t &= f_5(E_0, R, \rho, C, v) & (e)\end{aligned}$$

Dimensional analysis can be used to reduce these equations to the following non-dimensional relationships:

$$\frac{\sigma}{\rho C^2} = f_1 \left[ \frac{(\rho C^2)^{1/3} R}{E_0^{1/3}}, v \right] \quad (a)$$

By similar application of the method illustrated above, the relationships for the other variables can be shown to be

$$\frac{a E_0^{1/3}}{(\rho C^2)^{1/3}} = f_2 \left[ \frac{(\rho C^2)^{1/3} R}{E_0^{1/3}}, v \right] \quad (b)$$

$$\frac{v}{C} = f_3 \left[ \frac{(\rho C^2)^{1/3} R}{E_0^{1/3}}, v \right] \quad (c) \quad (5)$$

$$\frac{(\rho C^2)^{1/3} d}{E_0^{1/3}} = f_4 \left[ \frac{(\rho C^2)^{1/3} R}{E_0^{1/3}}, v \right] \quad (d)$$

$$\frac{(\rho C^2)^{1/3} t}{E_0^{1/3}} = f_5 \left[ \frac{(\rho C^2)^{1/3} R}{E_0^{1/3}}, v \right] \quad (e)$$

The relations previously expressed in equation 6 in terms of five independent variables are now expressed in terms of two independent variables. It is important to note that the relations involve three variables and, therefore, the functions must be considered in three-space.

A major advantage of equations 5 is that they immediately show how the variables should be scaled to determine if experimental data fit the proposed scaling. Range, for example, should be scaled by the inverse of the cube of energy or yield\* and, for experiments in different materials, by the cube root of the constrained modulus of the material. Cube root of yield scaling is common, but the material terms are not normally included. Hendron's

\*It should be noted that range scaling in ground motion literature usually considers charge size in units of weight rather than energy. Since weight is proportional to chemical energy release for a given type of explosive, the scaling is equivalent, but the range term is no longer non-dimensional.

treatment was simple and elegant but unfortunately the resulting  $\pi$ -terms do not collapse available data in different materials. Hendron's dimensional analysis is correct so it is necessary to search for other reasons for the scaling failure. Since dimensional analysis must include all physical parameters which influence the phenomena, even if they are constant, it is possible that some important parameters are absent from Hendron's approach. Westine (Ref. 6) introduced ambient atmospheric pressure but achieved only limited success. Higgins, et al. (Ref. 7) suggested that the peak pressure at the source may be an important parameter. An explosive source which at detonation is instantaneously converted to an ideal gas which contains the energy of the explosion as internal energy was considered. The source characteristics were categorized by the total mass of explosive,  $W$ , the internal energy per unit mass,  $\epsilon_0$ , the initial density,  $\rho_0$ , and the ratio of specific heats,  $\gamma_r$ . The peak pressure of such an ideal gas source is

$$P_0 = (\gamma_r - 1) \rho_0 \epsilon_0 \quad (6)$$

The total explosive energy used to derive equations 15 is simply  $\epsilon_0 W$ .

If  $P_0$  is included in the dimensional analysis then an additional  $\pi$ -term

$$\pi = \frac{P_0}{\rho C^2} \quad (7)$$

must be added to the relations expressed by equations (5). The relations between the dependent and independent parameters can then be written

$$\frac{\sigma}{\rho C^2} = f_1 \left( R \left( \frac{\rho C^2}{E_0} \right)^{1/3}, \frac{P_0}{\rho C^2}, v \right) \quad (a)$$

$$\frac{a}{C^2} \frac{E_0^{1/3}}{\rho C^2} = f_2 \left( R \left( \frac{\rho C^2}{E_0} \right)^{1/3}, \frac{P_0}{\rho C^2}, v \right) \quad (b)$$

$$\frac{v}{C} = f_3 \left( R \left( \frac{\rho C^2}{E_0} \right)^{1/3}, \frac{P_0}{\rho C^2}, v \right) \quad (c) \quad (8)$$

$$d \left( \frac{\rho C^2}{E_0} \right)^{1/3} = f_4 \left( R \left( \frac{\rho C^2}{E_0} \right)^{1/3}, \frac{P_0}{\rho C^2}, v \right) \quad (d)$$

$$Ct \left( \frac{\rho C^2}{E_0} \right)^{1/3} = f_5 \left( R \left( \frac{\rho C^2}{E_0} \right)^{1/3}, \frac{P_0}{\rho C^2}, v \right) \quad (e)$$

Recombination of  $\pi$ -terms can yield an alternate set of relations

$$\frac{\sigma}{P_0} = f_1 \left( R \left( \frac{P_0}{E_0} \right)^{1/3}, \frac{P_0}{\rho C^2}, v \right) \quad (a)$$

$$\frac{a}{c_2} \left( \frac{P_0}{E_0} \right)^{1/3} = f_2 \left( R \left( \frac{P_0}{E_0} \right)^{1/3}, \frac{P_0}{\rho C^2}, v \right) \quad (b)$$

$$\frac{\rho C v}{P_0} = f_3 \left( R \left( \frac{P_0}{E_0} \right)^{1/3}, \frac{P_0}{\rho C^2}, v \right) \quad (c) \quad (9)$$

$$d \left( \frac{P_0}{E_0} \right)^{1/3} = f_4 \left( R \left( \frac{P_0}{E_0} \right)^{1/3}, \frac{P_0}{\rho C^2}, v \right) \quad (d)$$

$$Ct \left( \frac{P_0}{E_0} \right)^{1/3} = f_5 \left( R \left( \frac{P_0}{E_0} \right)^{1/3}, \frac{P_0}{\rho C^2}, v \right) \quad (e)$$

There are many other possible formulations, all correct so long as six independent  $\pi$ -terms are included.

A comparison of equations (3) and (9) indicates that there is no unique way of scaling range or the dependent variables, as was the case in equations (5) when only a limited source description was included. The functional relationships are multivariate. They cannot be reduced to two-dimensions, as is often attempted when scaled response parameters are plotted versus some form of scaled range on log-log paper. Even if the explosive type is the same from event to event, (i.e.,  $P_0$  is constant) the relations remain multivariate as illustrated in figure 3. The solution must be determined empirically by seeking a fit to the data in three-space (four space if Poisson's Ratio is varied). The solution will be a multi-parametered general surface rather than a curve. As more and more parameters are considered (e.g. material nonlinearity, strength, depth of burial) the number of variables increases and the solution becomes more complex.

The scaling considering an ideal gas source was applied to one-dimensional elastic cylindrical calculations. The calculations utilized an ideal gas pressure boundary condition on three elastic materials with properties ranging from those of a soft soil to a moderately hard rock. The specific properties are given in Table 2.

Table 2  
Elastic Parameters Used in Material  
Property Scaling Calculations

Identifier	Unit Weight (lbs/ft <sup>3</sup> )	Elastic Wave Speed, C (ft/sec)	Poisson's Ratio, $\nu$
Elastic 1	109	825	0.3
Elastic 2	115	2750	0.3
Elastic 3	140	8000	0.3

It was found that the scaling without a source pressure term (Eq. 5 adjusted to cylindrical geometry) did not work but that the scaling expressed in equations (9) was needed to

collapse the data. Scaling terms which reduce the results to a two axis problem (i.e. scaled motion versus scaled range) cannot be derived explicitly. However, the results of the calculations were analyzed empirically, and it was found that simple scaling terms were present. The terms were

$$\text{Radial Stress: } \frac{\sigma}{P_0} \quad (a)$$

$$\text{Radial Velocity: } \frac{\rho C v}{P_0} \quad (b)$$

$$\text{Radial Displacement: } \frac{\rho C^2 d}{\gamma^{1/2}} \quad (c) \quad (10)$$

$$\text{Range: } \frac{R}{\gamma^{1/2}} \quad (d)$$

$$\text{Time: } \frac{Ct}{\gamma^{1/2}} \quad (e)$$

where

- $\sigma$  = radial stress
- $v$  = radial particle velocity
- $d$  = radial displacement
- $\rho$  = material mass density
- $C$  = material elastic dilational wavespeed
- $t$  = time
- $\gamma$  = lineal charge density
- $P_0$  = peak source pressure

These terms are precisely those which are implied by a closed form solution to the response of elastic material to a spherical ideal gas loading (Ref. 8).

The correlations which result from these terms are shown for radial stress, radial velocity, and radial displacement in figures 4, 5, and 6 respectively. The  $P_0$  term has been dropped in these figures because it is constant in the three problems. This of course would be the case in the field where a common explosive is used. It can be seen that the calculated results are collapsed very well by the scaling terms of equation 10. The scaling implies that stresses are material independent, the velocity scales by the material impedance ( $\rho C$ ) and the displacement scales by the material stiffness ( $\rho C^2$ ).

Although the scaling described is encouraging, it unfortunately still does not collapse measured data. Near-surface particle velocities from surface tangent HE explosions on different materials, as shown in figure 7, seem to be material independent. Drake and Little (Ref. 10) have observed similar behavior for velocities in different materials beneath surface explosions. Bratton (Ref. 11) has found that the high stress level data that he has analyzed, shown in figure 8, are not material

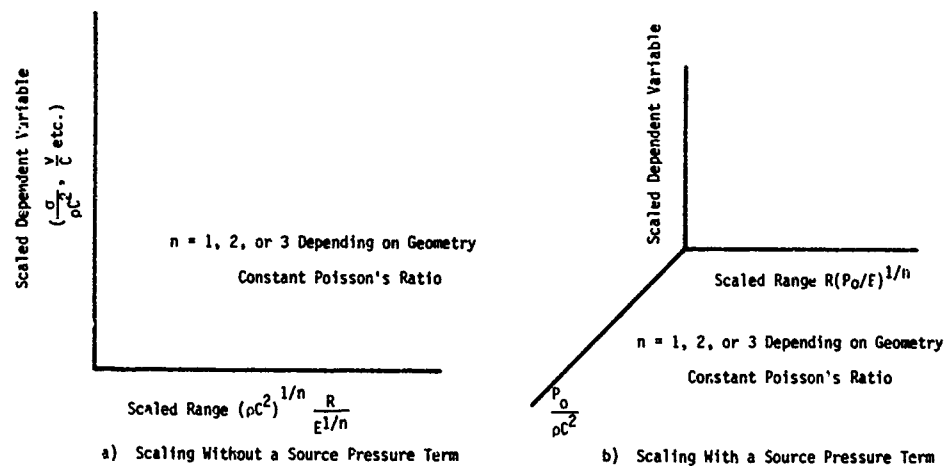


Figure 3. Scaling Implications of Including a Source Pressure Term

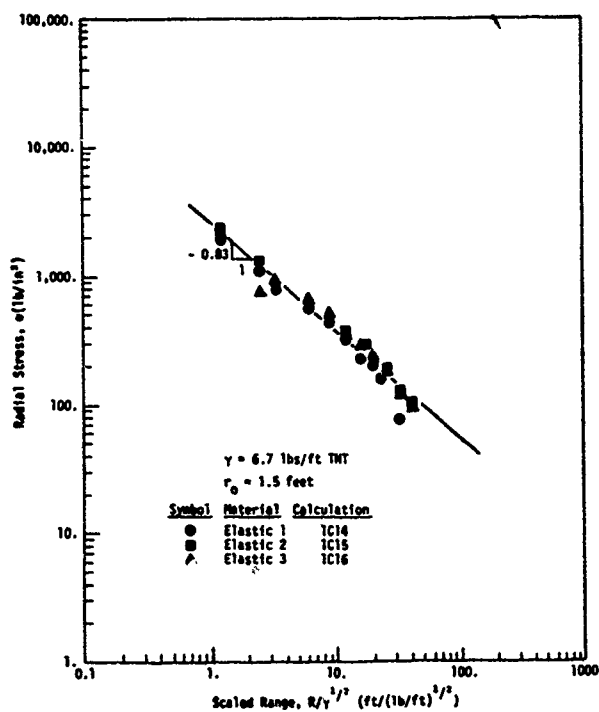


Figure 4. Radial Stress Versus Scaled Range in Different Elastic Materials Loaded by an Ideal Gas Source (Ref. 7)

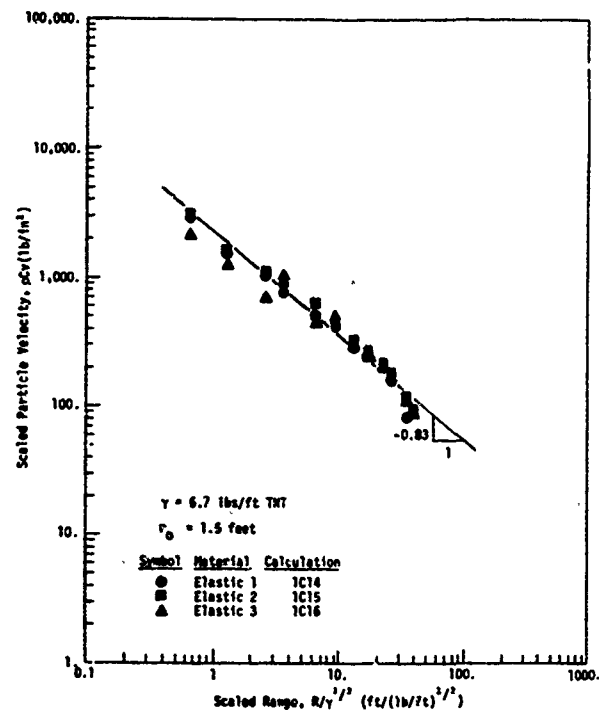


Figure 5. Scaled Radial Particle Velocity Versus Scaled Range in Different Elastic Materials Loaded by an Ideal Gas Source (Ref. 7)

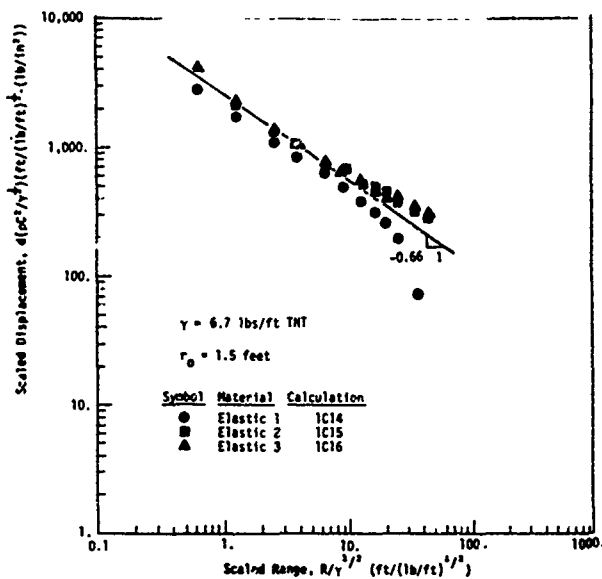


Figure 6 Scaled Displacement Versus Scaled Range in Different Elastic Materials Loaded by an Ideal Gas Source (Ref. 7)

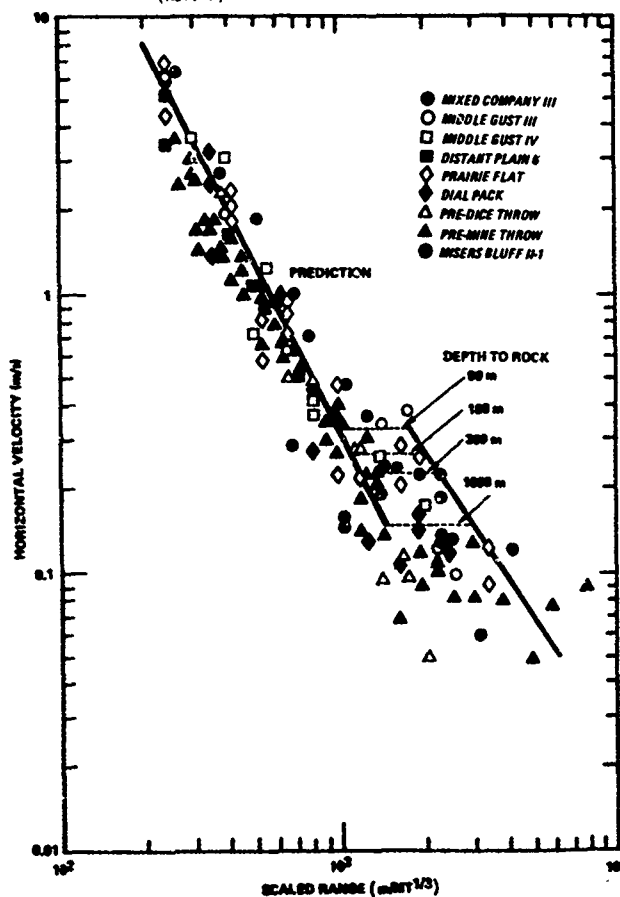


Figure 7. Peak Upstream-Induced Horizontal Velocity from Face Tangent HE Events (Ref. 9)

independent but, rather scale by the inverse of the impedance. All of this suggests that a high explosive source is more of a velocity boundary condition than a pressure boundary condition.

It appears that high explosive sources are much more complex than implied by the simple statement of a yield or total energy or modeled as an ideal gas. Consider a high explosive source which is characterized by the Chapman-Jouguet equation of state. The conditions behind the detonation front are given by:

$$P_{CJ} = \frac{1}{\gamma + 1} \rho_0 D^2 \quad (11)$$

$$\rho_{CJ} = \frac{\gamma + 1}{1} \rho_0 \quad (12)$$

$$e_{CJ} = \frac{\gamma}{(\gamma^2 - 1)(\gamma + 1)} D^2 \quad (13)$$

$$D = C + u \quad (14)$$

where  $P_{CJ}$ ,  $\rho_{CJ}$ , and  $e_{CJ}$  are the pressure, density and energy immediately behind the detonation wave,  $D$  is the detonation velocity,  $C$  is the sound speed behind the front and  $u$  is the particle velocity.

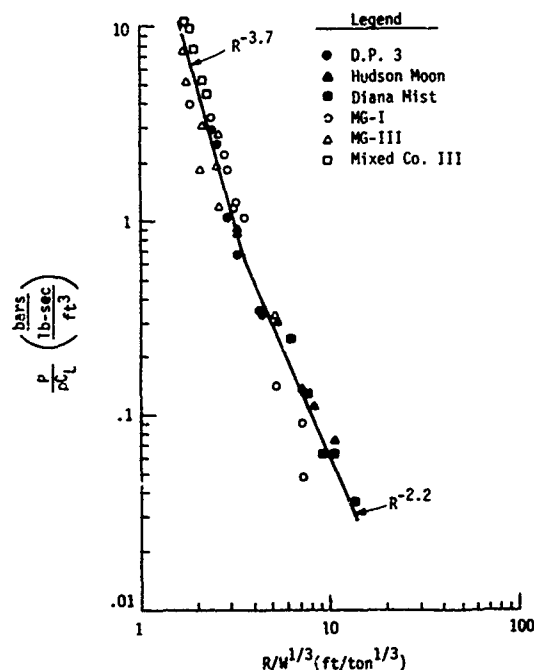


Figure 8. Scaled Peak Pressures for High Explosive Events (Ref. 11)

After detonation the explosive is converted to a very dense, high sound speed gas which has a very high acoustic impedance. This condition is illustrated in figure 9. In order to maintain continuity of stress and velocity across the explosive-soil interface, it is necessary to satisfy the standard interface condition (see e.g. Ref. 12).

$$\sigma_t = \frac{2}{1 + \psi_e} \sigma_i \quad (15)$$

where  $\sigma_t$  = stress transmitted into soil  
 $\sigma_i$  = incident stress in explosive  
 $\psi_e = \frac{\rho C}{\rho_0 D} = \frac{\rho C}{\rho_e C_e}$   
 $\rho$  = soil density  
 $C$  = soil seismic velocity  
 $\rho_0$  = explosive initial density  
 $D$  = explosive detonation velocity  
 $\rho_e$  = explosive density after detonation  
 $C_e$  = explosive sound speed after detonation

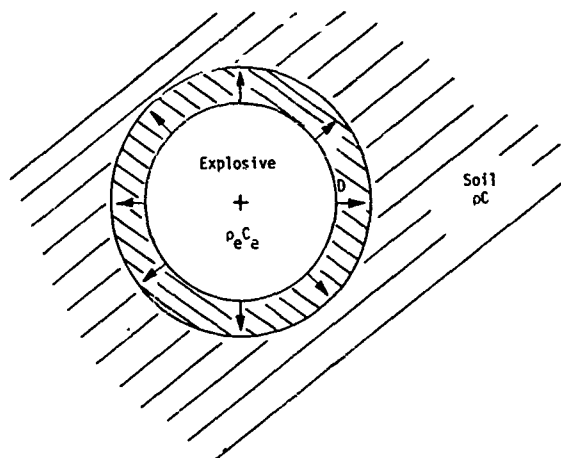


Figure 9. Real Explosive Initial Conditions

Equation 15 can be rewritten

$$\frac{\sigma_t}{\rho C} = K \frac{\rho C J}{\rho_e C_e} \quad (16)$$

$$\text{where } K = \frac{2}{1 + \psi_e}$$

Stress can be converted to velocity by the standard wave propagation relation

$$v = \frac{\sigma}{\rho C} \quad (17)$$

where  $v$  = particle velocity. The particle velocity is therefore

$$v = K \frac{\rho C J}{\rho_e C_e} \quad (18)$$

The factor  $K$  is simply the transmission factor for velocity across an interface. It is plotted versus the ratio  $\rho C / \rho_e C_e$  in figure 10. It can be seen that the maximum value of  $K$  is 2 while the minimum for most geologic materials is about 1.

The treatment of the continuity condition across the explosive-soil interface suggests that the proper scaling terms involving elastic material properties are:

$$\text{Stress: } \frac{\sigma}{\rho C} \quad (a)$$

$$\text{Velocity: } \frac{v}{K} \quad (b)$$

$$\text{Displacement: } \frac{v D}{K W^{1/3}} \quad (c) \quad (19)$$

$$\text{Acceleration: } \frac{a W^{1/3}}{K C} \quad (d)$$

$$\text{Time: } \frac{C t}{W^{1/3}} \quad (e)$$

Since  $K$  varies by no more than about a factor of 2 (within the scatter in a well instrumented experiment) and, on the average, is about 1.5, this analysis suggests that real explosives act more like velocity boundary conditions than pressure boundary conditions. The high impedance associated with case materials would be expected to enhance this effect. These results are now at least qualitatively consistent with the experimental results.

The scaling given in equation (19) was evaluated against one dimensional spherical calculations\* in which TNT explosive was detonated in two elastic materials, one representing soil and the other rock. The parameters used in the calculations are summarized in Table 3. Figures 11, 12, and 13 show the unscaled and scaled peak stress, velocity and displacement versus range for the two calculations. It can be seen that the boundary condition is neither pressure nor velocity but velocity is a better approximation. The scaling of equations (19) does a very good job of collapsing the two calculations. The collapse is not perfect, however. The remaining difference may be due to other explosive interaction not included in the scaling and modeling inadequacies in the numerical calculation due to grid size and artificial viscosity.

\*Made with the STEALTH finite difference code.



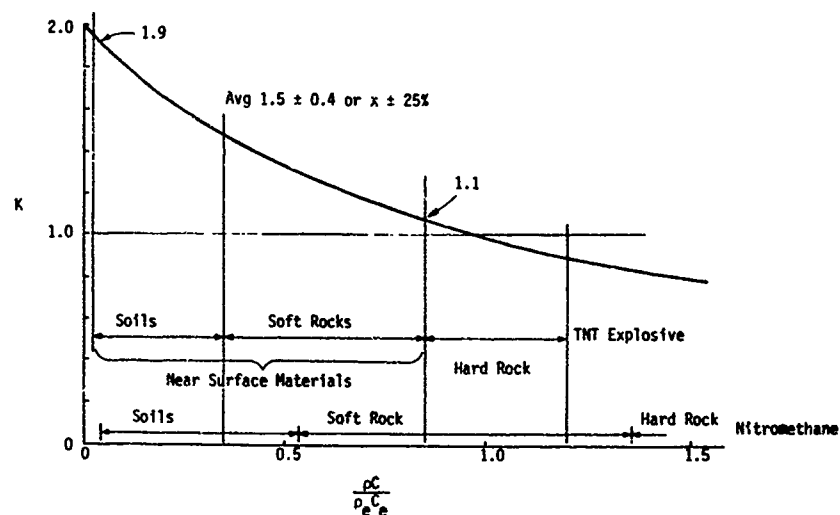


Figure 10. Velocity Transmission Factor

Table 3

Parameters Used in Elastic Calculations  
with HE Source

Explosive Type: TNT

Yield: 512 kg

Charge Parameters:

Radius: 0.42 m

$\rho_0$ , Density: 1650 kg/m<sup>3</sup>

$D$ , Detonation Velocity: 6930 m/s

$C_e$ , Sound Speed: 5070 m/s

$P_{CJ}$ , Chapman-Jouget Pressure:  $21 \times 10^9$  MPa

Ratio of Specific Heats = 2.728

$\rho_0 D = 1.14 \times 10^7$  kg/m<sup>2</sup>-s

Material Properties

Material	Density $\rho$ kg/m <sup>3</sup>	Seismic Velocity $C$ m/s	Impedance $\rho C$ kg/m <sup>2</sup> - s	Impedance Ratio $\rho C / \rho_e C_e$	K
Soil	1762	910	$1.60 \times 10^6$	0.14	1.75
Rock	2162	2440	$5.28 \times 10^6$	0.46	1.37

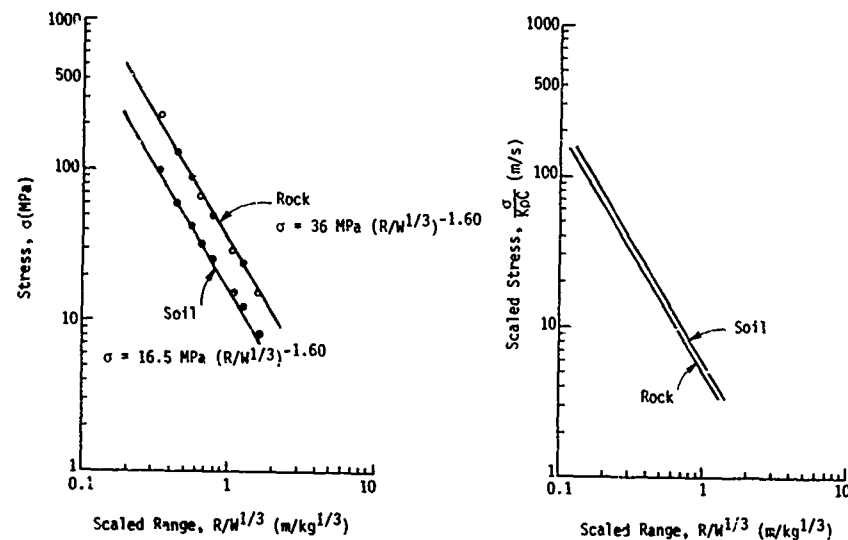


Figure 11. Peak Radial Stress in Elastic Calculations including an Explosive Source

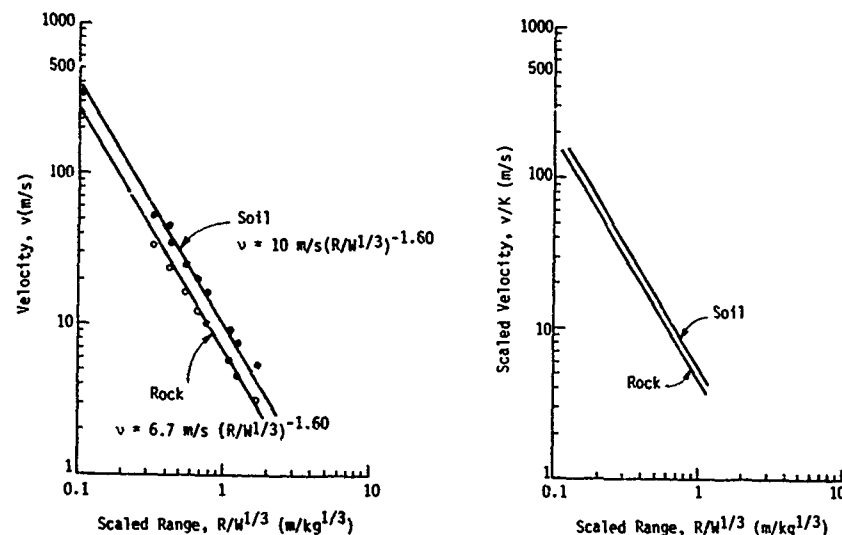


Figure 12. Peak Radial Velocities in Elastic Calculations including an Explosive Source

The calculations discussed to this stage have been elastic. Labreche and Auld (Ref. 13) performed calculations in inelastic materials involving nonlinear, hysteretic constrained moduli and failure surfaces. Those calculations were performed with an ideal gas source so that the amplitude scaling is different than observed for an explosive source but the attenuation rates that they computed are of interest. Figure 14 plots the attenuation rates for stress, velocity and displacement in the calculations versus a scaled hysteretic compaction parameter defined by

$$(1 - r)/C_L$$

where  $r = M_L/M_u$  = ratio of the loading constrained modulus to the unloading modulus (recovery ratio)  
 $C_L$  = loading wave speed associated with the loading modulus  $M_L$ .

The loading modulus is usually selected as the secant modulus to the stress level of interest. The loading wave speed is normally the speed used to relate stress and particle velocity in

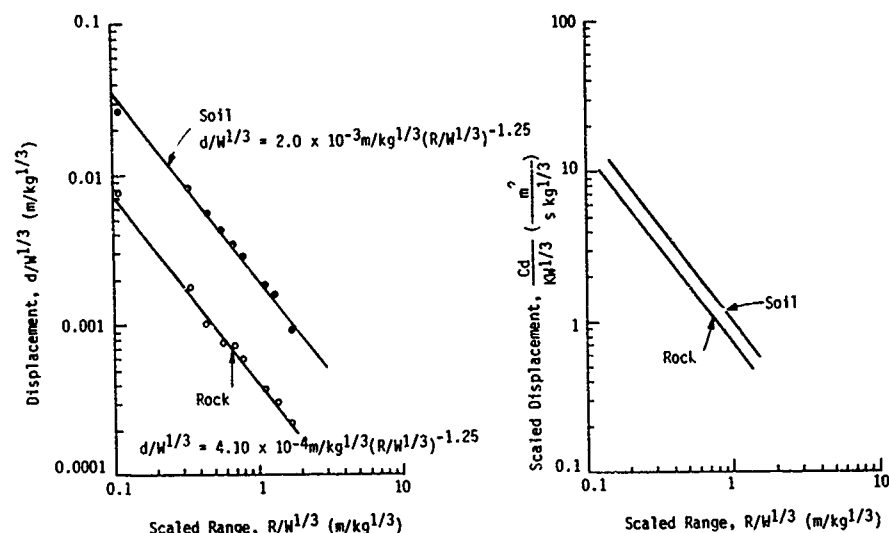


Figure 13. Peak Radial Displacements in Elastic Calculations Including an Explosive Source

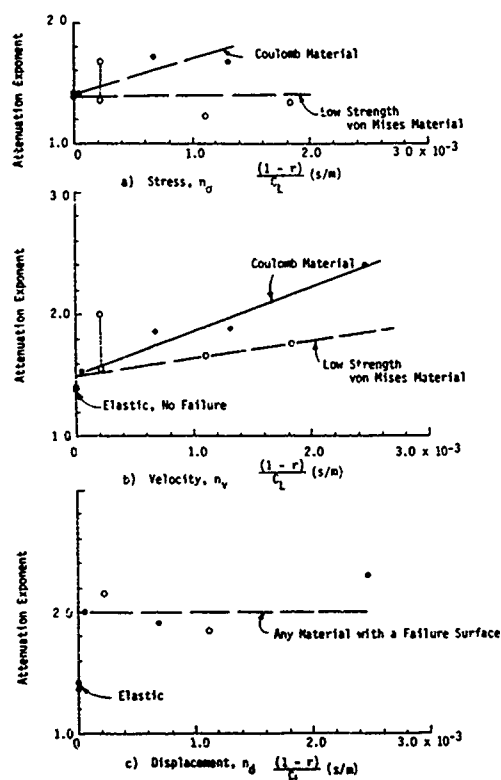


Figure 14. Attenuation Rates from Calculations in Different Inelastic Materials

inelastic materials. In dry soils it is about 0.5 times the seismic velocity, in wet soils about 0.75 and in rocks 0.8 to 0.9.

The attenuation rates for stress and velocity separate into two categories depending upon the form of the failure envelope. The attenuation rates in materials designated Coulomb material increase more rapidly with increasing compaction parameter than the rates in the low strength von Mises material. The Coulomb materials had shear strengths which increased with confinement. The failure envelope was encountered on unloading, not loading. Those materials designated as low strength von Mises materials had low values of shear strength which were independent of confinement. The failure envelope was encountered on loading. This later condition is similar to that which would occur in wet soils although none of the models evaluated had properties representative of wet soils. These results, however, suggest lower attenuation rates in wet materials than dry materials. The attenuation rate for displacement seems to be about constant in both materials. It appears that unloading along a failure surface, whether Coulomb or von Mises type, controls the displacement attenuation rate. It should be noted that the elastic attenuation rate in these calculations is -1.4 while in the calculations with the explosive source it was -1.6 which are quite a bit higher than the theoretical elastic attenuation rate. Hence there are numerical dissipation mechanisms evident in these calculations due to artificial viscosity, finite zoning and other approximations. This increased attenuation is common to all numerical calculations although its amount is dependent upon zone size, viscosity coefficients and actual material properties.

This evaluation of attenuation rates suggests that it will never be possible to collapse the data from different inelastic materials to a single relationship because the materials have inherently different attenuation rates. It may be possible, however, to collapse them at a single position, i.e., the source boundary.

#### CHARACTERISTICS OF A LIMITED DATA SET

One of the most comprehensive sets of contained HE data comes of the MOLE series (Ref. 14) conducted in the early 1950's. Although somewhat old, the data set contains substantial material and depth of burst variations. The data has two major shortcomings. The first is that there were no close-in measurements (no closer than about 1.8 ft/lb<sup>1/3</sup>). The second is that there is only limited material property information available. That consists of seismic velocity and density data. Table 4 summarizes the data. In addition, the table contains estimates of the strain recovery ratio, scaled hysteretic compaction parameters and predicted attenuation rates for velocity and displacement based on figure 14.

In spite of the MOLE shortcomings, the data reveal some important behavior and will be discussed here. Several additional tests have been conducted since MOLE and a paper by Drake in this conference provides a comprehensive analysis of that data.

Figure 15 shows the variation of particle velocity with range for all the tests at scaled depths of burst greater than 0.5 ft/lb<sup>1/3</sup>. This appears to be the depth of maximum coupling for particle velocity. Figure 15a shows the data using yield scaling only. Overall the data separates into two groups: wet material and dry material. Within the scatter of the data there does not appear to be a major distinction between materials in the two groups.

Figure 15b shows the data scaled by K, the velocity transmission coefficient. Wet and dry materials remain separated but the dry data appears to tighten up slightly. Table 5 summarizes the parameters for fits to the groups of data using the fit equation

Table 4  
Estimated Properties for MOLE Soils

Material	Seismic Velocity (ft/s)	$C_L$ (ft/s)	$r$	$\frac{1-r}{C_L}$ (s/ft)	$n_v$	$n_d$
gravel/sand	2900-3600	1600	0.1	$2.7 \times 10^{-2}$	2.5	2.0
Utah dry clay	1550	775	0.1	$1.2 \times 10^{-3}$	1.9	2.0
Calif wet sand	5000	3750	0.5	$1.3 \times 10^{-4}$	1.7	2.0
Calif moist clay	4000	3000	0.5	$1.7 \times 10^{-4}$	1.8	2.0

Table 5  
Coefficients and Attenuation Exponents  
for Fits to Velocity Data

Material	$n_v$	Unscaled (ft/s)	$\frac{C_1 - C_L}{C_C} \times 100$	Scaled (ft/s)	$\frac{C_1 - C_L}{C_C} \times 100$
gravel/sand	-2.86	77.4	-0.26	44.0	1.62
Utah dry clay	-2.90	78.9	1.7	42.0	-3.00
dry composite	-2.87	77.6	---	43.3	---
Calif wet sand	-2.10	86.4	-25.3	53.9	-24.4
Calif wet clay	-2.48	186.9	61.7	113.5	59.2
wet composite	-2.24	115.6	---	71.3	---

\* $C_C = C_1$  for composite

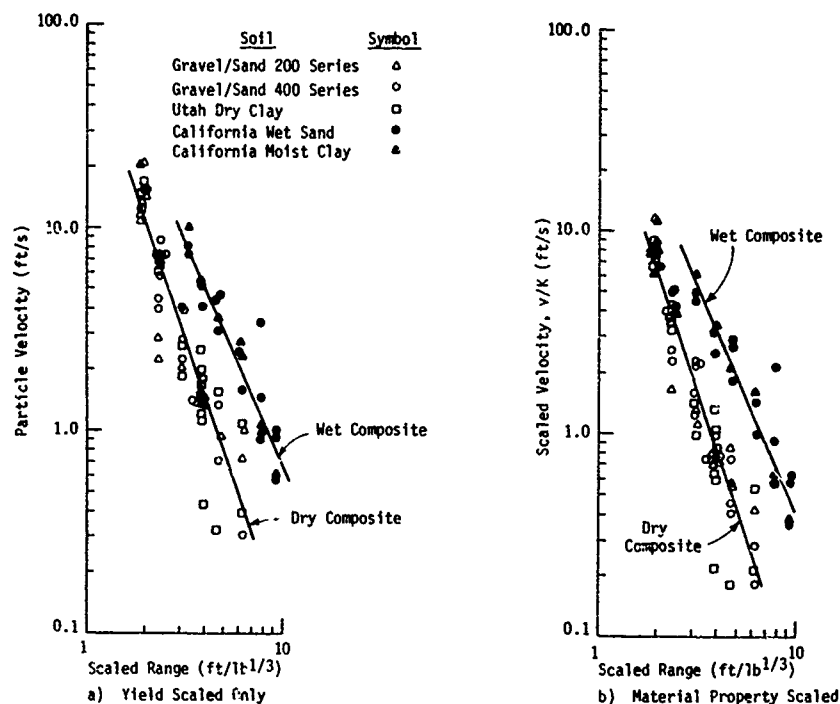


Figure 15. MOLE Particle Velocities at Depths of Burial of 0.5, 0.75, and 1.0 ft/lb<sup>1/3</sup>

$$v = C_1(R/W^{1/3})^{n_v} \quad (20)$$

without material property scaling and

$$\frac{v}{K} = \bar{C}_1(R/W^{1/3})^{n_v} \quad (21)$$

with the material property scaling. The first observation that can be made is that the attenuation exponents are significantly higher than predicted in Table 4. This is apparently due to the fact that the correlations of figure 14 are too simple. Other parameters must be considered.

A second observation is that there is no major improvement in the correlations using the material property scaling. This is shown by the parameters  $(C_1 - C_C)/C_C$  which is a measure of the difference between fits to individual events and the composites. If one solves for the range at which the wet and dry soil velocities become equal, the unscaled composite fits yield a range of 3.3 feet while the scaled fits yield 2.9 feet. Since the charge radius for 256 lbs of TNT is 0.84 feet, the result for the scaled fit is more reasonable. The fact that the velocities are equal 2 feet beyond the charge boundary may be due to a disturbed zone around the charge.

In summary, for velocities, the data reveal relative material independence within the two distinct groups of wet and dry materials. The

groups decay at different rates with the wet material exhibiting lowest attenuation. The proposed material property scaling only contributes a small improvement.

Figure 16 shows yield scaled MOLE displacements at depths of burst of 0.5, 0.75, 1.0 ft/lb<sup>1/3</sup>. The 0.5 ft/lb<sup>1/3</sup> depth of burst data have been separated from that for depths of burst of 0.75 ft/lb<sup>1/3</sup> or greater because coupling for displacement does not reach a maximum until 0.75 ft/lb<sup>1/3</sup>. Material property scaled displacements are not shown because the scaling involving seismic velocity provides no apparent improvement. As with velocities, the data in the different dry materials scatter together. The wet data, where comparisons can be made at 0.5 ft/lb<sup>1/3</sup> depth of burst, show a small difference between wet sand and moist clay.

The coefficients and decay exponents for the displacement data fit to equations of the form:

$$d/W^{1/3} = C_2(R/W^{1/3})^{n_d} \quad (22)$$

$$d/KCW^{1/3} = \bar{C}_2(R/W^{1/3})^{n_d} \quad (23)$$

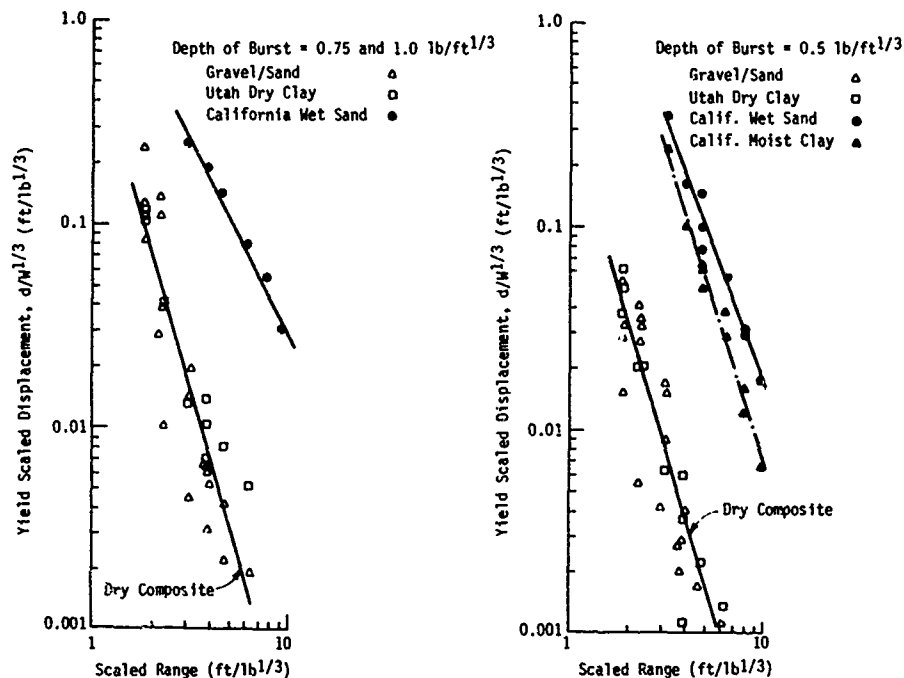


Figure 16. MOLE Displacements at Depths of Burst of 0.5, 0.75 and 1.00 ft/lb<sup>1/3</sup> (Yield Scaled Only)

with material property scaling are summarized in Table 6. The values of the parameter  $(C_2 - C_C)/C_C$  indicate that the proposed material property scaling does not improve the unscaled data collapse. In spite of the fact that the elastic scaling based upon an explosive source does not make major improvements, it is more consistent with the data than other approaches. The results suggest that it will be necessary to include additional material properties, quite likely strength parameters to collapse the data. Because of differences in the decay exponent, the data will never collapse entirely. But there may be some overall improvement in scaling in different materials.

The only comprehensive set of MOLE experiments on depth of burst effects was for the gravel/sand mix. Figures 17 and 18 shows the particle velocity and displacement data, respectively. Both sets of data show both a change in overall amplitude and a change in decay exponent with depth of burst. Table 7 summarizes the coefficients and decay exponents for the fits to the data in the form of equations (20) and (22). Figure 19 plots the parameters versus depth of burst.

It is interesting that the data from near-surface bursts exhibit a much shallower attenuation rate than when deeply buried ( $\alpha \approx -2$  vs  $-2.9$  for velocity). Measurements were made laterally on MOLE. This result suggests, however, that the attenuation vertically beneath

a near-surface charge may be greater than in a lateral direction to the side of a charge. The overall amplitude may be different as well.

The fact that both the overall amplitude and the decay exponent change with depth of burst implies that depth of burst effects cannot be completely collapsed with a simple coupling factor as is commonly attempted. Nevertheless, it is interesting to compare the coupling factor implied by the amplitude coefficients with those in use previously. Figure 20 compares Lampson's coupling factor with those computed here. The MOLE results suggest that maximum coupling is achieved at a much shallower depth than suggested by Lampson. Further, maximum coupling for velocity is achieved at a shallower depth than for displacements.

#### LOADS ON STRUCTURES

There are two components involved in determining loads on structures. The first is the freefield stress. The second is soil-structure interaction. Until recently, very few reliable stress measurements were available in geologic materials. Fortunately, this situation is improving and Drake provides stress correlations in a paper in this symposium. In the absence of stress data, it is common to use the simple wave propagation relation given in equation (24) to estimate stress:

$$\sigma = \rho C V \quad (24)$$

Table 6  
Coefficients and Attenuation Exponents  
for Fits to Displacement Data  
Scaled Depth of Burst of 0.75 and 1.0 ft/lb<sup>1/3</sup>

Material	$n_d$	Unscaled $C_2$ (ft/lb <sup>1/3</sup> )	$\frac{C_2 - C_c}{C_c} \times 100$	Scaled $\bar{C}_2$ (ft <sup>2</sup> /lb <sup>1/3</sup> -s)	$\frac{\bar{C}_2 - C_c}{C_c} \times 100$
gravel/sand	-3.9	1.25	47.0	2306	92.8
Utah dry clay	-2.78	0.53	38.0	437	-63.5
dry composite	-3.45	0.85	---	1196	---
Calif wet sand	-1.88	2.38	---	7438	---
Calif moist clay	---	---	---	---	---
wet composite	-1.38	2.38	---	7438	---

\* $C_c = C_2$  for composite

Scaled Depth of Burst of 0.5 ft/lb<sup>1/3</sup>

Material	$n_d$	Unscaled $C_2$ (ft/lb <sup>1/3</sup> )	$\frac{C_2 - C_c}{C_c} \times 100$	Scaled $\bar{C}_2$ (ft <sup>2</sup> /lb <sup>1/3</sup> -s)	$\frac{\bar{C}_2 - C_c}{C_c} \times 100$
gravel/sand	-3.2	0.30	-6.3	553	25.4
Utah dry clay	-3.32	0.37	15.6	305	---
dry composite	-3.22	0.32	---	441	-30.8
Calif wet sand	-2.56	5.97	-18.11	18600	5.091
Calif moist clay	-3.04	7.29	---	17700	---

\* $C_c = C_2$  for composite  
1 Wet sand is compared to moist clay.

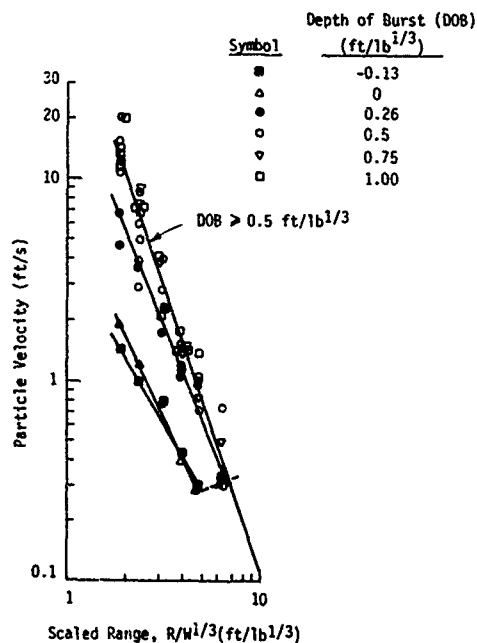


Figure 17. MOLE Velocities in Gravel/Sand as a Function of Depth of Burst

Table 7  
Coefficients and Decay Exponent  
for Depth of Burst  
Relations in Gravel Sand

Velocity:

$$v = C_1 (R/W^{1/3})^{n_1}$$

Depth of Burst (ft/lb <sup>1/3</sup> )	$C_1$ (ft/s)	$n_1$
>0.5	77.4	-2.86
0.26	30.4	-2.37
0	7.13	-2.07
-0.13	4.29	-1.66

Displacement

$$d/W^{1/3} = C_2 (R/W^{1/3})^{n_2}$$

Depth of Burst (ft/lb <sup>1/3</sup> )	$C_2$ (ft/s)	$n_2$
>0.75	1.25	-3.9
0.5	0.30	-3.2
0.26	0.09	-2.8
-0.13	0.0027	-1.52

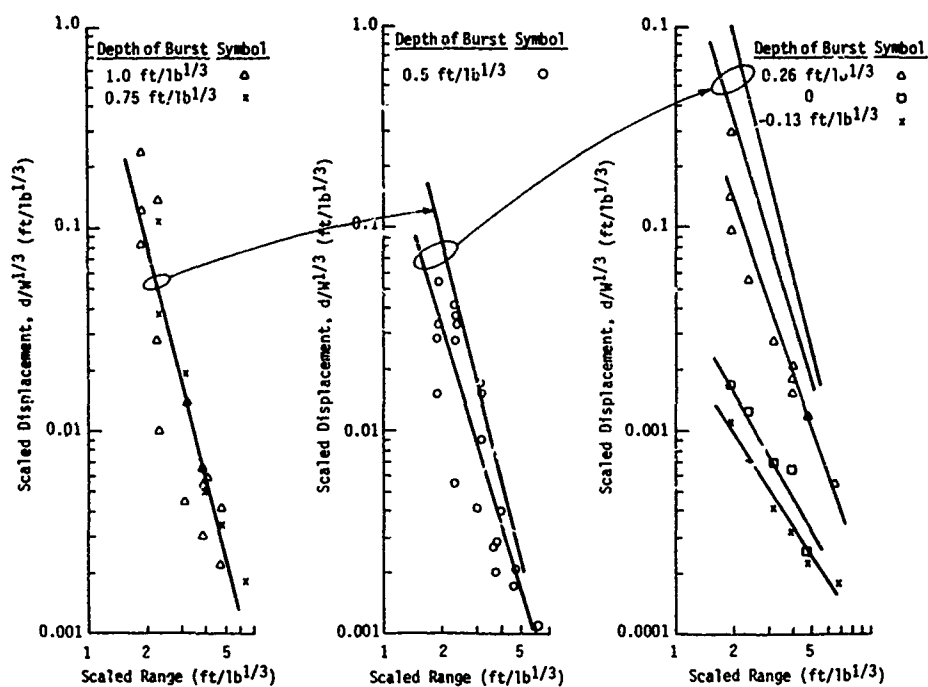


Figure 18. MLE Displacements in Gravel/Sand as a Function of Depth of Burst

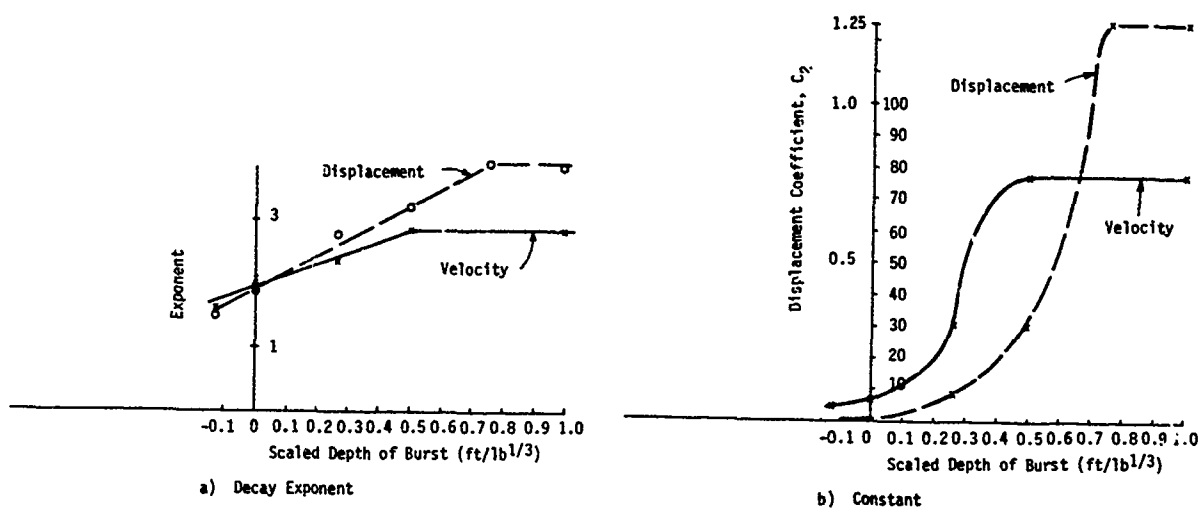


Figure 19. Depth of Burst Parameters for MLE Gravel/Sand



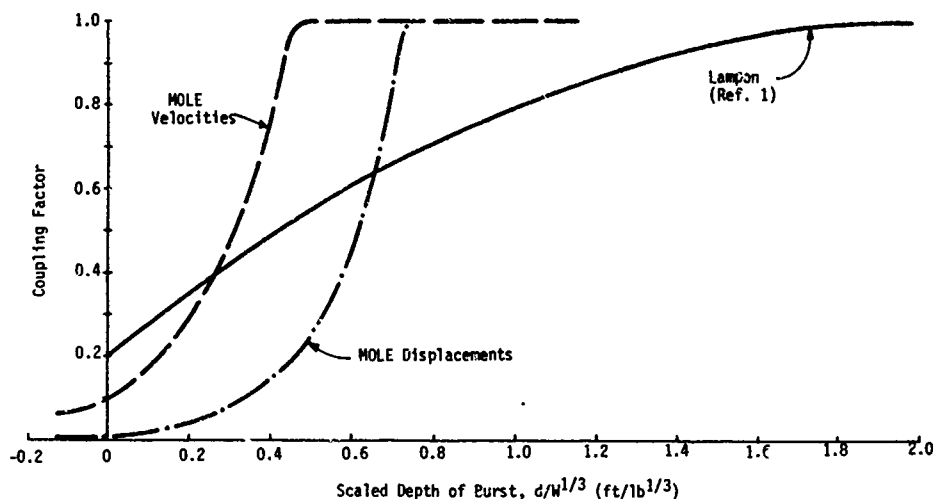


Figure 20. Coupling Factor Versus Depth of Burst

where  $\sigma$  = stress  
 $\rho$  = mass density  
 $C$  = wave speed  
 $v$  = particle velocity

The wavespeed is taken as an effective wave speed determined from the secant modulus to the stress level of interest.

The actual load on a structure is dependent upon the interaction of the incident stress wave with the structure. Arching, in the static sense, does not occur. Soil to the sides of the structure cannot possibly mobilize to carry loads away from the structure until a wave reflection has taken place and communicated the existence of a structure to the adjacent soil. This process takes time. For conventional explosives, the major wave reflection and interaction is over before the adjacent soil can "arch".

In general the interaction process is quite simple and is related to the relative velocity between the freefield and the structure (Ref. 12).

The stress acting at a point on the incident face of a structure buried at sufficient depth so that free surface reflections do not influence response may be approximated by

$$\sigma_t(t) = 2\sigma_{ff}(t) - \rho C_L v(t) \quad (25)$$

where

$\sigma_t(t)$  = total stress acting on the incident face

$\sigma_{ff}(t)$  = incident stress wave in the freefield at the location of the structure  
 $\rho$  = mass density of the soil  
 $C_L$  = compressional wave velocity of the soil  
 $v(t)$  = velocity of the structure

The stress acting on an aboveground structure, is approximately

$$\sigma_r(t) = \rho C_L v(t) \quad (26)$$

where  $\sigma_r(t)$  is the stress acting on the reactive face of the structure.

In general,

$$\sigma_t(t) = \sigma_{ff}(t) \pm \rho C_L \Delta v(t) \quad (27)$$

where

$\sigma_t(t)$  = total stress acting on a point on a structure surface perpendicular to the direction of incident wave propagation  
 $\Delta v(t) = v_{ff}(t) - v(t)$   
 $v_{ff}(t)$  = freefield particle velocity at the point of interest

The sign of the second term is taken as positive for incident faces and negative for reactive faces. Equation (27) indicates that the stress on a structure consists of the freefield stress plus or minus a term which is related to momentum exchange caused by the presence of the structure. These relations are approximate because they ignore communication between adjacent points on the surface. A similar

relation exists for shear stress but the maximum shear stress transmitted is limited by some failure criteria.

Equation 27 and its generalization lead to the obvious but important conclusion that whenever the structure velocity differs from the freefield velocity, stresses different from those in the freefield will act on the structure. Since buried structures of finite mass cannot respond instantaneously to an incident wave, reflections will persist on surfaces facing the propagating incident wave for some time following the arrival of the wave at the structure. The duration and importance of the reflections depend upon the mass and size of the structure, the properties of the medium, the rise time of the incident wave and the flexibility of the structure. The relatively large mass and stiffness associated with buried structures designed to resist conventional explosions suggest that a reflection factor of 2 should be applied to incident freefield stresses. As mentioned earlier, however, there are large spatial gradients in load which should be accounted for.

#### CONCLUSIONS AND RESEARCH NEEDS

The discussions and analyses of this paper lead to the following conclusions:

1. Dimensional analysis and scaling are useful in interpreting data and developing prediction relations but the analysis can be complex.

2. Parametric numerical calculations provide an excellent means of identifying physical trends and guiding data analysis.

3. The explosive source (not a simple pressure boundary) must be included in calculations and dimensional analyses.

4. Material inelasticity dominates response including attenuation rates and the relationship of stress to velocity. There is a marked difference between wet and dry soils. Material parameters involving strength, and possibly multi-phase behavior, will be necessary in dimensional analyses to scale data in various materials. In the meantime, existing data may be used directly for predictions.

5. The MOLE depth of burst data suggest different coupling relations for different ground shock parameters. Also, because the decay exponent varies with depth of burst, a simple coupling factor does not explain all effects.

6. Overall, data are sparse on the following topics:

- close-in (0.5 to 1.5 ft/lb<sup>1/3</sup>) parameters
- shape effects
- case effects
- lateral versus vertical behavior beneath burst
- stress/pressure measurements in general
- layering effects (especially dry/wet interfaces)
- blast-induced liquefaction
- load amplitudes and distributions on structure surfaces

This lack of adequate data leads to the following research needs:

1. Parametric experiments using modern fielding and measurement techniques to obtain comprehensive data on the main parameters governing ground shock. These should include measurements both laterally and vertically beneath the burst.

2. Parametric experiments in wet and dry over wet soils to characterize wet site behavior and blast-induced liquefaction.

3. Development of instrumentation and techniques for measuring total stress, effective stress and pore pressures.

4. Development of multi-phase geologic material models which include coupling between volumetric and deviatoric behavior.

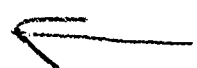
5. Parametric experiments to characterize loads on structures for various structure shapes, sizes and stiffness.

6. First principal calculations to guide and aid in the prediction of the experiments, as well as reveal the relative importance of different parameters.

#### REFERENCES

1. Lampson, C.W., "Explosions in Earth", in Effects of Impact and Explosion, Summary Technical Report of Division 2, National Defense Research Committee, Vol. 1, Washington, DC, 1946.
2. Sedov, L.I., Similarity and Dimensional Methods in Mechanics, Academic Press, New York and London, 1959.
3. Baker, W.E., et al., Similarity Methods in Engineering Dynamics, Sparten Books, Hayden Book Company, Inc., Rochelle Park, NJ, 1973.

4. Buckingham, E., Model Experiments and the Forms of Empirical Equations, Spring Meeting, American Society of Mechanical Engineers, June 1915.
5. Hendron, A.J., Scaling of Ground Motions from Contained Explosions in Rock for Estimating Direct Ground Shock from Surface Bursts on Rock, Technical Report No. 15, Omaha District Corps. of Engineers, Omaha, Nebraska, January 1973.
6. Westine, P.S., "Ground Shock from the Detonation of Buried Explosives", Journal of Terramechanics, Vol. 15, No. 2, pp. 69-79, 1978.
7. Higgins, C.J., Johnson, R.L. and Triandafilidis, G.E., The Simulation of Earthquake-Like Ground Motions with High Explosives, Final Report No. CE-45(78)NSF-507-I on National Science Foundation Grant No. NSF ENG 75-21580, The University of New Mexico, Albuquerque, NM 87131, July 1978.
8. Cooper, H.F., Generation of an Elastic Wave by Quasi-Static Isentropic Expansion of a Gas in a Spherical Cavity; Comparison Between Finite Difference Predictions and the Exact Solution, AFWL-TR-66-83, Air Force Weapons Laboratory, Kirtland AFB, NM, September 1966.
9. Review of "Parametric Nuclear Weapons Environments for MX Multiple Aimpoint Basing Systems Definition", DAMG-TR-3, Data Analysis Working Group, December 1978.
10. Drake, J.L., Ground Shock Beneath Near-Surface Bursts, Draft Report, Structures Laboratory, U.S. Army Engineer Waterways Experiment Station, Vicksburg, MS, January 1982.
11. Bratton, J.L. Personal communication.
12. Crawford, R.E., Higgins, C.J., and Bultmann, E.H., The Air Force Manual for Design and Analysis of Hardened Structures, AFWL-TR-74-102, Air Force Weapons Laboratory, Kirtland AFB, New Mexico, October 1974.
13. Labreche, D.A. and Auld, H.E., An Analysis of Tunnel Linings for Deep Basing Structures, AFWL-TR-80-5, Air Force Weapons Laboratory, Kirtland AFB, NM, September 1980.
14. Sachs, D.C. and Swift, L.M., Small Explosion Tests, Project MOLE, Vols. I and II, Final Report AFSWP-291, Stanford Research Institute, Menlo Park, CA, December 1955.



AD P001751

# CENTRIFUGAL MODELING TECHNIQUES

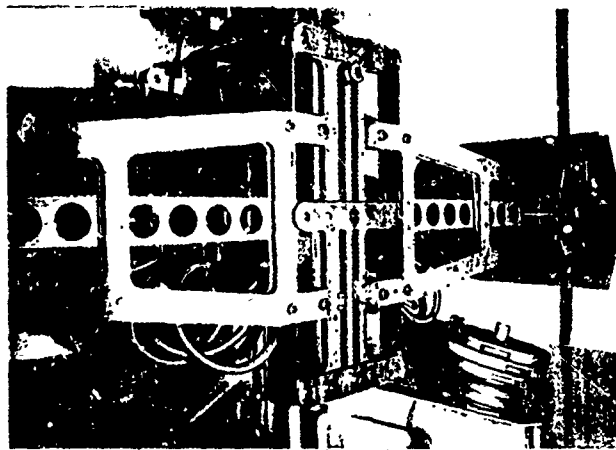
Paul L. Rosengren, Jr.  
Air Force Engineering and Services Laboratory  
Tyndall AFB, Fla

## ABSTRACT

This research effort explored the feasibility of using a centrifuge as an experimental simulator to measure free-field blast parameters very near the explosive charge. A series of experimental blast events was conducted in the 30 g to 80 g range using the centrifuge test facility located at Kirtland AFB New Mexico. The results of these tests concluded that the use of a centrifuge simulator is a workable concept for the determination of blast parameters. The simulation of high-explosive effects through gravity scaling permits the use of small charges in the centrifuge simulator and it can easily be refurbished after each test. More importantly, the use of the centrifuge simulator preserves the gravity scaling relationships which are usually distorted during replica model testing.

## ACKNOWLEDGEMENT

This paper presents a summary of the ongoing research efforts of Dr. John P. Nielsen and his staff at the New Mexico Engineering Research Institute (NMERI), Kirtland AFB, New Mexico, on the centrifugal simulation of blast parameters from February 1981 to the present [3]. This paper contains extracts from the draft report to be published this year by the sponsoring agency, the Air Force Engineering and Services Laboratory, Tyndall AFB, Florida.



Note counterweights in foreground.

Figure 2. Genisco centrifuge.

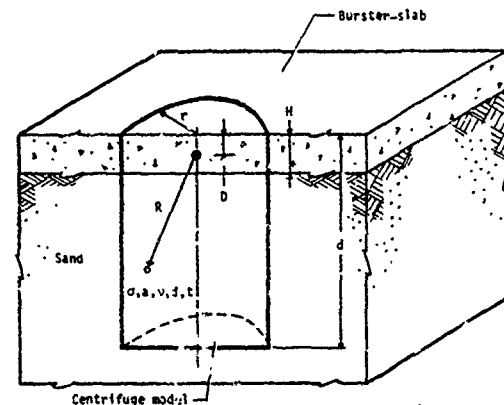
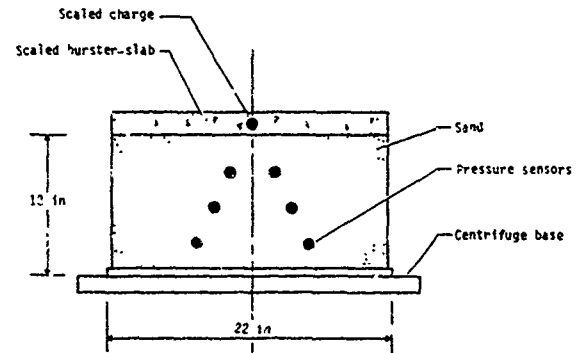


Figure 1. Prototype system and centrifuge model.

## INTRODUCTION

In the structural replica modeling process, it is most common to neglect the gravity distortion which occurs in the scaling relationships. Quite often this is justified because the effects of gravity are small [1]. However, in gravity sensitive phenomena (i.e., cratering, spalling, penetration, tension cutoff, dead load, inertia effects, etc...) the distortion of gravity may induce very large errors in the structural response. As the scale of the replica model becomes smaller, these distortions can become very great. It is therefore advantageous to develop an experimental technique which will preserve the gravity scaling relationships in replica structural modeling. The centrifuge offers such a technique.

## APPROACH

After a review of other blast simulation techniques, the centrifuge concept was decided upon because of its relative merits. A series of experimental blast tests was performed in an available centrifuge facility at Kirtland AFB, New Mexico. The particular problem under investigation at the time was the measurement of free-field blast parameters under a reinforced concrete burster slab as shown in Figure 1. The weapon was assumed to penetrate into the burster slab and then detonate creating a crater and inducing a shock wave beneath the burster slab. Table 1 and Table 2 illustrate the independent parameters and scaling relationships used in the modeling process. The acceleration (gravity) varies as the inverse of the linear dimension. A 1/50 scale model would be tested at 50 g's in order to preserve similarity.

Figure 2 shows a photograph of the 6-foot radius centrifuge apparatus which was used to mount the test articles. The test bed is approximately 22 inches in diameter and is secured to a free swinging platform so that the induced gravity force is always normal to the test article.

Figure 3 shows the installation of the simulated weapon in the burster slab. The weapon was simulated using commercially available "blasting cap" detonators and sized according to the energy scaling relationships. The detonators are available in a variety of sizes and shapes and the casing thickness can be machined to produce a replica of any particular weapon, if desired.

TABLE 1. INDEPENDENT PARAMETERS FOR THE CENTRIFUGAL MODELING OF BLAST PRESSURE.

Parameter	Description	Dimensions
Explosives	Energy, $E_0$	$ML^2T^{-2}$
	Pressure, $P_0$	$ML^{-1}T^{-2}$
	Depth of Burial, $D$	$L$
Bursting-Slab	Thickness, $H$	$L$
	Mass Density, $\rho_1$	$ML^{-3}$
	Dilatational Wave Speed, $C_1$	$LT^{-1}$
	Poisson's Ratio, $\mu_1$	---
Soil (Sand)	Mass Density, $\rho_2$	$ML^{-3}$
	Dilatational Wave Speed, $C_2$	$LT^{-1}$
	Poisson's Ratio, $\mu_2$	---
	Strength Parameter $\alpha_2$	$ML^{-1}T^{-2}$
Other Parameters	Gravity, $g$	$LT^{-2}$
	Bucket Dimensions, $r, d$	$L$
	Range	$L$

TABLE 2. SCALING RELATIONSHIPS FOR GRAVITY SCALING.

Quantity	Full Scale	Model Scale
Linear Dimension	1	$1/n$
Area	1	$1/n^2$
Volume	1	$1/n^3$
Time	1	$1/n$
Velocity	1	1
Acceleration	1	$n$
Mass	1	$1/n^3$
Force	1	$1/n^2$
Energy	1	$1/n^3$
Stress	1	$1/n$
Strain	1	1
Density	1	1

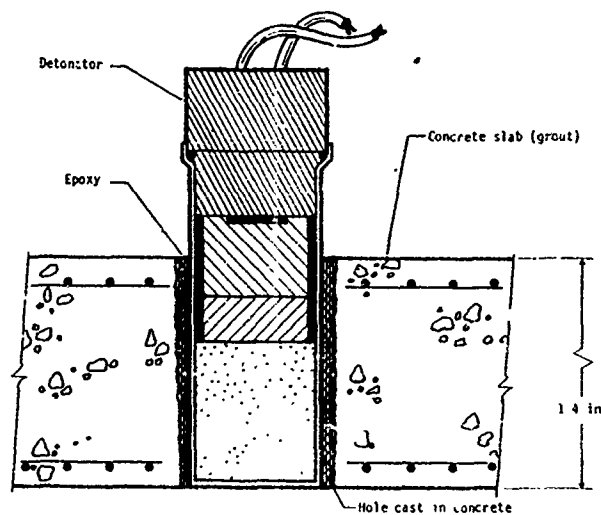


Figure 3. Placement of detonator in burster-slab

## RESULTS

Figure 4 shows the results of a typical burster-slab model after detonation at 50 g's. The separation of the wire reinforcement fabric extended around the diameter of the breach in this particular case. A variety of experiments involving various combinations of charge weights, gravity levels and scaled distances were performed. The test matrix is shown in Table 3. A comparison of the test results and predictions is presented in Figure 5. The free-field pressure was recorded from miniature pressure gages, using standard high-speed recording techniques.

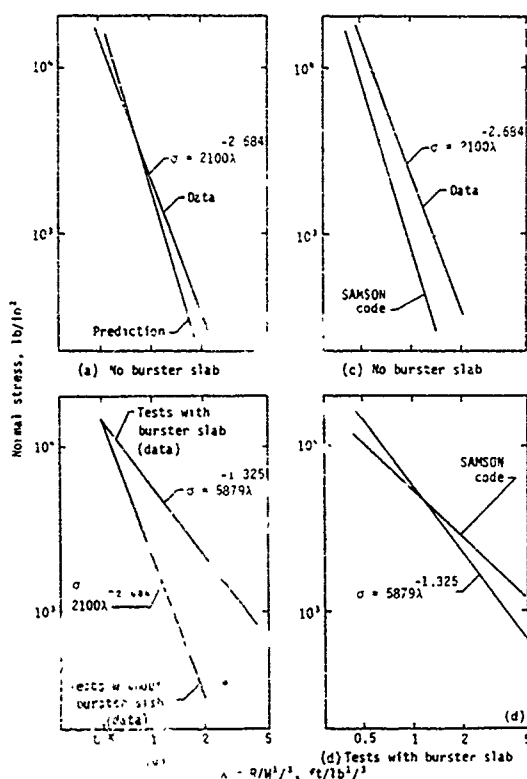


Figure 5. Comparison of test results, predictions, and SAMSON code values.

## CONCLUSIONS

Recent advances in the miniaturization of experimental gages have made the feasibility of structural modeling more attractive. Microetching techniques have been applied to the manufacture of very small strain gages and accelerometers. Microetching techniques are used to produce microprocessors and "microchips" in the computer industry. The result is a "microchip" gage which is extremely small and relatively inexpensive because of mass production techniques [2]. The gages are not only small but can contain microprocessors to process the data prior to transmission.

The use of a centrifuge as a simulator for the determination of blast parameters appears to be a workable concept. Using "microchip" gages and miniature replica structural models in a centrifuge simulator can provide meaningful response data very quickly and economically. This type of apparatus would lend itself to the economical production of large volumes of data.



Figure 4. Postshot condition of model burster-slab-440 mg at 50 g

TABLE 3 TEST MATRIX

Explosive weight, mg	q-Level																										
	32			32			40			40			46			50			55			72			79		
	Scaled Distance																										
	$\lambda_1$	$\lambda_2$	$\lambda_3$	$\lambda_1$	$\lambda_2$	$\lambda_3$	$\lambda_1$	$\lambda_2$	$\lambda_3$	$\lambda_1$	$\lambda_2$	$\lambda_3$	$\lambda_1$	$\lambda_2$	$\lambda_3$	$\lambda_1$	$\lambda_2$	$\lambda_3$	$\lambda_1$	$\lambda_2$	$\lambda_3$	$\lambda_1$	$\lambda_2$	$\lambda_3$	$\lambda_1$	$\lambda_2$	$\lambda_3$
880	1	2	3	.5	.8	5	1	2	3	.5	.8	5	---	---	---	.5	1	2	---	---	---	---	---	---	---	---	---
660	---	---	---	---	---	---	---	---	---	---	---	---	.5	.8	5	.5	1	2	---	---	---	---	---	---	---	---	---
440	---	---	---	---	---	---	---	---	---	---	---	---	---	---	---	---	---	---	.5	1	2	---	---	---	---	---	---
220	---	---	---	---	---	---	---	---	---	---	---	---	---	---	---	---	---	---	---	---	---	---	---	---	---	---	---

\*This series was also conducted in a test series without a burster-slab included in the test

#### REFERENCES

1. Baker, W. E., Westine, P. S., and Dodge, F. T., SIMILARITY METHODS IN ENGINEERING DYNAMICS: THEORY AND PRACTICE OF SCALE MODELING, Hayden Book Company, Inc., Rochelle Park, New Jersey, 1973.
2. Angell, J. B., Terry, S. C., and Barth, W. B., "Silicon Micromechanical Devices," Scientific American, April 1983, Page 44.
3. Draft report "The Centrifugal Simulation of Blast Parameters," by Dr. John P. Nielsen, New Mexico Engineering Research Institute, University of New Mexico, Albuquerque, New Mexico 87131, February 1983.



AD P001752

## IMPACT AND PENETRATION OF LAYERED PAVEMENT SYSTEMS

THOMAS E. BRETZ, JR.

AIR FORCE ENGINEERING AND SERVICES CENTER

TYNDALL AIR FORCE BASE, FLORIDA

PHILLIP T. NASH

SOUTHWEST RESEARCH INSTITUTE

SAN ANTONIO, TEXAS

### ABSTRACT

The Air Force is sponsoring research on damage-resistant runway designs. The designs are based upon principles which use high strength/high density materials to resist weapon momentum. Initially, two subscale pavement sections will be designed, one representing a rigid pavement for long-term aircraft traffic, and the other representing a redundant surface to withstand limited aircraft operations. The penetration resistance for both pavement sections will be determined experimentally. Penetration-resistant layers of rock or concrete rubble will then be designed as a sub-base to the pavement sections and these designs will be tested at subscale. Testing full-scale penetration-resistant rubble layers will be accomplished, and concept development should be complete in the late 1980s.

### BACKGROUND

The United States Air Force is vitally concerned with airbase recovery following a conventional air attack. One area in which a great deal of research and development is occurring is rapid runway repair (RRR). Two technical areas of research and development in the Air Force RRR Program Office are rapid crater repair and alternate launch and recovery surfaces (ALRS). In the rapid crater repair technical area, engineers are developing procedures to rapidly repair bomb craters. In the ALRS technical area, engineers are developing methods to construct alternate airfield pavements which will provide the capability to operate aircraft while the initial craters in the main runway are being repaired. These alternate pavements will be constructed during peacetime.

There are two aspects to the ALRS technical area. One is based on pavement redundancy. The idea here is to construct large areas of aircraft operating surfaces that are redundant to the main runway(s).

These redundant surfaces need only withstand a limited amount of fighter traffic since the surfaces are intended to function only until the main operating surface is repaired. The other aspect of the ALRS technical area is based on construction of hardened runways that, when attacked, will sustain only limited damage which can be quickly repaired. This is particularly important for airbases that have insufficient land area for construction of vast areas of redundant surfaces. The hardened or damage-resistant runway research will be discussed below.

### OBJECTIVE

The objective of the damage resistant runway research is to develop methods to construct runway surfaces that are less subject to bomb damage than existing surfaces. The term, "less subject," is based on time to repair. The time to repair damage in a damage-resistant runway must be less than 30 minutes per crater. Concepts for damage-resistant runways must be economically feasible for construction and must be compatible with aircraft and aircraft operations. Payoff from the damage-resistant runway research is expected in the late 1980's.

### RESEARCH PROGRAM

The Air Force Engineering and Services Center is sponsoring a research effort by the Southwest Research Institute to develop a concept for construction of hardened runways. The research is being performed to determine the ability of a layer of rock rubble or boulders placed beneath a pavement's surface to cause penetration path disruption or weapon malfunction.

### Background

During the attack of the Nicosia International Airport in 1974, damage created by 750-pound bombs was far less than expected [1]. Decreased damage was attributed to a hard cap rock located at



an average of 4-5 feet below the runway surface. In general, the bombs did not penetrate the cap rock and, therefore, detonated at shallow depths resulting in small diameter (12-24 feet), shallow (3-5 feet) craters. Many of the bombs either deflagrated or failed to function at all. Rock rubble overlays have proven effective as a means of defeating kinetic energy penetrators attacking protective shelters [2,3]. When properly sized, initial penetration resistance of the rock rubble closely duplicates the resistance of a semi-infinite mass of rock. If opposed by adequate resistance, penetrating bombs do not perform to full potential and result in much smaller craters, thus requiring significantly less repair time.

#### Technical Approach

The design parameters important to this study are shown in Figure 1. Although Figure 1 is not all inclusive in detail, it does illustrate the principles involved. Details are described below:

Weapon Threat - 500-pound class general purpose bomb;

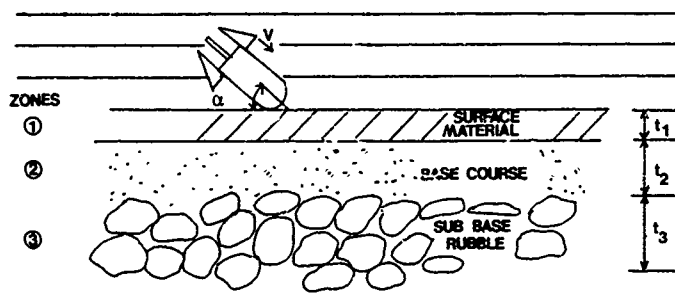
Impact Angle -  $\alpha$ , maximum of  $60^\circ$  (from horizontal) governed by delivery possibilities;

Impact Velocity -  $v$ , varies from 600 to 900 feet per second;

Surfacing Material - Zone 1: Rigid or flexible. Rigid surface designed to represent conventional runway; flexible surface designed to represent redundant surface.

Base Course - Zone 2: Materials to be comparable and compatible with anticipated repair backfill materials. Thickness based upon strength requirements to support aircraft loads and impart second shock loading at rubble zone in resonance with bomb's response to initial impact. Separation between zone 1 and 2 must be maintained to prevent material migration;

Sub-base - Zone 3: Individual pieces to be twice the diameter of the threat weapon. Depth of layer based upon weapon impact parameters and decelerations. Impact angles will be considered between the threshold for ricochet from surface ( $\alpha_{RS} \approx 40^\circ$ ) and delivery limited ( $\alpha_{DL} \approx 60^\circ$ ). Thickness and hardness of the layer to be determined from weapon characteristics and expected velocity when zone 3 is encountered.



#### DESIGN CONSIDERATIONS

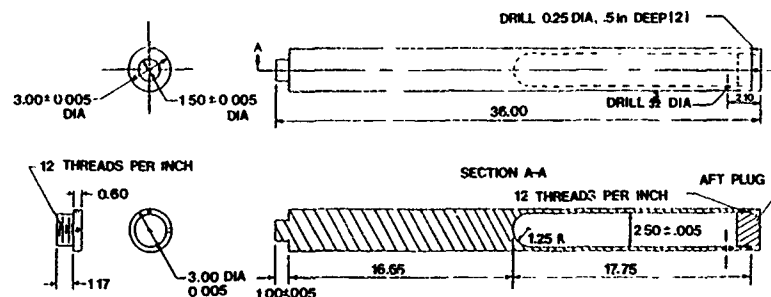
- ① CONVENTIONAL RIGID ( OR FLEXIBLE BASED UPON COST) DESIGN.
- ② STRENGTH AND MATERIALS COMPARABLE AND COMPATIBLE WITH BACKFILL MATERIALS USED IN RRR PROCEDURES.  $t_2$  BASED ON NATURAL FREQUENCY OF WEAPONS, IMPACT VELOCITY AND DECELERATION.
- ③ ROCK RUBBLE SUB-BASE DESIGNED TO DEFEAT WEAPON THREAT WITH RESIDUAL VELOCITY AFTER PENETRATING  $t_1$  AND  $t_2$ .

FIGURE 1. DAMAGE-RESISTANT RUNWAY CONCEPT.

### Weapon Response

Dominant response frequencies have been measured for runway penetrators impacting concrete targets. The penetrator shown in Figure 2 was instrumented as shown in Figure 3 and impacted with concrete targets in reverse ballistic testing at Eglin [4]. Strain data were analyzed using Fast Fourier techniques to determine dominant frequencies. Results from the analysis are shown in Figure 4. The first three natural frequencies of the penetrator in a preliminary analysis were determined using a three-degree-of-freedom lumped mass model. Frequencies determined analytically are also shown in Figure 4. Natural frequencies of 2108, 3292, and 7791 hertz correspond to natural periods of 0.47, 0.30, and 0.13 milliseconds. For impact velocities below 1000 feet per second into concrete sections approximately one foot thick, the penetrator is experiencing high impact loadings throughout the time period of maximum response which means the maximum response is the same as if the load duration had been

infinite. Larger class weapons such as the 750-pound general purpose bomb have natural periods in the 2 to 5 millisecond range. Thus, at higher impact velocities, larger weapons can penetrate thin surfaces before ever reaching maximum response. However, the process of penetrating a series of properly spaced hard layers of penetration barriers imposes a system of pulsating forces on the weapon. Referring to the concept of dynamic load factors presented in Reference 5, it can be seen that the maximum response increases tremendously when loads pulsate at frequencies near the natural frequency of the structural system. Figure 5 compares the dynamic load factor (DLF) with the ratio of load frequency ( $\Omega$ ) to structural frequency ( $\omega$ ) for sinusoidal loads. The proposed damage-resistant runway concept will take advantage of the dynamic response characteristics of the weapon threat and use spaced, hardened layers to impose pulsating loads into the penetrator. Although preliminary analysis has proven the concept feasible, more refined analysis techniques will be applied during the actual design of the concept.



ALL DIMENSIONS IN INCHES

FIGURE 2. TEST ITEM.

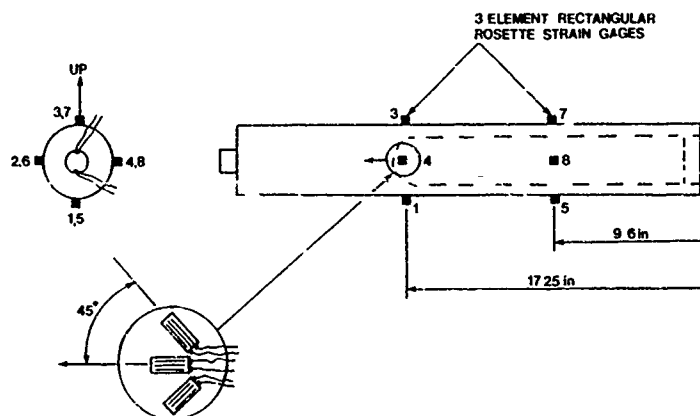


FIGURE 3. STRAIN GAGE CONFIGURATION, SLED TESTS NO. 2 THROUGH 4.

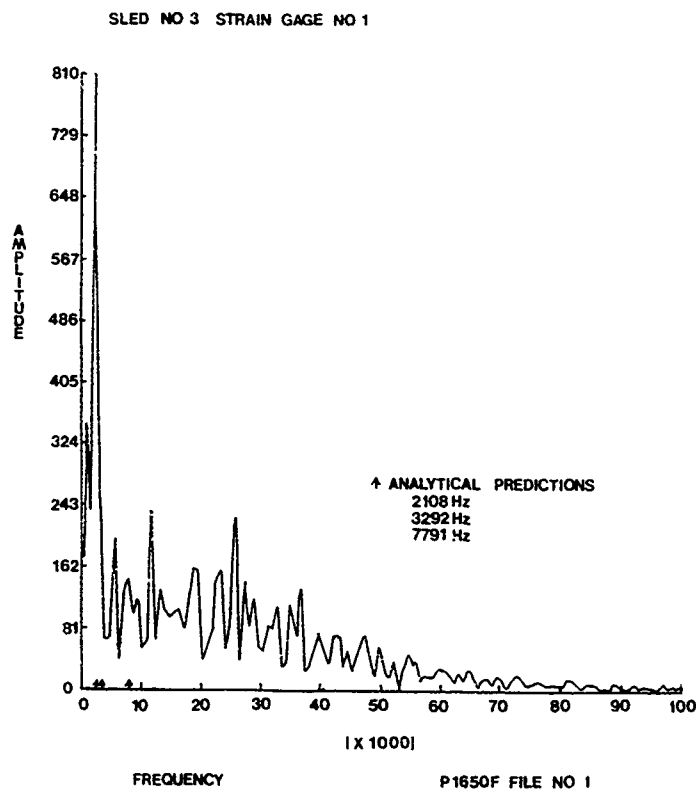


FIGURE 4. SLED 3 FREQUENCY ANALYSIS, STATION 1, GAGE 1.

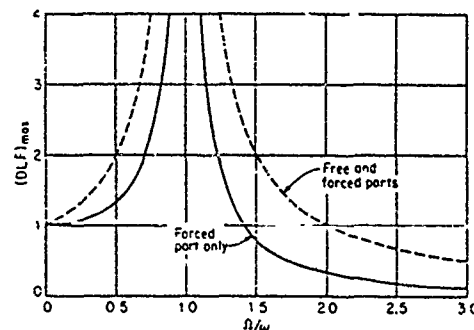


FIGURE 5. MAXIMUM DYNAMIC LOAD FACTOR FOR SINUSOIDAL LOAD  $F_1 \sin \Omega t$ , UNDAMPED SYSTEMS.

#### Penetration Modeling

Experiments will be conducted at subscale for economy and ease of testing. Scale modeling has been employed extensively in penetration testing. An entire chapter of Reference 6 is devoted to modeling penetration mechanics. Scale modeling penetration has proven valid, provided physical parameters important to the process are properly scaled in relation to each other.

The Buckingham Pi Theorem will be applied to the penetration conditions illustrated in Figure 1. Important parameters to be considered include weapon impact conditions, target response, and weapon response. Because response of the granular base and sub-base materials is deemed significant for proper modeling, gravity will be included as a parameter, and dissimilar modeling of both the penetrator and pavement surfacing material will be used.

#### Research Program

Concepts for damage-resistant runways will be developed and tested in research phases which are described below. Once concepts have been verified for subscale models, a test plan will be developed for full-scale test and evaluation.

##### 1. Phase I - Concept Development

Task 1: Two runway pavement sections will be designed for subsequent evaluations of damage resistant concepts: (a) main runway, and (b) redundant surface.

Task 2: A dimensional analysis will be performed for penetration of a weapon into the main runway and redundant surface sections designed in Task 1. The dimensional analysis will be used to design subscale experiments to determine penetration characteristics of the pavement sections with and without damage-resistant concepts.

Task 3: An experimental program will be conducted to establish baseline penetration characteristics of the two pavement types before employing damage resistant concepts. Penetration trajectories into targets will be recorded with high speed movies for the simulated full-scale impact conditions shown in Table 1. Target and projectile damage will be recorded following each test.

TABLE 1. TEST CONDITIONS

Impact Angle (Measured from the horizontal)	Prototype Impact Velocity (fps)		
	600	750	900
40°	X	X	X
50°	X	X	X
60°	X	X	X

Task 4: Sub-base rubble zones will be designed to resist penetration by the weapon threat. Designs will be based upon impact conditions listed in Table 1, weapon characteristics, penetration analysis, and results from Task 3 testing.

## 2. Phase II - Concept Verification

A sub-scale test program will be conducted to verify penetration resistance of pavement sections designed in Task 4. Testing will follow conditions and procedures used in Task 3. Each condition will be tested twice. Data will be recorded similar to Task 3 testing. Designs will be modified during testing as necessary for improved performance.

## 3. Phase III - Follow-on Development

Based on the results of Phases I and II above, a test program will be developed for full-scale testing of damage resistant runway concepts. This test program will include construction of target runway sections, both conventional and hardened. Live bombs will be air-delivered onto the sections and results will be compared to verify the reduction in damage in the hardened runway versus the conventional runway.

### SUMMARY

The Air Force Engineering and Services Center is performing a research effort to develop a concept for construction of runways that are resistant to conventional bomb damage. The concept being investigated consists of using a layer or layers of boulders in a flexible pavement's subbase course to disrupt penetration paths or to cause weapon malfunction. The research is expected to result in a payoff in the late 1980s.

### REFERENCES

1. Farmbrough, J. S., "Operation Annabelle," Royal Engineers Journal, 90, February 1976.
2. "Shielding Methodology for Conventional Weapons," U.S. Army Engineer Waterways Experiment Station, January 1980.
3. Austin, C. F., Halsey, C. C., and Berry, S. L., "Full-Scale Penetration Into Semiconfined Diorite Boulders by a Semi-Armor Piercing (SAP) Bomb and a Slender Penetrator," Naval Weapons Center NWC TP 6220, September 1980.
4. Heincker, W. R., "Dynamic Response of a Kinetic Energy Penetrator Vol I, Reverse Ballistic Sled Test of a Kinetic Energy Penetration Into Concrete," AFATL-TR-78-24, Volume I, March 1978.
5. Biggs, J. M., Introduction to Structural Dynamics, McGraw-Hill Book Company, 1964.
6. Baker, W. E., Westine, P. S., and Dodge, F. T., Similarity Methods in Engineering Dynamics, Hayden Book Company, Inc., 1973.

AD P001753

# CONCRETE PENETRATION AND RICOCHET TESTING OF TWO PROJECTILE TYPES

Richard D. Szczepanski

John A. Collins

Orlando Technology, Inc.  
Shalimar, Florida

U.S. Air Force Armament Laboratory  
Eglin Air Force Base, Florida

## ABSTRACT

The purpose of the work was to develop penetration/ricochet data for two projectiles launched against 5,000 psi concrete targets and, in addition, to measure the axial stress on the nose of a projectile during concrete penetration. The program employed projectiles 3.35 inches in diameter and approximately 27 inches long with two different nose shapes. Three different types of targets were used. Targets consisted of concrete slabs, 8-ft square and with thicknesses of 4 inches, 12 inches and 30 inches. A ricochet relation was developed from the data and the results seemed to correlate well with some previous work. One test was conducted in which an on-board shock resistant recorder was used to collect a time history of the output of a pressure transducer installed in the nose of a projectile. The results of the experiment were compared with a hydrodynamic code calculation and showed reasonable agreement for early times.

## RICOCHET TESTING

### Projectiles

The two types of projectiles used in the program are shown in Figure 1. Both projectile types were derived from the same basic design and had identical outside diameters and interior cavity geometries. The principal differences were in the nose shape and the aft baseplug design. The Type A projectile had a conical nose shape and had a baseplug which was screwed entirely into the aft end of the projectile until it was flush with the aft surface. The Type B projectile had a tangent ogive nose and included a baseplug which had an internal fitted threaded section and an aft closure equal to the outside body diameter of the projectile. The Type A projectile was approximately 27 inches long while the Type B was about 26.5 inches long with the baseplug installed. Both projectiles had blunt cylindrical nose tips 1 inch in diameter and were filled with a material that had a density of about 0.058 pounds per cubic inch (1.6 gms/cc). The projectiles were fabricated of E4340 steel, heat treated to a Rockwell C Scale hardness of 42 to 46. Total loaded weight was about 36 pounds for each projectile.

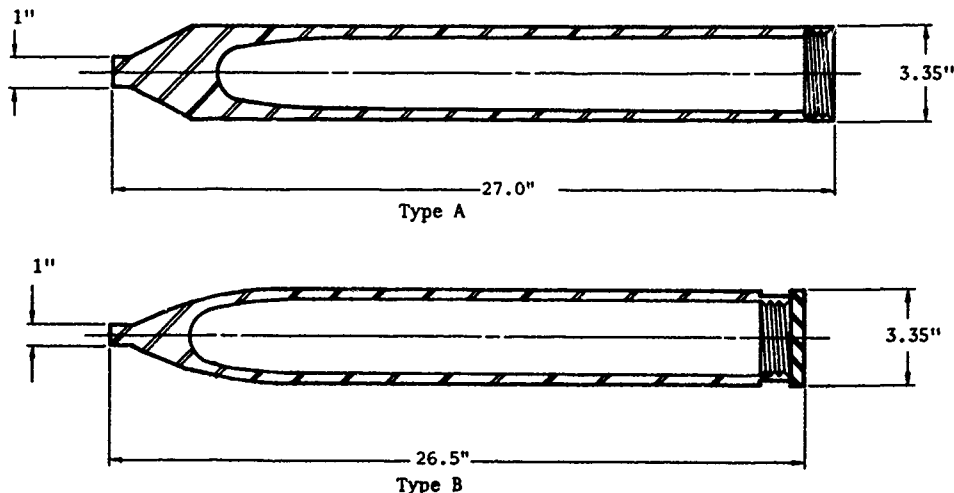


Figure 1. Projectile Geometries

### Targets

All targets were constructed of concrete using a mix design intended to yield a compressive strength of 5,000 pounds per square inch (psi) after 28 days. The limestone aggregate was specified to have a minimum compressive strength of 17,000 psi and a maximum nominal size of 3/4 inch. The targets were square slabs, 8 feet on a side with thicknesses of 4 inches, 12 inches and 30 inches. All targets were cast as monolithic pours without internal interfaces. At the time of pouring, tensile beam and compressive test specimens were taken from the concrete of each target. The compressive strength samples were tested two at a time, at intervals of 7 days, 28 days, and 90 days after pouring with all of the remaining samples tested during the week that the targets were used. Figure 2 is a time history plot of the average compressive strengths for the 12-inch thick target. The others were similar.

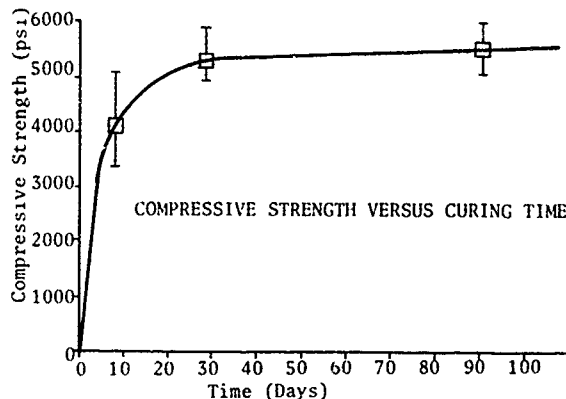


Figure 2. 12-Inch Thick Target Strength

Note that reinforcing rods were not used in the central area of the target. Figure 3 shows the geometry of a 12-inch thick target. The steel reinforcement was purposely omitted to insure that the ricochet data would be representative of the concrete and not be influenced by the steel reinforcement especially at the lower impact velocities. The lateral size of the targets, 8 feet on a side, was chosen to be as large as possible based upon the lift capability of a crane used to position the largest target which was 30 inches thick and weighed about 11 tons. In all tests, the distance from the centrally located impact point to the nearest edge was nominally 48 inches or about 14.3 calibers based upon a projectile diameter of 3.35 inches.

The final overall target configuration varied to the extent that the 4-inch and 12-inch thick targets were tested with the back side of each resting on a sandy clay soil surface, while the 30-inch thick targets were tested vertically with the back sides being free surfaces exposed to the air. The reason for the difference was

that the two thinner targets were intended to represent poured slabs resting on the ground, while the 30-inch target was a better representative of a semi-infinite concrete target. Thus, all tests involving the 4-inch and 12-inch targets were actually concrete-soil combinations. The soil beneath each target was lightly compacted by repeatedly driving a vehicle over the surface after it had been built up to the proper angle.

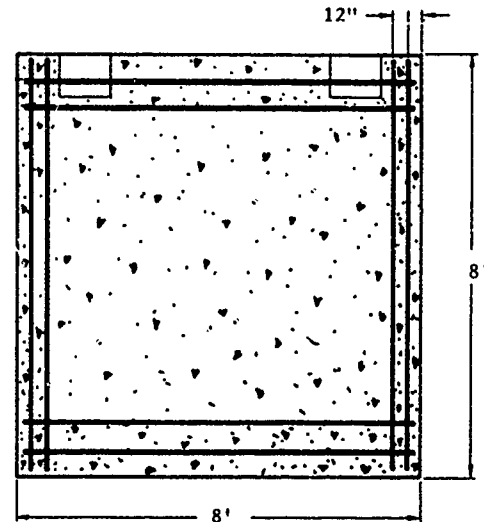


Figure 3. 12-Inch Thick Target Design

### Test Arrangement

The projectiles were launched from a 155mm gun fitted with an internal barrel sleeve which reduced the bore to about 85mm (3.35 inches). The gun was mounted on the rear of a 5-ton truck chassis and was capable of being moved in elevation only. Azimuth changes were made by turning the truck. The alignment of the projectile trajectory to the target normal was made using a surveyor's transit and a steel measuring tape. The measurement scheme was capable of determining the obliquity angle to less than 0.2 degree. While the target position relative to the line-of-sight trajectory could be measured to this accuracy, the targets could only be located within 2 degrees of a desired angle because of the difficulty associated with positioning the targets and/or the gun any more precisely.

Two impact velocities were of interest, 700 feet per second and 1100 feet per second. Projectile velocity was changed by varying the powder charge in the gun. The velocity was measured using two high speed framing cameras along with chronograph measurements of time between screens placed in the projectile's flight path to the target.

The test approach was based upon the up and down method developed by Dixon in Reference 1. Obtaining the critical ricochet angle at each

test condition required at least one ricochet and one penetration within 10 degrees of each other. Then, if the outcome was a ricochet, the angle between the target normal and the projectile trajectory was decreased by 5 degrees for the next test at that target/velocity combination. Conversely, if the outcome of the previous test was a penetration, the angle would be increased by 5 degrees. This procedure was used until both a ricochet and a penetration event had occurred at that particular combination. Figure 4 is a schematic view of the overall test arrangement for the slab targets.

Although these tests were not part of the data base used to develop the equations, and the projectile geometries were considerably different from those used in Roecker's work, the correlation with this data shows good agreement. The equations, as currently defined, were not applied to the 30-inch target data since none of those projectiles penetrated in the target and either ricocheted or rebounded. The 30-inch data fit is the dashed line.

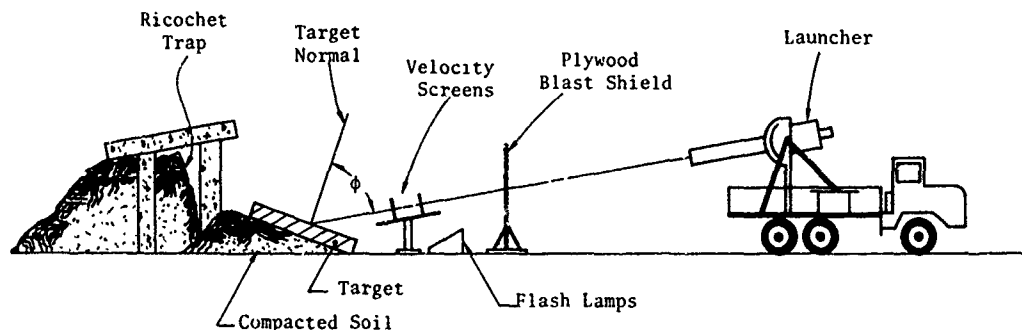


Figure 4. Overall Test Arrangement

### Results

Tables 1 and 2 contain a summary of the test results for the Type A and B projectiles, respectively. It may be noted that for the 4-inch and 12-inch thick targets, all penetrations were actually perforations, since the projectile passed completely through the target and was recovered in the underlying soil. For the 30-inch thick targets, all of the penetrations were rebounds and none of the projectiles stuck in the target or passed completely through. In most cases, the rebounded projectiles were found lying on the ground in front of the target, within 25 feet of the impact point.

Figures 5 and 6 are plots of the test data for the Type A and B projectiles, respectively. The data for all three target arrays is plotted on each graph. The solid points indicate a penetration and the open points indicate a ricochet. More scatter is evident in the Type A projectile data than in the other. These projectiles were fired first and some difficulty was experienced in obtaining the desired launch velocity due to gas blowby in the gun. As a result, a number of velocity conditions were repeated. By the time testing began with the Type B projectiles, these problems had been overcome and launch velocities were more precise.

After the testing was completed and during our analysis of the test data, an empirical correlation developed by Roecker (Reference 2) became available. These equations were used to plot the solid lines in Figures 5 and 6.

The correlation developed by Roecker is still under development and will not be presented in this paper. However, some information can be stated. The critical ricochet angle is determined by summing three terms. The first term has a relationship which explains the changes in ricochet angle as a function of the ratio of target thickness divided by the major body diameter ( $T/D$ ) and the ratio of body length divided by the major body diameter ( $L/D$ ). The second term relates changes in ricochet angle due to projectile strength and is a function of ( $L/D$ ) and the ratio of minimum wall thickness of the projectile to its major body diameter ( $W/D$ ). The third term related the changes in the ricochet angle as a function of velocity squared. Terms due to nose shape or concrete strength are not included at this stage of development.

### PENETRATION TESTING

#### Background

Penetration calculations conducted by Osborn using hydrodynamic computer codes (References 3 and 4) had resulted in a concrete loading model which could be used to predict the axial stress loading on the nose of steel projectiles penetrating concrete targets. The model was applicable for normal impacts in the range  $\sim 100$  to 500 meters/second and considered both finite and semi-infinite targets. The hydrocode calculations indicated that the steady state axial stress on the nose of a blunt projectile entering a concrete target, would be less than 4.5 kilobars (65,000 psi) for impact



TABLE 1. TYPE A TEST SUMMARY

TARGET THICKNESS (INCHES)	VELOCITY (FT/SEC)	OBLIQUITY (DEGREES)	OUTCOME <sup>1</sup> (R OR P)
30	1167	23	P
30	1030	28.9	P
30	999	35.7	R
30	783	24.5	R
30	741	20.6	P <sup>2</sup>
30	740	29.3	R
12	1159	34.3	P
12	1005	45.0	P
12	910	52.9	R
12	721	39.4	R
12	768	34.4	P
4	736	50.9	P
4	748	59.9	P
4	728	68.9	R
4	1079	76.5	R
4	1118	66.6	R
4	1088	60.3	P
30	970	33.6	R
12	1113	50.1	R
30	1097	33.8	R

## NOTES:

- 1- R indicates a ricochet; P indicates a penetration or rebound.  
 2 - Projectile was yawed 5 degrees at impact.

TABLE 2. TYPE B TEST SUMMARY

TARGET THICKNESS (INCHES)	VELOCITY (FT/SEC)	OBLIQUITY (DEGREES)	OUTCOME <sup>1</sup> (R OR P)
12	1185	50.2	P
12	1240	44.9	P
12	769	40.8	P
12	770	45.6	R
4	756	63.8	P
4	768	69.3	R
4	1186	70.8	R
4	1152	65.6	P
30	733	23.6	R
30	745	18.3	P
30	1094	35.6	P
30	1105	39.6	R

## NOTES:

- 1 - R indicates a ricochet; P indicates a penetration or rebound.

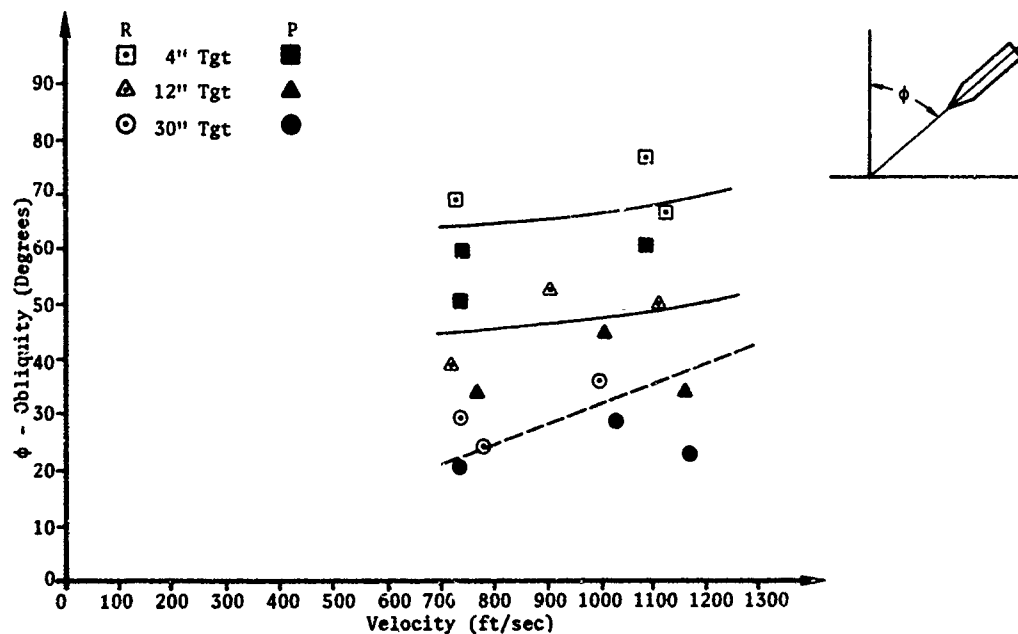


Figure 5. Type A Projectile Ricochet Data

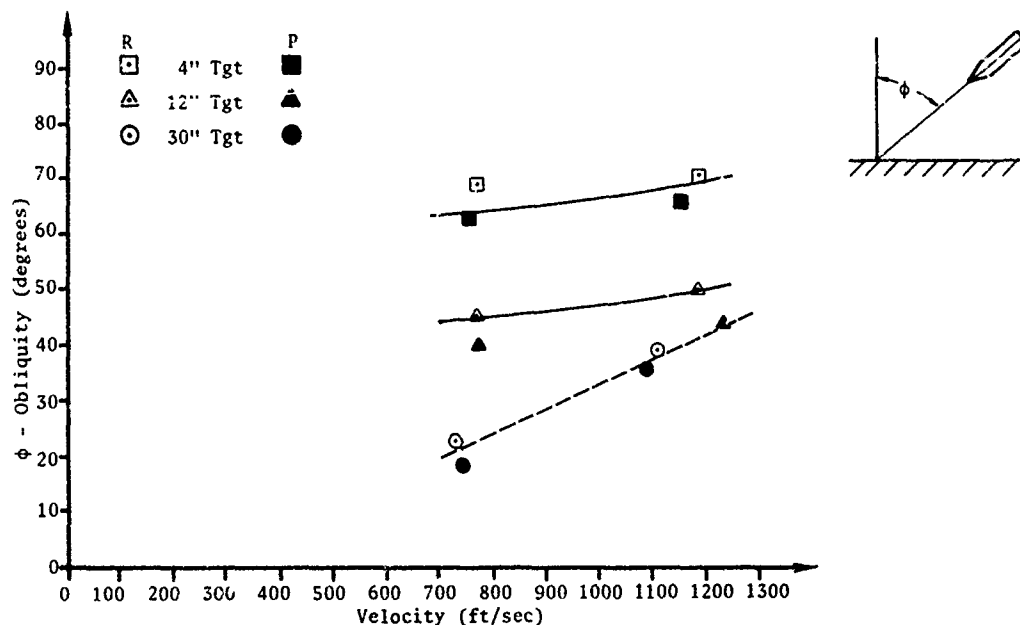


Figure 6. Type P Projectile Ricochet Data

velocities of less than 150 m/sec. Since pressure transducers used for ballistic applications are capable of reading pressures as high as 100,000 psi (6.9 Kbar) it appeared that, by including a recording package in a projectile and installing a suitable pressure transducer in the nose, it would be possible to obtain data which would confirm the basic aspects of the model and the concrete equation-of-state.

#### Instrumentation

The transducer selected was the Mod. 109A manufactured by PCB Piezotronics, a type ordinarily used to measure breech pressures in ballistic applications. The transducer features an internal transistor amplifier and is designed to withstand pressures as high as 100,000 psi, developing a low impedance output signal. The active element is a piezoelectric crystal which is strained by the external pressure applied to the diaphragm. The transducer requires a constant current source for driving the internal amplifier and the output is then coupled to the appropriate recording device using a blocking capacitor.

The recorder used for the test was furnished by the Fuze and Sensors Branch of the Air Force Armament Laboratory at Eglin Air Force Base, Florida. Originally developed by MBB (Messerschmitt-Bolkow-Blohm, GmbH), the device featured a single channel input with a solid state memory to record digital data. The maximum sampling rate was one word per 21.9 microseconds and the use of a 7-bit word resulted in an amplitude resolution of one part in 128. The recorder was powered by a rechargeable battery and after being turned on, was capable of oper-

ating from six to eight hours on a single charge. The actual writing of data into the recorder memory was initiated by an input signal from the transducer. Any output greater than 5 percent of the full scale signal was sufficient to turn on the recorder and store the data generated. The recorder had been previously used in other projectile test programs using accelerometer as the signal source and the data developed was judged to be satisfactory.

#### Testing

Figure 7 is a schematic depiction of the instrumentation arrangement as installed in the projectile. The test projectile was derived from the conical nose (Type A) projectile used in the ricochet test program with modifications to accommodate the transducer-recorder package. For the test, the projectile was launched at the center of a 4-inch thick vertical slab target which was one of those constructed for the ricochet test program. The target had a measured compressive strength of 5,542 psi. The projectile struck the target at a 90-degree obliquity angle and with no measurable yaw. The impact velocity as determined from the two high speed cameras was 360.6 and 360.5 ft/sec. The impact velocity measured by the velocity screens was 362.4 ft/sec. Because of the debris cloud and obscuration, the exit velocity of the projectile was only available from one camera and was determined to be 292 ft/sec. The projectile was recovered and the data stored was retrieved from the recorder.

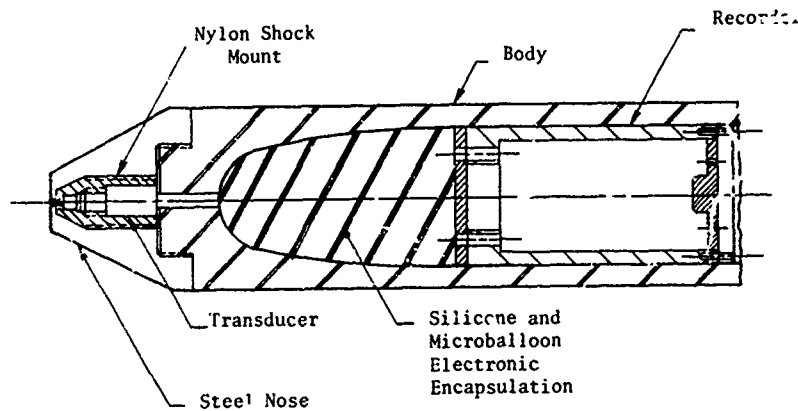


Figure 7. Sectional View of Projectile Design Used For Dynamic Pressure Measurements

### Results

Figures 8 and 9 show the data which was generated. The Figure 8 data is the complete record of the event and extends to times well after the projectile had exited the target. Since the transducer was a pressure device, the output indicating negative pressures was obviously erroneous. The large negative signal was believed to be caused by failure of the constant current power supply to the transducer which was battery operated and was found to be shock sensitive after the test. The transducer itself was returned to the manufacturer for checking and recalibration and no failure was evident. Based upon the transit time of the initial elastic wave into the silicone rubber shock attenuator which enclosed the battery, it was estimated

that the earliest possible failure time was about 35 microseconds after impact. Figure 9 is an expanded time scale of the early stages of the impact and indicates that the pressure trace was positive for about the first 150 microseconds before going slightly negative ( $\sim 1,350$  psi). Also shown on Figure 9 is a pressure time history derived from a HULL hydrodynamic code calculation of the penetration event. Figure 10 shows the calculational geometry. The pressure trace of Figure 9 shows relatively good agreement with the early portion of the recorded data, the principal difference being the initial stress peak which was not recorded because of the low sampling rate of the recorder. The recorded data also indicate the expected pressure relief in the transition from steady state penetration to the terminal phase in the region from 60 to 90 microseconds. Beyond 90

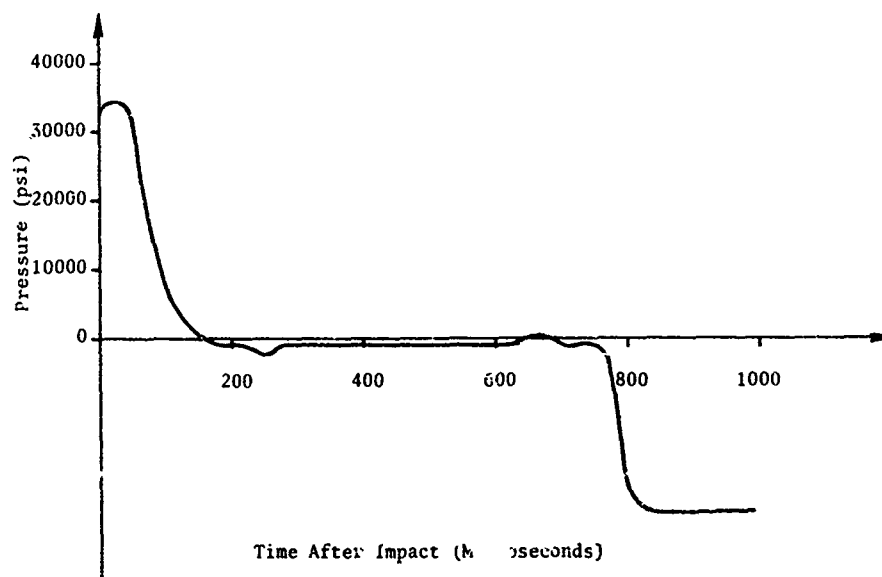


Figure 8. Recorded Pressure Record For First Millisecond

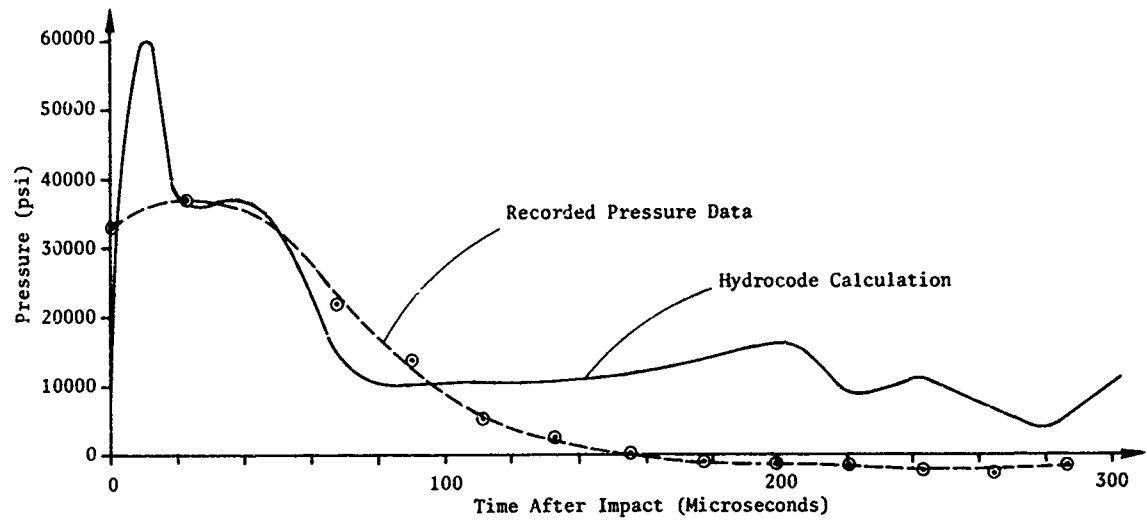


Figure 9. Early Time History Comparison of Recorded and Calculated Pressure

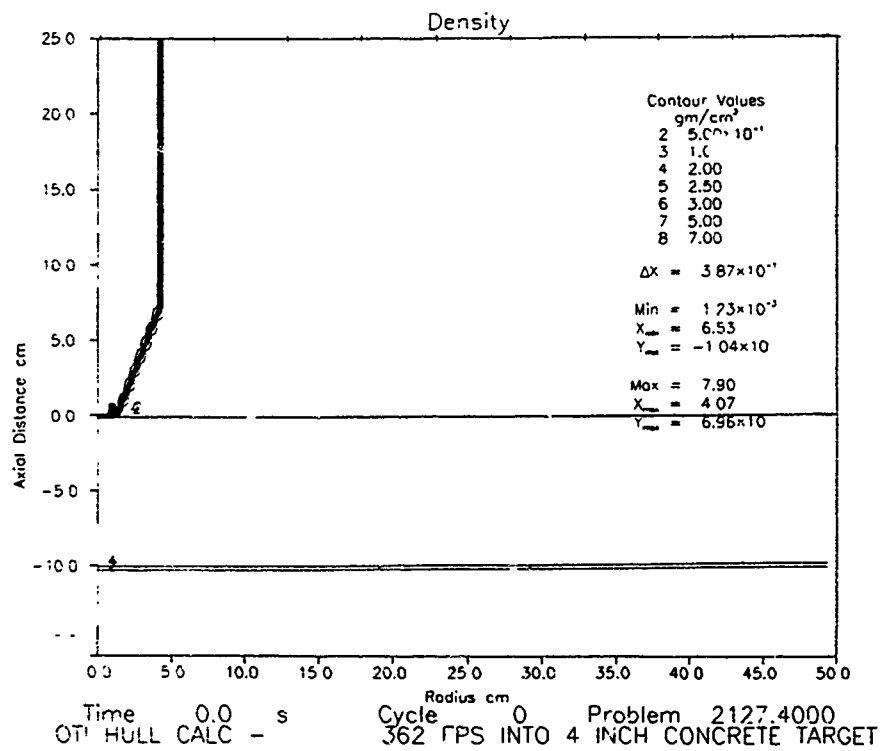


Figure 10. Calculation Geometry

microseconds, the calculated pressures are due to the loading caused by fractured concrete as it is forced ahead of the projectile. The recorded data did not show this loading, but the failure to do so was not completely unexpected since the transducer face was recessed about 0.060 inch from the front face of the projectile and the opening was only about 0.090 inch in diameter. Thus, concrete or aggregate particles much larger than 0.1 inch could have effectively blocked the transducer opening and prevented a signal from being generated at the diaphragm.

#### Summary

The program described above developed ricochet data for two types of projectiles and the results showed good agreement with an empirical correlation developed from a larger but different data base. A method was developed to record the pressure generated on the nose of a projectile during concrete penetration. Within limitations of the off-the-shelf equipment used, the data showed good agreement with a hydrodynamic code calculation of the event.

#### References

1. Dixon, W. J., "The Up and Down Method for Small Samples," Journal of the American Statistical Association, Volume 60, December 1965, pp. 967-978
2. Roecker, E., Private communication to J. A. Collins, U.S. Air Force Armament Laboratory, 24 February 1983
3. Osborn, J. J., "A Preliminary Model For Loads on a Penetrator Impacting Concrete," ARBRL-CR-00456, Ballistic Research Laboratory, June 1981
4. Osborn, J. J., "Loading on Penetrators in Concrete Slabs," AFATL-TR-82-9, Air Force Armament Laboratory, February 1982

The work reported in this paper was conducted for the U.S. Air Force Armament Laboratory, Eglin Air Force Base, Florida, under contract #08635-81-C-0050. The permission of the Air Force for publication is gratefully acknowledged.

AD P001754

## INTERACTION OF HIGH-VELOCITY ALUMINUM SHAPED-CHARGE JETS WITH FINITE STEEL AND CONCRETE TARGETS

David K. Davison

Physics International Company  
San Leandro, California

### ABSTRACT

Experiments were performed with 6.8-cm-diameter shaped charges that produced jets with tip velocities in excess of 1.0 cm/ $\mu$ s. The charges were fired at short standoff into 1-inch steel and 10-inch reinforced concrete targets, and the jets were radiographed to observe their shapes and the distributions of mass and velocity.

The experiments indicated that a mushroom-shaped jet tip can be effective in perforating hardened steel plates by the plugging process. Such jets can also be effective in perforating very thick concrete targets.

### Introduction

For many applications the depth of penetration is the primary criterion for the selection of a shaped-charge design. In some cases it is desirable to create a large-diameter hole in the target. This paper describes aluminum-lined shaped charges that were specifically designed to make large holes in both steel and concrete targets. It was found that a high-velocity aluminum jet with a large-diameter tip could be effective in such an application.

### Test Devices and Their Jets

Two liner shapes, designated "A" and "B," were tested. For each liner shape, two liner thickness profiles were evaluated. Figure 1 shows the test devices and the jets they produced. Table I summarizes the test results. The thickness profiles for the Type A (A1 and A2) liners were identical at the apex end of the liner; consequently, the jet tips are identical. The A1 and A2 jets were designed to have respective tail velocities of 0.82 and 0.70 cm/ $\mu$ s, respectively; the A1 liner is thicker than the A2 liner at the base end. The "lumps" in the Type A jets were not intended. They resulted from

systematic numerical errors associated with zoning boundaries in the two-dimensional hydrocode model of the shaped charges. The inner surfaces of the Type A liner were "wavy," yet the calculated jet velocity profiles were smooth. Special care was taken to reduce the influence of the zoning boundaries in the models of the Type B designs.

The B1 jet is more uniform than the Type A jet, except for a "fan" at the rear of the tip. The Type A jets had mushroom-shaped jet tips that apparently accounted for the large hole diameters in the armor plate targets. The B2 jet outline was not compared to the B1 jet outline because the B1 jet was not radiographed at a comparable time. The B2 armor target damage resembles that of the B1 jet, so it is likely that the jet tips resemble one another. The B1 liner is thicker than the B2 liner except close to the apex, where the B2 liner is thicker. The B1 and the B2 liners were designed to have the same jet velocity profiles; the B1 calculations were done with an advanced jetting algorithm.

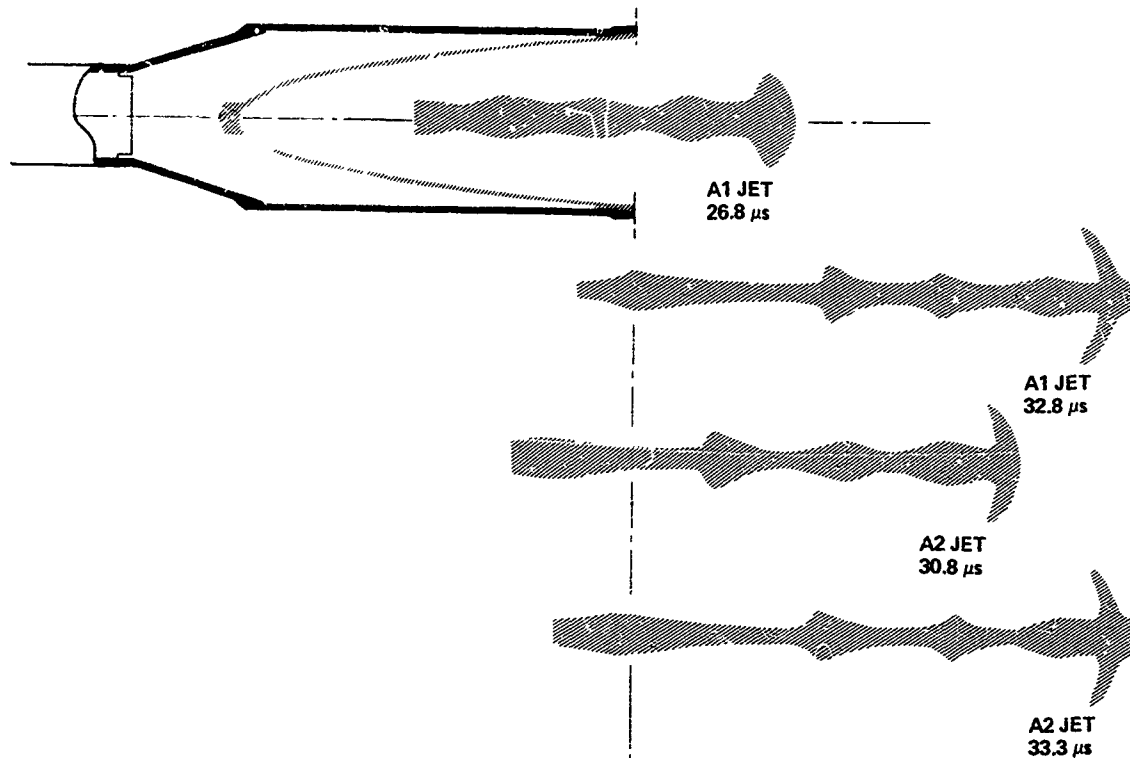
### Target Damage

The charges were fired at 2-caliber standoff against 1-inch armor plates and 10-inch concrete walls. The A1 charge was fired against 4 inches of armor plate in addition to the 1-inch target. Reliable penetration data were obtained for all of the steel targets.

The Type B charges were fired into large, specially built concrete walls. The walls had crossed, 0.5-inch reinforcing bars at 12-inch intervals near both surfaces. The concrete used in the walls had a maximum aggregate size of 0.75-inch; the specification minimized the influence of the aggregate on the hole dimensions. The compressive strength was measured to be 4000  $\pm$  400 psi.

The A1 design was fired against a concrete slab measuring 2 feet by 2 feet

LINER SHAPE A



LINER SHAPE B

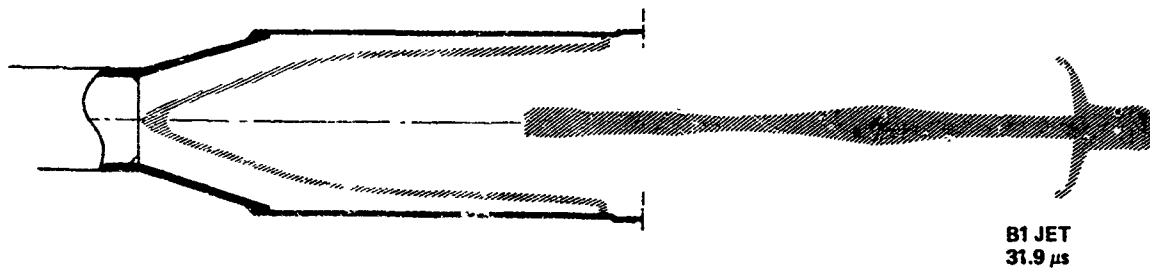


Figure 1. Warheads evaluated in test program. Liners are aluminum, 1100F, and the explosive is Octol. Times are relative to explosive initiation.

Table I. Experimental jet masses, velocities, and kinetic energies. Jet masses were calculated from jet outlines on early-time radiographs. Velocities (and experimental kinetic energies) were obtained from multiple-flash X-rays of the jets. The masses for the entries marked with asterisks (\*) were derived from radiographs taken at about the same time, relative to explosive detonations. The outlines of the jets are shown in Figure 1. The estimated total kinetic energy includes the part of the jet that extended beyond the range of the radiographs.

Design	Mass (g)	Jet Velocities (cm/μs)		Kinetic Energy (kJ)	
		Tip	Tail	Experimental	Total
A1	5.7	1.08	0.85	326	--
* A1	6.8	--	--	--	--
A2	6.6	1.08	0.84	351	379
* A2	7.2	1.05	0.76	345	--
* B1	6.3	1.06	0.88	334	414
B2	--	0.93	--	--	--

by 10 inches. The target was so small that it was destroyed by the shot, and no reliable data are available on the performance of the design against a concrete wall. The A2 design was fired against a large slab reinforced with parallel, 1-inch reinforcing bars centered between the surfaces. The slab fractured along its length and collapsed, so the hole did not remain intact. The shape of the hole was estimated from measurements on the fractured slab.

Figure 2 shows the holes 1 inch in armor produced by the four designs; it also compares saw-cut sections of the 1-inch target and of the first inch of the 4-inch target penetrated by the A1 charge.

For the 1-inch target perforated by the A1 charge the section taken along the plane of asymmetry of the jet reveals the history of the penetration process. The left edge of the hole was formed at an earlier time than the right edge. The front surface spall, caused by the tip of the jet, is symmetrical with respect to the axis, and the right edge of the hole, further from the axis, was formed by events occurring after the impact of the tip of the jet. On impact, the bulbous jet tip (about 3 cm in diameter) fractured the target, and the remainder of the jet removed the particles created by the fracturing process. It should be noted that the defeat mechanism observed for these very hard steel targets does not necessarily apply to targets made of softer steels. Hardened steel is brittle, and the defeat mechanism depends on this

material property.

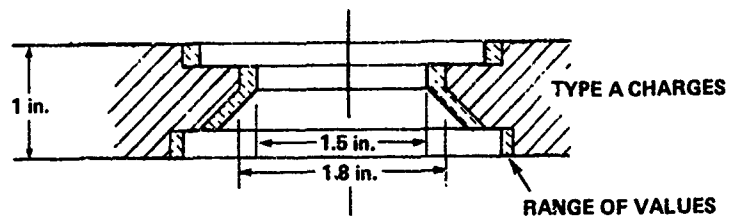
By comparison, the sectioned first inch of the thick steel target did not have a pronounced front surface spall ring, and the hole was narrower at its rear surface. The minimum hole diameter is about the same for both tests. Pronounced bending can be seen at both the front and rear edges of the first inch of the thick target. The volume of the hole created by the A1 jet in the thick steel target was 51.3 cubic centimeters.

The hole shapes in concrete are illustrated in Figure 3. Perforation was accompanied by considerable spall at both surfaces of the targets. Except for the A2 test, steel witness plates were spaced behind each of the concrete targets. None of the witness plates showed evidence of jet penetration, although a small amount of aluminum vapor appeared to have been deposited on their front surfaces. The charges were centered between the reinforcing bars to minimize the hole size.

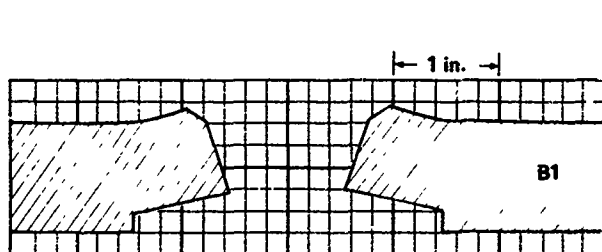
#### Conclusions

Efficient, aluminum-lined shaped charges can be designed to create large holes in both steel and concrete targets. A jet with a 3.0-cm-diameter, mushroom-shaped tip perforated a 1-inch-thick armor steel target by the plugging process, creating a hole approximately 4.0 cm in diameter. A similar jet perforated a 10-inch reinforced concrete target.

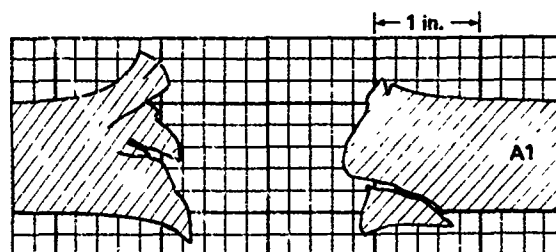




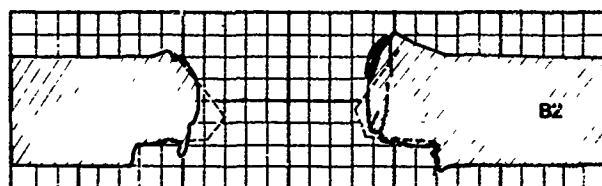
a. Cross section of holes in armor plate made by the Type A charges at 2-caliber standoff. The shape of the hole was estimated from measurements on the targets.



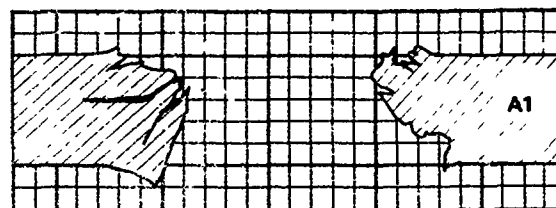
b. Cross section of the hole in the armor plate made by the B1 charge at 2-caliber standoff. The hole outline was constructed from measurements on the target.



d. Cross section of hole in the first of four armor plates, made by the A1 design at 2-caliber standoffs.



c. Saw-cut section of the hole in the armor plate made by B2 charge at 2-caliber standoff. The dotted line indicates the minimum hole dimensions obtained from measurements on the target. Obviously visible fractures are shown.



e. Cross section of hole in a single armor plate, made by the A1 design at 2-caliber standoff.

Figure 2. Holes in armor.

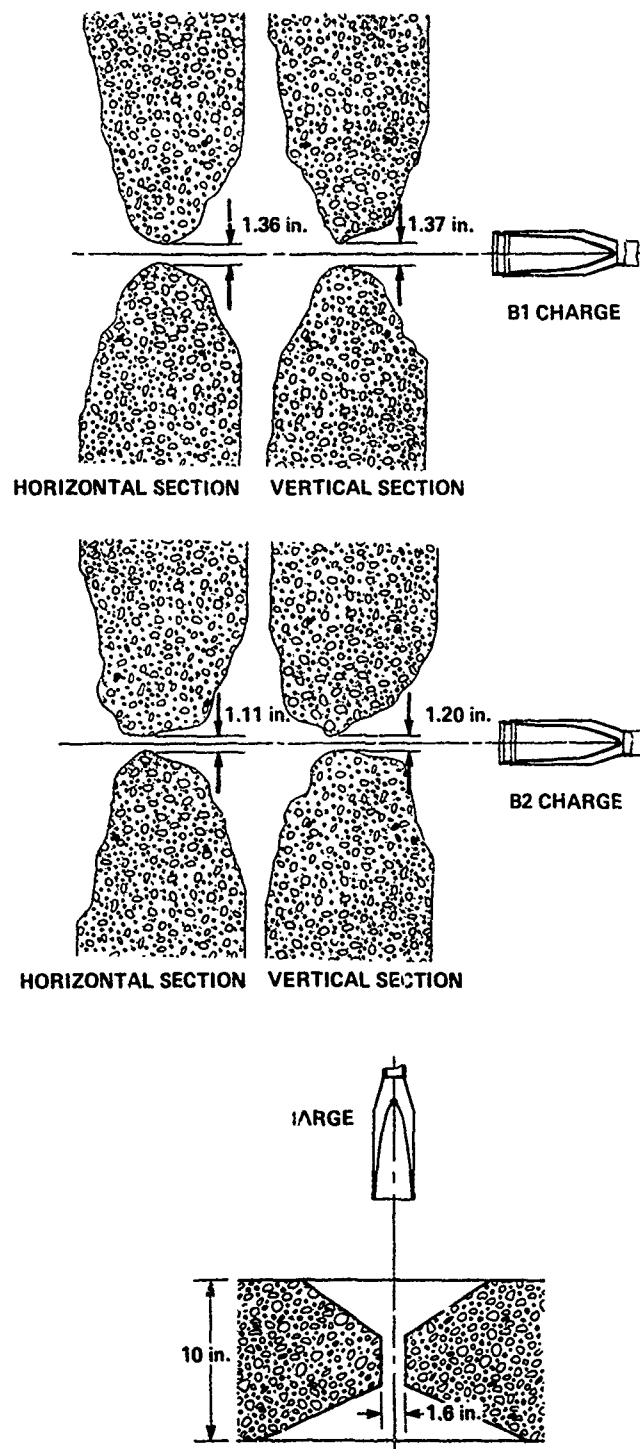


Figure 3. Holes in concrete. Nominal reinforcing bar locations are indicated.

AD P001755

PENETRATION EQUATION FROM STEEL, ALUMINUM, AND TITANIUM PLATES  
BY DEFORMING PROJECTILES AT OBLIQUITY

James S. O'Brasky  
Thomas N. Smith

Naval Surface Weapons Center  
Weapons Development Branch  
Dahlgren, Virginia

ABSTRACT

A similitude equation is offered for the penetration of steel, aluminum, and titanium plates at obliquities up to 70° by non-deforming steel projectiles. The proposed equation is confidence and compared to the accuracy achieved in single projectile-single material relationships.

OBJECTIVE

The objective of the work reported in this paper is to determine whether the classical similitude analysis could be applied to the general case of ductile target material, non-deforming projectile-medium velocity penetration phenomena.

DATA SOURCES

Since this effort was purely an exercise in data analysis, existing data sources were used. These sources are listed in Table I. Reference (h) contains the results of the most extensive armor material data analysis known to this writer, penetration of Class B armor at obliquity angles of up to 70°. References (i) and (j) extended the data set to HY80 and HY100 steels. Reference (k) was used for mild steel. Reference (g) contains data on aluminum and titanium alloys. References (k) and (g) data should be used with caution since these alloys were in the process of development during the period in which the data was acquired.

BACKGROUND

The penetration of armor by projectiles has become one of the classic applications of dimensional similitude techniques. One of the earlier, if not the earliest such application was made by L.T.E. Thompson, PhD, in 1927 at the Naval Proving Ground (NSWC predecessor), reference (a). During the 1930's and 40's, very extensive experimental work was conducted by A. V. Hershey, PhD, within similitude framework, references (b), (c), (d), and (e). Although the similitude analysis has included provision for considering materials of vastly different mechanical properties and indeed for different materials from the earliest derivation, no examples of such applications have been found by this writer. A similar comment can be found in reference (f) of 1973 vintage. The general data presentation for armor penetration seems to be a plot of  $V_{50}$  vs plate thickness for a given penetrator fired against a given plate material, reference (g). Such data presentations lead to very large armor handbooks of quite limited utility.

APPROACH

The non-dimensional variables for the non-deforming projectile-ductile plate problem are shown in Table II. These variables were tested using Analysis of Variation (ANOVA) Techniques to determine which variables were significant. For those cases in which a single dependent variable was significant, third degree regression equations were generated and confidence. For those cases in which multiple variables were significant, multiple linear regression techniques were used.

RESULTS

The results of the ANOVA are shown in Table III. Considering that three different materials

(steel, aluminum, and titanium) were involved, it is somewhat surprising that only three variable groups appear significant. Table IV contains the regression equations. Note that the single material equations and the multiple mechanical property equations have similar  $R^2$  values and standard deviations. The multiple material equation also appears to be reasonably accurate.

#### CONCLUSIONS

The similitude analysis provides a powerful tool which is applicable to the general case on ductile armor penetration by non-deforming projectiles in the medium velocity range.

A single equation may be used to predict penetration resistance of steel, aluminum, and titanium armors. Within a single material, the effects on penetration of mechanical property variation can be accounted for in the equation.

#### REFERENCES

- (a) L. Thompson and E. B. Scott, Memorial de l'Artillerie Francaise, Vol. 6, pg. 1253, 1927.
- (b) A. V. Hershey, The Plate Penetration Coefficient and Formulas for Penetration, 1st Seminar Report, Naval Proving Ground, Dahlgren, VA, 8 Jan 1942.
- (c) A. V. Hershey, Analytical Summary Pt IV: The Theory of Armor Penetration, Naval Proving Ground Report #9-46, 1946.
- (d) A. V. Hershey, Ballistic Summary Part I: The Dependence of Limit Velocity on Plate Thickness and Obliquity at Low Obliquity, Naval Proving Ground Report #2-46.
- (e) A. V. Hershey, Ballistic Summary Part IV: The Dependence of Limit Velocity on Plate Thickness and Obliquity at High Obliquity, Naval Proving Ground Report #1125.
- (f) W. E. Baker, P. S. Westine, and F. T. Dodge, Similarity Methods in Engineering Dynamics: Theory and Practice of Scale Modeling, Hayden Book Company, Inc., 1973, pg 183.
- (g) R. E. Cole, Armor and Ballistic Data Handbook, Naval Weapons Laboratory, Dahlgren, VA, TR.
- (h) A. V. Hershey, Construction of Plate Penetration Charts or Tables, Naval Proving Ground Report #1120.
- (i) W. H. Hall, Ballistic and Metallurgical Tests of HY60 Plate, Naval Proving Ground Report #1639.
- (j) Naval Weapons Laboratory, Dahlgren, VA, Letter Report, TEGM:HWP:av, Ballistic Tests of HY100 - Steel Plate, 22 Sept 1959.
- (k) Weapons Data, Fire, Impact, Explosion, OSRD Report #6053, 1945.

TABLE I

<u>Target Material</u>	<u>Projectile Material</u>	<u>Striking Velocity Range (ft/sec)</u>	<u>Obliquity Range (°)</u>	<u>Ref</u>
Class B, Steel Armor	Steel	500 - 3500	0 - 70	h
HY80 Steel	Steel	500 - 3500	0 - 70	i
HY100 Steel	Steel	500 - 3000	0 - 70	j
Mild Steel	Steel	500 - 3000	0 - 45	k
5083, 7039, Ti Aluminum	Steel	500 - 3000	0 - 45	q

TABLE II

## NONDIMENSIONAL VARIABLES

where:

- $m$  = Mass of the Projectile
- $V_L$  = Limit Velocity
- $\sigma$  = Yield Stress of the Target Plate
- $\alpha$  = Ultimate Stress of the Target Plate
- $d$  = Projectile Diameter
- $e$  = Target Plate Thickness
- $\theta$  = Obliquity Angle
- $\phi, \psi$  = Angle Components of Projectile Yaw
- $E$  = Young's Modulus of Target Plate Material
- $\mu$  = Poisson's Ratio of Target Plate Material
- $\epsilon$  = Strain to Failure of Target Plate Material
- $\dot{\gamma}$  = Change in Stress to Failure/Change in Strain Rate =  $\sigma/\dot{\epsilon}$
- $\rho$  = Density of Target Material

TABLE III  
ANOVA RESULTS, EQUATION<sup>1</sup>

<u>Source</u>	<u>DF</u>	<u>Sum of Squares</u>	<u>Mean Square</u>	<u>F Value</u>
Total	222	706.91	-	-
Regression Variable #	4	692.37	173.09	2543.50
$\frac{mV_i^2 \cos^2 \theta}{\sigma_{\epsilon d^3}}$	1	686.71	686.71	10289.28
$\frac{K_1 V_i^2 \cos^2 \theta}{\alpha_{\epsilon d^3}}$	1	1.72	1.72	25.73
$\frac{S}{E}$	1	.26	.26	3.84
$\frac{m}{\rho d^3}$	1	3.68	3.68	55.17
Residual	18	14.54	.06674	-

TABLE IV  
REGRESSION EQUATIONS

Target Material	DF	Equatio	Std D	R <sup>2</sup>
All	223	$\frac{e}{d} = .01634 (-7 + 1.4 X - Y + 11.65 Z)$	.258	.979
Class B, HY 80, HY 100, Mild Steel	147	$\frac{e}{d} = -1.54 + 20.18 (X) + 12.95 (X^2)^2 - 2.24 (X^3)^3$	1.05	.993
Titanium	34	$\frac{e}{d} = -4.08 + 118.32 Y + 214.6 - Y^2 + 193.4 Y^3$	6.15	.989
Aluminum 5083	51	$\frac{e}{d} = -1.48 + 142.91 Y - 28.66 Y^2 + 2.69 Y^3$	25.28	.81
Aluminum 7039	30	$\frac{e}{d} = .917 + 75.82 Y - 4.48 Y^2 + .883 Y^3$	29.64	.92
All Aluminums	89	$\frac{e}{d} = -3.02 + 151.40 Y - 35.24 Y^2 + 3.79 Y^3$	29.15	.85

where:  $X = \frac{m V_L^2 \cos^2 \theta}{\sigma \epsilon d^3}$

$Y = \frac{m V_L^2 \cos^2 \theta}{\sigma \epsilon d^3}$

$Z = \frac{m}{\rho d^3}$

DF = Degree of Freedom

AD P001756

## PLAIN CONCRETE LOADED AT HIGH STRAIN RATES

Rodney G. Galloway

Air Force Weapons Laboratory  
Civil Engineering Research Division  
Kirtland Air Force Base, New Mexico

### ABSTRACT

Failures to reinforced concrete structures subjected to blast and shock loads from nuclear and conventional weapons generally occurs at high strain rates from 0.1 to  $10.0 \text{ s}^{-1}$ . In order to analytically predict structural response, material models are needed to characterize the strain rate sensitive behavior. Data to verify and base the material models is also needed. Some information is available for strain rates from hydraulic testing machines and drop hammers. This report is to document the conclusions of the initial simplified calculations performed trying to define what information is known about strain rate sensitive behavior of concrete and how to set up an experimental program designed to answer pertinent questions. It was determined that the best constant strain rate loading device would consist of either a linearly increasing pressure load at the concrete specimen surface or a piston driven by a linearly increasing pressure.

### ANALYTICAL MODEL

A series of one dimensional, multi-degree of freedom, dynamic spring-mass calculations were performed to address possible parameters of interest in setting up an experimental program. The model was set up to determine what the critical parameters might be in testing a 6 inch by 12 inch concrete cylinder at strain rates of 0.1, 1.0 and  $10. \text{ s}^{-1}$ . The computer code used is called SPRINGMASS. It is capable of representing a series of masses interconnected by springs. Two types of material models were exercised in this series of calculations: Elastic and elastic-perfectly plastic.

The major question addressed by the calculations was the type of loading device that could be used to obtain a constant strain rate during the loading of the specimen. Four types of boundaries (or devices) were analyzed: (1) displacement driven, (2) projectile driven, (3) pressure driven, and (4) piston (pressure driving a projectile initially at rest). The displacement driven boundary was used as the basis of comparison for all other calculations. This was felt at the

beginning of the calculations to simulate what the best possible case would be in achieving a near constant strain rate in the test specimen. This was found to not be the case in the calculations as will be explained.

### DISPLACEMENT DRIVEN BOUNDARY

This set of calculations provided a good comparison between the numeric results and exact analytic solutions. The material was characterized as linearly elastic with a Young's modulus equal to about  $4 (10^6)$  psi. This produces a compressional wave speed of 11,414 ft/s. The stress wave produced by the constant velocity driven boundary takes 175  $\mu\text{s}$  to transit from top to bottom. The first wave produces a shortening of  $8.76 (10^{-5})$  times the strain rate as a step increase in local strain. After one wave transit, the next step increase is twice the first or  $1.75 (10^{-4})$  times the strain rate. Each transit thereafter increases the strain by  $1.75 (10^{-4})$  times the strain rate. This of course is true since the sample is exactly one foot long. In figure 1 the shape of the curves demonstrates the discretization error in the spring mass calculation. The exact solution is a square wave that propagates from top to bottom. The over-shoot and ringing is due to the spring mass approximation and directly related to the number of masses and springs used in the model. The results show the analytical approximation to this square wave propagating through the cylinder. It is also interesting to note that the material in the cylinder only experiences the prescribed boundary velocity while the stress wave passes by on the way to the fixed boundary. The reflected wave unloads all motion on the return trip. Therefore, local material will not experience the desired strain rate. It experiences a step increase in strain and not a constant strain rate. A point at middepth will be responding at the boundary velocity for only 1/2 the transit time under this case. This demonstrates that to obtain a constant strain rate a linearly increasing velocity at the boundary is needed.



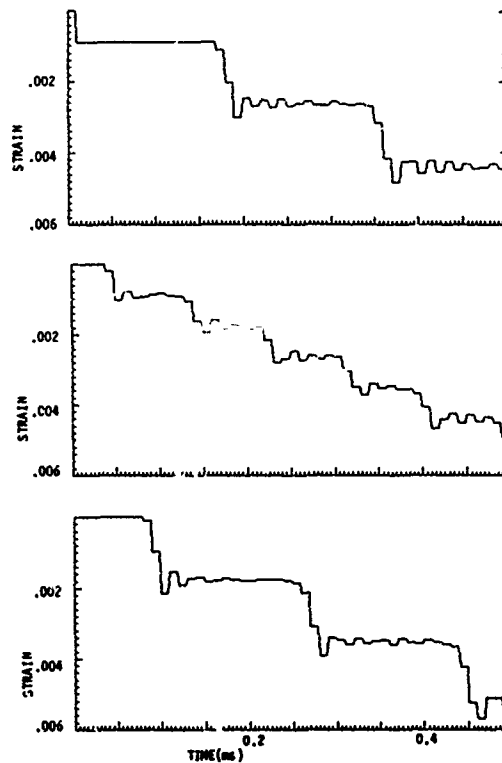
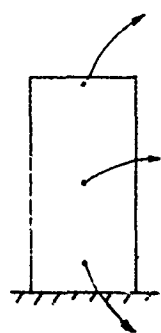
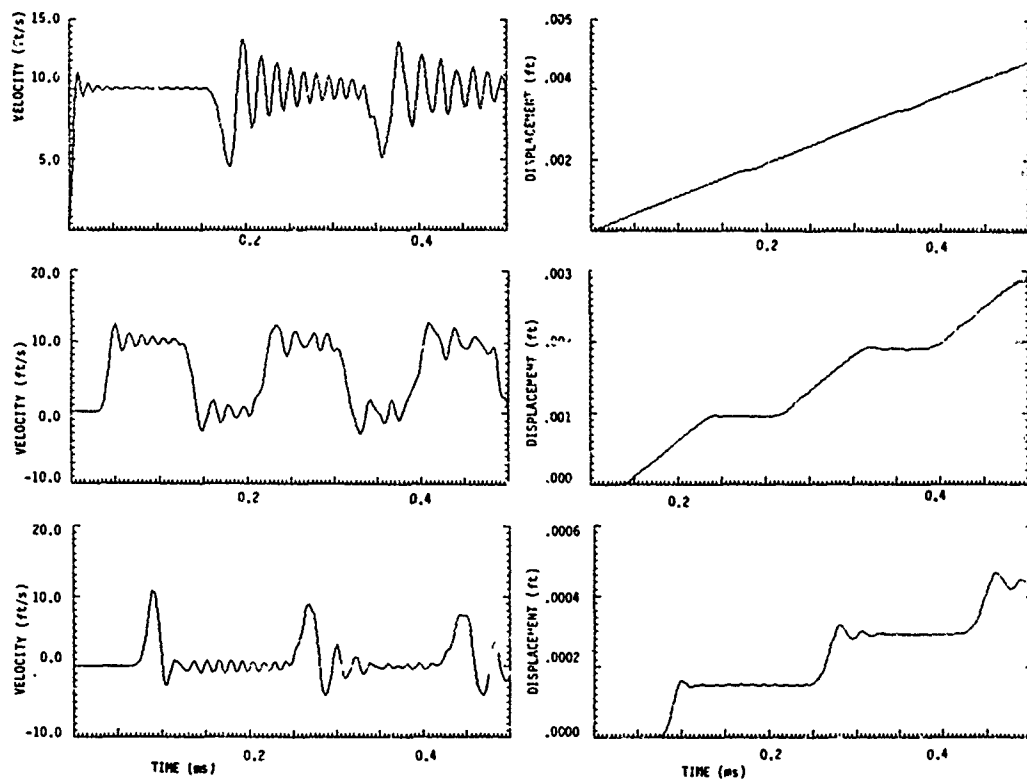


FIGURE 1. DISPLACEMENT DRIVEN BOUNDARY

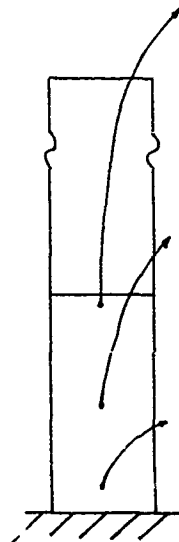
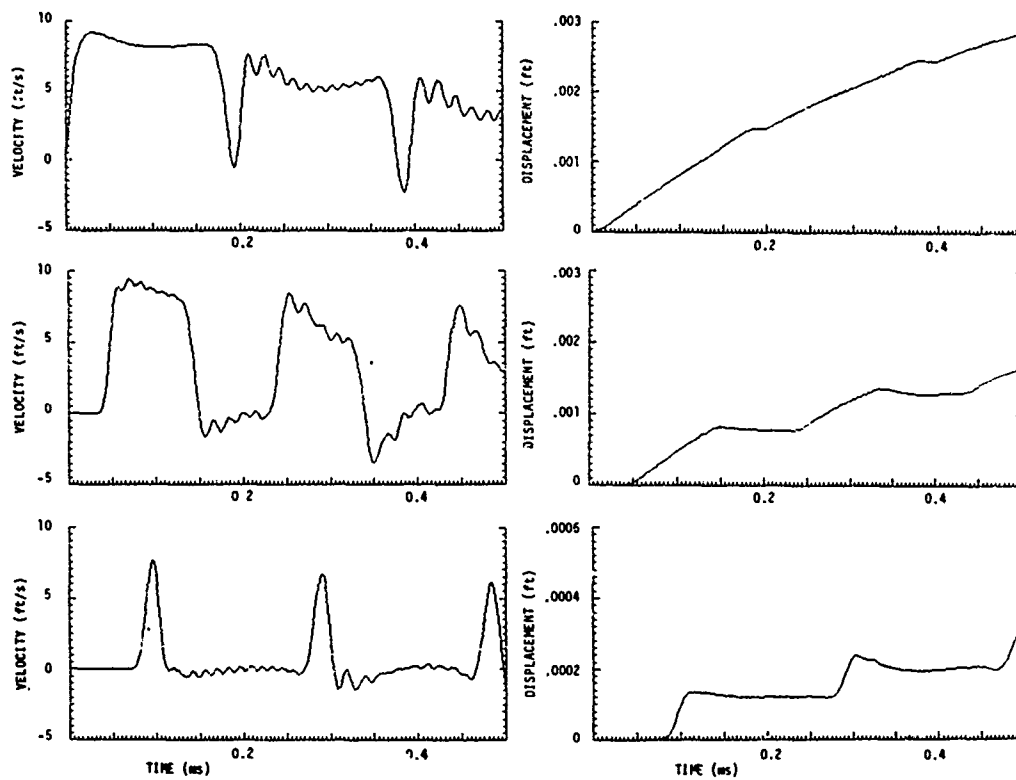
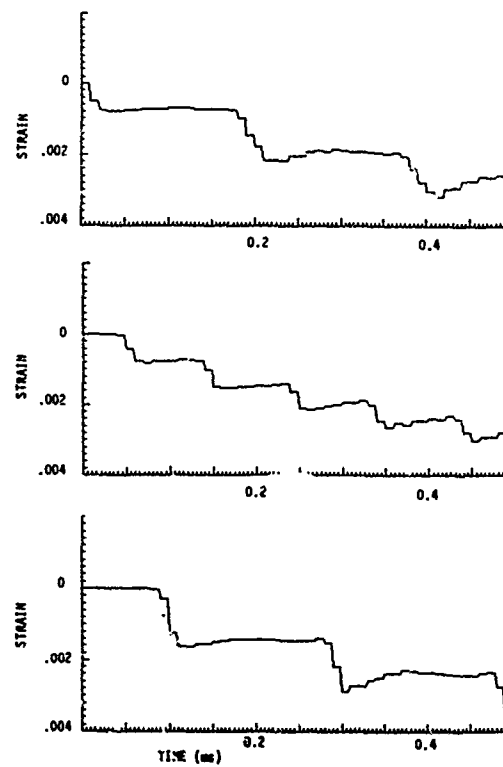


FIGURE 2. PROJECTILE DRIVEN BOUNDARY



#### PROJECTILE DRIVEN BOUNDARY

The second type of possible boundary condition is a projectile driven boundary. The force interaction is one of momentum transfer at the interface between the concrete specimen and the projectile. Some of the questions to be investigated concern the mass and stiffness of the projectile. In the cases investigated it was assumed that steel would be used as the projectile providing a stiff interface with respect to the concrete. It appears from the calculations that this made the projectile driven boundaries appear like the displacement driven boundaries generally through the first wave transit.

There is very good agreement between a 10.0 ft projectile impacting the concrete sample and the boundary driven calculation on elastic material. In figure 2 the load on the surface degrades as the concrete interacts with the projectile. By the third stress transit the input velocity has reduced from 10 to 5 ft/s.

A calculation was performed that demonstrates the extreme case of a small projectile. A projectile one inch long is driven into the concrete at 10.0 ft/s. This produced a shock wave that traveled through the sample and then the material unloads in tensile spall. A triangular decaying velocity wave propagates through the concrete to the bottom and back up and reflects as a tensile wave off the projectile's free surface.

The material does not have time to yield in compression before tensile failure occurs. This calculation would be similar to the case where projectiles of one type or another induce short transients in material. Even though response can be measured during the transmission of the stress wave, response occurs so rapidly that insufficient total strain might occur to damage the material. Also, if the stress wave is not sustained for sufficient time it would be a poor measure of strain rate sensitivity. It might be necessary in some cases to preload the sample into the nonlinear portion of response (above  $0.6 f'_c$ ) and then induce a stress transient so that the critical portion of response is measured. That would occur around the point of strain where  $f'_c$  would occur.

Still, in all the projectile driven boundaries that were considered, a poor constant strain rate is achieved. Projectiles model the displacement driven boundaries well.

#### PRESSURE DRIVEN BOUNDARY

Several types of pressure driven boundaries were considered. The one that was found to give the best results was a linear pressure increase equal to a stress rate of  $40(10^6)$  psi/s. This was used to simulate a strain rate of  $10 \text{ s}^{-1}$  on a elastic material with Young's Modulus equal to about  $4.0(10^6)$  psi. Figure 3 demonstrates that this type of load approximates a constant strain rate best. Even so, the strain rate varies from the top of the sample to the bottom. At the top,

the rate is about a constant  $10 \text{ s}^{-1}$ ; while at the bottom, the strain rate is twice or  $20 \text{ s}^{-1}$  over half the time and zero the other half. This is because of the dynamic transfer of the load. This type of loading approximates the desired strain rate better than any others tried. It is difficult to match this type of boundary by typical high explosives, so the rest of the pressure boundary calculations were used to investigate possible variations that could occur in the loading of the sample.

#### PRESSURE DRIVEN PISTON

The last type of boundary condition that was tried was where the projectile was at rest and then driven by a pressure on the far end. A steel piston one foot long was used in the calculation. The peak pressure was 5,000 psi. A linear rise to this pressure was used. This is the second case where the desired constant strain rate was achieved. It seems to be highly dependent upon the ability of the loading device to transmit as perfectly as possible a constant stress rate. This might be achieved by varying the material properties of the loading piston to allow some type of material to crush at a given rate or yield easily and gradually strain harden. This could be investigated in more detail in experiments (see figure 4).

#### SUMMARY

These calculations reveal that several points should be considered when designing a strain rate effects test.

1. A constant strain rate is best achieved by a constant stress rate. This is strictly true for elastic response. After the material begins to yield or fail, it is difficult to control specimen response. It might be necessary to use a strain controlled preload device to bring the test specimen to the level at which strain rate sensitivity is to be measured and then induce a constant stress rate at the boundary. Strain rate's influence on initial yield value should be measured first then the effect of strain rate on other parameters could be investigated.
2. If the piston or projectile driving the test article is moving at a constant velocity, the article will not respond at a constant strain rate but load up in a series of wave transients.
3. If a piston is driving the test article, a constant stress rate driving the piston will closely match a constant strain rate in the test article. High frequency pressure spikes with a half period greater than  $50 \mu\text{s}$  will influence the response. It is uncertain how small a pressure spike must be before it could be neglected.
4. A drop hammer would approximate a constant velocity at the boundary but, as described, be a poor device to give a constant strain rate.

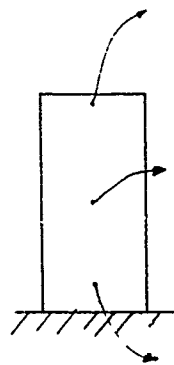
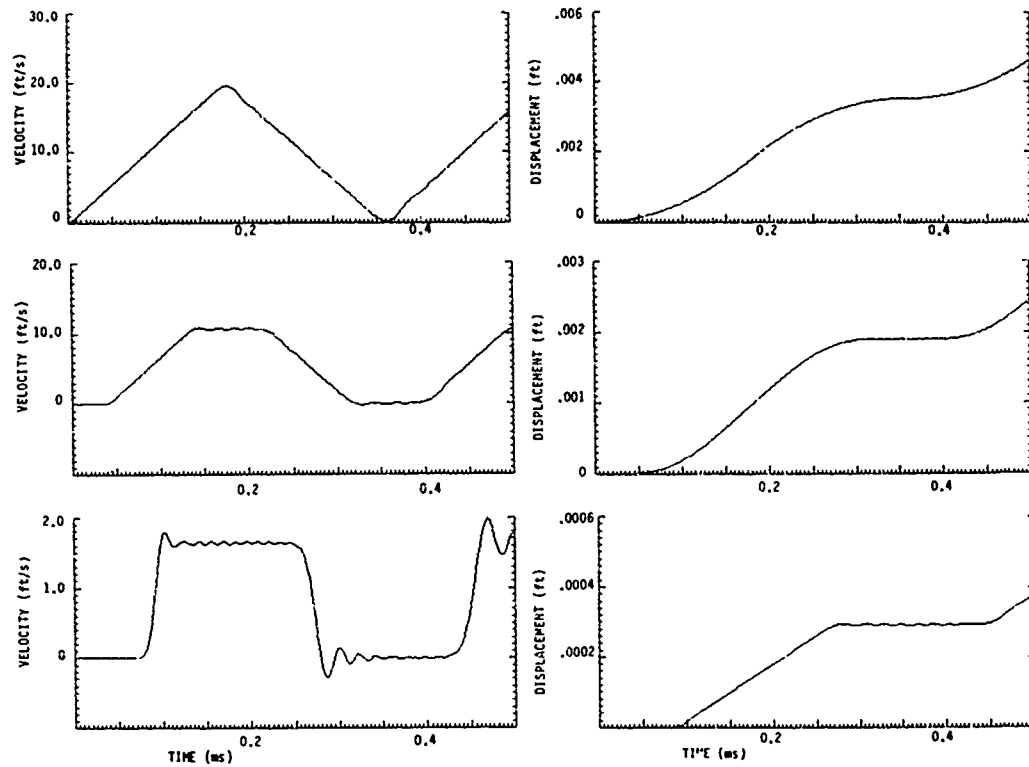
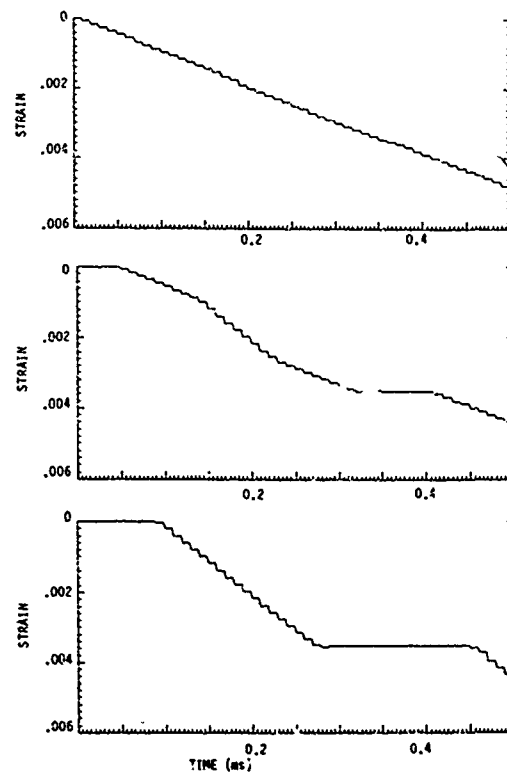


FIGURE 3. PRESSURE DRIVEN BOUNDARY



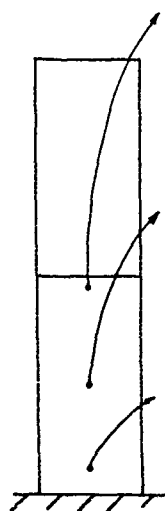
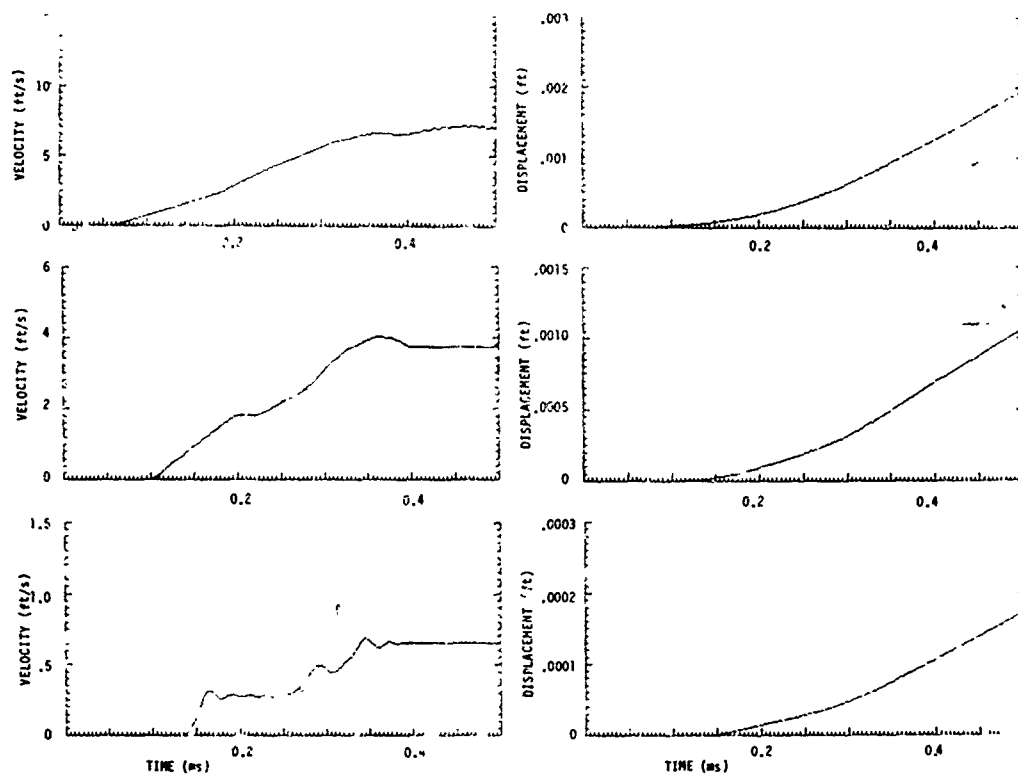
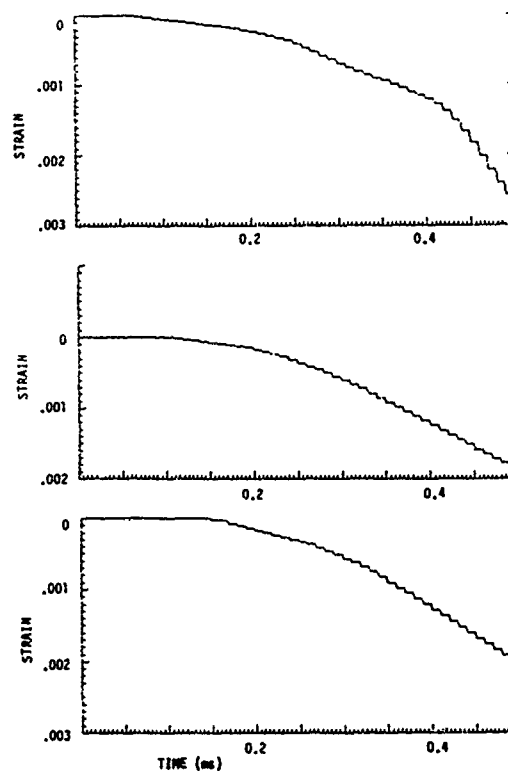


FIGURE 4. PRESSURE DRIVEN PISTON



AD P001752

LABORATORY TEST FACILITY FOR STATIC AND DYNAMIC  
LOADING OF STRUCTURES AND COMPONENTS

William J. Carter

Terra Tek Engineering  
400 Wakara Way  
Salt Lake City, Utah 84108

ABSTRACT

A large-volume test frame designed for standard tension, compression or fatigue loading of massive samples has been modified to allow dynamic loading at rates up to  $10^2/s$ . Scale model structures or structural materials in an arbitrary simulated environment may be tested in a variety of biaxial containment frames. Flat-jacks around the periphery of these frames allow application of independently controlled stresses or stress gradients. Dynamic overpressures between 85 MPa and 400 MPa are readily obtained in specimens ranging from 0.2 to 0.9 m<sup>3</sup> in volume. The facility allows for rapid and economic evaluation of structure or structural material response, soil-structure interaction mechanisms, and fundamental response of rocks or soils to dynamic loading.

INTRODUCTION

Although there is no completely satisfactory substitute for full-scale field testing under realistic explosive loading for effective evaluation of weapons effects, there are also several drawbacks to this approach. One is that of cost; full-scale simulators are time-consuming and expensive to build and operate, particularly if more than a few configurations are of interest. Another is flexibility, since only minor changes in test conditions, such as geologic setting, angle of attack, or type or frequency of munitions loading, may imply major changes in the facility. The attempt to simulate nuclear bursts, with their sharp rise time and extended pulse lengths, using high explosives has presented special problems, particularly those associated with ringing in the resonance chambers of HEST-type systems.

The alternatives to full-scale testing also present difficulties. One approach is to determine the basic material properties response of structural elements in the stress/strain regimes of interest and combine them by analytical means to determine the response of the composite structure. Obviously, this approach is limited by the capabilities of the computer codes used. Another, somewhat complementary method is to model the structure on a scale compatible with laboratory

facilities and determine the response directly. This approach is limited by constraints of scaling, requiring strict matching of material properties and dynamic loading parameters between model and prototype that can never be fully realized in practice. Nevertheless, with care, both these approaches can yield valuable insight into the dynamic response of materials and structures of interest, and do so cost effectively.

Excluding field-scale explosive systems, several alternatives exist for imposing large dynamic loads in the laboratory simulating those arising from conventional or nuclear blasts on ground materials, structures or construction elements. Such devices as Hopkinson bars operated in tension, compression or torsion modes, laboratory confinement vessels for scaled explosive tests, large diameter gas guns, or flying plates are all useful for limited ranges of experiments. All, however, suffer from restrictions either of size (test volume) or lack of flexibility in loading rates and paths, both serious factors for this application.

Inhomogeneous materials such as rocks and soils, concrete aggregates, and composite construction materials require measurements to be made over a test volume large in comparison with the inhomogeneities such as voids, inclusions, gravel or reinforcing rods, unless the entire system is scaled. Scaling, while useful and cost effective, also introduces additional uncertainty due to non-linearity of scale parameters or the effects of parameters which do not scale at all. In addition, small test cell volumes for shock wave studies introduce side wall or end plate rarefactions which can completely change the scope of the experiment, and may limit the useful data to very small regions of the cell and very early times. Finally, the importance of reproducing the loading strain paths and strain rates predicted for an actual explosive event has long been recognized, since the response, both deformation and fracture, of many materials is strain-rate or strain-history dependent at the high rates encountered in such applications.

Conventional laboratory loading frames operate at maximum loading rates several orders of magnitude below those generally of interest to the weapons community, and no piston-loading

device offers an arbitrary and controlled strain path as well. While the device described here is capable of achieving the high rates of interest, specification of the strain path would represent a substantial advance in the state-of-the-art. This development now appears to be technically feasible, and should be the next step in construction of a flexible and sophisticated test and simulation facility.

#### FACILITY DESCRIPTION

Terra Tek has recently modified a major laboratory test frame to attempt to overcome some of these limitations. A large volume test frame capable of standard tension-compression loading to  $1.7 \times 10^6$  lbf (7.6 MN) is shown in Figure 1. In its simplest configuration, the sample under study is installed in a massive biaxial containment frame of volume approximately  $0.9 \text{ m}^3$ . Flatjacks, or inflatable steel bladders, around the periphery of this frame allow the application of independently controlled horizontal stresses  $\sigma_1$  and  $\sigma_2$  to 3500 psi (24 MPa). The flatjacks may be installed in several zones independently, simulating a stress gradient. Sliding the biaxial containment frame into the large axial frame allows the application of a static vertical



Figure 1. Overall view of the facility, showing the press used with the large-volume containment frame. For testing, this frame moves on air bearings to its position beneath the loading ram.

stress,  $\sigma_3$ , of up to 5000 psi (35 MPa) over the area of  $8.6 \text{ ft}^2$  ( $0.8 \text{ m}^2$ ), representing a reaction load of  $6.12 \times 10^6$  lbf (27 MN). Modest strain rates can be achieved in this configuration as well, since the axial load can be applied at the rate of nearly  $2 \times 10^6$  lb/s (9.0 MN/s) using a slow rate of 1.0 in/s (0.025 m/s) with a total stroke of 10 in. (0.25 m). This is too slow for explosive simulations, except for evaluating far-field effects.

Figure 2 shows schematically the modifications recently made to allow high-rate loading. The basic parameters of the machine remain unchanged except for the loading rate. A high-pressure gas reservoir is used to drive the loading ram through a maximum run of about 10 in., compressing the specimen under test. Ordinarily, much shorter strokes would be used. Pulse tailoring may be achieved, within limits, by varying the driver plate mass, thickness, or composition, or by introducing additional layers of varying impedance into the driver system. Loading rates can be varied by changing the total mass of the driver, impedance mismatching, or changing the driving gas reservoir pressure, when

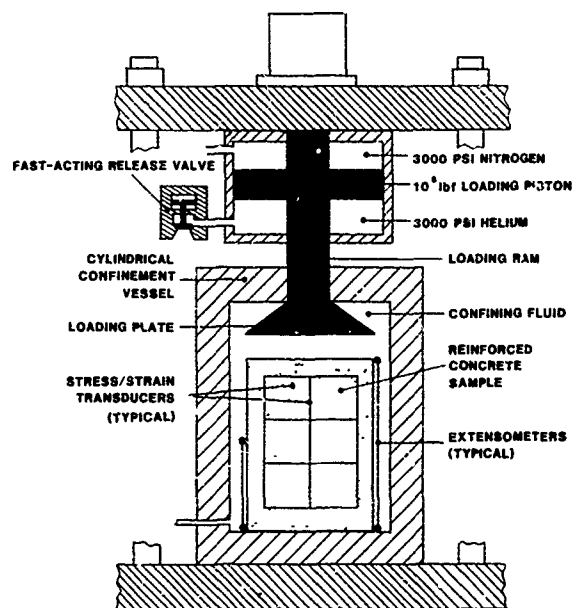


Figure 2. Schematic diagram of the gas-driven, modified version of the facility. The loading piston is driven by the high-pressure nitrogen reservoir when the helium pressure in the lower reservoir is released through the fast-acting valve. A cylindrical confinement vessel with a reinforced concrete sample is shown here; overstresses up to 90,000 psi can be achieved in this geometry.

such changes are compatible with the requirements of the specific experiment. Finally, the overpressure imposed on the sample can be varied within wide limits by stepping down the loading plate diameter and decreasing the sample size, with proper consideration of the model scaling limitations. Several confinement vessels are available, allowing significantly higher axial overstresses at the sacrifice of sample size. Figure 2 illustrates the press used with an 8-inch biaxial containment frame using a confining fluid and a jacketed sample instead of flat-jacks. Steady-state axial stresses as high as 90,000 psi (600 MPa) can be achieved in this geometry.

While the dynamic modifications to the machine are not yet completely operational, the critical components have been individually analyzed and tested. The important question, of course, is the flow rate of helium from the lower chamber, which controls the differential pressure across the loading piston as a function of time and therefore the displacement of the ram with time. A schematic of the fast-acting valve, which ultimately controls this flow rate, is shown in Figure 3. Gas pressure from the helium chamber of the loading ram is used to seat the poppet valve. Firing is achieved by introducing pressure to the lower chamber of the fast-acting valve, which quickly opens the poppet valve to its full extent and allows rapid depressurization of the lower chamber of the loading ram. Since large ram displacements are not normally required for testing of solid specimens, except for attaining extreme conditions in soils, inertial effects can be minimized by using only a small part of the loading ram stroke. With the loading ram piston one inch from the bottom of the stroke, maximum ram displacement rates of 890 ft/s (270 m/s) are achievable within 20 ms. For a 10 inch (25 cm) sample, this implies a maximum strain rate of over  $10^3/s$ . Realistically, strain rates of  $10^1$  to  $10^2/s$  can be expected on samples of interest for blast effects modeling.

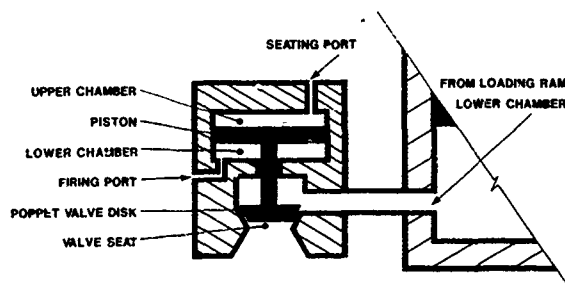


Figure 3. Detailed schematic of the fast-acting release valve used to drawdown the helium-filled lower reservoir. The valve is mechanically simple, rugged, and reliable. Firing is achieved by pressurizing the lower chamber through the firing port by solenoid release.

Data from the instrumented test specimens are collected using a CAMAC-based digital data acquisition system. Thirty-two data channels collected at a maximum rate of  $10^5$  data points/channel/second are stored in the LeCroy/CAMAC memory and then trickled to a DEC PDP 11/34 for data reduction purposes. Up to 64 channels of data may be collected at slower acquisition rates. Typical instrumentation includes stress and strain transducers of various types, as well as total deformation indicators such as extensometers. A 12,000 frame per second rotating prism camera is available to record dynamic events photographically if the test geometry permits; fiber optics access has been used successfully for specific applications.

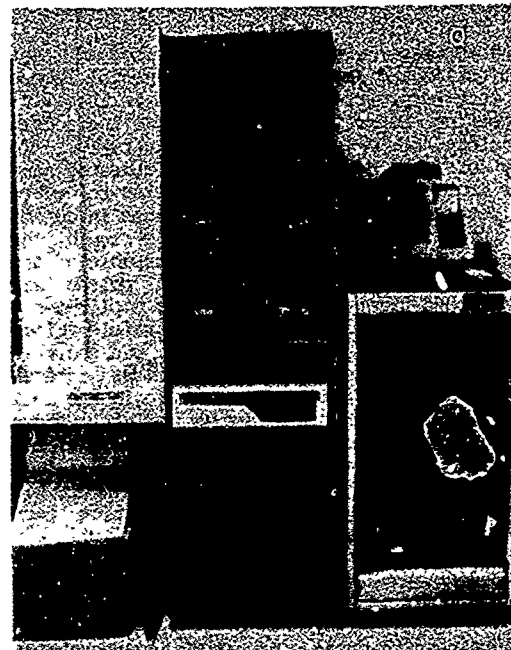


Figure 4. Overall view of the dedicated computer system for digital data acquisition and rapid data reduction and display.

#### SUMMARY

A test facility has been described which allows dynamic loading of structures and materials under confinement and to high axial stress levels. The facility is of sufficient size to allow testing of large-scale models under laboratory-quality control and reproducibility, while remaining cost-effective and allowing rapid turnaround.

#### ACKNOWLEDGEMENTS

The design engineering and preliminary testing for this facility was performed by Michael Wilson and Alan Black. Khosrow Bakhtar was responsible for implementing the data acquisition system.





# BLAST INDUCED SOIL LIQUEFACTION - State-of-the-Art -

Wayne A. Charlie    George E. Veyera    Steven R. Abt    Howard D. Patrone  
Associate Professor    Instructor    Associate Professor    Student Assistant

Civil Engineering Department  
Colorado State University  
Fort Collins, Colorado, U.S.A.

## ABSTRACT

This paper reviews blast induced soil liquefaction and describes an experimental laboratory testing program being conducted in the Civil Engineering Department's Geotechnical Engineering Laboratory at Colorado State University. The study of the behavior of water saturated sands under shock loadings is being conducted to evaluate potential blast induced changes in dynamic soil properties and soil shear strength loss (liquefaction). The facility is capable of generating single and multiple shock pulses with milli-second rise times, peak stress amplitudes of up to 35,000 KPa (5000 psi), peak particle velocities of 1000 cm per second (400 in. per sec.) and peak accelerations of 2,000 g. Of major interest is the behavior of the water pressure in the soil, both during and after the passage of the stress wave, as a function of strain, soil density, initial confining stress and the number of loadings. The information gained from the experiments will assist in improving ground shock prediction techniques for water saturated sands.

Such soil behavior may indicate that liquefaction, described as a process in which a saturated cohesionless soil loses shear strength as a result of increased pore pressures, may have occurred at these sites. As such, an explosion detonated in a soil having a high liquefaction potential could result in damage disproportionate to the energy released.

A study of the behavior of saturated cohesionless soils under blast loadings was initiated at Colorado State University in 1978. This study has resulted in the development of a laboratory testing facility capable of subjecting a saturated soil sample to single and multiple shock pulses with milli-second rise times.

## ASSESSMENT OF PREDICTION METHODS

The state-of-the-art for assessing blast induced residual porewater pressure increases and liquefaction potential is limited at best. Theoretical approaches are almost non-existent and have not been verified by experimental testing. Empirical scaling factors have been derived from a limited number of field tests. A logical approach would be to determine possible threshold particle velocities, stresses or strains below which blast induced porewater pressure increases should not occur. Lyakhov (1961) noted that blast induced liquefaction did not occur in water saturated sand with densities greater than 1.6 gm per cubic cm. For saturated soils at lower densities, Puchkov (1962) found that soils did not liquefy below a peak particle velocity of 4 cm per second. Damitio (1978) and Kok and Studer (1980) have reported empirical relationships to predict the maximum radius of liquefaction from contained point charges. These relationships for loose saturated sands indicate liquefaction may occur above particle velocities of 4 cm per second. Obemeyer (1980) measured no significant increase in residual porewater pressures in a hydraulic fill tailings dam subject to blast generated peak particle velocities of 2 cm per second. Several earthfill dams have been subjected to subsurface nuclear detonations including Navajo Dam, New Mexico (peak particle velocity of 1.3 cm per second) and Rifle Gap Dam (peak particle velocity of 2.5

## INTRODUCTION

Engineering designs presently incorporate the assumption of little or no blast induced soil property changes. However, evidence indicates that blast induced soil property changes, such as changes in shear strength, shear wave velocity, damping and water pressure are likely to have occurred at some test sites having loose saturated granular soils (Charlie et al., 1981). For porewater pressure response, the three stages of interest which may occur as a result of blasting are the milli-second transient response directly associated with the passage of the stress wave, the residual response shortly after the passage of the stress wave, and the longer term dissipation of the residual porewater pressures. Blast induced residual porewater pressure increases have been reported by Florin and Ivanov (1961), Kumenje and Eide (1961), Terzaghi (1965), Damitio (1972), Langley et al. (1972), Perry (1972), Banister and Ellett (1974), Yamamura and Koga (1974), Charlie (1977), Rischbieter (1977), Arya et al. (1978), Charlie (1978), Damitio (1978), Kok (1978), Marti (1978), Studer and Kok (1980), Long et al. (1981), Prakash (1981), and other research-

cm per second). Measurements taken a few hours after the tests showed little or no increase in porewater pressures (Rouse et al., 1970; Ahlberg et al., 1972).

Increased residual porewater pressure increases were measured in a riverbed consisting of clayey silty soils subjected to peak particle velocities exceeding 11 cm per second from an underground nuclear explosion (Banister and Ellett, 1974). Residual porewater pressures from other field explosive tests have been reported at peak particle velocities as low as 1 cm per second. Marcuson (1982) suggests that liquefaction should not occur where the peak particle velocity is less than 2.5 cm per second. Sanders (1982) and Seed (1982) related earthquake induced liquefaction to peak particle velocity indicating that a threshold particle velocity of 5 to 10 cm per second was a value that may also hold for blasts. For a 500 ton TNT surface explosion, Langley et al. (1972) measured up to 45 KPa residual porewater pressure increases out to distances of 170 meters from the detonation point. The estimated peak airblast over pressure at 170 meters was 2000 KPa. Perry (1972) conducted shock tube tests and determined that a loose saturated sand could be liquified at peak over pressures as low as 250 KPa.

#### PROPOSED THRESHOLD STRAIN APPROACH

A threshold strain approach may prove very useful for assessing blast induced residual porewater pressure increases since shear or compression strain of less than  $10^{-2}$  percent is generally considered not to generate residual porewater pressures upon unloading since strains are in the elastic range (Dobry et al., 1982). Utilizing equations given by Rinehart (1975) and Richart et al. (1970), Table 1 shows that a compression strain of  $10^{-2}$  percent in water saturated soils at a void ratio equal to one corresponds to about 15 cm per second peak longitudinal particle velocity. Shear strains of  $10^{-2}$  percent correspond to about 1 cm per second peak transverse particle velocity for soils at a void ratio equal to one located near the ground surface. Based on scaling factors given by Dupont (1980), for a single contained detonation of 100 kg of explosives, peak particle velocities would exceed 1 cm per second within 200 meters from the detonation point. Table 2 presents several empirical scaling factors based on threshold strain, particle velocity and field tests to determine the potential radius of liquefaction and residual porewater pressure increases for various charge weights. Although there are differences in the predictions, the predicted residual porewater pressure increases occur at distances greater than is generally considered to be hazardous to blast resistant structures. Based on the Russian research with multiple charges, unless complete dissipation of the residual porewater pressure can occur between stress waves or between detonations, the predicted maximum radius of residual porewater pressure increases may be greater than that given in Table 2.

#### LABORATORY FACILITY AND INSTRUMENTATION

Laboratory testing is currently being conducted at Colorado State University to evaluate the empirical scaling factors listed in Table 2, to evaluate the effects of multiple shock loadings, and to extend the state-of-the-art in understanding stress wave mechanics of two phase materials. The objectives of the testing program are to generate and determine the number of axial compressive stress pulses required to induce liquefaction in saturated cohesionless soils as a function of:

- Initial Relative Density
- Initial Effective Stress
- Peak Particle Velocity
- Peak Strain Amplitude
- Peak Stress Amplitude

Data collection objectives include measuring and recording both transient and long term response of the soil's:

- Porewater Pressure
- Particle Velocity
- Strain
- Stress

The soil is being tested in an undrained state since little or no short term drainage would occur in deep field deposits of saturated soils.

The laboratory shock facility, shown schematically in Figure 1, consists of separate but intimately related elements which include a gas-charged cannon, two fluid filled stainless steel tubes between which the soil sample is placed, a rigid stainless steel sample container, flexible membranes, an electronic control system, and an electronic monitoring and recording system. The membranes are utilized to apply the confining pressure and allow the soil to be tested in an undrained state. The cannon is designed to fire 7 cm diameter projectiles of various masses which impact a piston at the end of the fluid filled stainless steel impact tube. The piston imparts a stress wave to the fluid which then transmits a compressive shock pulse to the soil sample.

A pressure transducer, positioned just upstream of the sample is used to determine the intensity of the stress imparted to the sample. A second pressure transducer measures the pressure in the fluid just downstream of the sample, and a third pressure transducer measures porewater pressures in the soil. The transducers measure both the peak and long-term porewater pressure response. The pressure transducers are ENDEVCO Model 8511A-5K which have a porous metal. The resonant frequency is greater than 500 k. Hz over a dynamic range of 0 to 35,000 KPa. Although particle velocities and strains in the sample have not been measured to date, inductance strain gages with very small masses (Bison Model 4104) and accelerometers are currently being evaluated. To minimize reflections, an energy trap, which consists of a 10 cm diameter, three meter long solid

polyvinyl chloride (PVC) bar, is utilized. In current testing the energy trap is placed at the end of the sample.

Other instrumentation consists of a set of three signal conditioners (ENDEVCO Model 4470), three amplifiers (ENDEVCO Model 4476.1A), a dynamic strain gage (Bison Model 4101A), a four channel high speed digitizer (Biomation Model 2805), a desk top computer (Hewlett Packard Model 9835) and a plotter (Hewlett Packard Model 9872C). A time interval counter (Hewlett Packard Model 5300) is used to determine the impact velocity of the projectile.

#### LABORATORY RESULTS

Tests are being conducted on saturated sand at densities ranging from 1.4 to 1.7 gm per cubic cm (0 to 100 percent relative density) with initial effective stresses from 100 to 1000 KPa. This stress range corresponds to the effective vertical geostatic stress at a depth of approximately 5 to 100 meters below the ground surface. All tests to date have been conducted in water saturated Monterey No. 0/30 (Muzzy, 1983) sand at a dry density of 1.47 gm per cubic cm under initial effective confining stresses of 170, 345 and 690 KPa.

Figures 2, 3 and 4 give the preliminary results of shock testing of two samples of saturated Monterey No. 0/30 sand r ced at a dry density of 1.47 gm per cubic cm. In each of these figures, part (a) shows the impact stress in the fluid upstream of the sample, part (b) shows the sample's porewater pressure response to this impact stress, and part (c) combines both the input shock and the sample's porewater pressure response. For the sand under an initial effective stress of 170 KPa, Figure 2 shows that the sample liquefied under one shock loading of 4000 KPa. For an identical sample under an initial effective stress of 690 KPa, Figure 3 shows that the sample's residual porewater pressure increased by 200 KPa after being subjected to a peak input stress of 2000 KPa. This porewater increases is about 30 percent of the increase required to cause liquefaction. Figure 4 shows that the same sample liquefied when subjected to a second shock of 4100 KPa. The preliminary results of these and other tests are summarized in Table 3. The relationships given earlier in this paper predict residual porewater pressure increases at these impact stresses and strains.

#### CONCLUSIONS

Today's understanding of blast induced liquefaction has advanced only slightly beyond the point of recognition of its existence. Documented occurrence, although sketchy and often incomplete, is available in the open literature. Although considerable work remains to be done in projecting this information into a comprehensive method of predicting liquefaction for actual or hypothetical blasts, the limited data indicates that residual porewater pressure increases should not occur in

soils subjected to strains less than  $10^{-2}$  percent. The laboratory facility described in this paper is assisting in developing testing techniques for the evaluation of blast induced liquefaction potential. The data will also be useful in verifying and developing empirical correlations and mathematical models.

#### ACKNOWLEDGMENTS

Support for this work was in part provided by the Air Force Office of Scientific Research and the Civil Engineering Department at Colorado State University. The writers acknowledge and appreciate the technical assistance received from Nancy C. Patti of Science Applications Inc., Steamboat Springs, Colorado, S. Melzer of Civil Systems, Inc., Midland, Texas, and J. Shinn of Applied Research, Inc., S. Royalton, Vermont, and M. W. Muzzy of Colorado State University. The writers are also grateful to C. Emanuel who typed the manuscript.

#### REFERENCES

1. Ahlberg, J. E., Fowler, J. and Heller, L. W. (1972), "Earthquake Resistance of Earth and Rock Fill Dams: Analysis of Response of Rifle Gap Dam to Project Rulison Underground Nuclear Detonation," U.S. Army WES, Misc. Paper 5-71-17, June.
2. Arya, A. S., Nandakumaran, P., Puri, V. K. and Mukerjee, S. (1978), "Verification of Liquefaction Potential by Field Blast Tests," Proc. of the 2nd Int. Conf. on Microzonation, Vol. II, San Francisco, California, November-December.
3. Banister, J. R. and Ellett, D. M. (1974), "Pore Pressure Enhancement Observation on Rio Blanco," Report SLA-74-032, Test Effects Department 1150, Sandia Laboratories, Albuquerque, New Mexico, August.
4. Charlie, W. A. (1977), "Liquefaction Potential of Soils Under Blast Loads," Air Force Office of Scientific Research, Report No. 40, Volume 2, AFOSR-TR-78-0349.
5. Charlie, W. A. (1978), "The Dial Pack Event," Int. Workshop on Blast-Induced Liquefaction, Organized by Dames and Moore, London, and sponsored by U.S. Air Force, Maidenhead, U.K., September.
6. Charlie, W. A., Mansouri, T. A. and Ries, E. R. (1981), "Predicting Liquefaction Induced by Buried Charges," Proc. of the Int. Conf. on Soil Mechanics and Foundation Eng., Stockholm, June.
7. Crawford, R. E., Higgins, C. J. and Bultmann, E. A. (1974), The Air Force Manual for Design and Analysis of Burdened Structures, AFWL-TR-74-102, Air Force Systems Command, Kirtland AFB, NM, October.

8. Damitio, C. (1972), "La Consolidation des Sols Sans Cohesion par Explosion," *Construction*, Vol. 27, No. 3 (In French), France.
9. Damitio, C. (1978), "Field Experience on Blast-Induced Liquefaction," Int. Workshop on Blast-Induced Liquefaction, Organized by Dames and Moore, London, and sponsored by U.S. Air Force, Maidenhead, U.K., September.
10. Dobry, R., Ladd, R. S., Yokel, F. Y., Chung, R. M. and Powell, D. (1982), "Prediction of Pore Water Pressure Buildup and Liquefaction of Sands During Earthquakes by Cyclic Strain Method," NBS Building Science Series 138, National Bureau of Standards, July.
11. Dupont (1980), *Blasters Handbook*, 16th Edition, E.I. duPont de Nemours and Co., Explosive Products Division, Wilmington, Delaware.
12. Florin, V. A. and Ivanov, P. L. (1961), "Liquefaction of Saturated Sandy Soils," Proc. 5, Int. Conf. Soil Mechanics and Foundation Engineering, ICSMFE, Vol. 1.
13. Kok, L. (1978), "Empirical Predictions of Blast-Induced Liquefaction," Proc. Int. Workshop on Blast-Induced Liquefaction, Dames and Moore/U.S. Air Force, Maidenhead, U.K.
14. Kummeneje, D. and Eide, O. (1961), "Investigation of Loose Sand Deposits by Blasting," Proc. 5th ICSMFE, Vol. 1.
15. Langley, N. P., et. al. (1972), "Dial Rock Event - Soil Pore Pressure and Shear Strength Test," Aerospace Corp. Report No. TOR-0172 (S2970-20)-1, February.
16. Long, J. H., Ries, E. R. and Michalopoulos, A. P. (1981), "Potential for Liquefaction Due to Construction Blasting," Proc. Int. Conf. on Recent Advances in Geotech. Eng. and Soil Dynamics, Univ. of Missouri-Rolla, St. Louis, Missouri.
17. Lyakhov, G. M. (1961), "Shock Waves in the Ground and the Dilatancy of Water Saturated Sand," *Zhurnal Prikladnoy Mekhaniki i Tekhnicheskoy Fiziki*, Vol. 1., pp. 38-46, Moscow.
18. Marcuson, W. (1982), U.S. Army Waterways Experiment Station, Vicksburg, Miss., Personal Communication, July.
19. Marti, J. (1978), "Blast-Induced Liquefaction: A Survey," Report by Dames and Moore for the U.S. Air Force Office of Scientific Research, Report No. TR-78-3, May.
20. Muzzy, M. W. (1983), "Cyclic Triaxial Behavior of Monterey No. 0 and No. 0/30 Sands," M.S. Thesis, Colorado State University, Department of Civil Engineering.
21. Obermeyer, J. R. (1980), "Monitoring Uranium Tailing Dams During Blasting Program," Symp. on Uranium Mill Tailings Management, Colorado State University, Fort Collins, CO, Nov.
22. Perry, E. B. (1972), "Movement of Variable-Density Inclusions in Wet Sand Under Blast Loading," U.S. Army Eng. Waterways Experiment Station, Misc. Paper S-72-37, September.
23. Prakash, S. (1981), *Soil Dynamics*, McGraw-Hill Book Company, N.Y.
24. Puchkov, S. V. (1962), "Correlation Between the Velocity of Seismic Oscillations of Particles and the Liquefaction Phenomenon of Water-Saturated Sand," Issue No. 6, Problems of Engineering Seismology, Study No. 21, Edited by S. v. Medvedev, translated by Consultants Bureau, New York.
25. Rischbieter, F. (1977), "Soil Liquefaction: A Survey of Research," Proc. of the Fifth Int. Symp. on Military Applications of Blast Simulation, Organized by the Royal Swedish Fortifications Administration, Stockholm, Sweden.
26. Richart, F. E., Hall, J. R. and Woods, R. D. (1970), *Vibrations of Soils and Foundations*, Prentice-Hall, N.J.
27. Rinehart, J. S. (1975), *Stress Transients in Solids*, Hyperdynamics, Santa Fe, New Mexico.
28. Rouse, G. C., Roehm, L. H. and Cozart, C. W. (1970), "Vibration of Vega Dam Following Rulison Subsurface Nuclear Blast," U.S. Dept. of Interior, Bureau of Reclamation, REC-OCE-70-15, April.
29. Sanders, S. G. (1982), "Assessment of the Liquefaction Hazards Resulting from Explosive Removal of the Bird's Point - New Madrid Fuze Plug Levee," Misc. Paper GL-82-5, U.S. Army Engineer WES, Vicksburg, Miss., April.
30. Seed, H. B. (1982), Letter and review to S. G. Sandeers, WES, dated March 16, 1982. Letter and review printed in WES Misc. Paper GL-82-5 referenced to Sanders (1982) above.
31. Stuger, J. and Kok, L. (1980), "Blast-Induced Excess Porewater Pressure and Liquefaction Experience and Application," Int. Symp. on Soils under Cyclic and Transient Loading, Swansea, U.K., Jan.
32. Terzaghi, K. (1956), "Varieties of Submarine Slope Failures," Proc. of the Eighth Texas Conf. on Soil. Mech. and Fdn. Eng., Univ. of Texas, Austin, Sept. and Harvard Soil Mechanics Series, No. 52, Cambridge, Mass.
33. Yamamura, K. and Koga, Y. (1974), "Estimation of Liquefaction Potential by Means of Explosion Test," Proc. of the Sixth Joint Panel Conf. of the U.S.-Japan Coop. Program in Natural Resources, National Bureau of Standards, May.

Table 1. Predicted Peak Compression Strains and Peak Compressive Stresses vs. Peak Longitudinal Particle Velocities for Loose Saturated Sand.

Peak Longitudinal Particle Velocity (cm/sec)	Peak Compression Strain (Percent)	Peak Compression Stress (psi)	Peak Compression Stress (KPa)
1.5	0.6	6	40
2.5	1	10	70
5	2	20	140
10	4	40	280
15	6	60	400
25	10	100	700
150	60	600	4000

(1) Assumptions: Loose saturated sand and void ratio = 1.

Rinehart (1975) for relations between particle velocity, strain and stress. Rinehart et al. (1970) for density and compression wave velocity.

Table 3. Summary of Residual Porewater Pressure Increases in Mortar No. 0/30 Sand Subjected to Shock Loadings.

Sample	Density (gm/cm <sup>3</sup> )	Initial Effective Confining Stress (KPa)	Impact Number	Peak Impact Stress (KPa)	Estimated Peak Strain (Percent)	Residual Porewater Pressure Increase Ratio (Percent)
4/23/83	1.47	170	1	4000	0.1	100
4/25/83	1.47	345	1	1400	0.04	60
4/25/83	1.47	345	2	1400	0.04	100
4/27/83	1.47	690	1	2000	0.05	30
4/27/83	1.47	690	2	4100	0.1	100
(3)	1.47	200	1	> 14000	> 0.4	100

(1) Estimated from Table 1.

(2) Porewater pressure increase ratio = Residual Porewater Pressure Increase / Initial Effective Confining Stress

Zero for zero increase in residual porewater pressure. One hundred percent for liquefaction.

(3) Several tests conducted in late 1982.

Table 2. Predicted Maximum Radius of Liquefaction and Residual Porewater Pressures for Detonation of Contained Point Charges in Loose Saturated Cohesionless Soils.

Charge Weight TNT (kg) (4)	Predicted Maximum Radius (meters) (1)					
	Liquefaction (2)		Porewater Pressure Increase (3)			
	Russian (5)	Russian (6)	Comp. (7)	Shear (8)	Liq. (9)	Peak (10)
	Peak Particle Velocity > 4 cm/sec	$R_{max} = k_3 C^{1/3}$ Relative Density 40%	Strain > $10^{-2}\%$	Strain > $10^{-2}\%$	Coeff. > 0.1	Particle Velocity > 1 cm/sec
1	7	25	8	4	24	15
10	23	55	20	12	75	20
100	75	130	40	40	240	50
1,000	230	730	80	120	750	600
10,000	750	540	170	400	2400	2000
100,000	2300	1200	370	1200	7500	6000

Notes: (1) Predicted maximum radius may be higher under multiple detonations and some geologic and confinement conditions.

(2) Maximum radius for the residual porewater pressure increase equal to the initial effective vertical stress.

(3) Maximum radius for same increase in residual porewater pressure.

(4) For larger charge weights see Sanders (1980) or Crawford et al. (1974) for particle velocity scaling factors.

(5) Dupont (1980) for peak particle velocity.

(6) Puchkov (1982) for particle velocity.

(7) Daulton (1972 and 1978) and West (1978)

(8) Daulton (1972 and 1978) and Rinehart (1975) for compression wave velocity of 1500 meters per second and void ratio equal to one.

(9) Dupont (1980) and Rinehart (1975) for shear wave velocity of 150 meters per second and void ratio equal to one.

(10) Kok and Stuber (1980)

(11) Dupont (1980)

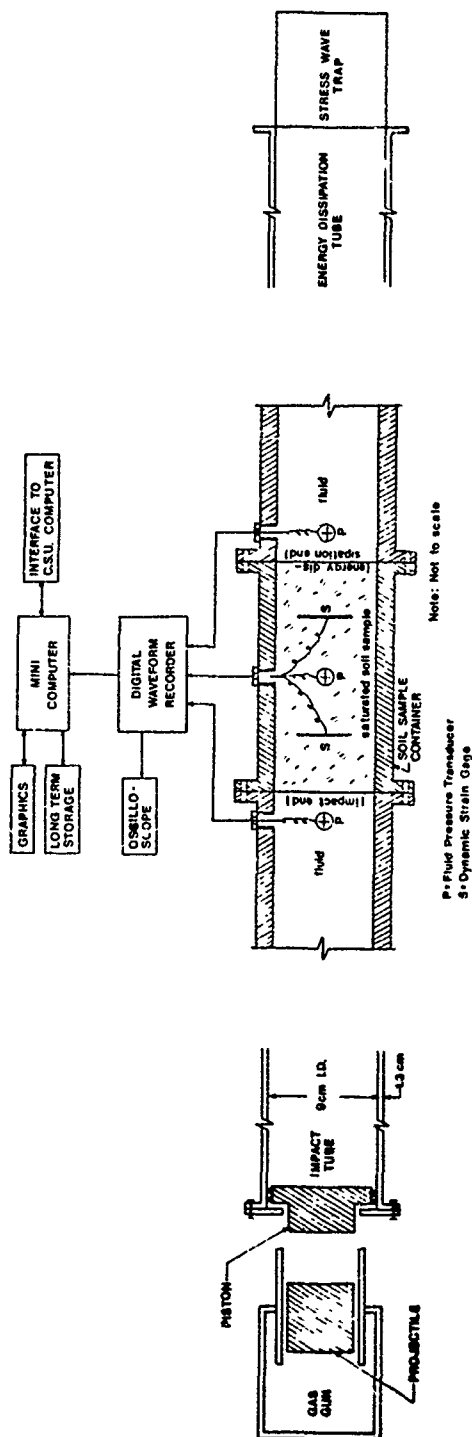


Figure 1. Schematic of shock facility to study blast induced liquefaction.

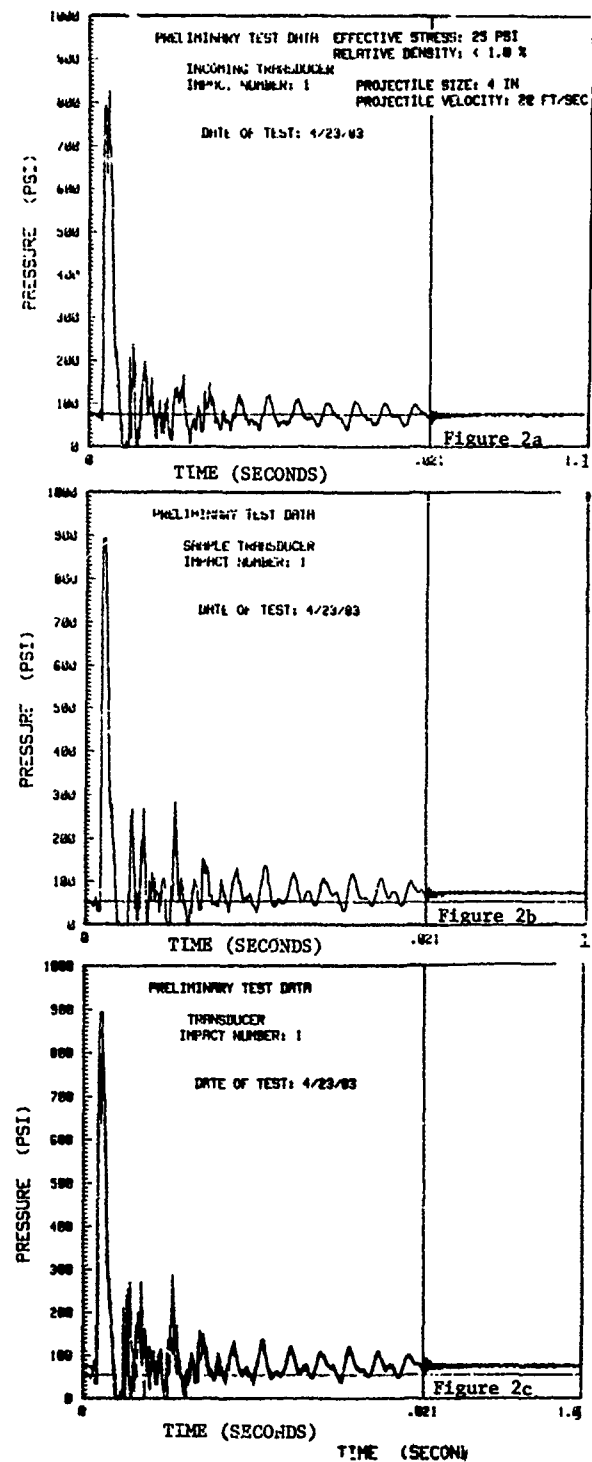


Figure 2. Response of the sample's porewater pressure which lead to liquefaction under one shock loading: initial effective stress of 170 KPa (1 KPa = 6.895 psi).

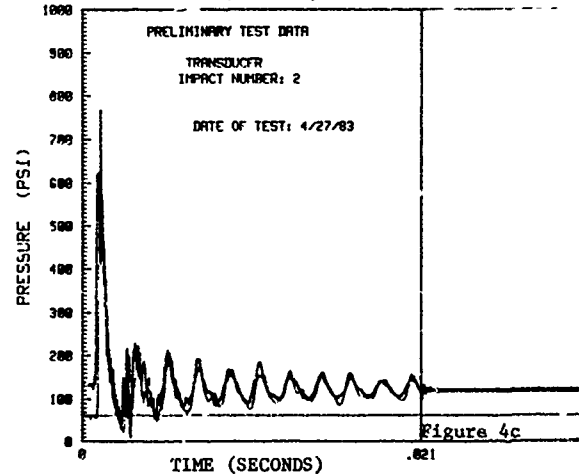
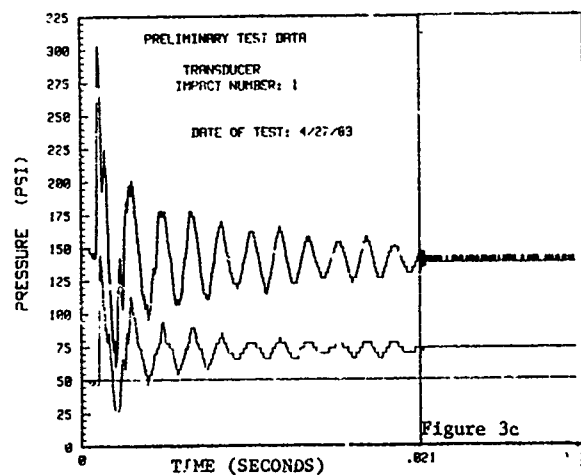
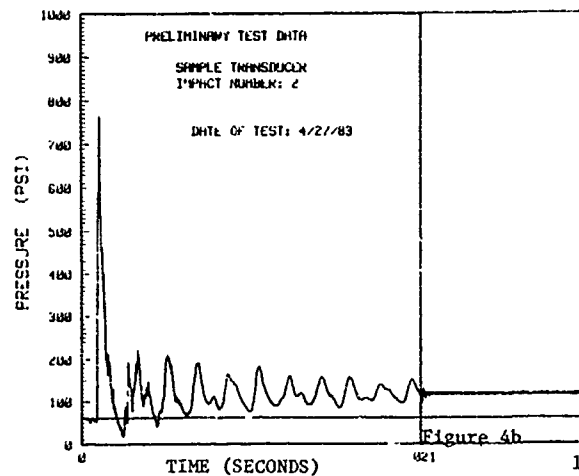
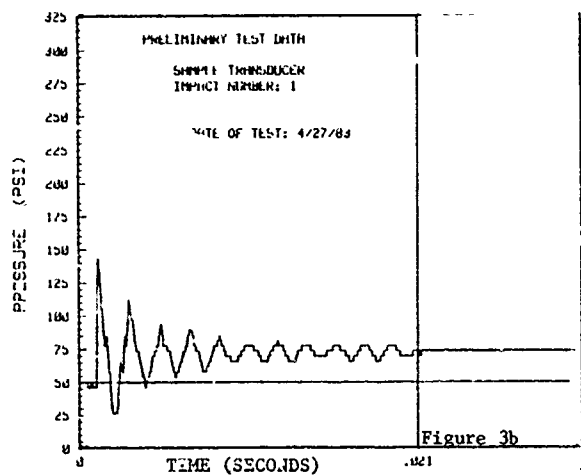
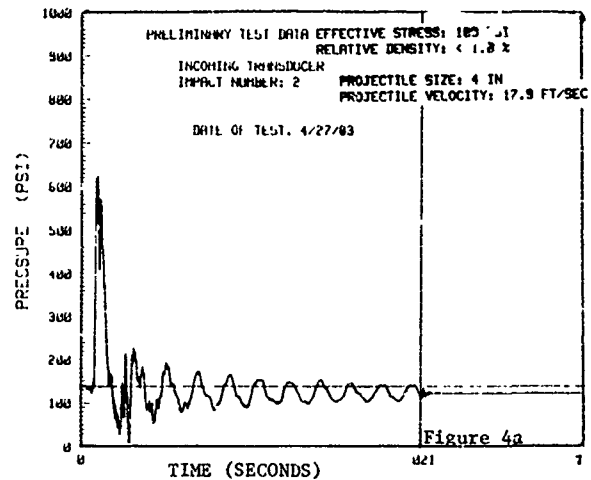
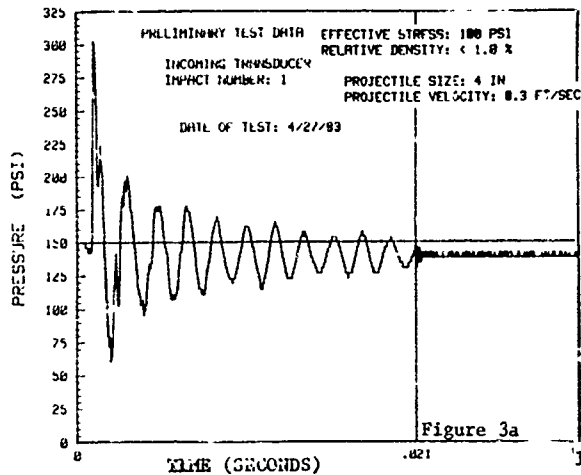


Figure 3. Response of the sample's porewater pressure leading to limited increase in residual porewater pressure under the first shock loading: initial effective stress of 690 KPa (1 KPa = 6.895 psi).

Figure 4. Response of the sample's porewater pressure leading to liquefaction under the second shock loading: initial effective stress of 690 KPa (1 Kp = 6.895 psi).

AD P001759

# SOIL CHARACTERIZATION FOR NON DESTRUCTIVE IN SITU TESTING

K. Arulanandan

Professor of Civil Engineering, University of California, Davis, CA 95616

A. Anandarajah

Asst. Professor of Civil Engineering, South Dakota School of Mines and Technology, Rapid City, SD 57701

N.J. Meegoda

Graduate Student University of California, Davis, CA 95616

## ABSTRACT

A non destructive method of characterizing particulate systems using electrical properties is presented. The application of this methodology to the classification of soils is demonstrated. The significance of this approach is that electrical properties of soils such as conductivity,  $\sigma$ , and dielectric constant,  $\epsilon$ , as a function of frequency, can be measured in situ. These properties when suitably interpreted can be used to quantify the structure of particulate systems. These structural properties can then be correlated with mechanical properties such as  $C_{max}$ ,  $K$ , and  $M$ . This approach provides a non destructive method of characterizing soils for the prediction of mechanical behavior.

## INTRODUCTION

The solution of most geotechnical engineering problems requires a knowledge of engineering properties. One of the major difficulties in obtaining soil properties accurately is the disturbance during sampling or the use of penetration methods of in situ testing which alters the engineering properties. In situ testing techniques, however, have begun to play an increasing important role in the determination of soil properties. This trend towards in situ testing techniques could be ascribed to several reasons as follows: (1) the soil is tested in its in situ environmental conditions which influence the engineering properties, (2) continuous data through the profile may be obtained and (3) properties can be obtained in cases where obtaining undisturbed samples is very difficult, such as in the case of saturated sands.

Presently several in situ testing techniques are employed for the evaluation of soil properties and for the establishment of empirical criteria for the prediction of potential behavior of soils. The standard penetration test (SPT) and the cone penetration test (CPT) are the most widely used in situ testing techniques. Other in situ testing techniques such as the pressure meter test (PMT), the Iowa Bore Hole Shear Test (BST) and the dilatometer are being used on a modest scale.

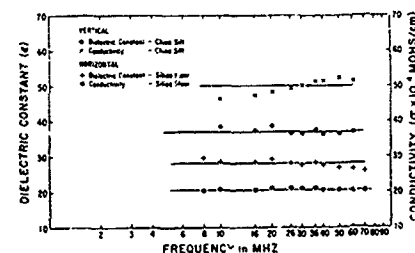
The reliability and usefulness of test results obtained from the in situ testing techniques described above are limited owing to various reasons. The drainage conditions in soils during in situ testing may be unknown in some tests. The failure modes may not simulate those anticipated for the actual project and in some cases the exact failure mode is unknown. Due to these unknown drainage and failure conditions, and the specific

nature of testing procedures and the failure mode simulated in different techniques, interpretation of the test results is highly empirical at the present time. The generalization of the test results, obtained from the current in situ testing techniques in order to analyse soil behavior under general loading conditions and various drainage and boundary conditions, is very difficult.

A non destructive method of characterizing particulate systems is presented by considering the electrical properties of soils which can be determined in situ without causing disturbance to the soils.

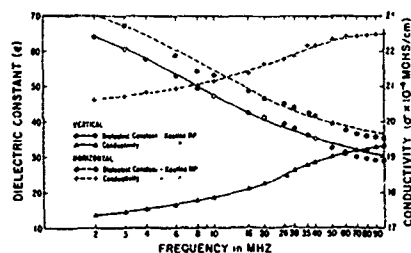
## Characterization of Soils by Electrical Method for Soil Classification

When an electrical impulse in the form of an alternating electric field is applied to a soil water system, a response is produced that can be measured in terms of two volume properties, the apparent dielectric constant,  $\epsilon'$  and the conductivity,  $\sigma$ . When the  $\epsilon'$  and  $\sigma$  values of a heterogeneous soil water system are measured as a function of frequency in the radio frequency range, the  $\epsilon'$  and  $\sigma$  values remain constant as shown in Fig. 1 for granular soils. In the case of cohesive soils the values of  $\epsilon'$  decrease and the values of  $\sigma$  increase as the frequency of the alternating current is increased as shown in Fig. 2. Those responses can be used to classify soil.



1. Variation of Dielectric Constant and Conductivity as a Function of Frequency for Granular Soils

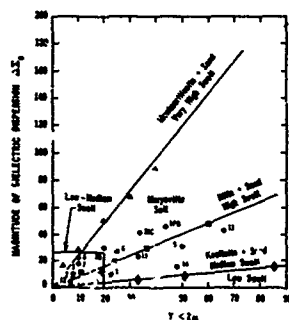




2. Variation of Dielectric Constant and Conductivity as a Function of Frequency for Cohesive Soils

It has been shown that the principal factors influencing the electrical dispersion of fine grained soils in the radio frequency range (1 MHz-100 MHz) are the compositional properties of the different phases and the heterogeneous nature of the system, Arulanandan et. al. (1969) Arulanandan et. al. (1973), Smith (1971). The difference between the maximum and minimum values of the dielectric constant in the radio frequency range is defined as the magnitude of dielectric dispersion,  $\Delta\epsilon_0$ .

A classification method for characterizing cohesive soils is shown in Fig. 3.



3. Correlation Between the Magnitude of Dielectric Dispersion  $\Delta\epsilon_0$  and Clay Fraction for Various Clay Types.

From the low frequency ( $\approx 1$  KHZ) conductivity measurements, the formation factor  $F$  is defined as the ratio of the pore fluid conductivity,  $\sigma_s$  to the soil sample conductivity,  $\sigma$  as follows.

$$F = \sigma_s / \sigma \quad (1)$$

The formation factor has been shown to relate to the porosity and anisotropy of sand particles, Arulanandan et. al. (1979).

The formation factor was shown to be a tensorial parameter with tensorial components related to the microstructural features in sands Dafalias et. al., (1979a). The average formation factor  $\bar{F}$  and the anisotropy index,  $A$  are defined, for a transversely isotropic soils, as follows:

$$\bar{F} = (F_V + 2F_H)/3 \quad (2)$$

$$A^2 = F_V/F_H \quad (3)$$

where  $F_V$  = formation factor in the vertical direction and  $F_H$  = formation factor in the horizontal direction.

An integration technique proposed by Bruggeman (1935) was used by Dafalias and Arulanandan (1978) to derive an expression for average formation factor,  $\bar{F}$ , as a function of porosity,  $n$ , and average shape factor,  $\bar{f}$ , as

$$\bar{F} = n^{-\bar{f}} \quad (4)$$

The average shape factor  $\bar{f}$  is the negative slope of the log  $\bar{F}$ -Log  $n$  plot. It is the first invariant of the second order shape factor tensor  $f$  and it relates the electric fields inside and outside the sand particles. It has been shown both theoretically and experimentally that the shape factor is direction dependent and depends on porosity, gradation and particles' shape and orientation, Arulanandan et. al. (1979) Arulmoli (1980), Dafalias et. al. (1979), Kutter (1978). Since the average formation factor is independent of orientation of particles, the average shape factor, for a given sand, is expected to be a function of porosity and the shape of particles.

The electrical parameters  $\bar{F}$ ,  $A$ ,  $\bar{f}$  of sand deposits are governed by the grain and aggregate characteristics of the particles.

The preceding paragraphs have shown that  $F$  is a unique function of porosity, 'A' quantifies particle's orientation and  $\bar{f}$  is a measure of the shape of the particles. Thus  $\bar{F}$  and  $A$  may be used to quantify the aggregate property. The aggregate property is sensitive to sampling disturbance and needs to be measured in situ. Grain property (shape) is insensitive to sampling disturbance and can be determined on disturbed samples. It should therefore be possible to correlate certain soil properties such as liquefaction potential, friction angle, permeability and compressibility, with a combination of the parameters  $\bar{F}$ ,  $A$  and  $\bar{f}$ . Empirical correlations of this type could be extremely useful in evaluating the performance of sites which contain sand deposits.

For example the method of prediction of maximum dynamic shear modulus of a sand deposit is described below.

#### Laboratory Correlation Between Electrical Parameters and Shear Modulus

One way of predicting maximum shear modulus,  $G_{max}$ , is by measuring the in situ shear wave velocity,  $V_s$ , and using the equation

$$G_{max} = \rho V_s^2 \quad (5)$$

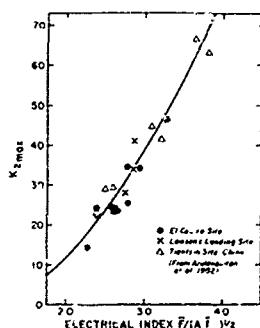
where  $\rho$  is the mass density of the deposit at the depth of measurement. Investigations have shown that the maximum shear modulus values for sands are strongly influenced by the confining pressure and the void ratio Hardin et. al. (1970), Seed et al (1970). A relationship between the shear modulus,  $G$ , in psf, and mean effective confining pressure,  $\sigma'_m$ , in psf, was given by Seed and Idriss (1970) as:

$$G = 1000 K_2 (\sigma'_m)^{1/2} \quad (6)$$

where the parameter  $K_2$  depends on void ratio, strain amplitude, geological age of the sand mass and in situ stresses. Thus, the maximum shear modulus at very low shear strain amplitudes is related to  $\sigma'_m$  through  $K_{2 \max}$ , the maximum value of  $K_2$ , and is given by the equation

$$G_{\max} = 1000 \cdot K_{2 \max} (\sigma'_m)^{1/2} \quad (7)$$

In eq. (7),  $K_{2 \max}$  depends largely on void ratio and also on the age of the deposit Seed et. al. (1970). A correlation between  $K_{2 \max}$  and an electrical parameter  $\bar{F}/(A \cdot \bar{f})^{1/2}$  was developed using measurements made both in the laboratory and in the field Arulanandan et. al. (1982). Field shear wave velocity measurements were made using cross hole seismic methods and the electrical measurements in the field were made using an Geo electronic electrical probe. The correlation is shown in Fig. 4.



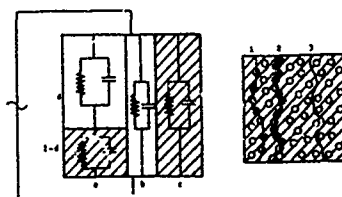
4. Correlation Between Electrical Index  $\bar{F}/(A \cdot \bar{f})^{1/2}$  and  $K_{2 \max}$

Provided that the parameter  $\bar{F}/(A \cdot \bar{f})^{1/2}$  can be obtained from field electrical measurements,  $K_{2 \max}$  can be predicted using Fig. 4 and  $G_{\max}$  calculated from Eq. (7) for the depth of the deposit under consideration.  $G_{\max}$  can, in turn, be used to determine the threshold peak ground surface acceleration,  $a_{\max}$ , required to initiate the development of excess pore water pressure at a given depth. A similar approach to that described above has been used to predict liquefaction potential Arumoli et. al. (1981), Arulanandan et. al. (1981) and pore pressure generation and dissipation during earthquake, Arulanandan et. al. (1982).

#### Quantification of Structure of Fine Grained Soils

A three element electrical network model has been used to explain the dispersion phenomena assuming

the validity of Maxwell-Wagner relaxation mechanism Arulanandan et. al. (1973, 1983). The concept of clusters, i.e. the primary soil particles existing in clusters in fine grained soils Michaels et. al. (1954) and Quirk (1959), has been utilized in deriving theoretical dispersion relationships. According to this concept, a particulate system is considered to have clusters, primary particles + intra cluster pores and inter cluster pores.



5. Three Element Cluster Model Representing Current Paths Through Clusters, Solution and Cluster and Solution

The electrical model shown in Fig. 5 considers that the total current through a soil sample consists of three components Arulanandan et. al. (1983); (1) through inter cluster solution and clusters in series, (2) through clusters in contact with each other and (3) through inter cluster solution only. The apparent dielectric constant,  $\epsilon'$  and the apparent conductivity  $\sigma$  for the model can be evaluated by elementary electrical network analysis.

The inter and intra cluster void ratios ( $e_p$  and  $e_l$ ) have been expressed in terms of the three element electrical model parameters Arulanandan et. al. (1983) and Anandarajah et. al. (1982) by relating the Olsen's cluster model (Olsen, 1961) to the electrical model. The detailed derivation of three element model and obtaining inter and intra cluster void ratios from model parameters are presented by Arulanandan et. al. (1983).

The parameters utilized in developing the non-destructive method of characterizing the behavior of fine grained soils are  $\bar{F}$ ,  $\bar{f}$ ,  $A$ ,  $e_p$ ,  $e_l$ , and  $\Delta \epsilon_0$ . Based on the mechanisms controlling different aspects of mechanical behavior of soils and the factors influencing the electrical parameters, appropriate correlation between the electrical parameters and the mechanical parameters  $\lambda$ ,  $\chi$ , and  $M$  would be established in the following sections.

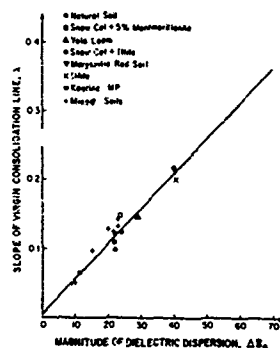
#### Slope of Isotropic Consolidation Line, $\lambda$

Bolt (1956) attempted to predict the compressibility characteristics of clays based on the concept of osmotic pressure using Gouy-Chapman diffuse double layer theory and Van't Hoff's theories of parallel platy particles. Experimental compression characteristics of Na-montmorillonite and Na-illite were found to be close to the predicted relationships. The theory, however, was found to be valid only for clays exhibiting very strong colloidal properties such as montmorillonite. Derivations from Bolt's findings have been reported by Mitchell (1960) and Olson and Mitronovas (1962) and are ascribed mainly to particle orientation. Quigley and Thompson (1966) have observed fabric changes in natural Leda clay during consolidation

using X-ray diffraction methods. It has been shown by Rosenquist (1958) that the compressibility of clay is dependent on the type as well as the valence and concentration of ions adsorbed on the surface of the clay particles. Further, Olson and Mesri (1970) have concluded that both mechanical and physico chemical factors influence the compressibility of soils in general, although one or the other may dominate depending on the soil type.

The factors influencing the magnitude of dielectric dispersion,  $\Delta\epsilon_0$  were investigated in detail by Arulanandan et. al. (1973). It has been found that  $\Delta\epsilon_0$  is significantly influenced by type and amount of clay mineral. The values of  $\Delta\epsilon_0$  were shown to increase in the sequence kaolinite < illite < montmorillonite. The compression index of these soil also increases in this sequence. The magnitude of dispersion decreases with an increase in percentage of sand in sand-clay mixtures Arulanandan et. al. (1973) so does the compression index as it is widely known. Olson et. al. (1970) have shown that the compression index of kaolinite is decreased when the electrolyte concentration is increased from 0.0001 N Sodium to 1.0 N Sodium and Arulanandan et. al. (1973) have shown that  $\Delta\epsilon_0$  also decreased with increasing electrolyte concentration.

The preceding discussion suggests that the factors influencing the mechanisms controlling the compression of clays and magnitude of dielectric dispersion are the same. Based on this mutual dependency,  $\Delta\epsilon_0$  has been correlated with  $\lambda$ . Sharlin, J.R. (1972) has shown that there is a linear relationship between  $\Delta\epsilon_0$  and  $\lambda$  for natural clays as shown in Fig. 6. Further results confirm the general validity of this relationship between  $\Delta\epsilon_0$  and  $\lambda$ .

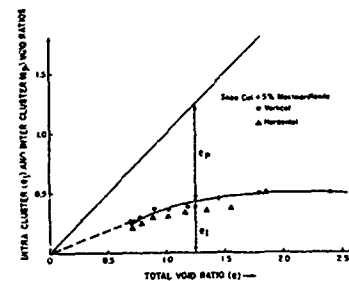


6. Correlation Between the Slope of the Isotropic Consolidation line,  $\lambda$ , and the Magnitude of Dielectric Dispersion,  $\Delta\epsilon_0$ .

#### Slope of Isotropic Swelling Line, $\kappa$

The swelling characteristic of saturated clays due to the removal of external load has been investigated by many, either by mechanical models such as the one used by Terzaghi (1929) where swelling is assumed to result from elastic rebound of bent particles or by physico-chemical models such as the one used by Bolt (1956) where osmotic repulsive forces are assumed to be responsible for swelling. Although it has been possible to explain the mechanism controlling swelling characteristics by the above concepts it was not very successful owing to the complicated structural arrangements of particles in clays.

The concept of clusters in fine grained soils (Michael et. al. 1954 and Quirk, 1959) has been utilized by Olsen (1961) in his study of hydraulic flow through saturated clays and he concluded that the discrepancy between the measured permeability and the one predicted by Kozeny-Carman equation in clays is mainly due to unequal pore sizes due to grouping of clay particles in clusters. The existence of primary particles aggregation has been observed by many using electron microscope, Quigley et. al. (1966).

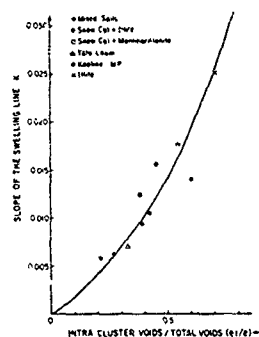


7. Variation of Intra Cluster ( $e_i$ ) and Inter Cluster ( $e_p$ ) Void Ratio With Total Void Ratio for (95%) Snow Cal + (5%) Montmorillonite

Fig. 7 shows variation of intra ( $e_i$ ) and inter cluster ( $e_p$ ) void ratios with total void ratio evaluated using electrical dispersion data for Snow Cal (95%) + Montmorillonite (5%). The results corresponding to measurements made in the vertical and horizontal directions are identical and is very similar to the one predicted by Olsen (1961).

It has been shown that the swelling of fine grained soils is caused by swelling of clusters Smith and Arulanandan (1981) and the decrease in inter cluster pores during compression is irreversible Meegoda (1983).

If the ratio of intra cluster to total void ratio is large for a given soil, the elastic compression due to an increase in the external load would be high and consequently swelling would also be high when the load is removed. Assuming this mechanism of swelling, the ratio,  $e_i/e_t$  is correlated with  $\kappa$  as shown in Fig. 8.



8. Correlation Between the Slope of the Isotropic Swelling Line,  $K_s$ , and the Ratio of Intra Cluster to Total Void Ratio,  $e_i/e_t$

#### Slope of Critical State Line M of the Bounding Surface Theory

When a soil element is sheared under drained or undrained conditions, experimental results indicate that the soil element fails when the stress path reaches the critical state line independent of the initial stress state of the soil element (Schofield et. al., 1968). At failure, the void ratio,  $e$ , and the effective mean normal pressure,  $p$ , lie on a unique line, referred to as a critical state line on the  $e$ - $p$  space. This concept is widely known as the critical state concept (Roscoe et. al., 1968). The slope of the critical state line, on the  $p$ - $q$  space, therefore represents the ultimate shear strength of soils.

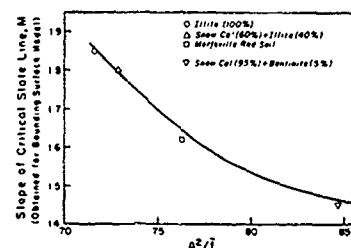
Lambe (1960) has discussed the factors controlling ultimate shear resistance of fine grained soil which is considered to be due to friction and interference between particles. These components of ultimate shear resistance and hence  $M$  would depend on many factors such as particle size, shape, surface texture and the structure of the soils resulting from the attractive and repulsive forces between the adjacent clay particles. In fine grained soils, the shape factor would reflect in addition to shape of the particles the physico-chemical interaction between particles. In other words, the shape factor,  $\bar{f}$ , is a function of the shape, composition and arrangement of particles.

Soils which exhibit higher anisotropy were found to have lower strength when measurements are made in the direction of the major principal axis. Based on these considerations, an attempt is made here to correlate  $M$  with an electrical index defined as a function of  $A$  and  $\bar{f}$ .

The values of  $M$  are obtained from the normally consolidated undrained test results. A computer program developed by Herrmann et. al. (1980) for the calibration of bounding surface theory (i.e. evaluation of model parameters by matching theoretical and experimental stress-strain relationships) was used to obtain the values

of  $M$ . A direct assessment from the failure value of  $q/p$  could only be approximate on account of the inaccuracies in measurement of the stress parameters at large strain and would underestimate  $M$  because failure intervenes before the critical state line.

The correlation between  $M$  and  $A^2/\bar{f}$  based on results corresponding to four different soils tested is shown in Fig. 9. A reasonable non linear correlation between  $M$  and  $A^2/\bar{f}$  is evident.



9. Correlation Between the Slope of the Critical State Line in Bounding Surface Model and Electrical Parameter  $A^2/\bar{f}$ .

#### Summary and Conclusions

The need for characterizing soils in their composite undisturbed state for the prediction of mechanical behavior is discussed. An electrical method of classifying soils into two broad groups (granular and cohesive) is presented. The conductivity,  $\sigma$ , and dielectric constant  $\epsilon$ , of granular soils are shown to be independent, whereas  $\sigma$  and  $\epsilon$  of cohesive soils are shown to vary with the frequency of the alternating current. The above electrical behavior has been used to quantify the compositional and heterogeneous nature of particulate systems. The magnitude of dielectric dispersion,  $\Delta\epsilon_0$ , in combination with the percentage of clay fraction has been used to develop a new classification system for soils.

Granular soils are characterized by the average formation factor which is shown to be uniquely related to porosity. The electrical anisotropy index  $A^* = F_v/F_H$  where  $F_v$  is the vertical formation factor,  $F_H$  is the horizontal formation factor is used to characterize the orientation of particles. The shape of the particles are quantified by  $\bar{f} = -\frac{\log \bar{F}}{\log \bar{n}}$ . The grain and aggregate

properties are quantified by  $\bar{f}$ ,  $A$  and  $\bar{F}$ . The values of  $A$  and  $\bar{F}$  can be measured in situ to describe the aggregate property. A combination of the parameters  $\bar{F}$ ,  $A$  and  $\bar{f}$  is used to predict the maximum dynamic shear modulus of granular soils.

A three element electrical network model is used to quantify the inter and intra cluster void ratios of cohesive systems. The significance of intra cluster void ratio to swelling is shown by establishing a correlation between the swell index  $\kappa$  and  $e_i/e_t$  where  $e_i$  and  $e_t$  are the intra cluster and total void ratio respectively.

The magnitude of dielectric dispersion which is dependent on the compositional and heterogeneous nature of the cohesive system is shown to be directly related to the compression index  $\lambda$ .

A combination of the parameters 'A' and  $\bar{f}$  of cohesive systems is shown to be uniquely related to M, the slope of the critical state line.

The significance of this paper is that electrical properties of soils such as the conductivity  $\sigma$  and dielectric constant,  $\epsilon$ , as a function of frequency can be measured in situ. These electrical properties when suitably interpreted can be used to quantify the structure of particulate systems. These structural properties can then be correlated with mechanical properties such as  $G_{max}$ ,  $\kappa$ ,  $\lambda$ , and M.

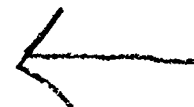
#### ACKNOWLEDGEMENTS

The study described in the preceedings pages was supported by a research grant from the Air Force Office Scientific Research. This support is gratefully acknowledged.

#### REFERENCES

1. Anandarajah, A., (1982) "In Situ Prediction of Stress-Strain Relationships of Clays Using A Bounding Surface Plasticity Model and Electrical Methods", Dissertation Presented to the University of California, Davis, California, in 1982, in partial fulfillment of the requirements for the degree of Doctor of Philosophy.
2. Arulanandan, K., Arulmoli, K., Dafalias, Y.F. and Herrmann, L.R., (1982) "In Situ Prediction of Shear Wave Velocities and Stress Strain Relationship of Soils," Report to the Air Force Office of Scientific Research.
3. Arulanandan, K. and Kutter B., (1978) "A Directional Structural Index Related to Sand Liquefaction," Proceedings on the Speciality Conference on Earthquake Engineering and Soil Dynamics, ASCE, Pasadena, California, June 1978, pp. 213-229.
4. Arulanandan, K. and Dafalias, Y.F., (1979) "Significance of Formation Factor in Sand Structure Characterization," Letters in Applied and Engineering Sciences, Vol. 17, 1979, pp. 109-112.
5. Arulanandan, K., Arulmoli, K. and Dafalias, Y.F., (1982) "In Situ Prediction of Dynamic Pore Pressure in Sand Deposits" International Symposium on Numerical Models in Geomechanics, Zurich, September 1982.
6. Arulmoli, K., Arulanandan, K., Seed, H.B. (1981) "A New Method For Evaluating Liquefaction Potential In Situ" ASCE National Convention on In Situ Testing to Evaluate Liquefaction Susceptibility, St. Louis, Missouri, October, 1981.
7. Arulanandan, K., Harvey, S.J. and Chak, J.S. (1981) "Electrical Characterization of Soil for In Situ Measurement of Liquefaction Potential" International Conference on Recent Advances in Geotechnical Earthquake Engineering and Soil Dynamics, St. Louis, Missouri, April 1981, pp. 1223-1230.
8. Arulanandan, K. and Smith, S.S., (1973) "Electrical Dispersion in Relation to Soil Structure", Journal of the Soil Mechanics and Foundation Division, ASCE, Vol. 99, No. SM12, Proc. Paper 10235, December 1973.
9. Arulanandan, K., Anandarajah, A. and Meegoda, N.J. (1983) "Quantification of Inter and Intra Cluster Void Ratios Using Three Element Electrical Model" U.C.D. Report to be published.
10. Arulmoli, K., (1980) "Sand Structure Characterization for In Situ Testing," Thesis Submitted in Partial Satisfaction of the Requirements for the Degree of Master Science in Engineering, University of California, Davis, June 1980.
11. Arulmoli, K., (1982) "Electrical Characterization of Sand for In Situ Prediction of Liquefaction Potential," Thesis in Preparation to Satisfy the Requirements for the Degree of Doctor of Philosophy, University of California, Davis, September 1982.
12. Bruggeman, D.A.G., (1935) "Berechnung Verschiedener Physikalischer Konstanten Von Heterogenen Substanzen," Ann. Phys. Lpz. 5, Vol. 24, pp. 636.
13. Bolt, G.H. (1956) "Physico-Chemical Analysis of the Compressibility of Pure Clays", Geotechnique, Vol. 6, pp. 86-93.
14. Dafalias, Y.F. and Arulanandan, K., (1978) "The Structure of Anisotropic Sands in Relation to Electrical Measurements," Mechanics Research Communications, Vol. 5, No. 6, pp. 325-330.
15. Dafalias, Y.F. and Arulanandan, K., (1979a) "The Formation Factor Tensor in Relation to Structural Characteristics of Anisotropic Granular Soils," Proceedings, Colloque International du C.N.R.S., Euromech Colloquium 115, Villard-de-Laus, France, June 1979.
16. Dafalias, Y.F. and Arulanandan, K., (1979) "Electrical Characterization of Transversely Isotropic Sands," Archives of Mechanics, 31, 5, Warsaw, 1979, pp. 723-739.
17. Hardin, B.O. and Drenevich, V.P., (1970) "Shear Modulus and Damping in Soils: I. Measurement and Parameter Effects, II. Design Equations and Curves," Technical Reports UKY 27-70-CE 2 and 3, College of Engineering, University of Kentucky, Lexington, Kentucky, July 1970.
18. Herrmann, L.R., Dafalias, Y.F. and DeNatale, J.S., (1980) "Bounding Surface Plasticity for Soil Modeling" Oct. 1980, Final Report to Civil Engineering Laboratory, Naval Construction Battalion Center, Port Hueneme, CA 93043.

19. Kutter, B.L., (1978) "Electrical Properties in Relation to Structure of Cohesionless Soils," Thesis submitted in Partial Satisfaction of the Requirements for the Degree of Master of Science in Engineering, University of California, Davis 1978.
20. Lambe, T.W., (1960) "A Mechanistic Picture of Shear Strength in Clay", Proceedings, Research Conference on Shear Strength of Cohesive Soils, Soil Mechanics and Foundatory Division, ASCE, University of Colorado, Boulder, Colorado, June 1960.
21. Meegoda, N.J., (1983) "Prediction of In Situ Stress State Using Electrical Method" Thesis submitted in Partial Satisfaction of the Requirements for the Degree of Masters of Science in Engineering, University of California, Davis, March 1983.
22. Michaels, A.S. and Lin, C.S. (1954) "The permeability of Kaolinite", *Ind. and Eng. Cheml*, Vol. 46, pp. 1239-1246.
23. Mitchell, J.K., (1960) "The Application of Colloidal Theory to the Compressibility of Clays", Proceedings, Seminar on Interparticle Forces in Clay-Water-Electrolyte System, Commonwealth Scientific and Industrial Research Organization, Melbourne, Australia, pp. 2.92-2.97.
24. Olsen, H.W., (1961) "Hydraulic Flow Through Saturated Clays", Submitted in Partial Fulfillment of the Requirements for the Degree of Doctoral of Science in Civil Engineering, M.I.T.
25. Olson, R.E. and Mitronovas, F. (1962) "Shear Strength and Consolidation Characteristics of Calcium and Magnesium Illite", *Proc. 9th Nat. Conf. Clays and Clay Minerals*, pp. 185-209.
26. Olson, R.E. and Mesri, G., (1970) "Mechanisms Controlling Compressibility of Clays", *ASCE, J. of Soil Mechanics and Foundation Division*, SM6, Nov. 1970.
27. Quigley, R.M. and Thompson, C.D., (1966) "The Fabric of Anisotropically Consolidated Sensitive Marine Clay", *Canadian Geotechnical Journal* 3, Vol. 2, pp. 61-73.
28. Quirk, J.P., (1959) "Permeability of Porous Media", *Nature*, Vol. 183, pp. 387-388.
29. Roscoe, K.H. and Burland, J.B., (1968) "On the Generalized Stress-Strain Behavior of "Wet Clay", *Engineering Plasticity*, ed. J. Heyman and F.A. Leckie, Cambridge University Press, pp. 535-609.
30. Rosenqvist, I. Th., (1958) "Physico-Chemical Properties of Soils" *Soil Water Systems*, *Journal of Soil Mechanics and Foundations Division, ASCE*, Vol. 85, No. SM2, Proc. Paper 2000, Apr. 1958, pp. 31-53.
31. Schofield, A.N. and Wroth, C.P., (1968) "Critical State Soil Mechanics", McGraw-Hill, London.
32. Seed, H.B. and Idriss, I.M., (1970) "Soil Moduli and Damping Factors for Dynamics Response Analysis," Report No. EERC 70-10, University of California, Berkeley, December.
33. Smith, S.S., (1971) "Soil Characterization by Radio Frequency Electrical Dispersion", Dissertation presented to the University of California, Davis, California, in partial fulfillment of the requirements for the degree of Doctor of Philosophy.
34. Smith, S.S. and Arulanandan, K., (1981) "Relationship of Electrical Dispersion to Soil Properties", *J. of Geotechnical Engineering Division, ASCE*, Vol. 107, No. GT5, May 1981.
35. Terzaghi, K., (1929) "Technisch - Geologische Beschreibung der Bodenbeschaffenheit für bautechnische Zwecke", Chapter IX, Part A, *Ingenieurgeologie*, by K.A. Redlich, K. Terzaghi, and R. Kampe, Julius Springer, Wien and Berlin.



AD P001760

# SOIL MODEL EVALUATION UNDER DYNAMIC LOADINGS

William C. Dass  
Jimmie L. Bratton

Applied Research Associates, Inc.  
Albuquerque, New Mexico

## ABSTRACT

Many different types of constitutive relationships are available for calculating the response of geologic media to impulsive loading. Choosing a material model which is suitable for a particular situation can be difficult. Model selection is often based on personal experience of the calculator, and this may or may not result in optimum efficiency and response. This paper describes a computer code which has been developed as an aid for studying material constitutive models. The Soil Element Model (SEM) can calculate the response of a given material model to laboratory and in-situ test conditions, arbitrary strain paths, or one-dimensional wave propagation. It is useful for developing models, performing parametric studies to determine model component influence, and comparing model behaviors. A study is presented which illustrates the use of this code to compare the ability of several material models to replicate laboratory and in-situ data. The study focuses on sand from a site near Yuma, Arizona, and examines the advantages and disadvantages of each model selected.

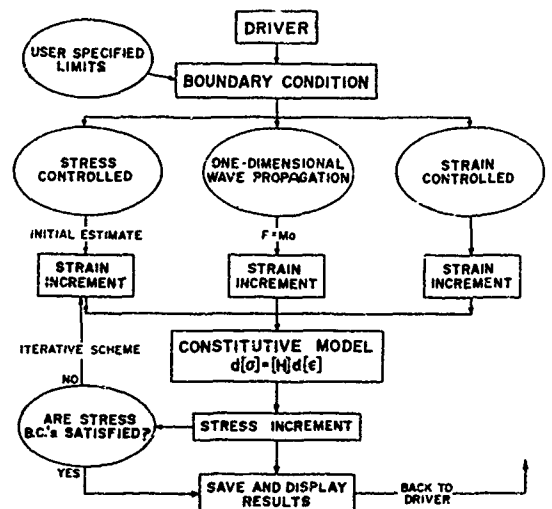
## INTRODUCTION

Accurate numerical simulation of dynamic events in soil requires an advanced constitutive relationship capable of accounting for many fundamental static and dynamic response phenomena. This requirement is complicated by the diversity of soil types (sands-silts-clays) and the varying conditions in which any one type of soil may be found (i.e., degree of saturation, consolidation state, etc.). It is difficult for any one material model to accommodate all variations in soil behavior. The net result has been the use of many different types of models, each particularly suited to the problem at hand, but potentially lacking if extrapolated to other dynamic problems. The identification of material model capabilities and deficiencies is therefore necessary, and is the topic of this paper.

## METHODOLOGY

In both the finite element and finite difference techniques, constitutive relationships are generally formulated to yield an incremental change in the stress tensor, given

an incremental change in the strain tensor. The Soil Element Model (SEM) is a computer code developed at Applied Research Associates, Inc. [1,2] which can exercise any constitutive model so formulated over an arbitrary strain path. Stress paths may also be followed, but usually require estimating strain increments and iterating to achieve the correct stress increment. Several common material models have been implemented in the SEM, as well as a variety of laboratory and in-situ test boundary conditions. Figure 1 shows a schematic of the



### BOUNDARY CONDITIONS

- ISOTROPIC COMPRESSION
- UNIAXIAL STRAIN
- TRIAXIAL COMPRESSION/EXTENSION
- SIMPLE SHEAR
- STRAIN CONTROLLED TRUE TRIAXIAL
- ARBITRARY STRAIN PATHS
- ONE-DIMENSIONAL WAVE PROPAGATION
  - UNIAXIAL STRAIN
  - AXISYMMETRIC
  - SPHERICAL

### CONSTITUTIVE MODELS

- LINEAR ELASTIC
- VISCOELASTIC
- HYPERBOLIC CURVE-FIT
- ELASTIC-PLASTIC
- AFNL ENGINEERING
- EFFECTIVE-STRESS CAP
- LADE'S COHESIONLESS
- JWL (HE)

Figure 1. SEM logic and options.

program logic and lists its present capabilities. A model implemented in the SEM is essentially ready for finite element/ difference use. The SEM provides an economical opportunity for gaining familiarity with a particular model, as well as studying its numerical implementation, fitting parameters, exercising options, and comparing it with other models.

#### EXAMPLE APPLICATION

##### Problem Description

The example below concerns development of a constitutive relationship for a dry alluvium which is subjected to high intensity explosive loading. A limited amount of laboratory test data is available and several in-situ explosive tests have been performed nearby.

##### Soil Description

The site in question is a desert site near Yuma, Arizona. The alluvium is mostly silty sand and clayey sand with occasional gravel. Due to localized fluvial action, the degree of cementation varies almost randomly. Average physical properties for the alluvium vary somewhat with depth. Those for the depth of interest in this particular study are given in Table 1. These are estimates based on typical test results from the U.S. Army Engineer Waterways Experiment Station (WES).

Table 1. Physical Properties for Example Alluvium

Volume (cc)	Mass (g)
1.000	
0.266	AIR
0.348	
0.082	WATER
0.652	SOLIDS
	1.830
	1.748

$$\gamma = 1.83 \text{ g/cc} \quad G_s = 2.68$$

$$\gamma_d = 1.75 \text{ g/cc} \quad e = 0.53$$

$$w = 7\% \quad n = 0.35$$

$$V_2 = 26.6\% \quad S = 23.6\%$$

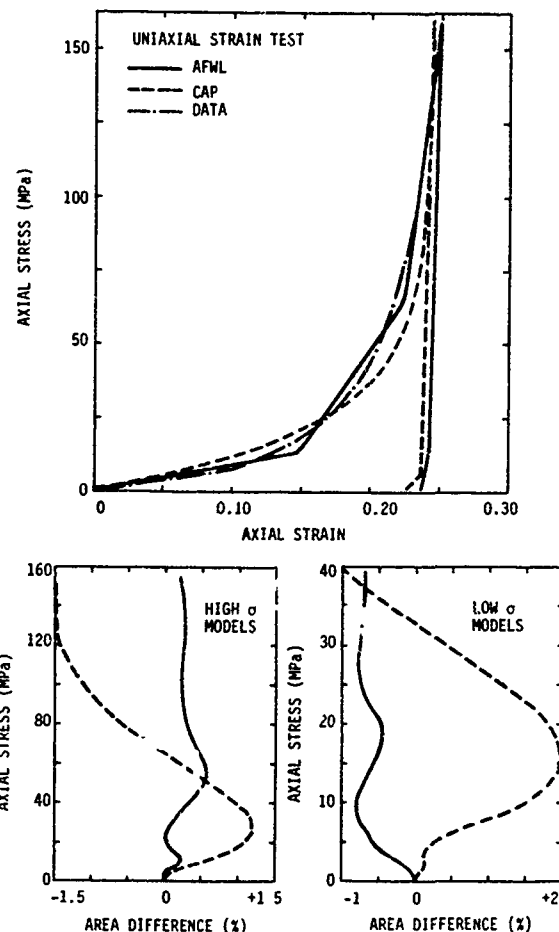


Figure 2. Uniaxial strain behavior.

##### Laboratory Behavior

The WES information was used to determine parameters for laboratory-based Air Force Weapons Laboratory (AFWL) Engineering and Cap models. The behavior of these models under laboratory test boundary conditions is compared with data in Figures 2 and 3. Figure 2 shows uniaxial strain behavior to an axial stress level of 160 MPa. The adequacy of such model fits may be evaluated by many techniques. The bottom figures show results of one evaluation method in which the area between the calculated and measured curves is accumulated with increasing stress. This area is then normalized to the net area under the data curve. A calculation which exactly coincided with the data would result in a constant area difference of zero. Note that two different sets of parameters were determined for each model: one set for axial stresses up to 40 MPa and one for stresses up to 160 MPa. This approach allows a



closer model fit to data over a wider range of stress than would be possible using only one set of parameters. No very high stress or temperature behavior involving phase changes, etc., was considered.

Figure 3 shows triaxial compression behavior. Tests were performed on undisturbed samples in a standard triaxial test device (with drainage allowed) at several different constant confining pressures. The overall trend of the triaxial data is for a softening shear modulus with increasing strain. The AFWL Engineering model uses a constant Poisson's Ratio, which results in a shear modulus directly proportional to the bulk modulus. As seen in the AFWL response at 3.60 MPa confining pressure, this can yield a stress-strain response curve with opposite inflection from the data. Tracking shear behavior is a weak point of the AFWL Engineering model. The Cap model is much better at predicting a softening shear modulus. It is seen, however, that the Cap model is much too stiff at high confining pressures. This is a direct result of the choice of parameters for this example which causes the material to lock up at the higher pressures. The parameters could be refined to yield improved behavior.

#### In-Situ Behavior

Several large scale field tests and material property tests have been performed near the site in question. Figure 4 shows three tests, each producing a geometrically different ground motion field: planar, cylindrical, and spherical. Note that loading in each test produced substantially different stress levels

and stress waveform frequency content. The velocity waveforms measured in these tests are shown in Figure 5. For each test, the waveforms are plotted with their origins located proportionally according to depth or range so that propagation velocities may be observed directly. The variation in propagation velocity of the initial arrival ( $V_i$ ) and the peak particle velocity ( $V_{pk}$ ) between events is most likely a result of loading function differences, as shown in Figure 4, and frequency dependent attenuation.

One-dimensional wave propagation calculations were done for each of the three in-situ events shown in Figure 4 using an elastic model, the AFWL Engineering model, and the Cap model. Elastic parameters were chosen to match initial arrival times. AFWL and Cap model parameters were chosen to provide a preliminary fit to the cylindrical in-situ test velocity waveforms.

Calculated attenuation of peak velocities is shown in Figure 6. The elastic calculations illustrate numerical effects (artificial viscosity, zone size, and timestep) on calculated attenuation. Calculated elastic attenuation coefficients are 0.1 for planar propagation (versus 0.0 theoretical), 0.7 for cylindrical (versus 0.5 theoretical), and 1.4 for spherical propagation (versus 1.0 theoretical). Numerical distortion is seen to increase in progressing from planar to spherical geometry and in going from a low-level, low-frequency loading function to a high-level, high-frequency loading function. The AFWL and Cap models produce similar results, but the AFWL model demonstrated a better fit to the data.

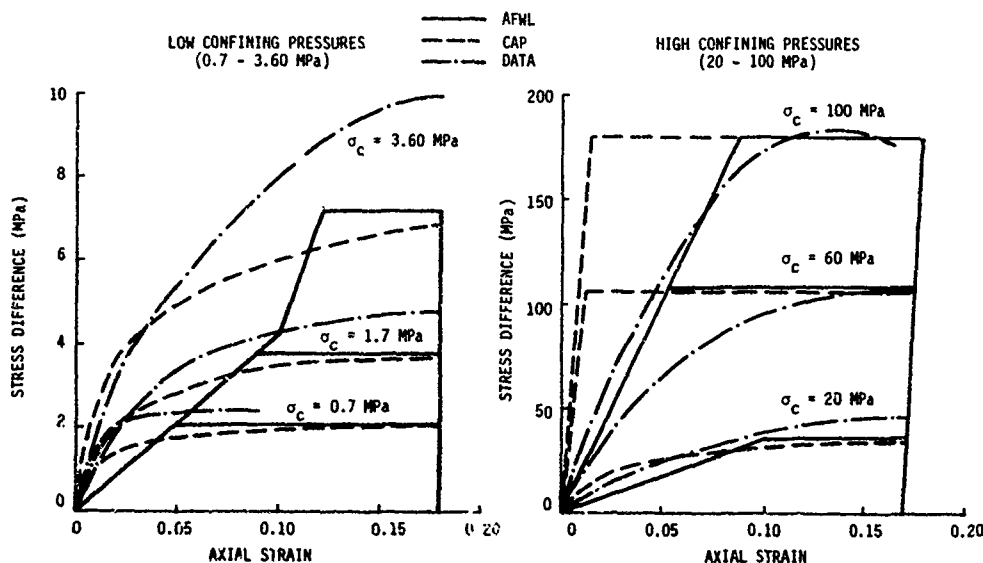


Figure 3. Triaxial Compression Behavior.

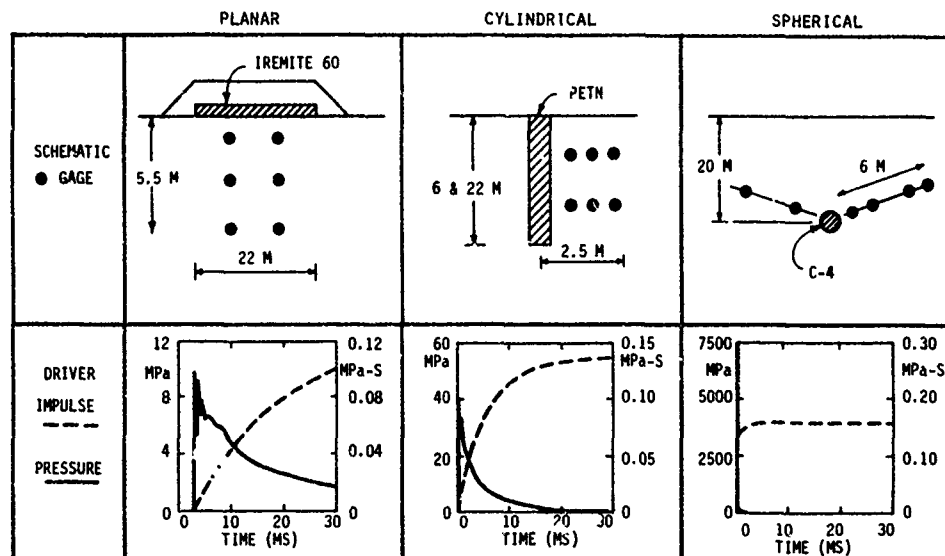


Figure 4. In-situ tests.

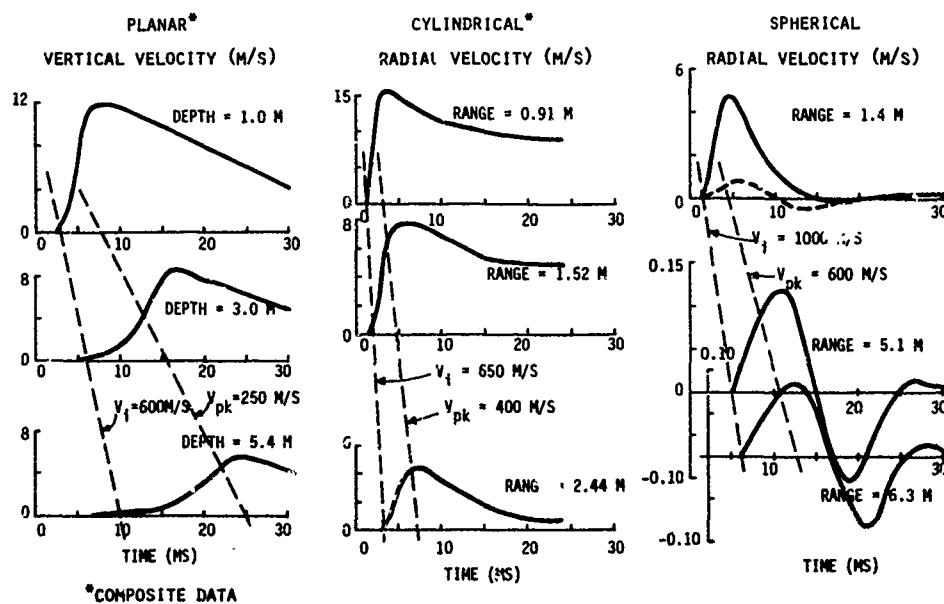


Figure 5. In-situ data - velocity waveforms.

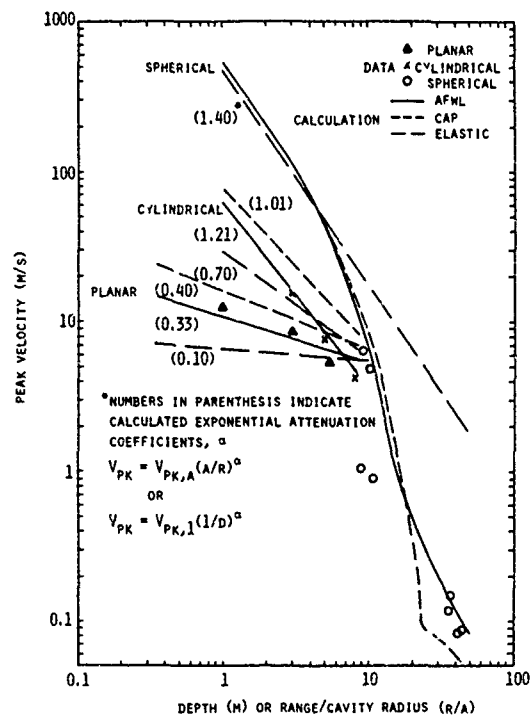


Figure 6. Calculated attenuation.

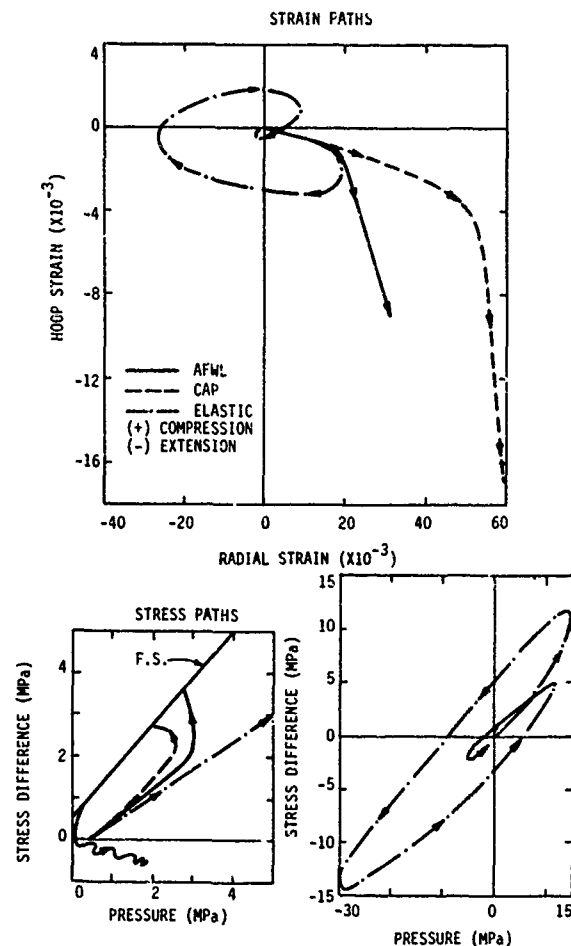


Figure 7. Stress/strain paths.

Results from the spherical event calculations are shown in Figures 7, 8, and 9. These calculations were driven using an exponentially decaying pressure function at the spherical cavity boundary. Although it is clear that the properties of the surrounding medium will affect the pressure history at the source, it was felt that a constant loading function was adequate for this type of comparative study.

Calculated stress and strain paths are shown in Figure 7 for a fairly close-in range (1.5 m) which experienced significant yielding in shear. Note that the elastic stress and strain paths are linearly proportional to each other and show substantial tensile behavior. The paths for the AFWL and Cap models, however, are greatly influenced by the presence of a failure surface. It is evident that the strain paths predicted by the AFWL and Cap models are similar in nature but different in magnitude. Note that it would be possible to force these two models into close agreement by adjusting their parameters.

Figure 8 compares the velocity waveforms calculated using the AFWL and Cap models with spherical data at several ranges. Given the order of magnitude differences in velocity between the 1.4 m and 5 m to 6 m ranges, the calculations do a fair job of matching the data. It appears that there is a problem in predicting the frequency content of the data, and this is better shown in Figure 9. Here, the calculated and observed particle velocity Fourier amplitude spectra are compared. The elastic model deviates considerably from the data, as might be expected. The AFWL and Cap models show very good agreement with the data at 1.4 m, but deviate to the high frequency side of the data farther out in range. Frequency dependent attenuation is observable in both the data and calculations.

#### CONCLUSIONS

Some general conclusions may be drawn from this comparative modeling study:

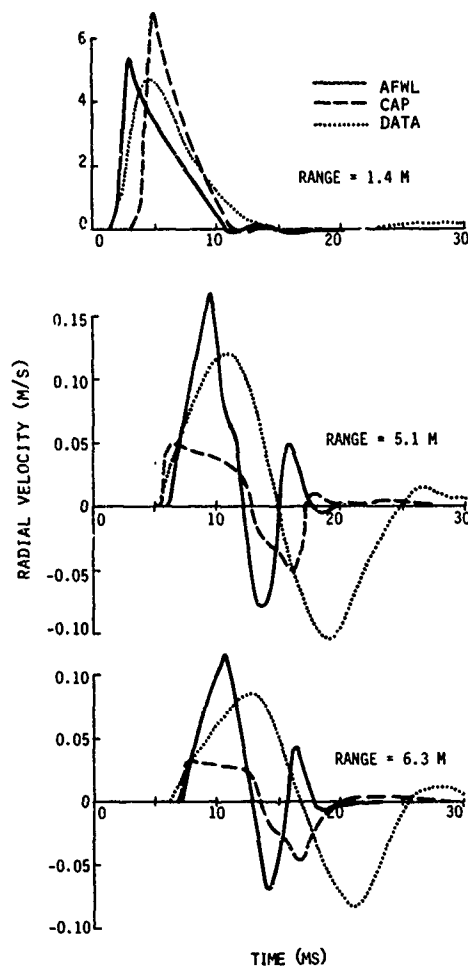


Figure 8. Calculated Velocity Waveforms.

i. In choosing a type of material model to use for soil, necessary model complexity will vary with specific problem requirements. For example a spherical calculation, with stress and strain paths like those shown in Figure 7, poses a more difficult modeling problem than a uniaxial-strain wave propagation calculation.

ii. Fundamentally different models (e.g. the AFWL Engineering and Cap models) may yield similar results when used in a particular problem. Additionally, user familiarity with a particular model will affect results.

iii. Laboratory data is essential for modeling soil, but it must be extrapolated to the in-situ condition. Both simple and more expensive in-situ tests can provide the necessary correlation.

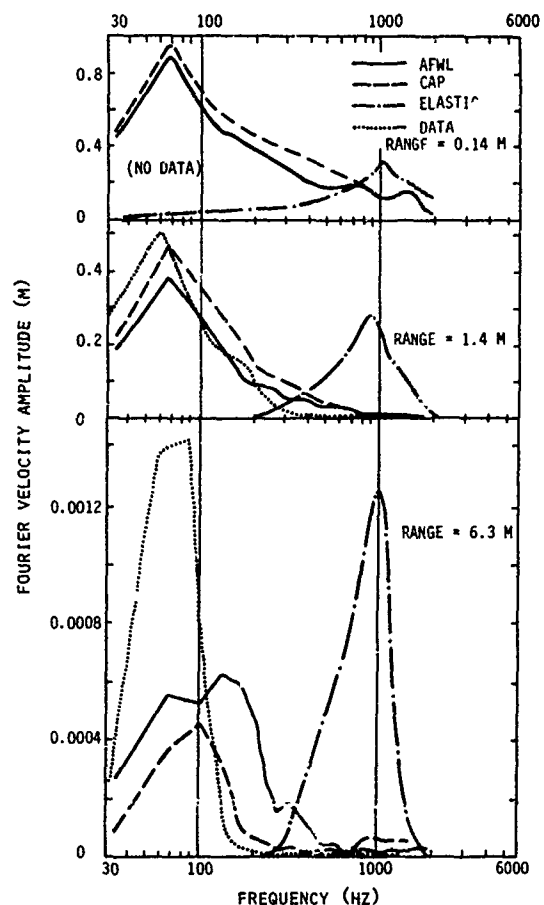


Figure 9. Fourier Velocity Amplitude Spectra.

iv. A material model may be evaluated through single element studies (like the SEM exercises) or through finite element/difference boundary value problems (like one-dimensional wave propagation).

#### REFERENCES

- (1) Dass, W.C., Bratton, J.L., and Higgins, C.J., "Fundamental Properties of Soils for Complex Dynamic Loadings," Report No. AFOSR-TR-82-0101, Applied Research Associates, Albuquerque, NM, September 1981.
- (2) Dass, W.C., Merkle, D.H., and Bratton, J.L., "Fundamental Properties of Soil for Complex Dynamic Loadings: Constitutive Modeling of Sandy Soils," Report to AFOSR, Applied Research Associates, Albuquerque, NM, May 1983.

## CONSTITUTIVE MODELS FOR SATURATED SOILS

Ranbir S. Sandhu

The Ohio State University  
Department of Civil Engineering  
Columbus, Ohio

## ABSTRACT

Theories of mechanical behavior of saturated geologic materials are reviewed. Various approaches to defining the mechanical and kinematic variables and their interrelationships are described.

## INTRODUCTION

Terzaghi [76] derived the equations for one-dimensional consolidation. These were extended [45] to the case of variable material properties and later to finite strain [31]. Biot [6-13] proposed theories for three dimensional problems of fluid saturated solids based on certain postulates.

Theories of interacting continua were proposed by Truesdell [76] and further developed by several investigators [e.g. 1-5, 14, 32-37]. These were applied to the flow of fluids through solids by Crochet [21] and others [62, 70]. Recent work [14, 18, 51-53, 59, 80] has extended these applications to finite deformation and nonlinear constitutive laws.

Constitutive models relate mechanical quantities associated with a physical problem to the kinematic or state variables. Typically, for a solid, the stress tensor is represented as a set of functionals of the history of deformation of the body and its temperature. For fluid-saturated solids, one additional mechanical quantity is the fluid stress. For flow of the fluid relative to the solid matrix, the diffusive resistance is introduced to reflect the interaction.

In this brief review, we describe several different viewpoints regarding choice of mechanical and kinematic variables and constitutive relationships for a fluid-saturated solid.

## KINEMATICS

To apply the principles of continuum mechanics, it is customary to regard a fluid-saturated solid as superposed continua. The mixture is defined by the current coincident configurations of the two constituents. It is assumed that, in the current configuration, each point of space is occupied by a particle of each of the constituents.

a. Density of each constituent and the mixture. For each constituent to fill the body, a 'bulk' description of density is used [4, 5, 14, 21, 22, 28, 32-37, 51-53, 57, 59, 69, 78, 80]. The

$$\rho = \sum \rho^{(\alpha)} \quad (1)$$

where  $\rho^{(\alpha)}$  is the bulk density of the constituent  $\alpha$  and  $\rho$  is the density of the saturated solid (the mixture). The bulk densities are related to the intrinsic or true densities  $\rho^{(\alpha)*}$  [14, 15, 29, 51-53, 57] as

$$\rho^{(\alpha)} = n^{(\alpha)} \rho^{(\alpha)*} \quad (2)$$

where  $n^{(\alpha)}$  represents the volume fraction of constituent  $\alpha$  in the current configuration. Combining (1) and (2), for a binary mixture,

$$\rho = n^{(1)} \rho^{(1)*} + n^{(2)} \rho^{(2)*} = n^{\alpha} \rho^{\alpha*} \quad (3)$$

implying summation in repeated indices not enclosed in parentheses. Terzaghi's theory differs from most others in that  $n^{(2)}=1$  and, therefore, the solid has the 'buoyant' bulk density

$$\begin{aligned} \rho^{(1)} &= \rho - \rho^{(2)*} \\ &= (1 - n^{(2)}) (\rho^{(1)*} - \rho^{(2)*}) \end{aligned} \quad (4)$$

## b. Motion of the constituents.

Several approaches have been used to describe the motion of the constituents. One is to refer the motion of each constituent to its reference configuration, another is to refer the motion of every constituent to the current configuration of the solid, and often it is convenient to refer to the current configuration of each constituent. If  $x_i^{(\alpha)}(\tau)$  is the place occupied at time  $\tau$  by the material particle described by  $X_i^{(\alpha)}$  in the reference configuration for  $\alpha$ , the displacement gradient is [14, 21, 22, 33]

$$F_{ij}^{(\alpha)} = \frac{\partial x_i^{(\alpha)}}{\partial X_j^{(\alpha)}} = x_{i,j}^{(\alpha)} \quad (5)$$

$$\text{with} \quad \det \| F_{ij}^{(\alpha)} \| > 0 \quad (6)$$

The velocity vectors are derived from  $x_i^{(\alpha)}$  as the material rate

$$v_i(\alpha) = \frac{Dx_i(\alpha)}{Dt} = \left( \frac{\partial}{\partial t} + v_m(\alpha) \frac{\partial}{\partial x_m(\alpha)} \right) x_i(\alpha) \quad (7)$$

$$\text{where } v_m(\alpha) = \frac{\partial x_i(\alpha)}{\partial t} \quad (8)$$

is the Lagrangian description of velocity. An Eulerian description of motion too has been used. [18, 79]. The rates of deformation are

$$d_{ij}(\alpha) = v_{(i,j)}(\alpha) \quad (9)$$

Westmann [80] and others [e.g. 18] used Eulerian description for deformation. Often, a mean or barycentric velocity for the mixture in terms of velocities  $v_i(\alpha)$  of the constituents is introduced by

$$w_i = \frac{\rho^\alpha v_i}{\rho} \quad (10)$$

Atkin [4] noted that the mixture velocity has no particular physical meaning in continuum mechanics. This is because a mixture defined by (3) is a set of centers of mass and cannot be regarded as a set of material particles in motion [64] except in the case of no relative motion between the constituents.

Crochet [21] showed that all kinematic variables were functions of  $d_{ij}(\alpha)$ ,  $d_{ij}(\alpha)$ , the relative velocity vector  $v_i = v_i^{(1)} - v_i^{(2)}$  and the relative vorticity

$$\omega_i = \omega_i^{(1)} - \omega_i^{(2)} \quad (11)$$

#### c. Measures of deformation.

Assuming small deformation (linear theory), the components of strain in the solid are [6-11]

$$e_{ij}^{(1)} = u_{(i,j)}^{(1)} \quad (12)$$

Where  $u_i^{(1)} = x_i^{(1)} - x_i^{(2)}$  are components of the displacement of the solid. A measure of volumetric strain of the solid is  $e_{kk}^{(1)}$ . Garg [35] and Krause [42] related it to change of density of the solid as

$$\rho^{(1)} = \rho_0^{(1)} (1 - e_{kk}^{(1)}) \quad (13)$$

Where  $\rho_0^{(1)}$  is the density in the reference configuration. Biot [6, 11, 12] used the change in water content of a reference material volume of the solid as the kinematic variable. Garg's [35] use of  $n^{(1)}$  as kinematic variables in addition to  $e_{ij}^{(1)}$  may be regarded as an extension of this concept. The quantity  $n^{(1)}$  was referred to the current configuration of the solid. Westmann's earlier work [80] followed similar reasoning.

Carroll [15] regarded  $e_{ij}^{(1)}$  to consist of two parts i.e.

$$e_{ij}^{(1)} = e_{ij}^{(s)} + e_{ij}^{(p)} \quad (14)$$

Where the superscripts s, p refer to the solid material and the pore space respectively. The volumetric strain of the solid phase was shown to be

$$\frac{\Delta V}{V} = \frac{\Delta V_s}{V_s} + \frac{\Delta n}{n^{(1)}} \quad (15)$$

Where  $V$ ,  $V_s$  are the total volume and the solid volume fraction i.e.  $V_s = n^{(1)}V$  and  $\Delta$  indicates an incremental quantity. Recently, Carroll [16] wrote for a binary mixture

$$\begin{aligned} e_{ij}^{(1)} &= n^{(1)} e_{ij}^{(s)} + n^{(2)} e_{ij}^{(p)} \\ &= e_{ij}^{(s)} + n^{(2)} (e_{ij}^{(p)} - e_{ij}^{(s)}) \end{aligned} \quad (16)$$

Aifantis [3] used the density, the gradient of density and the relative velocity of the fluid as the basic variables for flow of a fluid in a solid.

#### MECHANICAL QUANTITIES

##### a. Partial stresses

Stresses in the constituents are obviously the primary mechanical variables. Assuming partial stresses to act over entire area of internal surfaces the total stress

$$\sigma_{ij} = \sigma_{ij}^{(1)} + \sigma_{ij}^{(2)} \quad (17)$$

For isotropic fluid stress  $\sigma_{ij}^{(2)} = \pi \delta_{ij}$  and

$$\sigma_{ij} = \sigma_{ij}^{(1)} + \pi \delta_{ij} \quad (18)$$

Biot regarded  $\sigma_{ij}^{(1)}$  as the bulk stress but  $\pi$  as an intrinsic quantity so that

$$\sigma_{ij} = \sigma_{ij}^{(1)} + n^{(2)} \pi \delta_{ij} \quad (19)$$

Garg [30], Morland [51-53], Pecker [57] and Carroll [15], among others, introduced the notion of intrinsic stresses  $\sigma_{ij}^{(\alpha)*}$  for each constituent leading to

$$\sigma_{ij} = n^\alpha \sigma_{ij}^{(\alpha)*} \quad (20)$$

##### b. Effective stress

Terzaghi [76] termed  $\sigma_{ij}^{(1)}$  in (17) the effective stress related to deformation of the solid. Biot [6-8, 11] regarded the total stress  $\sigma_{ij}$  and the fluid pressure  $\pi$  as the mechanical variables. It was found [e.g. 55] that the fluid pressure did in fact influence the effective stress-strain relationship when the solid grains had compressibility comparable to that of the matrix as a whole and the fluid was not incompressible. To allow for this the effective stress related to deformation was defined as

$$\sigma_{ij}' = \sigma_{ij} - \lambda \pi \delta_{ij} \quad (21)$$

$$= \sigma_{ij}^{(1)} + (1-\lambda) \pi \delta_{ij} \quad (22)$$

Where  $\lambda = 1$  implies Terzaghi's definition and  $\lambda = 0$  would correspond to total stress being

regarded as effective. Suklje [75] discussed selection of appropriate values of  $\lambda$ . Schiffman [67] expected  $\lambda$  to be between  $n^{(2)}$  and 1. Nur [55] derived the equation

$$\lambda = 1 - \frac{K}{K_s} \quad (23)$$

Where  $K$ ,  $K_s$  are the bulk and the intrinsic compressibility of the solid. For incompressible grains and highly deformable pore space,  $K \rightarrow 0$ , Terzaghi's definition is recovered. Schiffman [67] gave a more general form for (20) allowing fluid pressure to be a second rank tensor and  $\lambda$  a fourth rank tensor. For clays, Mitchell [46] would include attractive and repulsive forces within the material in defining the effective stress.

Tsien [79] divided the total stress into stress deviation and the hydrostatic stress  $\sigma_{kk}$ . The hydrostatic stress was expected to be distributed over the solid and the fluid in proportion of their volume fractions  $n^{(\alpha)}$ .

Garg [35] proposed a dual definition for effective stress. For strength of rock he would set  $\lambda = 1$  in (21) but for constitutive relations another value of  $\lambda$  would be used.

For large deformation, an incremental form of the stress tensor was introduced by Biot [12]. Carter [18] and Prevost [59] used the Jaumann stress rate to ensure frame indifference. Its relation to the Cauchy stress  $t_{ij}$  is

$$\dot{\sigma}_{ij}^{(1)} = t_{ij}^{(1)} - t_{ik}^{(1)} L_{kj}^{(1)} - t_{jk}^{(1)} L_{ki}^{(1)} \quad (24)$$

Where  $L_{ij}^{(1)}$  are components of the antisymmetric rate of rotation tensor for the solid in an Eulerian description.

#### c. Diffusive Resistance.

Diffusive resistance was introduced as a mechanical variable by Green [33-37] and Crochet [21]. For non-chemically reacting continua, in the absence of inertia effects,

$$(\sigma_{ij}^{(1)} + \sigma_{ij}^{(2)})_{,i} + (\rho f^{(\alpha)})_{,j} = 0 \quad (25)$$

Where  $f^{(\alpha)}$  is the body force per unit mass associated with the constituent  $\alpha$  (25) can be rearranged as

$$(\sigma_{ij}^{(1)} + \rho^{(1)} f^{(1)})_{,i} = (\sigma_{ij}^{(2)} + \rho^{(2)} f^{(2)})_{,i} \quad (26)$$

Each side of the equality (26) representing interaction between the constituents is set equal to the diffusive resistance  $D_i$ . Evidently, a set of single constituent stresses in equilibrium can be added to the stresses on either side without affecting the definition of  $D_i$ . For hydrostatic fluid stress,

$$D_i = -(\pi + \rho^{(2)} f^{(2)})_{,i} \quad (27)$$

## CONSTITUTIVE EQUATIONS

Crochet [21] has shown that under isothermal conditions and in the absence of chemical reactions, the constitutive relations will involve  $d_{ij}^{(\alpha)}$ ,  $d_{ij}^{(\alpha)}$ ,  $v_i$  and  $\omega_i$ .

#### a. Diffusive Resistance.

Green [33-37] introduced diffusive resistance as a mechanical quantity for which a constitutive relationship is required. For the linear theory of irrotational relative motion and non-Newtonian behavior this immediately leads to an expression of the type

$$D_i = -(\pi + \rho^{(2)} f^{(2)})_{,i} = -C_{ji} v_i \quad (28)$$

The inverse form of this equation is the well-known darcy flow rule [58, 66]. Thermodynamics of darcy's law was discussed by Mokadam [48-50]. Schiffman [68] extended darcy's law to non-isothermal consolidation. Further generalizations based on Onsager's principle have been proposed [e.g. 12, 56, 62, 63, 65, 71]. Generalization to nonlinear cases has been proposed [47] assuming  $C_{ij}$  to be functions of porosity  $n^{(2)}$ .

#### b. Stresses in the Solid and the Fluid.

Tsien [79] proposed a linear elastic isotropic relation for  $\sigma_{ij}^{(1)}$  in terms of  $e$  (1) using Terzaghi's definition i.e.  $\alpha = 1$  in (21). Biot [5] assumed a quadratic energy function in  $e_{kk}$  and  $\theta$ , the change in water content per unit volume of the solid leading, for isotropic linear elastic soil and incompressible fluid, to

$$\sigma_{ij} = 2\mu e_{ij} + \lambda e_{kk} \delta_{ij} + M\theta \delta_{ij} \quad (29)$$

$$\pi = M e_{kk} + N\theta$$

In later work, [10], the total stress in (29) was replaced by effective stress  $\sigma_{ij}^{(1)}$ . In extension to anisotropic elastic [7] materials and compressible fluid the relationship was stated as

$$\sigma_{ij}^{(1)} = C_{kl ij} e_{kl}^{(1)} + M_{ij} e_{kk}^{(2)} \quad (30)$$

$$\pi = M_{ij} e_{ij}^{(1)} + M e_{kk}^{(2)}$$

Similar construction was used for viscoelastic soils [8]. In [11] the quantity  $e_{kk}^{(2)}$  was again replaced by  $\theta$  as used in (29). The same concept was extended to the case of finite elastic deformation [12].

Skempton [72, 73] and Henkel [38] stated fluid pressure as a linear combination of the effective stress components. A more general statement of this type would be

$$\pi = b_1 J_1 + b_2 J_2^{1/2} + b_3 J_3^{1/3} \quad (31)$$

Where  $b_i$  are material constants and  $J_i$  are the invariants of  $\sigma_{ij}$ , the total stress tensor. To reflect the difference in fluid pressures observed during loading and unloading cycles, and their steady increase with plastic straining, Lo [43]

proposed use of strain invariants  $I_i$  of  $e_{ij}$  (1) instead of  $J_i$ . The coefficients  $b_i$  have been found [44] to depend upon stress. These approaches are entirely empirical and need not be pursued further.

Krause [42] added terms to the right side of (29) to reflect linear dependence of the fluid pressure on the deformation rate  $\dot{\epsilon}_{ij}$  (2) of the fluid. This assumes viscous component for fluid flow.

Adkins [1] assumed that the stress in each component depended only on the density and the kinematic quantities associated with only that constituent. Nur [55] assumed the effective stress to be given by (21) along with (23) to be related to  $e_{ij}$  (1). This admitted a certain dependence of  $\sigma_{ij}$  (1) upon the fluid pressure. Explicitly,

$$\sigma_{ij} = \sigma_{ij}^{(1)} + (1-\lambda)\pi\delta_{ij} = c_{kl ij} e_{kl}^{(1)} \quad (32)$$

Hence

$$\sigma_{ij}^{(1)} = c_{kl ij} e_{kl}^{(1)} - (1-\lambda)\pi\delta_{ij} \quad (33)$$

Carroll [15] carried out a similar development. These approaches were based on the superposition of effects of the hydrostatic stress and the shear stress. Carroll [15] determined, for the linear case,

$$\lambda_{kl} = \delta_{ki}\delta_{jl} - E_{kl ij} c_{ijmm}^{(s)} \quad (34)$$

Where  $E_{kl ij}$  are components of the elasticity tensor for the dry solid material and  $c_{ijkl}^{(s)}$  is the intrinsic compliance under hydrostatic stress. Schiffman [67] proposed a generalization of (33) in the form

$$\sigma_{ij}^{(1)} = c_{kl ij} e_{ij}^{(1)} - (\delta_{ik}\delta_{jl} - A_{kl ij})\sigma_{kl}^{(2)} \quad (35)$$

(34) apparently defines the structure of  $A_{kl ij}$  in (35). For isotropy (34) as well as (35) reduces to (23). Garg [30] obtained a relationship between the intrinsic and the bulk behavior of rocks under hydrostatic stress. Interpretation of coefficients appearing in his equations were attempted by Biot [9]. Additions to this discussion have appeared from time to time [e.g. 39-41, 55, 61].

Aifantis [3] assumed effects of changes in fluid pressure and the solid stress to be additive and proposed a compliance relationship

$$\Delta n^{(2)} = a\Delta\pi + b\Delta\sigma_{kk}^{(1)} \quad (36)$$

where the symbol  $\Delta$  indicates change in the quantity following it.

In extending the theory to the nonlinear case, Westmann [80] assumed  $\sigma_{ij}^{(1)}$  to be a function of the Cauchy deformation tensor for the solid and the rate of deformation (Eulerian description) of the fluid. The fluid stress was expected to

consist of a hydrostatic component and another component depending upon the same quantities as  $\sigma_{ij}^{(1)}$ . It was noted that in this formulation it would be difficult to design experiments to evaluate the parameters. A simplification proposed assumed fluid pressure to be hydrostatic and related to the velocity field through darcy's law. This is similar to Sandhu's [62-64] argument that the constitutive equation for diffusive resistance is a sufficient relationship between fluid partial stress and kinematics of the mixture. Westmann [80] wrote relative velocity as a function of  $\pi$ ,  $\pi_i$ , and the Cauchy deformation tensor for the solid. This would reflect, among other factors, the dependence of permeability on the porosity of the solid.

Sandhu [62-65], Westmann [80] and Morland [51-53] have followed Adkins' [1] original idea that the stresses in each constituent depend upon the kinematics of only that constituent. However, Morland [51-53] would use this for the intrinsic rather than the bulk stresses. This brings back some dependence of  $\sigma_{ij}^{(1)}$  upon the fluid pressure because the porosity was postulated to be a linear function of the partial stresses.

Adkins [2] and Green [32] admitted interdependence of stress of each constituent upon the kinematics of all. This was in line with the principle of equipresence stated by Truesdell [77]. In application to elastic materials, the existence of an energy function for the mixture was assumed by Biot [6-12]. This has been consistently followed by numerous investigators [e.g. 4, 5, 14, 21, 22, 32-37, 69]. Sandhu [64] pointed out that as the mixture could not be regarded as a continuum in motion, it was inappropriate to assume energy functions for it in the form that has been popular. An expression for energy would be the sum of energies for each constituent.

Morland [51-53] did not assume the existence of an energy function for the mixture but still admitted interdependence. This gave relations of the type postulated by Biot (equation (30')) with  $M_{ij}$  in the second equation replaced by say  $N_{ij}$ , not necessarily equal to  $M_{ij}$  in the first equation. Schiffman [67] had earlier proposed nonsymmetric relationships. For  $\lambda = n^{(2)}$  he expected the constitutive equations for  $\sigma_{ij}$  and  $\pi$  to become uncoupled.

The explicit form of dependence of stresses in the solid upon the strains will not be discussed here. Those relations may be linear or nonlinear elastic, viscoelastic, hypoelastic or elasto-viscoplastic. A large volume of literature on the subject exists. As examples of recent work on a variety of models we cite Desai [23-25], Prevost [60], Dragsun [27], Digby [26], Christoferson [19], Coon [20] and Mullenger [54]. In developing plasticity theories for saturated porous media, Carroll [16] has pointed out the difficulty in defining plastic strains.

#### ACKNOWLEDGEMENTS

This work is part of a research program



supported by the Air Force Office of Scientific Research under contract 715107 with the Ohio State University.

#### REFERENCES

1. Adkins, J.E., *Phil. Trans., Roy. Soc. Series A*, 255, 607-650, 1963.
2. Adkins, J.E., *Arch. Rat. Mech. Anal.*, 15, 222-234, 1964.
3. Aifantis, E.C., *Acta Mechanica*, 37, 265-296, 1980.
4. Atkin, R.J., *ZAMP*, 18, 803-825, 1967.
5. Atkin, R.J.; and Craine, R.E., *Quar. J. Mech. App. Math.*, 29 Pt. 2, 209-244, 1976.
6. Biot, M.A., *J. App. Phys.*, 12, 155-164, 1941.
7. Biot, M.A., *J. App. Phys.*, 26, 182-185, 1955.
8. Biot, M.A., *J. App. Phys.*, 27, 459-467, 1956.
9. Biot, M.A., and Willis, D.G., *J. App. Mech.*, ASME, 594-601, 1957.
10. Biot, M.A., *J. App. Phys.*, 33, 1482-1498, 1962.
11. Biot, M.A., *J. Math. Mech.*, 12, 521-541, 1963.
12. Biot, M.A., *Indiana Univ. Math. J.*, 21, 597-620, 1972.
13. Biot, M.A., *J. Geophy. Res.*, 78, 4924-4937, 1973.
14. Bowen, R.M., *Int. J. Engrg. Sci.*, 20, 697-735, 1982.
15. Carroll, M.M., *J. Geophy. Res.*, 84, 7510-7512, 1979.
16. Carroll, M.M., Schatz, J.F., and Yamada, S.E., *Trans. ASME*, 48, 976-978, 1981.
17. Carroll, M.M., and Kotsube, N., *J. Energy*, ASME, to be published.
18. Carter, J.P., Small, J.C., and Booker, J.R., *Int. J. Solids Struct.*, 13, 467-478, 1977.
19. Christofferson, J., Mehrabadi, M.M., and Nemat-Nasser, S., *J. App. Mech.*, ASME, 48, 339-344, 1981.
20. Coon, M.D., and Evans, R.J., *Proc. ASCE*, J. SMFD, 97, SM2, 375-391, 1971.
21. Crochet, M.J., and Naghdi, P.M., *Int. J. Engrg. Sci.*, 4, 383-401, 1966.
22. Demiray, H., *Int. J. Engrg. Sci.*, 19, 253-268, 1981.
23. Desai, C.S., *Int. J. Numer. Anal. Methods Geomech.*, 4, 361-376, 1980.
24. Desai, C.S., and Siriwardane, H.J., *Int. J. Numer. Anal. Methods Geomech.*, 4, 377-388, 1980.
25. Desai, C.S., Phan, H.V. and Sture, S., *Int. J. Numer. Anal. Methods Geomech.*, 5, 295-311, 1981.
26. Digby, P.J., *J. App. Mech.*, ASME, 48, 803-808, 1981.
27. Dragsun, L., *Int. J. Engrg. Sci.*, 19, 511-552, 1981.
28. Firoozbakhsh, K., *Int. J. Solids Struct.*, 12, 649-654, 1976.
29. Garg, S.K., *J. Geophy. Res.*, 76, 7947-7962, 1971.
30. Garg, S.K. and Nur, A., *J. Geophy. Res.*, 78, 5911-5921, 1973.
31. Gibson, R.E., England, G.L. and Hussey, M. J.L., *Geotechnique*, 17, 261-273, 1967.
32. Green, A.E., and Adkins, J.E., *Arch. Rat. Mech. Anal.*, 15, 235-246, 1964.
33. Green, A.E., and Naghdi, P.M., *Int. J. Engrg. Sci.*, 3, 231-241, 1965.
34. Green, A.E., and Naghdi, P.M., *Arch. Rat. Mech. Anal.*, 24, 243-263, 1967.
35. Green, A.E., and Naghdi, P.M., *Int. J. Engrg. Sci.*, 6, 631-635, 1968.
36. Green, A.E., and Naghdi, P.M., *Quart. J. Mech. App. Math.*, 22, Pt. 4, 427-438, 1969.
37. Green, A.E., and Naghdi, P.M., *Acta Mechanica*, 9, 329-340, 1970.
38. Henkel, D.J., *Geotechnique*, 10, 41-54, 1960.
39. Kenyon, D.E., *Arch. Rat. Mech. Anal.*, 62, 117-129, 1976.
40. Kenyon, D.E., *Arch. Rat. Mech. Anal.*, 62, 131-147, 1976.
41. Kenyon, D.E., *J. App. Mech.*, ASME, 45, 727-732, 1978.
42. Krause, G., *Die Bautechnik*, 95-103, March 1977.
43. Lo, K.Y., *Proc., 5th Int. Con. SMFE*, 1961.
44. Mesri, G., Adachi, K., and Ullrich, C.R., *Geotechnique*, 26, 317-330, 1976.
45. Mikasa, M., *Civil Engineering in Japan*, Japan Soc. Civ. Eng., 21-26, 1965.
46. Mitchell, J.K., *Clays and Clay Minerals*, 9, 162-184, 1962.
47. Monte, J.L. and Krizek, R.J., *Geotechnique*, 26, 495-510, 1976.
48. Mokadam, R.G., *J. App. Mech.*, ASME, 208-212, June 1961.
49. Mokadam, R.G., *Inzhenernyi -fizicheski Zhurnal*, 6, 1963, (in Russian).
50. Mokadam, R.G., *Inzhenernyi-fizicheski Zhurnal*, 9, 1966 (in Russian).
51. Morland, L.W., *J. Geophy. Res.*, 77, 890-900, 1972.
52. Morland, L.W., *Geophy. J. Roy. Astr. Soc.*, 55, 393-410, 1978.
53. Morland, L.W., *Geotechnical and Environmental Aspects of Geopressure Energy*, Ed. S. K. Saxena, Engineering Foundation, New York, 363-366, 1980.
54. Mullenger, G., and Davis, R.O., *Int. J. Numer. Anal. Methods Geomech.*, 5, 285-294, 1981.
55. Nur, A., and Byerlee, J.D., *J. Geophy. Res.*, 76, 6414-6419, 1971.
56. Olsen, H.W., *Proc., Soil Sci. Soc. Am.*, 33, 338-344, 1969.
57. Pecker, C., and Deresiewicz, H., *Acta Mechanica*, 16, 45-64, 1973.
58. Polubarinova-Kochina, P.I., *The Theory of Ground Water Movement*, Princeton Univ. Press, Princeton, 1962.
59. Prevost, J.H., *Comp. Methods Engrg. App. Mech.*, 20, 3-18, 1982.
60. Prevost, J.H., *Int. J. Numer. Anal. Methods Geomech.*, 6, 323-338, 1982.
61. Rice, J.R., and Cleary, M.P., *Rev. Geophy. Space Phy.*, 14, 227-241, 1976.
62. Sandhu, R.S., *Fluid Flow in Saturated Porous Elastic Media*, Ph.D. Thesis, Univ. of California at Berkeley, 1968.
63. Sandhu, R.S., *Finite Element Analysis of Soil Consolidation*, Report OSURF-3570-76-3, The Ohio State University, Columbus, Ohio, 1976.

64. Sandhu, R.S. and Liu, H., Numerical Methods in Geomechanics, Aachen, 1979, Ed. W. Witke, Balkema, 1255-1263, 1979.
65. Sandhu, R.S., U.S.-Venezuela Forum on Land Subsidence due to Fluid Withdrawal, Fountainhead, Oklahoma, 1982.
66. Scheidegger, A.E., The Physics of Flow Through Porous Media, Macmillan, 1960.
67. Schiffman, R.L., J. Geophy. Res., 75, 4035-4038, 1970.
68. Schiffman, R.L., Environmental and Geophysical Heat Transfer, Vol. 4, Heat Transfer Div., ASME, 78-84, 1972.
69. Shi, J.J., Rejagopal, K.R., and Wineman, A.S., Int. J. Engrg. Sci., 19, 871-889, 1981.
70. Tabaddor, F., and Little, R.W., Int. J. Solids Struct., 7, 825-841, 1971.
71. Taylor, A., and Cary, J.W., Proc., Soil Sci. Soc. Am., 28, 167-172, 1964.
72. Skempton, A.W., Geotechnique, 4, 143-147, 1954.
73. Skempton, A.W., and Bjerrum, L., Geotechnique, 7, 168-178, 1957.
74. Skempton, A.W., Pore Pressures in Soils, Butterworths, London, 1960.
75. Suklje, L., Rheological Aspects of Soil Mechanics, Interscience, 1969.
76. Terzaghi, k., Theoretical Soil Mechanics, Wiley, 1943.
77. Truesdell, C., and Toupin, R.A. Handbuch der Physik, III/1, Ed. S. Flugge, Springer-Verlag, 1960.
78. Truesdell, C., J. Chem. Phy., 37, 2336-2344, 1961.
79. Tsien, H.S., Problems of Continuum Mechanics, Muskhelishvili Anniversary Volume, Noordhoff, 1961.
80. Westmann, R.A., Nonlinear Three Dimensional Theory of Consolidation, Unpublished Report, 1967.

AD P001762

# THE RESPONSE OF REINFORCED CONCRETE STRUCTURES UNDER IMPULSIVE LOADING

William A. Millavec and Jeremy Isenberg

Weidlinger Associates  
Menlo Park, California

## ABSTRACT

A finite element method is presented to analyze the effects of airblast-induced ground shock on shallow-buried, flat-roofed, reinforced concrete structures. A finite element based on Timoshenko beam theory is adopted. Material properties are defined in terms of nonlinear stress-strain relations in each of several layers through the thickness of the element. Elastic, ideally plastic constitutive properties for plain concrete are cast in terms of shear-stress/normal-stress variables. Elastic, strain-hardening constitutive properties are assumed for steel. Dynamic explicit and implicit and static solution algorithms are available. This analysis method is applied to simulation of static beam-column tests reported by ACI Committee 318-77. It is then applied to simulation of structural response of experimentally tested shallow-buried box structures subjected to airblast loads in which shear, flexure and combined shear-flexure damage was observed.

A special type of shear damage and shear failure at the supports of clear spans can only occur under very high rates of loading present in impulsive loads. Large displacements accompanied by extensive cracking, crushing and yielding may occur without actually causing the total failure of the span. These two aspects of the behavior of reinforced concrete structures under impulsive loading motivate the development of special layered finite element. Shear deformation is introduced as an independent variable and the nonlinear terms in the strain-displacement relations are retained.

In a recent series of explosive field tests, shallow-buried rectangular structures and roof slabs were tested to the point of severe damage. In each, dynamic loading and response, nonlinear soil-structure interaction and large deformations accompanied by extensive cracking, crushing and yielding or fracture of steel must be considered. Analysis methods, such as lumped parameter models or Hiltiwanger et al. [7] and the rigid plastic model of Symonds [15], provide helpful insight but omit important details of geometry and loading. Several nonlinear beam elements have been published (Bathe [1], Pifko et al. [14]) but these are formulated directly in terms of stress resultants and to use them for reinforced concrete members requires knowledge of nonlinear properties of concrete under combined moment, thrust and shear, for which

experimental data is incomplete. In the layered finite element approach (Buykozturk [5], Hand et al. [8], Wittmer [13]), material nonlinearity is introduced in each layer as biaxial stress-strain properties which we believe are better known (Kupfer et al. [11]).

A new layered beam element, which includes shear deformation, is developed in this paper. Material and geometric nonlinearity, using the Lagrangian approach, are included. Nodal degrees-of-freedom are transverse and axial displacements and flexural and shear rotations are included. Each element is divided into an arbitrary number of layers in which stress-strain properties of plain concrete are represented by an elastic, ideally plastic model. Longitudinal reinforcing is modeled discretely and is represented by an elastic, strain-hardening plasticity model. Although an elastic, ideally plastic model is currently implemented in our computer program, recent advances (Levine [12]) will soon replace it. A computer program, RCBEAM, incorporates the features of the layered beam finite element described above. Static equations of equilibrium are solved incrementally with equilibrium iteration. Dynamic equations of motion are solved either by a variety of implicit integration operators, including Wilson's Theta or Newmark's Beta methods [2], with equilibrium iteration or by explicit, second-order central difference.

The goal of the present work is to qualify the structural element by comparison with a suite of static beam-column tests and with dynamic tests. To eliminate as much as possible uncertainty in dynamic loads, we use measured interface pressures. Once qualified, RCBEAM can easily be coupled to an explicit continuum finite element program, such as TRANAL, for complete soil-structure analysis.

## MATERIAL PROPERTIES

The material properties assumed for each layer of plain concrete are illustrated in Fig. 1a. The important property is the strength under a state of combined direct (tension or compression) and shear stresses [3,9,11]. These states lie in the tension-compression quadrant of the concrete failure surface for biaxial stress (third principal stress equal to zero). The failure surface in this quadrant has a complicated shape when expressed either in  $\sigma_1 - \sigma_2$  plane or in  $\sigma_{xy} - \sigma_{xx}$  plane. We approximate the failure relation as linear in  $\sigma_1 - \sigma_2$  plane or elliptical in  $\sigma_{xy} - \sigma_{xx}$  plane, as

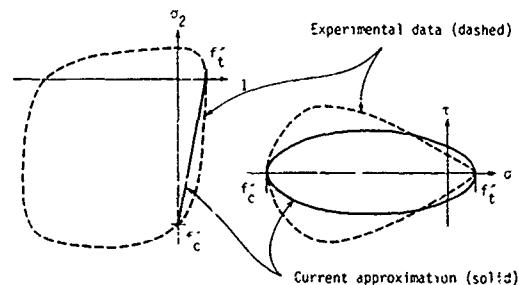
Fig. 1 illustrates. The failure criterion  $f$  is regarded

$$f = \sigma_{xx}^2 + (f_c' - f_t') \sigma_{xx} + \frac{(f_c' + f_t')^2}{f_c' f_t'} \sigma_{xy}^2 - f_c' f_t' = 0 \quad (1)$$

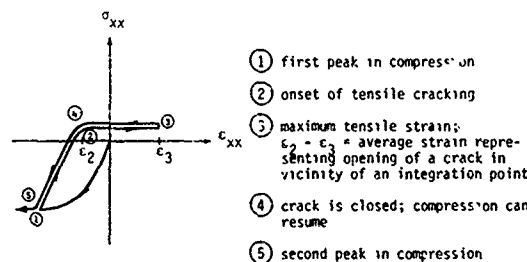
as a yield criterion where  $f_c'$ ,  $f_t'$  = uniaxial compressive and tensile strengths, respectively.

In the zone of compressive axial stress, it is assumed the yielding is associated with ductile behavior and the plastic strains are computed from the associated flow rule in a standard manner. In the zone of tensile axial stress, it is assumed that yielding implies cracking and the direction of cracking is specified by the outward normal to the yield surface at first tensile yielding. Moreover, it is assumed that as long as the crack is open the direction of cracking remains constant.

The procedure is illustrated in Fig. 1b. Notice that tensile stress is allowed to be transmitted across the crack because strain softening following cracking is not incorporated within the present version of plasticity theory.



a. Approximation to failure criterion for plain concrete



b. Stress-strain properties of plain concrete in direction parallel to longitudinal axis of element

Fig. 1. Summary of plain concrete modeling.

A similar approach is used to express the properties of the longitudinal reinforcing steel. A strain-hardening yield criterion of the Mises type

$$f = \sigma_{xx}^2 + 3\sigma_{xy}^2 - \sigma_0^2(\epsilon) = 0 \quad (2)$$

is adopted, where

$$\sigma_0(\epsilon) = f_y + H\epsilon^p \leq 1.4f_y$$

where

$$d\epsilon^p = [(d\epsilon_{xx}^p)^2 + \frac{1}{3}(d\epsilon_{xy}^p)^2]^{\frac{1}{2}}$$

Shear strain in the bar is computed from the assumption that shear strain is constant through the thickness. Longitudinal strain in the bar is computed by linear interpolation. Perfect compatibility between steel and concrete currently is assumed. Bond slip could be incorporated, however.

#### ILLUSTRATIVE EXAMPLE: BEAM-COLUMN

In order to illustrate the properties of the element described above, a series of small displacement calculations neglecting shear deformations were performed in which a cantilever beam is subjected to various fixed ratios of thrust-to-moment. The combinations of maximum thrust ( $T$ ) and moment ( $M$ ) form an envelope in  $M$ - $T$  plane which, when safety factors are removed, can be compared with recommendations published by ACI Committee 318-77 [4]. The parameters of the numerical experiment, finite-element discretization (note 5 layers through thickness) and comparison of RCBEAM results with the ACI committee's recommendations are shown in Fig. 2. The shapes of the two curves are virtually identical. The worst agreement is at the balance point, where RCBEAM results are about 20% higher than the ACI recommendations. This numerical experiment increases confidence in the present method of defining material properties under combined loading.

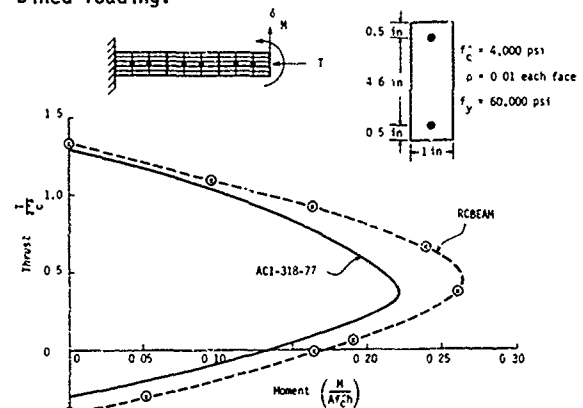


Fig. 2. Moment-thrust interaction generated by RCBEAM compared with ACI 318-77.

#### RESULTS OF EXPLOSIVE TESTS

The geometry of the A, B and C test articles is shown in Fig. 3. A is deemed to be a direct shear failure in which "the principal steel reinforcing bars were necked down and broken at the wall supports. An inspection of the reinforcement bars near the center of the roof slab did not indicate the occurrence of significant flexure" [10]. B exhibits flexural damage which is characterized by hinges at the supports and center span. The latter is diffused over a distance of a foot or so,

rather than being concentrated. C exhibits characteristics of combined flexure and shear damage. Failure occurred for a distance of about 6 ft (2m) along one edge of the roof where principal steel reinforcing bars were necked down and broken. Numerous bars were also necked down and broken at midspan. Concrete cover from the center was spalled and the concrete confined between the steel was cracked such that gaps extended through the slab [6].

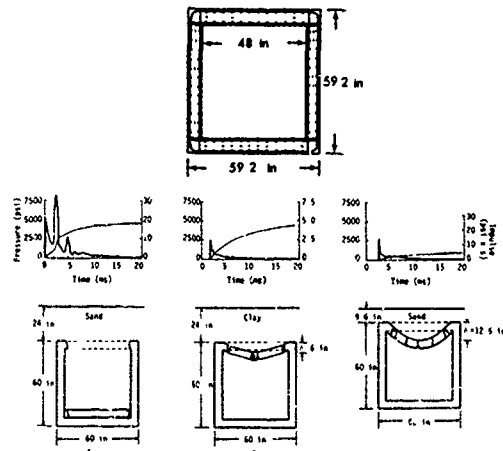


Fig. 3. Surface pressure- and impulse-time histories, geometry and damage modes for A, B and C.

#### RESULTS OF TEST SIMULATIONS

Two basic RCBEAM models were used to simulate A, B and C. These were (1) a model of the roof slab only, with a built-in support representing the rest of the structure and (2) a model of the entire structure. Discretization is illustrated in Fig. 4 in terms of nodal points. Three Gauss points along the length of each element and five layers through the thickness were used. Analysis options included Newmark's method ( $\beta = 1/4$ ), stiffness matrix update at every time step ( $\Delta t = 2.5 \mu s$ ) and equilibrium iteration within each time step (maximum number of iterations equal ten, although three at most were

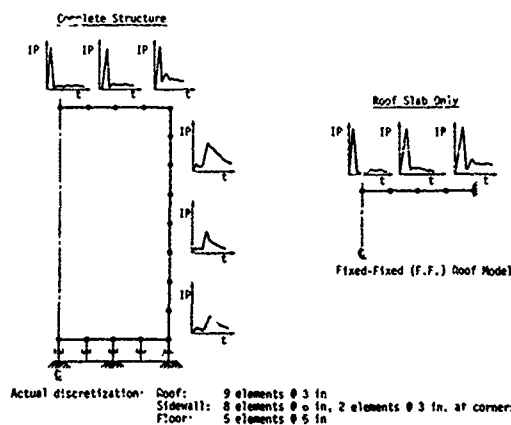


Fig. 4. RCBEAM models for A, B and C.

required). Measured interface pressure-time histories are used as input.

#### Model A

The deformed shape of the roof slab, modeled as a fixed-fixed beam, is shown in Fig. 5 at selected instants of time. At  $t \leq 2.5$  ms, the deformed shape suggests the formation of a shear hinge at the support, while the remainder of the span exhibits little deformation. At  $t = 2.5$  ms, the shear strain in the element adjacent to the support is 0.18 radians, which we interpret as failure.

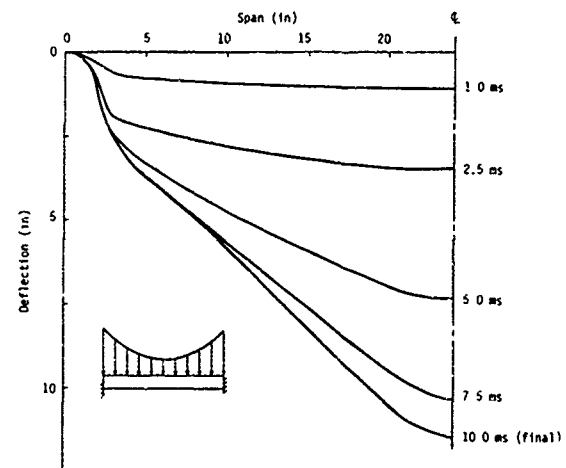


Fig. 5. Deflected shapes calculated for A using fixed-fixed roof model.

#### Model B

The deformed shape of the roof slab, modeled as a fixed-fixed beam is shown in Fig. 6a at selected instants of time. The same tendency for the center span to remain flat at early times is observed here that was observed in A. However, the magnitude of shear rotation at the support is 0.015 radians at  $t \leq 2.5$  ms in the B simulation, which is much less than in A. The final deflection at midspan is reached at about  $t = 15$  ms, by which time a hinge has formed at midspan. The calculated final deflection is about 7 inches (18 cm), slightly greater than the observed deflection of 6 inches (15 cm). The deformed shape of the roof slab, modeled as part of a continuous structure, is shown in Fig. 6b. The complete structure appears stiffer, as is illustrated in the midspan velocity-time history, Fig. 7; the initial peak velocity is about 620 in/s (1575 cm/s) for the fixed-fixed model and about 530 in/s (1346 cm/s) for the complete structure model.

#### Model C

The deformed shape of the roof slab, modeled as a fixed-fixed beam, is shown in Fig. 8a. A moderate degree of shear deformation appears at the support at  $t \leq 5$  ms. At later times, the shear hinge tends to give way to flexural hinges at the support and center span. The maximum calculated

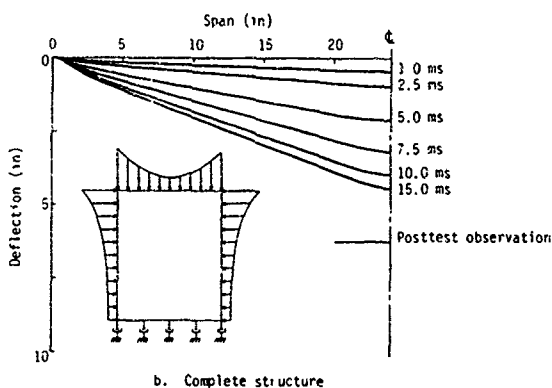
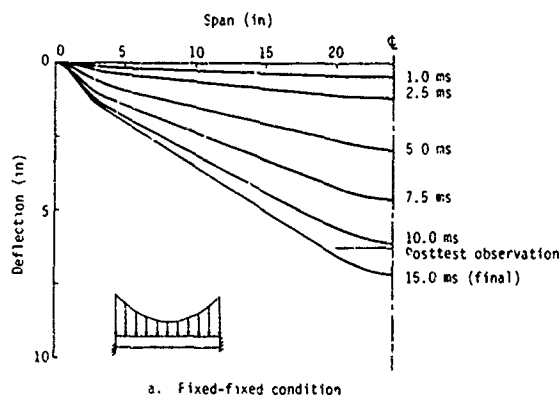


Fig. 6. Deflected shapes calculated for models of B.

deflection of 15 inches (38 cm) is slightly greater than the measured deflection of about 12.5 inches (32 cm). The deformed shape of the roof slab, modeled as a complete structure, is illustrated in Fig. 8b. Stronger evidence of a shear hinge appears at the sidewall and a flexural hinge appears at midspan. In contrast to the fixed-fixed model of the roof slab and in contrast to the data, the

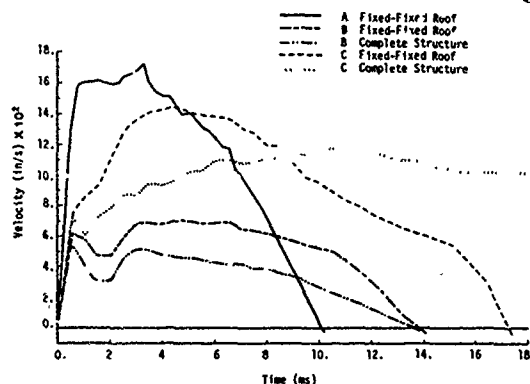


Fig. 7. Velocity-time histories calculated at midspan of roof for A, B and C.

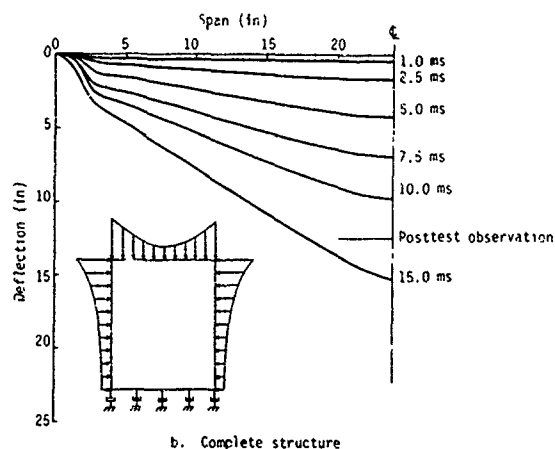
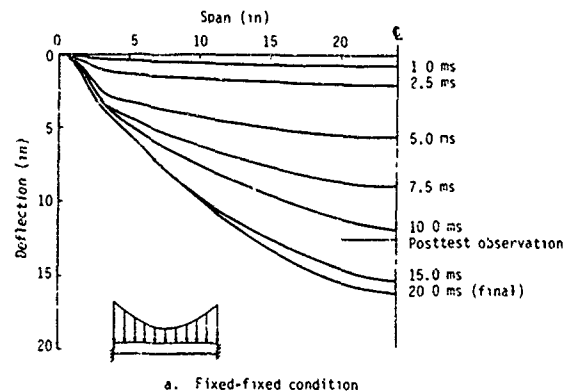


Fig. 8. Deflected shapes calculated for models of C.

complete structure model predicts complete collapse. The velocity-time histories at midspan obtained from the different models are shown in Fig. 7. In the complete structure model, a small decrease in midspan velocity follows the initial peak, signifying that the initial load does not exhaust the flexural resistance of the member, as was observed in the B complete structure simulation. At later times, however, the accumulation of sidewall pressure helps to collapse the structure with fully developed three-hinge mechanisms at the wall and roof. This is manifested as large lateral deflection at the top of the sidewall. In contrast, the maximum flexural resistance of the same roof slab modeled as a fixed-fixed beam is reached by the initial load, with the result that the peak velocity is much higher. In the fixed-fixed model, there are no sidewall pressures to be transmitted as in-plane compression, so that enough membrane tension eventually develops to reduce the velocity to zero.

The time history of shear strain at the support of the C roof slab modeled as a fixed-fixed beam is shown in Fig. 9. Inelasticity in shear is indicated because  $\gamma$  exceeds 0.02 radians and the peak value of shear strain is intermediate to the values for A and B; this signifies an intermediate

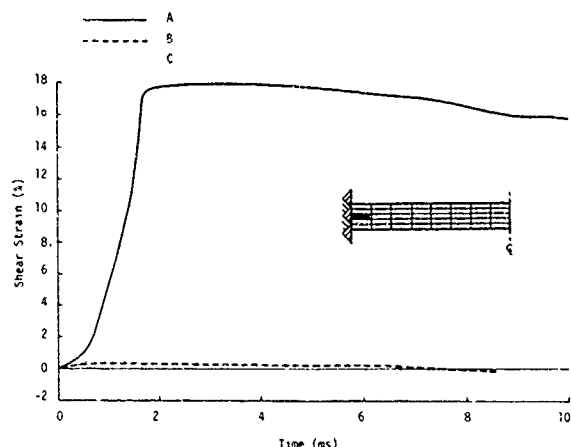


Fig. 9. Calculated shear strain-time histories at third Gauss point for A, B and C.

or mixed mode of damage, which includes both shear and flexure.

#### Shear Failure

In the past year, box structures with an  $L/d$  of 7 were dynamically tested in an effort to investigate the nature of shear failure. As the  $L/d$  is decreased, the ratio of bending to shear resistance decreases to the point where shear failure dominates. The anticipated shear failure mode is depicted in Fig. 10a. This mode is characterized by the formation of hinges near the support, while the center span remains relatively flat. The configuration details are also given in Fig. 10b.

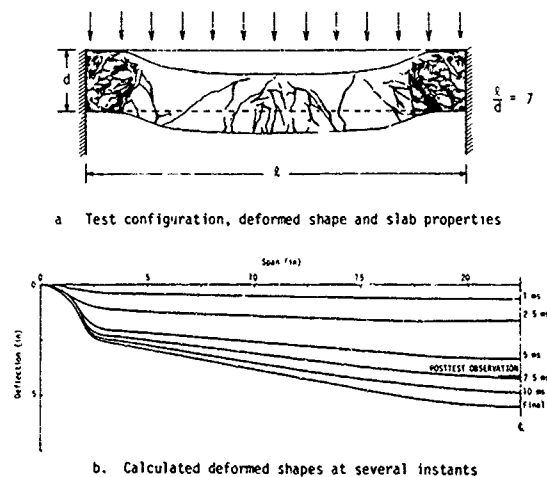


Fig. 10. Results of analysis of shear deformation mode.

Since this test series was designed to investigate shear failure modes, the number of interface pressure measurements was reduced. This prevented the formulation of an adequate interface pressure distribution, as was assumed in the previous section. Therefore, a simplified soil-structure

interaction model, assuming a bilinear soil, of the form

$$\sigma_{IP}(x,t) = \sigma_{ff}(t) - (\rho c) \{v_s(x,t) - v_{ff}(t)\}$$

where

$\sigma_{IP}$  = interface pressure

$\sigma_{ff}$ ,  $v_{ff}$  = free-field stress and velocity obtained from a one-dimensional analysis

$$\rho c = \begin{cases} \rho c_2 & \text{for } v_s \leq v_{ff} \\ \rho c_u & \text{for } v_s > v_{ff} \end{cases}$$

$$\rho c =$$

$$\rho c_u \text{ for } v_s > v_{ff}$$

$\rho$  = soil density

$c_2, c_u$  = loading and unloading soil wavespeeds

$v_s$  = structure velocity

was employed. This simplified model was evaluated for box structures in [16]. The surface pressure employed to drive the free-field analysis was derived from the measured blast pressures. The calculated deformed shapes are presented in Fig. 10b. Note the characteristics associated with shear failure are observed in the presented deformed shapes. Overall, agreement with the available test data is good.

#### CONCLUSIONS

On the basis of favorable comparison with previously published beam-column data, we conclude that the elastic, ideally plastic model of concrete properties in conjunction with the finite element model presented above is adequate to represent behavior under combined flexure and thrust; we except from this conclusion the "dome" effect observed in restrained slabs which we have not yet investigated with this model. It appears that the present assumption of a constant shear rotation through the thickness of the element is adequate. Modes of damage observed in dynamic tests include shear, flexure and combined shear-flexure; these are simulated by the analytic method described above. Modes of damage are recognized in the calculation by tail-tale features of the midspan velocity-time histories and the shear strain at the supports. A dip in the velocity-time history following the initial peak indicates flexure is dominant; monotonic increase to peak velocity indicates shear is dominant. Also, the shear strain at the support at early times (present calculation, 2.5 ms) is about 50-100 times higher when shear damage will ultimately dominate than when flexural damage will dominate. We find that the predominant damage mode is determined by early-time impulse (0-2.5 ms for the present roof slab, in which soil-structure interaction limits the duration of the load). In agreement with Symonds [15] and with test data, we find that high early-time impulse leads to shear failure.

# REFERENCES

- [1] Bathe, K. J., "A Finite Element Program for Automatic Dynamic Incremental Nonlinear Analysis," Rep. 82448-1, Acoustics and Vibration Laboratory, Mech. Eng. Dept., MIT, Cambridge, MA, September 1975, Revised December 1978.
- [2] Bathe, K. J. and Wilson, E. L., Numerical Methods in Finite Element Analysis, Prentice-Hall, Englewood Cliffs, NJ, 1976, p. 322.
- [3] Bresler, B. and Pister, K. S., "Strength of Concrete Under Combined Stress," J. Am. Conc. Inst., 55, No. 3, September 1958, pp. 321-345.
- [4] American Concrete Institute, "Building Requirements for Reinforced Concrete," ACI Standard 318-77, 1977.
- [5] Buykozturk, D., "Nonlinear Analysis of Reinforced Concrete Structures," J. Comp. and Strcts., 7, February 1977.
- [6] Getchell, J. V. and Kiger, S. A., "Vulnerability of Shallow-Buried Flat-Roof Structures," Tech. Rep. SL-80-7, Report 2, USAEWES, October 1980.
- [7] Haltiwanger, J. D., Hall, W. J. and Newmark, N. M., "Approximate Methods for the Vulnerability Analysis of Structures Subject to the Effects of Nuclear Blast," N. M. Newmark Consulting Engineering Services Report No. U-275-76, June 15, 1976.
- [8] Hand, F. R., Pecknold, D. A. and Schnobrich, W. C., "Nonlinear Layered Analysis of RC/Plates and Shells," J. Struct. Div., ASCE, 99, ST7, July 1973, pp. 1491-1503.
- [9] Isenberg, J., "Inelasticity and Fracture in Concrete," Ph.D. Dissertation, Univ. of Cambridge, October 1966.
- [10] Kiger, S. A. and Getchell, J. V., "Vulnerability of Shallow-Buried Flat-Roof Structures," Tech. Rep. S1-80-7, Report 1, USAWES, September 1980.
- [11] Kupfer, H. H., Hilsdorf, H. K. and Rüschi, H., "Behavior of Concrete Under Biaxial Stresses," J. Am. Conc. Inst., 66, No. 8, August 1969.
- [12] Levine, H. S., "Development of a Two-Surface Plastic and Microcracking Model for Plain Concrete," AFML-TR-(to be determined), Final Report on Contract F29601-81-C-0028 by Weidlinger Associates, December 1981.
- [13] Meredith, D. and Witmer, E. A., "A Nonlinear Theory of General Thin Walled Beams," J. Comp. Strcts., 13, 1981, pp. 3-9.
- [14] Pifko, A. B., Levine, H. S. and Armen, H., "PLANS--A Finite Element Program for Nonlinear Analysis of Structures," I, Theoretical Manual,

NASA CR-2568, November 1975.

- [15] Symonds, P. S., "Plastic Shear Deformations in Dynamic Load Problems," Engineering Plasticity, eds., Heyman, J. and Leckie, F. R., C.U.P., 1968, pp. 647-664.
- [16] Wong, F. S., "Transfer Function Analysis for Statistical Survival/Vulnerability Assessment of Protective Structures," AFML-TR-82-32, II, October 1982.

## NOTATION

The following symbols are employed in this paper:

- A = cross-sectional area
- $f \geq$  yield criteria
- $f_c$  = uniaxial compressive concrete strength
- $f_t$  = uniaxial tensile concrete strength
- $f_y$  = uniaxial steel yield strength
- H = strain-hardening constant for steel
- h = beam thickness
- I.P. = interface pressure at soil-structure interface
- M = bending moment
- $\bar{Y}$  = axial thrust
- t = time
- $\Delta$  = increment
- $\delta$  = transverse displacement
- $\epsilon_{xx}$  = axial strain
- $\epsilon_{xy}, \gamma$  = shear deformation
- $\rho$  = volume ratio of steel to concrete
- $\sigma, \sigma_{xx}$  = axial stress
- $\tau, \sigma_{xy}$  = shear stress
- $\sigma_0$  = effective yield strength
- $\sigma_1, \sigma_2$  = principal stresses

Subscripts: p = plastic

## ACKNOWLEDGMENT

Support for this research, provided by the Defense Nuclear Agency, is gratefully acknowledged.



A Review of The 1983 Revision of TM 5-855-1 "Fundamentals of Protective Design" (Nonnuclear)

S. A. Kiger and J. P. Balsara

USAE Waterways Experiment Station  
Vicksburg, MS

The current version of the Army TM 5-855-1 dated July 1965 is a reprint of former EM 1110-345-405 dated 1946, and has not been updated since 1946. Because of the large amount of data on such things as penetration, ground shock, and structural response from conventional weapons effects collected since World War II, the manual has become so outdated it is of limited usefulness. A revised version of the manual is needed so that contractors can be furnished specific guidelines for the design of protective structures.

The Structural Mechanics Division of the Structures Laboratory at the Waterways Experiment Station (WES) has been tasked by the Office, Chief of Engineers (OCE) to revise the manual. Dr. Jimmy P. Balsara, WES, is the Project Officer in charge of the revision, and Mr. Dick White, OCE, is the Program Monitor. Writing the revised manual has been a joint effort among the WES, the Army Chemical and Nuclear Agency (CNA) (Chapter 7), and the USAE Division, Huntsville, (HND) (Chapter 12).

The purpose of this paper is to make potential users of the manual aware of the revision, aware of its scope, and indicate how and when it can be obtained. Because of space limitations only a few selected graphs from the manual will be presented as an indication of its content.

Comparison of the Table of Contents in Table 1 with the contents of the original shows that the revised manual is completely new with very little material retained from the original version. For example, the revised manual places a great deal more emphasis on structural response

calculations, structural design, and includes a chapter on calculating instructure shock levels.

The chapters on weapon characteristics and penetration have been updated to include modern weapons with high slenderness ratios, about 8, while retaining some of the older weapons with slenderness ratios of about 3 (see Table 2).

Table 2. Characteristics of Typical Bombs

	Class	W(lb)	D(in.)	L(in.)	C/W%	(L/D)	$\frac{4W}{\pi D^2}$	
	GP	250	260	11	36	48	3.3	2.7
	*GP	250	280	9	75	35	8.3	4.4
	GP	500	520	14	45	51	3.2	3.4
	*GP	500	550	11	90	35	8.2	5.8
	*GP	750	830	18	85	44	5.3	4.1
	GP	1000	1020	19	53	54	2.8	3.6
	*GP	1000	1000	14	120	42	8.6	6.5
	GP	2000	2090	23	70	53	3.0	5.0
	*GP	2000	2000	18	150	48	8.3	7.9
	*GP	3000	3000	24	180	63	7.5	6.6
	SAP	500	510	12	49	30	3.9	4.5
	SAP	1000	1000	15	67	31	3.8	5.6
	SAP	2000	2040	19	66	27	3.5	7.2
	AP	1000	1080	12	58	5	4.8	9.5
	AP	1600	1590	14	67	15	4.8	10.3

Figure 1 summarizes the available data, and gives a best estimate, on projectile penetration into rock. This type of presentation provides the user with both a best estimate of a bomb penetration, from which ground shock calculations can be made, and an indication of the uncertainty associated with the penetration estimate.

A summary of data on penetration of mild steel fragments into massive concrete is presented in Figure 2. Like much of the material in this revision, the curves in Figure 2 were obtained from another Government publication, in this case from Picatinny Arsenal Technical Report 4903, dated December 1975.

To calculate loads on a buried structure protected by a concrete burster layer, the depth of penetration and a coupling factor must be known. The coupling factor, for an airburst or penetrations up to fully contained in soil or concrete, can be obtained from Figure 3. This coupling

Table 1. Table of Contents

CHAPTER 1	INTRODUCTION
CHAPTER 2	WEAPON CHARACTERISTIC
CHAPTER 3	BLAST EFFECTS
CHAPTER 4	PENETRATION
CHAPTER 5	CRATERING AND GROUND SHOCK
CHAPTER 6	FRAGMENTATION
CHAPTER 7	FIRE, INCENDIARY, AND CHEMICAL AGENTS
CHAPTER 8	LOADS ON STRUCTURES
CHAPTER 9	MECHANICS OF STRUCTURAL ELEMENTS
CHAPTER 10	DYNAMIC RESPONSE OF STRUCTURES
CHAPTER 11	IN-STRUCTURE SHOCK AND
CHAPTER 12	AUXILIARY SYSTEMS

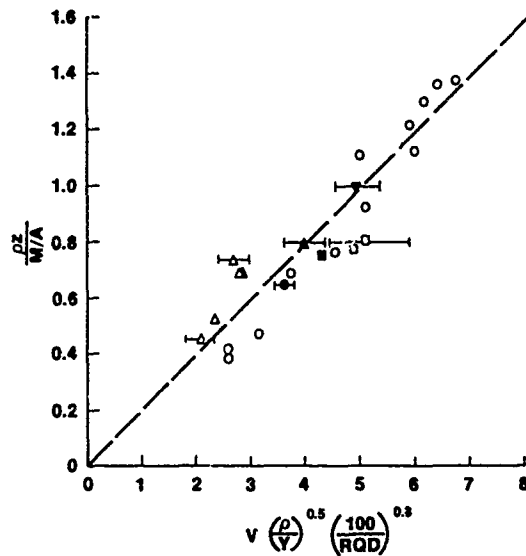


Figure 1. Empirical analysis of projectile penetration in rock

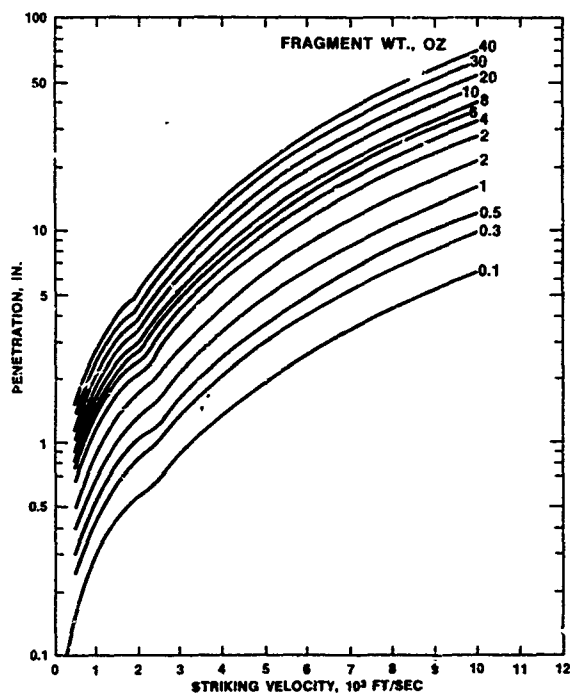


Figure 2. Penetration of mild steel fragments into massive concrete

factor can be used, along with equations presented in the manual to compute free-field stress, impulse, velocity, acceleration, or displacement. The free-field stress can then be used along with Figure 4 to estimate an "equivalent" uniform load on a buried structure. This equivalent load is

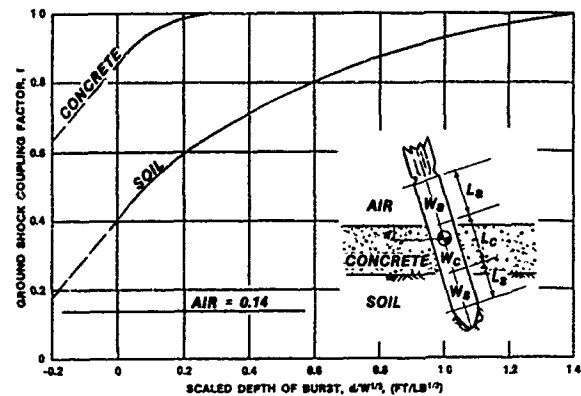


Figure 3. Ground shock coupling factor as a function of scaled depth of burst for air, soil and concrete

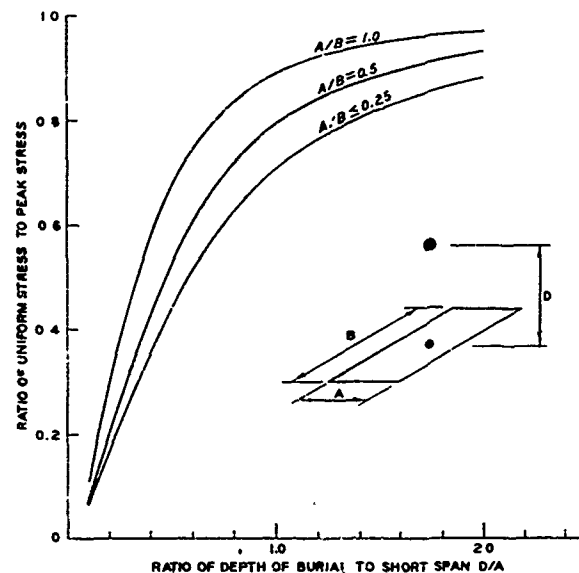


Figure 4. Equivalent uniform load in flexure

that uniform load that will produce the same structural deflection as a  $P_0(R/r)^3$  load distribution; where  $P_0$  is the peak free-field stress,  $R$  is the perpendicular distance between the center of gravity (c.g.) of the bomb and center of the structure roof (or wall), and  $r$  is the slant distance between the bomb c.g. and a point on the structure roof. This concept of an equivalent load for use in simplified structural response calculations has been recently developed at WES and has been carefully checked against available data. It is very useful for design calculations since a worst case burst position, i.e. near the center of the roof or wall, is normally assumed.

For aboveground or surface flush structures, cratering may be more of a threat than structural response. Crater dimensions in reinforced or unreinforced concrete can be estimated from Figure 5.

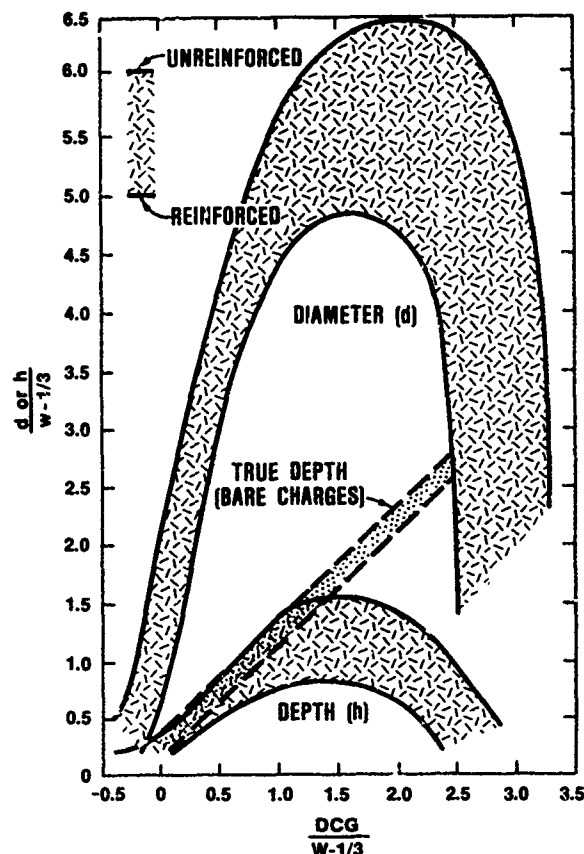


Figure 5. Estimated crater dimensions in massive concrete

As the final example, free-field acceleration, velocity, and displacement can be used along with the procedures given in Chapter 11 (Instructure Shock) to calculate instructure shock spectra. These shock spectra can be used in conjunction with the fragility curves shown in Figure 6 to design shock isolation devices for critical elements within the protective structure.

The examples shown in Figures 1 through 6 are a representative sampling from the revised manual. References that these figures were taken from, or data they were based on, are given in the manual. The intent here is to show that the manual attempts to present the most recent developments in the design of structures to resist conventional weapons effects. Also, the manual is complete in the sense that, given a conventional weapon threat, an aboveground or buried structure can be completely designed to defeat the threat using only the information contained in the manual.

The current status of the revised manual is that a first draft has been reviewed by a large sample of the technical community. Comments returned from this review have been incorporated into the manual and a final draft, reflecting the review comments, will be ready in May 1983. A

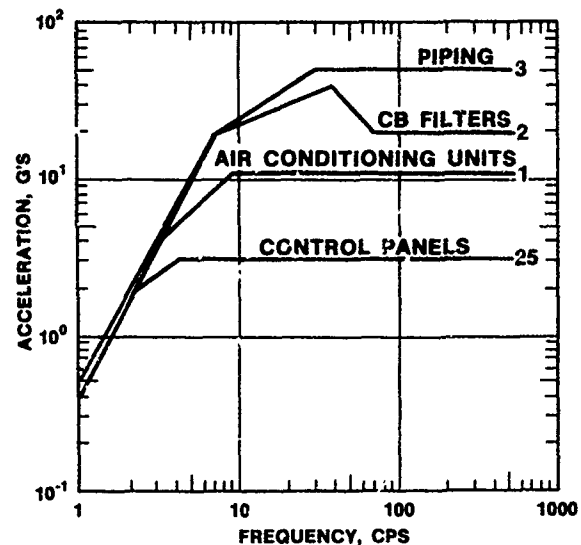


Figure 6. Equipment shock resistance

camera-ready copy will be furnished the HND in July 1983 for publication. Copies of the manual will be available from the Government Printing Office or through other standard channels for obtaining Department of the Army technical manuals.

AD P001764

## MODEL LAW FOR CONCRETE STRUCTURES UNDER DYNAMIC LOADS

Dr. H. R. Fuehrer, P.E.

Martin Marietta Orlando Aerospace

## ABSTRACT

Most physical systems can be studied by means of scale models whose behavior relates in a known way to that of a prototype. The problem is to write a valid scaling law that accurately displays this similarity. This requires a certain familiarity with the physical concepts involved in the system. Certain laws of similitude must be observed to ensure that model test data can be applied to the prototype. The following sections provide insight and rationale for use in defining a scaling law for reinforced concrete under dynamic loads.

## INTRODUCTION

A model law for high explosive can be determined by a consideration of equations describing motion of a shocked fluid.<sup>1</sup> In essence, this law states that pressure and other properties of the shock wave will be unchanged if the length and time scales are unchanged by the same factor,  $n$ , as the dimensions of the explosive loading source. That is:

$$L_p = n L_m \quad (1)$$

$$T_p = n T_m \quad (2)$$

$$W_p = n^3 W_m \quad (3)$$

where  $L$ ,  $T$ , and  $W$  are dimensional symbols for length, time, and charge weight, respectively, and the subscript  $p$  denotes the prototype and  $m$  designates the model. Since the density scale must therefore be unity, the scaling factor for the mass of the explosive is:

$$M_p = n^3 M_m \quad (4)$$

where  $M$  is the dimensional symbol for mass.

The same geometric scaling which governs the shock transmission process also provides proper modeling for structural response to pressures generated during the blast process. Motion of the structure due to applied blast loads is expressed by Newton's second law  $F = M(T)^{-2} L$  and, therefore, it follows that:

$$F_p = n^2 F_m \quad (5)$$

where  $F$  is the dimensional symbol for force. In those structures where the mode of action is primarily in the plastic range, similitude between the model and prototype system will be realized when the dimensionless ratio of the external work to the stored strain energy is the same for both systems. For example, the kinetic energy, associated with the momentum of the structure imparted by the blast loads will be numerically equal to the strain or potential energy of the structure for both the model and prototype systems.

The kinetic energy may be expressed in terms of the impulse,  $I$ , of the blast loads or,  $KE = I^2/2M$ , where the impulse is a function of force and time. Therefore,

$$(KE)_p = n^3 (KE)_m \quad (6)$$

The potential energy of a structure is numerically equal to the area under its resistance-deflection curve and, therefore, is a function of force and length. Thus,

$$(PE)_p = n^3 (PE)_m \quad (7)$$

On the basis of the above relationships, it may be concluded that the similarity principle which applies to the blast loads applies equally well to the modeling of the structural response to the transient forces generated by the interaction of the blast waves and the structure. Certain limitations do appear in the application of these scaling laws. The rate of strain associated with the structural response of the prototype may differ significantly from that of the model. This variation will depend upon the model size and differences in the materials used in both systems. Another limitation imposed by the scaling laws is due to the invariance of gravitational forces which will distort the scaling effects for parameters such as dead loads. In blast-resistant design, the effects of dead loads and other such physical parameters will usually be small in comparison to the effects of the blast environment and, therefore, may usually be neglected in the model design.

With the ideal scale for length, time, and force (or mass), it is possible to derive an ideal scale for each specific parameter involved in the

model design. These scales are obtained by proceeding in the manner employed above for kinetic and potential energies. A summary of the more pertinent quantities and their ideal scales is given in Table I. From Table I, the concept of scaled distances,  $Z$ , is introduced.

$$Z = L_p / W_p^{1/3} \quad (8)$$

#### PRESSURE LOADING DUE TO BLAST

Pressure exerted on the front face of a structure is approximately twice that measured in free earth. Pressure on a massive target in earth can be represented by the following expression<sup>2, 3, 4</sup>, provided normal explosives are used at depths of the order of  $2W^{1/3}$  and at distances from the target between  $2W^{1/3}$  and  $15W^{1/3}$  (all measured in feet):

$$P_r = 2 k E Z^{-3} \quad (9)$$

where  $P_r$  is the reflected pressure and the scaled distance is:

$$Z = r / w^{1/3} \quad (10)$$

For the scale law selected,  $Z$ , and hence the reflected pressure, will be the same for the prototype and the model, i.e.,

$$Z = r_p / w_p^{1/3} = r_m / (n^3 w_m)^{1/3} \quad (11)$$

$$= r_m / w_m^{1/3} \quad (12)$$

Using scaled charge weights, i.e.,

$$w_p = n^3 w_m \quad (13)$$

at scaled distances:

$$r_p = n r_m \quad (14)$$

the resultant stress levels in the beam will be the same.

Consider the case where an 8-pound charge is detonated 6 feet from a scale model structure. The scaled distance is:

$$Z = 6 / (8)^{1/3} = 3. \quad (15)$$

The prototype will experience the same stress and strains as the model if a 1000-pound charge is detonated 30 feet from it; i.e.,

$$Z = 30 / (1000)^{1/3} = 3. \quad (16)$$

#### SMALL-DEFLECTION ELASTIC RESPONSE

Scaling law for the elastic response of structures to blast loading has been considered by H.N. Brown<sup>5</sup> on the basis of the general, small-deflection equations of elastic motion of solids. He demonstrates that the same geometrical scaling which governs the shock transmission process also

TABLE I  
Computations of Ideal Scales

Quantity	Symbol	Typical Units	Ideal Scale
Length	$l$	ft	$l_p / l_m = n$
Depth	$d$	ft	$d_p / d_m = n$
Area	$A$	ft <sup>2</sup>	$A_p / A_m = n^2$
Mass	$M$	lb-sec <sup>2</sup> /ft	$M_p / M_m = n^3$
Area of rein	$A_s^1$	in <sup>2</sup>	$(A_s^1)_p / (A_s^1)_m = n^2$
Area of rein per foot	$A_s$	in	$(A_s)_p / (A_s)_m = n$
Unit resistance	$w$	lb/in <sup>2</sup>	$w_p / w_m = 1$
Total resistance	$R$	lb	$R_p / R_m = n^2$
Weapon	$W$	lb	$W_p / W_m = n^3$
Distance	$r$	ft	$r_p / r_m = n$
Scaled distance	$Z$	ft/lb <sup>1/3</sup>	$Z_p / Z_m = 1$
Total impulse	$I$	lb-ms	$I_p / I_m = n^3$
Unit impulse	$i$	lb-ms/in	$i_p / i_m = n$
Scaled impulse	$\bar{i}$	lb-ms/in <sup>2</sup> - lb <sup>1/3</sup>	$\bar{i}_p / \bar{i}_m = 1$
Pressure	$p$	lb/in <sup>2</sup>	$p_p / p_m = 1$
Kinetic energy	$KE$	ft-lb	$KE_p / KE_m = n^3$
Density	$\rho$	lb-sec <sup>2</sup> /ft <sup>4</sup>	$\rho_p / \rho_m = 1$
Elastic modulus	$E$	lb/in <sup>2</sup>	$E_p / E_m = 1$
Deflection	$\delta$	in	$\delta_p / \delta_m = n$
Moment	$M$	ft-lb	$M_p / M_m = n^3$
Moment per foot	$\bar{M}$	lb	$\bar{M}_p / \bar{M}_m = n^2$
Shear	$V$	lb	$V_p / V_m = n^2$
Shear per foot	$\bar{V}$	lb/ft	$\bar{V}_p / \bar{V}_m = n$
Stress	$\sigma$	lb/in <sup>2</sup>	$\sigma_p / \sigma_m = 1$
Strain	$\epsilon$	-	$\epsilon_p / \epsilon_m = 1$
Velocity	$V$	ft/sec	$V_p / V_m = 1$
Time	$t$	sec	$t_p / t_m = n$
Moment of inertia	$I$	in <sup>4</sup>	$I_p / I_m = n^4$
Frequency	$f$	cycles/sec	$f_p / f_m = 1/n$
Acceleration	$a$	ft/sec <sup>2</sup>	$a_p / a_m = 1/n$

provides the proper modeling for structural response to the transient pressures generated during the blast process. In his analysis, the effect of gravity and strain-rate effects are assumed negligible.

Perhaps the geometrical modeling indicated above can best be described by imagining the following experiment. An energy source of characteristic dimension  $W^{1/3}$  is initiated a distance  $R$  from an elastic structure of characteristic dimension  $L$ , producing a transient pressure loading on the structure of amplitude  $P$  and duration  $\tau$ , causing the structure to respond in its natural modes of vibration with periods  $T_1, T_2, \dots, T_n, \dots$ , and corresponding displacement amplitudes  $X_1,$

$X_2, \dots, X_n, \dots$ . Strain-time histories of the structure's response are characterized by the periods  $T_n$  and corresponding strain amplitudes  $e_n$ . Let the entire experiment be scaled geometrically by a scale factor  $n$ , making the energy source of characteristic dimension  $nW^{1/3}$  and locating the structure of characteristic dimension  $nL$  at a distance  $nR$  from the source. Then, geometrical modeling predicts that the pressure loading on the structure will be similar in form to that obtained in the first experiment, with amplitude  $P$  and duration  $n\tau$ , and that the structural response will also be similar in character, with the natural periods being  $nT_1, nT_2, \dots, nT_n, \dots$ , displacement amplitudes  $nX_1, nX_2, \dots, nX_n, \dots$ , and strain amplitudes  $e_1, e_2, \dots, e_n, \dots$ .

#### LARGE-DEFLECTION ELASTIC RESPONSE

The equations of motion of elastic solids from which Brown deduced the geometrical scaling laws are valid for infinitesimal strains and displacements. An excellent discussion of the limitations of the infinitesimal theory is given by Novozhilov<sup>6</sup>, who points out that this theory is quite inadequate for the description of such problems as transverse deflections of slender beams or thin plates, or of buckling problems. Both Novozhilov<sup>6</sup> and Murnaghan<sup>7</sup> generate the equations for large deformations of elastic bodies, making no assumptions which restrict the magnitudes of elongations, displacements, or angles of rotation.

The equations of motion, neglecting body forces, are:

$$\begin{aligned}\frac{\partial \sigma_{xx}}{\partial x} + \frac{\partial \sigma_{xy}}{\partial y} + \frac{\partial \sigma_{xz}}{\partial z} &= \rho \frac{\partial^2 x}{\partial t^2} \\ \frac{\partial \sigma_{yx}}{\partial x} + \frac{\partial \sigma_{yy}}{\partial y} + \frac{\partial \sigma_{yz}}{\partial z} &= \rho \frac{\partial^2 y}{\partial t^2} \\ \frac{\partial \sigma_{zx}}{\partial x} + \frac{\partial \sigma_{zy}}{\partial y} + \frac{\partial \sigma_{zz}}{\partial z} &= \rho \frac{\partial^2 z}{\partial t^2}\end{aligned}\quad (17)$$

At first glance, these equations appear identical in form to the usual infinitesimal equations of elastic motion. They are in reality much more complex because the Cartesian coordinates  $x, y, z$  are the coordinates of points in the body after deformation, and the stress-components,  $\sigma_{ij}$ , and density,  $\rho$ , also refer to these Lagrangian coordinates. We can write:

$$\begin{aligned}x &= x_0 + u(x_0, y_0, z_0, t) \\ y &= y_0 + v(x_0, y_0, z_0, t) \\ z &= z_0 + w(x_0, y_0, z_0, t)\end{aligned}\quad (18)$$

where  $x_0, y_0, z_0$  are the Cartesian coordinates of points in the body before deformation;  $t$  is time; and  $u, v, w$  are the displacement components. (In the infinitesimal theory, no distinction is made between differentiation with respect to  $x_0$ ,

$y_0, z_0$ ; in considering forces acting on elements of the body, one neglects changes in position and direction due to deformation.)

Equations describing the stress-strain law and the boundary conditions must also be satisfied in addition to Equations (17). Novozhilov shows that the stress-strain law which corresponds to Hooke's law for infinitesimal theory is:

$$\sigma_{x_0 x_0}^* = A_2 + A_1 \epsilon_{x_0 x_0} + A_0 \left( \epsilon_{x_0 x_0}^2 + \frac{1}{4} \epsilon_{x_0 y_0}^2 + \frac{1}{4} \epsilon_{x_0 z_0}^2 \right) \quad (19)$$

for normal stresses, and:

$$\sigma_{x_0 y_0}^* = \frac{1}{2} \left\{ A_1 \epsilon_{x_0 y_0} + A_0 \left[ (\epsilon_{x_0 x_0} + \epsilon_{y_0 y_0}) \epsilon_{x_0 y_0} + \frac{1}{2} \epsilon_{x_0 z_0} \epsilon_{y_0 z_0} \right] \right\} \quad (20)$$

for shear stresses. In these two equations, the  $\epsilon_{ij}$  are strain-components, the  $\sigma_{ij}^*$  are stress-components referred to the dimensions of an element before deformation, and the  $A_i$  are elastic constants. Strain-rate effects are assumed negligible in this stress-strain law. The boundary conditions merely require that the pressures acting on the external surfaces of the body must equal the appropriate normal stress-components at the surfaces.

Let us now apply geometrical scaling to the response to blast loading of a body whose motion is governed by the preceding equations. If we let  $x^1 = nx, x_0^1 = nx_0, t^1 = nt$  then, from Equation (18) displacements are given by  $u^1 = nu$ , etc. Strains in the scaled structure are unchanged because they are functions of the first derivatives of the displacements with respect to the space coordinates which are not altered by the scaling. We can see from Equations (19) and (20) that the stress-components must then be unchanged if the elastic constants of the material are unchanged. The equations of motion become:

$$\frac{\partial \sigma_{xx}^1}{\partial x^1} + \frac{\partial \sigma_{xy}^1}{\partial y^1} + \frac{\partial \sigma_{xz}^1}{\partial z^1} = \rho \frac{\partial^2 x^1}{\partial t^2}; \text{ etc.} \quad (21)$$

These reduce to:

$$\frac{1}{n} \left[ \frac{\partial \sigma_{xx}}{\partial x} + \frac{\partial \sigma_{xy}}{\partial y} + \frac{\partial \sigma_{xz}}{\partial z} \right] = \rho \frac{n}{n^2} \frac{\partial^2 x}{\partial t^2}; \text{ etc.} \quad (22)$$

which are identical to Equations (17).

The boundary conditions are also unchanged by the scaling, with the scaled blast pressures properly matching the boundary tractions at each scaled instant of time.

We predict, from the above analysis, that the geometrical modeling which applies to the small-deflection response of elastic structures to blast

loading describes the large-deflection response equally well. The same restrictions, i.e., neglect of gravity and strain-rate effects, must hold.

#### ELASTIC-PLASTIC RESPONSE

If one wishes to scale damage to structures from blast loading, he must investigate the scaling of the structural response for strains exceeding the elastic limit, i.e., for plastic strains. One should, if possible, establish such scaling by considering the most general equations of elastic-plastic structural response. The equations of motion, Equations (17), and the associated boundary conditions, generated for elastic structures, apply equally well to large deflections of structures undergoing plastic deformation. However, the stress-strain law for plastic structures differs from the elastic stress-strain law. In elastic bodies, the stress-components are unique functions of the strain-components, and deformations are therefore reversible. In plastic bodies, the stresses associated with increasing strains are usually different from those associated with decreasing strains, and the deformations are irreversible. One must assess the effect of the differences in the stress-strain law of scaling or response.

Novozhilov has shown that, when the strains are monotonically increasing in magnitude, the stress-strain laws for finite elastic deformations, given by Equations (19) and (20), include Hencky's theory for elastic-plastic bodies as a special case. Therefore, geometrical scaling of response to blast loading will apply to the deformation of elastic-plastic bodies while the strains are increasing in magnitude. This scaling then assures one that the limiting strain magnitudes for the initial stress-strain law are the same in the fullscale and model structures. When the strains start decreasing in magnitude, the initial stress-strain law is no longer valid. But relations of the same form as Equations (19) and (20), with different values for the constants  $A_i$  determined by the maximum strains, will then hold. This new stress-strain law for the geometrically-scaled model should be identical to that for the original structure because the maximum strains and the physical properties which determine the  $A_i$  are identical. One can therefore conclude that the entire elastic-plastic response of a structure to blast loading should be scaled geometrically in the manner previously described for elastic structures.

#### CASE STUDIES

To confirm the model law discussed above, several authors have performed a series of experiments on the response of structures. One of the earlier works by Baker, et. al.<sup>8</sup> involved using spherical Pentolite explosive charges detonated in air and slender cantilever beams. Forty-nine elastic response tests were conducted and agreement of the vibration frequencies with values calculated from a simplified form of the equations of motion from which response scaling was predicted, and scaling of strain amplitudes in the predicted manner assume validity of scaling of response of elastic structures.

Thirty-one permanent deformation tests were conducted also. The model law predicts that, for properly scaled experiments, the deformed shapes of the beam should be similar and the permanent deformation should scale in proportion to the linear scale factor,  $n$ . Results showed the data could be described by a single functional relationship between scaled parameters, as is predicted by the model law, for the range of charges, i.e., approximately 1/8- to 8-pounds of explosive.

More recently, Dobbs and Cohen<sup>9</sup> conducted a series of full- and scale-tests of reinforced concrete structures. Models ranged from full scale employing 7500 pounds of TNT to one-tenth scale. For the smaller scale models, specific attention was paid to modeling of reinforcement. Most wire sizes are available to scale the physical characteristics of the reinforcement bars for one-tenth scale models and larger. However, because steel wire is cold drawn and, therefore, brittle, adjustment of the wire's properties to simulate the mechanical properties of the hot-rolled reinforcement of the larger models is accomplished by annealing the wire. The annealing process required after cold drawing reduces the wire's strength but appreciably increases its ductility. For example, cold drawn wire whose ultimate strength is 250,000 psi will have an elongation of less than 2 percent while the same wire which is annealed will have a strength in the order of 90,000 to 120,000 psi and elongations of 7 to 9 percent (8-inch test specimen). To select the correct wire and the specific heating and cooling times required in the annealing process, the mechanical properties of the reinforcement in the prototype structure should first be known. If the prototype has not yet been constructed, the properties of its reinforcement will be unknown. In this case it should be assumed that the steel used in the prototype structure will have the minimum mechanical properties specified by the governing code and then the model can be designed accordingly.

Results of their work indicated that damage sustained by the models and full-scale structures is similar if each is tested in a similar manner, thereby establishing that model tests may be used to evaluate the structural response of large, full-scale, reinforced concrete structures to high explosive detonations.

Whether a problem is related to design or research, concern is always focused on working (service) load behavior or ultimate (failure) load behavior or both.

Little, et. al.<sup>10</sup>, in their studies have shown that structural models can be used effectively for studying a wide range of problems in each of these areas. While knowledge of reliability is by no means complete, and in some instances appears to be negative, techniques and materials are available today to apply with confidence to many problems. For these situations where a linear elastic solution is deemed to be satisfactory, structural models seem limited only by possible complexity and cost of fabrication, loading, and instrumentation.

One exception to this position is for model studies of massive structures which are intended to reveal prototype self-weight behavior. In that situation, the similitude requirements usually are incompatible with the available model materials and desired model scale.

In those cases, such as shrinkage, creep, stiffness, and strength, where behavior cannot be considered to be linearly elastic, an additional limiting parameter comes into play. This parameter, and it is a key one, is correct simulation of the concrete and reinforcement materials. This material simulation difficulty is what places creep and shrinkage model studies beyond today's state of the art. Affecting the whole range of stiffness and strength situations are two material property items that have not yet been satisfactorily resolved. Improper simulation of prototype deformed reinforcing bar surfaces and of prototype concrete strength characteristics can lead to unreliable model test results. For instance, reasonable cracking simulation has only been established for scale reductions down to the order of 1/4. It may be possible to use smaller models if more sophisticated crack detection methods are used, but this is yet to be established. Similarly, bond failures cannot be modeled.

Above all, it must be emphasized that confidence levels can best be established by comparing similar structures or members of different size. As indicated by several of the case studies, reinforced mortar models reasonably predict the deflections, mode of failure load for beams, columns, plates, and shells.

#### THE MODEL LAW

The model law, when referred to in connection with physical tests, is a term generally applied to a set of rules derived through dimensional reasoning by which the results of a set of properly designed experiments can be extended to larger or smaller scales of phenomena. The term "scale effect" has been somewhat loosely applied to any deviations from the model law that arise in an analysis of experimental results derived from models. The presence of such effects, which apparently do occur in some classes of experiments, greatly complicates the analysis of the results. Fortunately, no such effects have been detected in explosion testing and the model law results can be extended with an accuracy as good as that of the original measurements.

If it is assumed that the velocity of propagation of the effect of an explosion only depends on the stress and not on such quantities as the rate of deformation, the effect of an increase in all dimensions of the experiment by the length scale factor  $n$  results in an increase of the time of propagation to an equivalent point by the same factor  $n$ . It is then possible to make a table (Table I) in which any quantity such as pressure, impulse, velocity, etc. is represented by its dimensional components of mass  $M$ , length  $L$ , and time  $T$ , and to arrive at an expression for the relative magnitude of this quantity in the new system

which is expanded in length scale by the factor  $n$ . In present experiments,  $W^{1/3}$ , the cube root of the weight of explosive charge in pounds, has been selected as being a length characteristic of the scale of the experiment. This may seem dimensionally misleading but it merely means that a unit of length whose cube is proportional to the weight or volume of the charge has been chosen for reference. Then if an experiment is performed with a charge-weight of  $W_1$  lb and it is required to know the effects that would occur with a charge-weight of  $W_2$  lb, the scale ratio  $n = (W_2/W_1)^{1/3}$ , and at the distance  $r$ , the magnitudes of the quantities in question can be determined from the original measurements at distance  $r$  multiplied by the factors given in the table. The model law, of course, tells nothing of the manner in which the quantities vary with distance, but states only that if the effect is of magnitude  $E_1$  in the experimental system at a distance  $r$  from the charge, then in the new system the effect will be  $-n^p E_1$  at a distance  $nr$  from the charge,  $p$  depending on the quantity in question and being given in Table I.

An example that illustrates the use of the model law is the comparison of the peak pressures produced by the explosion of 1 and 1,000 pounds of the same explosive. It is assumed that experiment has shown that at a distance of 4 feet from the 1-pound charge the peak pressure is 80 psi. The length-scale ratio between the two cases is  $(1,000/1)^{1/3} = 10$ , and Table I shows that the scale factor for pressure is 1; consequently, at a distance of 40 feet ( $=nr$ ) from the 1,000-pound charge the peak pressure is again 80 psi. This is equivalent to the statement that if  $r/W^{1/3}$  is the same for the two cases then pressure is the same.

A comparison of the impulse per unit area,  $I$ , for these two weights of explosive at the scaled distances 4 and 40 feet is made in the same way, except that, from Table I the scale factor for impulse per unit area is  $n$  ( $=10$ ). Thus, if the impulse per unit area from a 1-pound charge at 4 feet is 0.2 psi-sec, then at 40 feet from a 1000-pound charge the impulse per unit area is 2 psi-sec. This comes about by virtue of the fact that, although the peak pressures at these scaled distances are the same, the time scale of the phenomena is multiplied by 10, the scale factor, so that the duration of the pressure is increased tenfold. The impulse, being proportional to the product of pressure and time, must then be increased by a factor of 10 as indicated.

It will be noted that most of the experimentally determined quantities can be represented by empirical equations which have as coefficients a constant and various combinations of the parameters  $W$ ,  $p$ ,  $r$ , and  $Z$ .

The manner in which these parameters enter into the empirical equations can be determined very simply by equating the dimensions on both sides of the equality sign. The variables can be determined from physical considerations, but the manner in which they enter the equation may be determined by dimensional considerations. The form of these

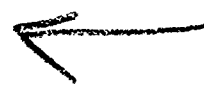


equations, of course, needs to be tested against the experimental data in each case and correlated with the first order of approximation. The test for correctness consists in determining to what extent the dimensionless constant in the equations really is constant for widely varying values of the parameters.

This section would be incomplete without a specific mention of target and damage relations to the model law. One of the primary objectives of any program is, of course, to determine the accuracy of the model law as applied to target damage. The chief cause of the initial uncertainty is the fact that there are certain things in nature that do not scale, the chief offender being the effect of gravity. By changes of density of component materials, efforts to overcome this defect can be made, but it is not easy to find structural materials of comparable strength and with greatly different densities. Consequently, if gravity is a controlling factor in an experiment, modification of the model law must be made. It has been found experimentally, as had been inferred but not proved, that the impulsive forces involved in the damaging of a massive structure are very large compared to gravity forces, so that essentially no deviation from the model law was detected. The conclusion is that the structural dimensions can be scaled, at least over a factor of 5, and probably 10, without encountering significant deviation from the law as far as explosive damage is concerned.

#### REFERENCES

- 1 Cole, R.H., "Underwater Explosions," Princeton University Press, Princeton, New Jersey, 1948.
- 2 Soper, W.G., "Scale Modeling," Science and Technology, No. 62, February 1967.
- 3 Redwood, M., "Mechanical Waveguides," Pergamon Press, New York, 1960.
- 4 Rinehart, J., and Pearson, J., "Explosive Working of Metals," The MacMillan Company, New York, 1963.
- 5 Brown, H.N., "Effect of Scaling on the Interaction between Shock Waves and Elastic Structures," Ballistics Research Laboratories Report No. 1011, Appendix I, March, 1957.
- 6 Novozhilov, V.V., "Foundations of Non-Linear Theory of Elasticity," translated from the first Russian edition, Graylock Press, Rochester, New York, 1953.
- 7 Murnaghan, F.D., "Finite Deformation of an Elastic Solid," John Wiley & Sons, Inc., New York, 1951.
- 8 Baker, W.E., et. al., "Laws for Large Elastic Response Subjected to Blast Loading," Ballistic Research Laboratories, Report No. 1080, Aberdeen Proving Grounds, Maryland, December, 1958.
- 9 Dobbs, N., and Cohen, E., "Model Techniques and Response Tests of Reinforced Concrete Structures Subjected to Blast Loads," ACI Publication No. 24, American Concrete Institute, Detroit, Michigan, 1970.
- 10 Little, W., et. al., "Accuracy of Structural Models," ACI Publication No. 24, American Concrete Institute, Detroit, Michigan, 1970.



AD P001765

# RESPONSE OF DRAG-SENSITIVE, STEEL-FRAMED, INDUSTRIAL-TYPE STRUCTURES TO AIRBLAST LOADING

H. S. Levine and E. M. Raney

Weidlinger Associates  
Menlo Park, California

## ABSTRACT

Simple one-dimensional predictions of the response of drag-sensitive, steel-framed structures have greatly overestimated the peak deflections using the measured dynamic pressures, and commonly accepted drag coefficients for the beam, column and truss components. Renewed interest in the behavior of these structures has initiated recent efforts to explain the reasons for the discrepancies between analysis and experiment. Complicating the analysis is that the structures are covered with siding and roofing of a frangible type.

A three-dimensional structural dynamics code was used to predict the response of the framed structures to drag loading. The objective was to see whether discrepancies might be due to oversimplification of the structural model and applied load distribution. The results of a series of three-dimensional calculations and the comparison of response with test data are reported in the paper.

## INTRODUCTION

In 1955, four industrial-type structures were subjected to drag and diffraction loading from a nuclear airblast. Simple one-dimensional predictions of the response of the two drag-sensitive structures greatly overestimated the peak deflections using the measured dynamic pressure, and commonly accepted drag coefficients for the beam, column and truss components [1]. Renewed interest in the behavior of these structures under long duration impulsive loading has initiated recent efforts and reawakened interest in explanations of the reasons for the discrepancies between analysis and the experiments.

A complication in the analysis of these steel frame structures is that they are covered with siding and roofing of a frangible type. The determination of the importance of the impulse imparted to the structure and the disturbance of the flow field around the structures, as a result of the blowing away of the frangible material, introduces two difficult phenomena into the determination of the actual loading on the steel frame and roof truss. The relative shielding of downstream portions of the structure as a result of the presence of upstream structural components, i.e., the determination of the exposed drag area, is another question that has to be resolved.

To support the renewed interest in drag-sensitive structures, full-scale and one-third scale models of the drag structure were included in a recent high explosive event. Loads, strains and deflections for both structures were monitored in an effort to obtain the actual force-time histories acting on these industrial targets and evaluate the relative importance of the drag loads, and the effects of the frangible siding and roofing on the impulse imparted to these structures.

For the current investigation, a three-dimensional structural dynamics code, Weidlinger Associates' version of DYCAST [2], was used to predict the response of the framed structures to the drag loading. The objective was to see whether the discrepancies in the experimental and theoretical predictions might be due to the oversimplification of the structural model and the applied load distribution. During the course of the investigation, it was found necessary to develop a simplified procedure for the analysis of combined bending and St. Venant torsion of open beam cross sections stressed into the inelastic regime.

Three-dimensional discretizations of the structure were developed and used to evaluate the drag coefficients necessary for analysis of this structure. Actual measured free-field dynamic pressures of the nuclear event and a uniform distribution of these pressures with some shielding in the roof truss was assumed.

The 3-D model was then used for pretest predictions of the response of test structures in a High Explosive (HE) Event and to determine where they should be placed. Posttest analysis of the HE Event using the actual measured pressures on the frames from surviving gauges and an assumed uniform spatial interpolation over the height of the frame overpredicted the peak response. Several variations of the measured pressure loadings with height were then assumed in an effort to correlate measured loads and predicted responses. The results of this series of calculations and the comparison of response with test data are reported in the paper and possible explanations for the differences are discussed.

## DESCRIPTION OF STRUCTURE AND ASSUMPTIONS

A drag structure is defined to be one that is relatively open with only beams, columns or trusses (members with small frontal areas) exposed to the blast. Each of these members receives a small

impulsive loading as the blast engulfs the structure and then it is exposed to drag from the wind accompanying the blast. The duration of the diffraction loading (including the impulse accumulated by any frangible siding) is assumed to be small compared to the drag loading and can presumably be neglected. Since drag targets are sensitive to increases in dynamic pressure duration, and hence weapon yield, it is interesting to determine whether the response of realistic structures can be predicted using appropriate drag coefficients and dynamic pressures for weapons and structures of interest. Structures having a degree of complication representative of a large class of targets were selected to be tested. Uncertainties anticipated were due to the magnitude and duration of the impulse spikes from diffraction loading of the beams and breakaway of the siding, determination of the areas over which drag forces are assumed to act, the extent to which some members shielded others, the proper magnitude of the drag coefficients for different member shapes, and disturbances in the flow field as a result of the presence of the frangible siding and roofing.

The drag structure actually chosen to be tested is typical of small industrial buildings. It was assumed to be representative of interior bays of a multiple-bay building. A picture of one-half of the structure, symmetric with respect to the centerline, and some typical dimensions, is shown in Fig. 1. Certain spans were reduced to keep the cost of the structures as low as practicable. The roof structure was a Warren truss with the center 20 feet left out to ensure the probability of failure in the columns rather than the roof. Columns in the end frames were reduced in size relative to the center frame in proportion to their contributory drag areas so that all three frames would deflect nearly equally in a manner typical of a long, multiple-bay building. Design specifications are outlined in [1]. The columns were designed with hinged base connections and the roofing

and siding were specified to be light, frangible material incapable of withstanding the blast forces.

An average yield strength of 40 ksi for the steel beams and columns based upon experimental data was used in the analysis of the nuclear event. Average ultimate strength was 60 ksi. The frangible material was chosen to be a corrugated asbestos cement board. Pulldown tests were performed on the structure to determine the natural period and load-deflection relationship for the structure. The computed fundamental period was 480 ms, whereas the measured periods from a shake test and the blast record were 530 and 650 ms, respectively.

#### METHOD OF ANALYSIS

Single-degree-of-freedom representations of the structure were used in [1] to predict its response to the blast loading. Only the drag loading was considered important, and impulse imparted to the structure through diffraction was neglected. A thorough series of posttest calculations indicated that an unrealistically low drag coefficient of 0.5 to 0.75 was required to match the test deflections. This compared to commonly used values of 1.5 to 2.0 for individual members. To obtain this coefficient, it was assumed that the rear roof truss members were fully shielded from the airstream. An exposed drag area of almost 60,000 in<sup>2</sup>/bay was used for the analysis.

The purpose of the current investigation was to determine whether oversimplification of the structural model was responsible for the low drag coefficients. A more realistic finite element model of the structure, including a realistic distribution of drag loading, higher order deformation modes, and local inelastic response might lead to a better prediction of the response with conventional drag coefficients. The DYCAST code [2] was chosen to predict the behavior of the structure. DYCAST is a finite element transient analysis

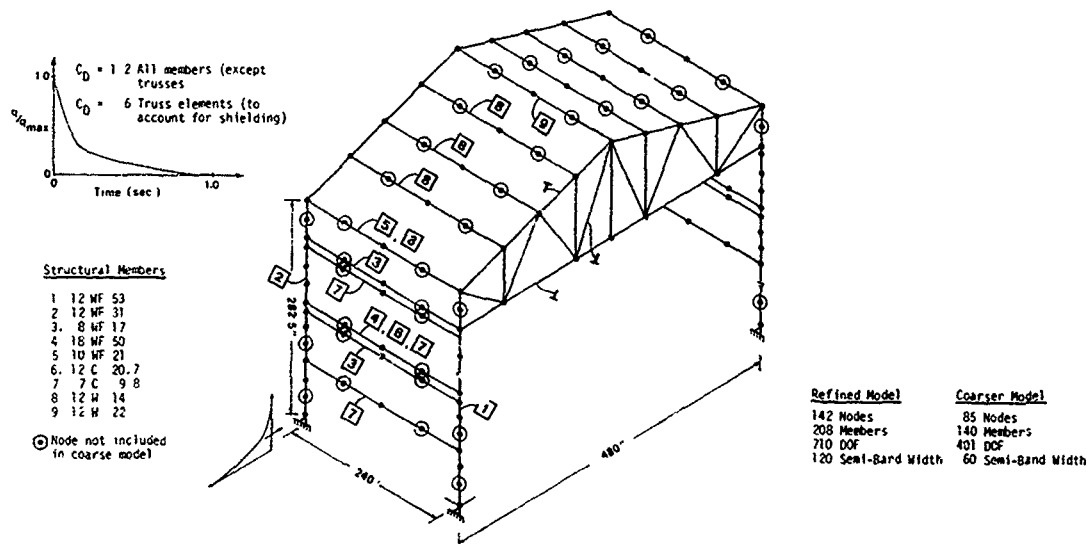


Fig. 1. Discretization of drag-sensitive structure.

code that has the capability for predicting the material and geometric nonlinear response of three-dimensional structures. Geometric nonlinearity is included using an updated Lagrangian approach. The procedure is valid for small strains and large rotations. Material nonlinearity can be represented by a variety of yield criteria and hardening rules. For the current series of problems, the Von Mises Yield Criterion was chosen. Both Prager-Ziegler kinematic linear strain-hardening [3,4] and ideally plastic material models were used. A subincrementation procedure was used to ensure the calculated response was reasonably close to the specified hardening.

The beam element in DYCAST has a wide variety of cross-sectional shapes available and capability for eccentric attachment points. The I, channel, and T-section shapes were used for the members in the current analysis. Stress recovery is monitored at Gauss points in each leg of the cross section. As a result, the cross section of the beams can progressively plasticize as the load increases. A linear variation of plastic strain between beam nodes is also assumed. Because of deficiencies in the treatment of St. Venant torsion for open sections, and the possibility, based upon test observation, that torsional deformation of the beams might be significant energy absorbers, a new procedure was developed and implemented to represent the inelastic St. Venant torsion of open sections (see Appendix A). Restrained warping and local cross-sectional deformations were not included in the analysis. The Newmark-Beta implicit time integration technique was used in all calculations.

#### STUDY OF OVERALL DRAG COEFFICIENT

The actual structural discretization of the steel frame is shown in Fig. 1. A refined model and a coarser model were used for the initial analyses. For the initial part of the study, the dynamic pressure from the nuclear test (shown normalized in Fig. 1) was applied simultaneously to all nodes. This was multiplied by the drag coefficient and the respective beam areas normal to the flow to get the drag forces, i.e.,

$$F = C_D q A \quad (1)$$

where  $q$  is the dynamic pressure,  $C_D$  the drag coefficient and  $A$  the beam area normal to the flow. Although each member could have its own drag coefficient specified, the same drag coefficient was used for all members. The initial objective was to simulate the one-degree-of-freedom analysis to determine whether the detailed structural modeling and local inelastic response, i.e., local energy absorption, would explain the low drag coefficients required in [1]. The same shielding in the roof was also assumed and diffraction effects were neglected.

A comparison of the measured and theoretical deflections at the lower chord column connection are shown in Fig. 2. Two different drag coefficients and yield stresses of 40 and 50 ksi were assumed. The 50 ksi yield strength was chosen to

investigate what effect variations in strength resulting from high strain rate loading in the material might have on the peak deflections. We see from the data that an overall drag coefficient of 1.0-1.2 based upon the assumed shielding and steel strength will give good correlation with the peak deflections. Although this is an improvement over the single-degree-of-freedom model, it does not explain fully the differences between the individual member drag coefficients [5,6] and the overall drag coefficient for the structure. Calculations for the refined and coarser model showed negligible differences in response. Consequently, the coarser model was used in all subsequent calculations.

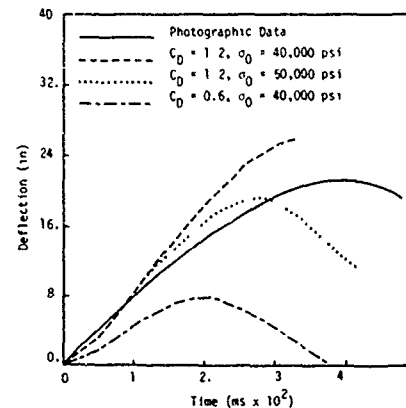


Fig. 2. Comparison of measured and theoretical deflections for framed drag structure at the lower chord-column connection.

#### PRETEST PREDICTION AND POSTTEST CORRELATION WITH HIGH EXPLOSIVE DATA

To help resolve questions about the differences in overall drag coefficient for the structure and those for individual members, and to establish the importance of representing the shielding effects, the structure in Fig. 1 was recently tested in a High Explosive Event. Various beam cross sections were tested in a different event [6] to determine drag coefficients for these members in the unsteady flow fields of interest. Again, the range of 1.5-2 for the drag coefficients of individual members was found to be reasonable.

In Fig. 3 elevation deflection profiles are shown for the center frame subjected to the high explosive (HE) dynamic pressure at the anticipated range peak deflections would equal the nuclear response. The failure mechanism consists of a plastic hinge forming at the lower column-chord connection of the columns to the roof truss. This is the type of failure mode observed in the nuclear tests and in previous calculations. The calculation had to be terminated after the section became fully plastic because of a singularity, and hence a decomposition error, in the Cholesky scheme for the effective stiffness matrix used in the implicit solution technique. Changing the hardening rule to linear strain hardening did not significantly improve the situation. It is hypothesized that

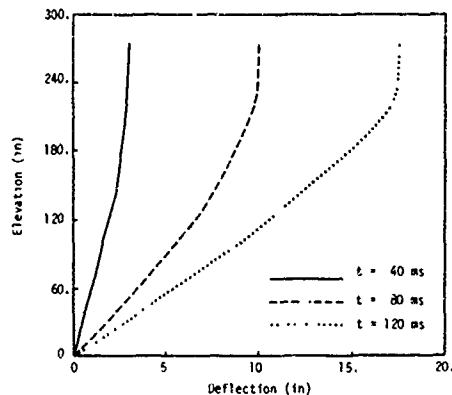


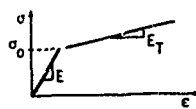
Fig. 3. Deflection profiles of center column for steel-frame drag structure subjected to HE dynamic pressures.

use of a much smaller time step (or maybe a switch-over to an explicit scheme for economy) could have allowed the calculation to proceed. This could not be accomplished using the code as then configured so the peak deflection was extrapolated based upon results for lower load levels. Another procedure that could be used is to insert a hinge element with a nonlinear rotational spring at the nodes where a hinge forms. In the actual test, some bolts at the windward, center, chord-to-column connection were torn out. Severe yielding in this region for all columns was observed, including localized buckling of the flanges and localized yielding and buckling of the web.

Actual net pressures measured on the frames during the test were used for posttest response. A suggested spatial distribution for these pressures is shown in Fig. 4. These had to be guessed at because full data recovery was not achieved when some gages were destroyed by impacts from pieces of the frangible siding or electrical malfunctions. The pressures were swept across the structure using the measured airstblast propagation speed based upon time of arrival (1156 ft/s). Free field dynamic pressures were also measured. Linear strain hardening was assumed and Table 1 shows the strengths and properties used in the calculations.

Table 1. Material properties of HE test event simulation

Member Type	$\sigma_0$ (ksi)	$E_T/E$
4F 53	58.5	.004
12 WF 50	44.9	.004
8 WF 17	45.6	.003
18 WF 50	49.2	.003
10 WF 21	43.1	.002
Roof Tees	51.7	.0025
All Others	45.7	.003



as shown in Figs. 5 - 7, is excellent. Use of the dynamic free-field pressures multiplied by the average drag coefficient previously determined also yielded peak deflections of more than 20 inches.

Fig. 4. Assumed pressure distribution for posttest calculations of steel-frame drag structure (HE Event).

In an attempt to reconcile the measured windward and leeward pressures with the actual response, several reasonable variations of the pressures on the columns with structure height were hypothesized to reduce the net horizontal force and reduce deflections to the measured values. These included:

$$\frac{p}{p_0} = (h/h_0)^{1/3} \quad [7] \quad (2)$$

$$\frac{p}{p_0} = \frac{\ln(1+h/h_0)}{\ln 2} \quad [7] \quad (3)$$

$$\frac{p}{p_0} = h/h_0 \quad (4)$$

Use of the measured pressures, as described, resulted in peak displacement of over 20 inches, which significantly overpredicted the peak displacements of 14 inches measured in the test. However, if only the pressures on the front (windward) members are applied (no pressures on roof or leeward members), correlation for peak deflections and strain,

Here  $h_0$  is the reference height on the column at which net pressures were measured (either 198 or 117 inches) and  $p_0$  represents those pressures. All pressures at the base were assumed to be zero and pressures above the measured level were assumed equal to the measured level. Unfortunately, all these different assumptions also resulted in significant overpredictions of the response.

It should also be noted that the frangible siding had still not completely blown away at the end of 80 ms and pictures showed the disturbance of the flow field was quite substantial at this late time for the HE Event. This compares to a positive phase duration of 180 ms for the dynamic pressures.

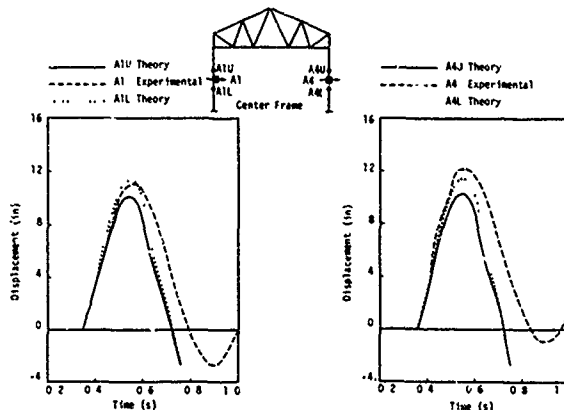


Fig. 5. Comparison of experimental and theoretical deflections for full-scale, steel-frame drag structure at HE Event (front face loading only).

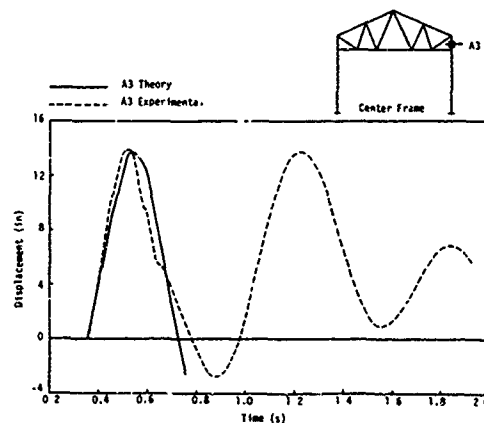


Fig. 6. Comparison of experimental and theoretical deflections for full-scale, steel-frame drag structure at HE Event (front face loading only).

#### CONCLUSIONS

Based upon the calculations presented in this paper, it appears the inclusion of detailed modeling effects is not sufficient to reconcile differences between measured drag coefficients for individual structural elements and those required for overall structural response. Typical structural components have drag coefficients that vary between 1.5 and 2.0, and those required to predict the peak response of industrial-type drag sensitive structures with frangible siding using free field dynamic pressures lie between 0.6 and 1.2. The major questions still to be resolved are those involving

the actual drag loading on the structure and quantifying what effects the frangible siding has on the loads imparted to the structure. With regard to the actual drag loading, the determination of shielding effects of upstream on downstream members and the spatial (especially height) variation of the dynamic pressure forces needs to be better defined. Obviously, inclusion of diffraction-type impulse imparted to the structure by the frangible shielding would increase the already high theoretical loads on the structure. The more significant effect is determination of how the flow field disturbances apparently reduce and change the distribution of the drag force on the frame members. This, of course, is more significant for an HE versus nuclear event because the ratio of duration of flow field disturbance to dynamic pressure duration is higher.

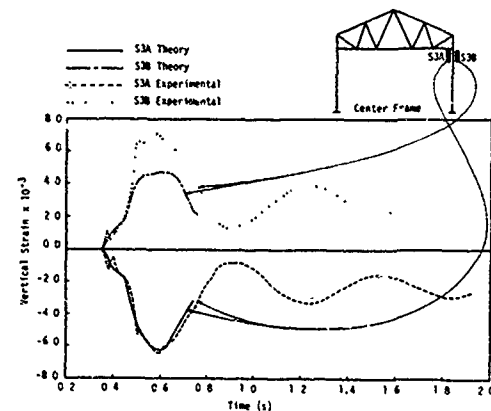


Fig. 7. Comparison of experimental and theoretical strains for full-scale, steel-frame drag structure at HE Event (front face loading only).

#### REFERENCES

- [1] Sinnamon, G.K., Haltiwanger, J.D., Matsuda, F. and Newmark, N.M., "Effect of Positive Phase Length of Blast on Drag and Semidrag Industrial Buildings, Part I," Report No. WT 1129, A.F. Special Weapons Center, Air Research and Development Command, Research Directorate, Structures Div., Kirtland AFB, NM and University of Illinois, Urbana, IL, Dec. 1, 1958.
- [2] Pifko, A.B., Levine, H.S. and Armen, H., Jr., "PLANS--A Finite Element Program for Nonlinear Analysis of Structures, Vol. 1, Theoretical Manual," NASA-CR-2568; also published as Grumman Research Department Report, RE501, 1974.
- [3] Prager, W., "A New Method of Analyzing Stress and Strains in Work-Hardening Plastic Solids," *J. Appl. Mech.* 23, 1956, p. 493.
- [4] Ziegler, H., "A Modification of Prager's Hardening Rule," *Quart. Appl. Math.* 17, No. 1, 1959, p. 55.
- [5] "Wind Forces on Structures," *Trans. ASCE* 126, 1961.

- [6] Binninger, G., Deel, D. and Thomas, C., "Air Blast Drag Loading Experiments, Mighty Mach III," DNA 5719F, Defense Nuclear Agency, Washington, DC, April 1, 1981.
- [7] Hoerner, S.F., "Fluid-Dynamic Drag," Hoerner Fluid Dynamics, Brick Town, NJ, 1965.
- [8] Wang, C.T., "Applied Elasticity," McGraw-Hill Book Co., Inc., New York, NY, 1953.
- [9] Sokolnikoff, I.S., "Mathematical Theory of Elasticity," McGraw-Hill Book Co., Inc., New York, NY, 1956.

#### APPENDIX A

##### SIMPLIFIED PROCEDURE FOR INELASTIC ANALYSIS OF COMBINED BENDING AND ST. VENANT TORSION OF OPEN-WALLED SECTIONS

Open-walled beam sections may be represented by combinations of relatively narrow rectangles properly assembled kinematically to form the cross section of interest, e.g., I, T, Z and channel sections. The elastic torsional rigidities, neglecting cross-sectional warping, of such sections are usually obtained by assuming the concentrations present at fillets, and other local effects, are negligible, and by summing the torsional rigidities of the individual rectangular elements [8]. A similar concept is employed here.

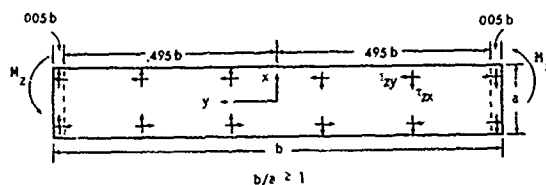


Fig. 8. Geometry of rectangular segment of open beam under St. Venant torsion.

For an elastic rectangle under pure St. Venant torsion without restraints, an elasticity solution for the strains for an arbitrary aspect ratio,  $b/a$ , (see Fig. 8 for rectangular geometry) may be given by the first term of a series solution [9],

$$\gamma_{zy} = \alpha \left[ 2x \frac{8a}{\pi^2} \frac{\cosh \pi y/a}{\cosh \pi b/2a} \sin \frac{\pi x}{a} \right] \quad (A1)$$

$$\gamma_{zx} = -\frac{8a\alpha}{\pi^2} \frac{\sinh \pi y/a}{\cosh \pi b/2a} \cos \frac{\pi x}{a} \quad (A2)$$

where  $\alpha$  is the angle of twist of the cross section per unit length.

This leads to an error in the moment and peak stresses of less than 0.5 percent [9]. We assume the strain variation throughout the cross section does not significantly change upon initiation of inelastic behavior. We also assume the bending

stresses across the thickness of the rectangular segment (flange or web) are constant and note that the shear strains  $\gamma_{zy}$  are antisymmetric with respect to  $x$ , while the shear strains  $\gamma_{zx}$  are symmetric with respect to  $x$ .

The increment of angle of twist per unit length may be obtained by the difference in the increment in rotations at the two ends of the beams divided by the length, i.e.,

$$\Delta\alpha = \frac{\Delta\theta_2 - \Delta\theta_1}{L} \quad (A3)$$

This quantity is calculated at the end of each time or load step from the solution to the structural equations of motion. Increments of strain can then be calculated from eqs. (A1) and (A2). Increments of bending strain at points in the section can be calculated by conventional Bernoulli-Euler relations. Since the bending strains (stresses) are assumed constant through the thickness ( $x$  direction), these strain increments, together with those from eqs. (A1) and (A2), may be used in the plasticity relations to determine stress increments at appropriate integration points. For the Von Mises yield criterion,

$$\sigma_z^2 + 3\tau_{zx}^2 + 3\tau_{zy}^2 = \sigma_0^2 \quad (A4)$$

because of the antisymmetry (symmetry) of the shearing strains and the assumed uniformity of the bending strains about the  $x$  axis, the constitutive relations need only be calculated for the positive  $x$  regime, and then

$$\begin{aligned} \tau_{zy}(-x) &= -\tau_{zy}(x) \\ \tau_{zx}(-x) &= \tau_{zx}(x) \end{aligned} \quad (A5)$$

Resultant torsional moments may be calculated from

$$M_z = \iint (x\tau_{zy} - y\tau_{zx}) dA \quad (A6)$$

This may be simplified using the obvious symmetries to:

$$M_z = 2 \int_{-b/2}^{b/2} \int_0^{a/2} (x\tau_{zy} - y\tau_{zx}) dy dx$$

For the problems considered, two-point Gaussian quadrature was used in the  $x$  direction (stress recovery was needed at only one point because of antisymmetry). In the  $y$  direction, because of the extreme gradient of the shear stresses near the ends in the  $y$  direction, a combination of four-point Gaussian quadrature encompassing 99 percent of the long direction, used with a one-point integration of the shear stresses at .4975b over the remaining 1 percent of the span, gave results with less than 20 percent error for the ultimate torsional moment for the sections of interest. Torsional moments for the entire cross section were obtained by summing the torsional moments of the individual rectangles. For formation of required tangent stiffness matrices, the same integration rules were used, together with the obvious symmetries and antisymmetries.

#### NOTATION

The following symbols are employed in this paper:

- $A$  = cross-sectional area
- $C_D$  = drag coefficient
- $D$  = drag force
- $E$  = Young's modulus
- $E_T$  = linear strain-hardening modulus
- $h$  = height
- $M_z$  = moment about longitudinal axis of beam
- $p$  = pressure
- $q$  = dynamic pressure,  $q = \frac{1}{2}\rho V^2$
- $\alpha$  = angle of twist per unit length
- $\gamma_{zx}, \gamma_{zy}$  = shear strains
- $\theta$  = rotational degree of freedom about longitudinal axis of beam
- $\sigma_0$  = yield stress
- $\sigma_z$  = axial stress in beam (bending + membrane)
- $\tau_{zx}, \tau_{zy}$  = shear stresses

#### ACKNOWLEDGMENT

Support for this research, provided by the Defense Nuclear Agency, is gratefully acknowledged.





AD P001766

RESPONSE OF BURIED CONCRETE STRUCTURES TO BURIED HIGH EXPLOSIVE CHARGES;  
A REVIEW IN SIMILITUDE FORMAT

James S. O'Brasky

Naval Surface Weapons Center  
Weapons Development Branch  
Dahlgren, Virginia

ABSTRACT

The results of some 250 experiments conducted since 1942 are reviewed and analyzed using nondimensional techniques. Data is in chart format for the most significant variables.

DATA SOURCES

The classic experiment on this subject was conducted by the NDRC/NRC in 1943-44. The experiments were conducted in strict nondimensional format and were reported in reference (a). While in hindsight, these experiments can be criticized for a variety of reasons, they represent the most extensive and methodical series done to date. The principal criticisms are that the larger scale targets had inadequate curing time and the data reduction was much less extensive than is desirable. In 1976, Naval Surface Weapons Center conducted a series of full scale experiments on buried charges against buried field fortifications. These experiments lead to the Shoulder Launched Multi-purpose Assault Weapon. In 1977, Orlando Technology, Inc. conducted a series of scale model experiments for Air Force Armament Laboratory (AFAL) to determine the effects of varying thickness-to-span ratios on scaled damage level using structures which were stronger and more heavily reinforced than the NDRC study. Also in 1977, Waterways Experiment Station conducted a series of experiments for the AFAL to evaluate a new explosive. In both sets of experiments, far less damage resulted from a scaled test condition than would have been expected from the NDRC results. Table 1 summarizes these data sources.

Upon examination of the above cited data sources, the writer decided to rederive the nondimensional analysis and to conduct a data reduction incorporating the entire data base.

OBJECTIVE

The objective of this effort was to determine which nondimensional variables were significant and to develop relationships characterizing the data base.

BACKGROUND

The effects of buried high explosive charges on buried concrete structures has been studied in the United States episodically for the last forty years. The initial interest concerned the adequacy of coastal defense structures. This interest was rapidly replaced by an interest in bombing effectiveness against such structures. In recent years, emphasis came to be placed on vulnerability of hardened aircraft shelters to accurately delivered large charges and on field fortifications to small close-in charges. The vulnerability of missile silos/capsules to the detonation of earth penetrating warheads containing nuclear devices is surely of some current interest.

The technical problem was fortunately of such complexity and full scale experiments were so expensive that scale experiments were a necessity.

#### APPROACH

The data sources were reviewed. The nondimensional analysis was derived. The nondimensional variables were computed and subjected to analysis of variance. The significant variables were identified and data plots were developed.

#### RESULTS

Table II contains the variable list for the problem. Table III contains the nondimensional variables resulting from the nondimensional analysis. Figure 1 contains the set-up. Figure 2 contains data plots for the original NRDC data. Figure 3 contains data plots for the 5,000 psi concrete, four edge structure case. Figure 4 contains data plots for the 6000 psi concrete case, two edge structure.

#### REFERENCES

- a. National Research Council, Committee on Fortification Design, Effects of Underground Explosions - Subsurfaces and Target Phenomena, Appendices A thru C, Vol I, Washington, D. C., Interim Report #26, 30 June 1944.
- b. H. R. Fuehrer and J. W. Keeser, Response of Buried Concrete Slabs to Underground Explosions, AFATL-TR-77-115, Orlando Technology, Inc., Orlando, Florida, Feb-Aug 1977.
- c. NRDC, Effects of Impact and Explosion, Summary Technical Report of Division 2, Vol. 2, Washington, D. C., 1946
- d. V. F. DeVost, L. A. Vagnoni, and M. C. Shamblen, Study of Explosive and Assault Weapon Effects on Fighting Bunkers, Naval Surface Weapons Center Technical Report NSWC/WOL TR-75-207, Silver Spring, Maryland, Dec 1975.

TABLE I

<u>Performing</u>	<u>Agency</u> <u>Sponsor</u>	<u># Shots</u>	<u>c (MPa)</u>	<u>Target</u> <u>%R</u>	<u>Type</u>
Princeton Univ. (1977)	NRC-NDRC	104	20.7 - 53.8	0.5(B)	Box
Orlando Tech Inc (1977)	AFAL	23	41.4	2.0(B)	Box
Orlando Tech Inc (1977)	AFAL	20	41.4	2.0(B)C	□
WES (1977)	AFAL	5	27.6	1.2(T)	Box, Tunnel
NSWC	NAVMAT	23	34.5 - 37.9	0.5	Box
Total		175			

TABLE II

"DEFEAT OF BURIED CONCRETE STRUCTURES  
BY  
BURIED HIGH EXPLOSIVES" MODEL

VARIABLES

ENERGY IN EXPLOSIVE	W
DEPTH OF BURIAL	d
RADIUS TO STRUCTURE	R
DENSITY OF SOIL	$\rho$
SOIL STRENGTH	$\sigma$
SOIL DEAD WT.	K
SPAN OF TARGET	l
THICKNESS OF TARGET	t
MIDSPAN DEFLECTION	$\delta$
STRENGTH OF CONCRETE	$\Omega$
REINFORCEMENT STRENGTH	X

TABLE III

DEFEAT OF BURIED CONCRETE STRUCTURE BY BURIED HE CHARGES  
MODEL

$$\left[\frac{g}{d}\right]^{0.9} \left[\frac{d}{l}\right]^{0.7} = f \left[ \left[\frac{R}{d}\right]^{0.4}, \left[\frac{\sigma d^3}{w}\right]^{0.5}, \left[\frac{Kd^4}{w}\right]^{0.6}, \left[\frac{t}{d}\right]^{0.8}, \left[\frac{\Omega d^3}{w}\right]^{0.10}, \left[\frac{d^3 X}{w}\right]^{0.11} \right]$$

NOTE: 8 VARIABLES

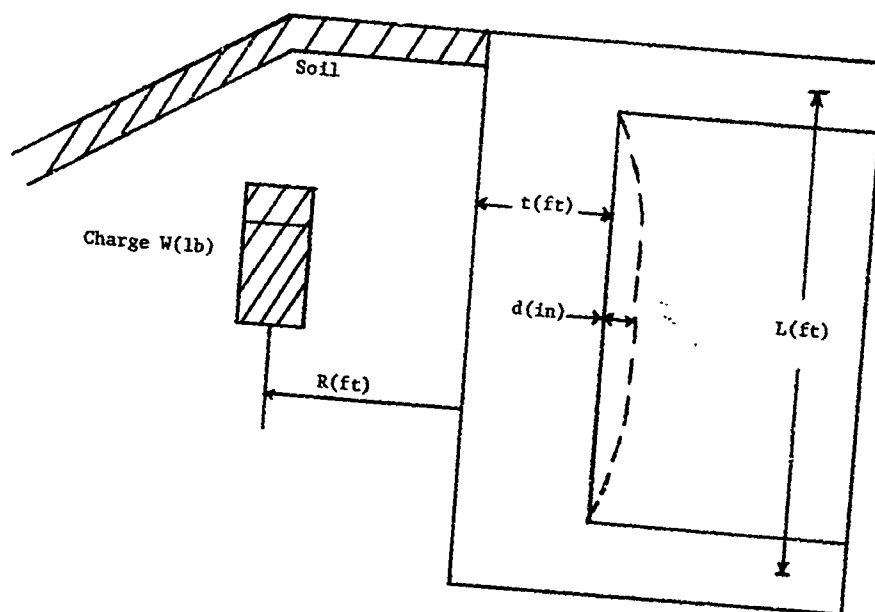


FIGURE 1

Damage to Buried Reinforced Concrete Structures  
4000 psi Concrete  
1.0% Reinforcing, Volume (.25% Tensile)  
2 Edge Support

1. Average Crater Radius
2. Slight Damage (light cracks)  $\frac{d}{L} \geq 0.1$
3. Moderate Damage (cracks, light spall)  $\frac{d}{L} \leq 0.1$   $\frac{d}{L} \leq 0.1$
4. Heavy Damage (spall)  $\frac{d}{L} \leq 0.2$   $\frac{d}{L} \leq 0.2$
5. Breaching  $\frac{d}{L} \leq 0.5$   $\frac{d}{L} \leq 0.5$
6. Tangent Sphere Explosive Radius

Ref: OSD-5405

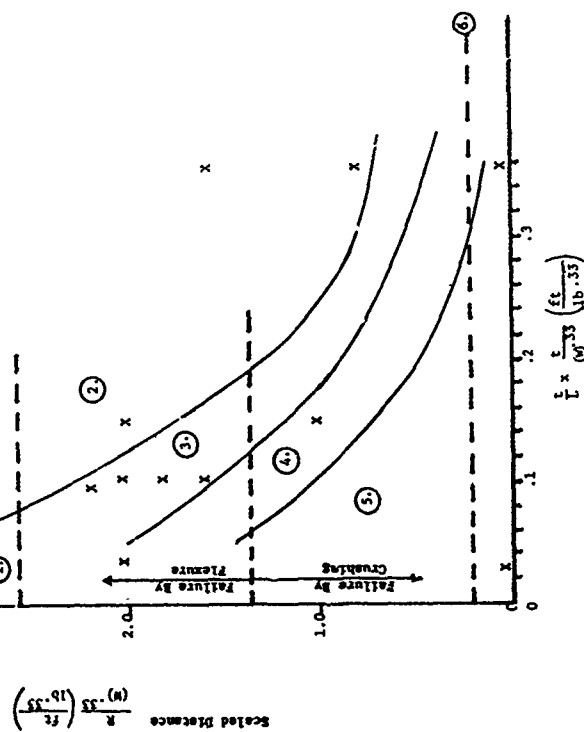


FIGURE 2

Damage to Buried Concrete Structures  
5000-6000 psi Concrete in Sand  
1.5-2% Reinforcing, Volume (.15-1% wt)  
4 Edge Structure

1. Tangent Explosive Sphere
2. Breaching
3. Heavy Damage (spall, heavy cracks)
4. Moderate Damage (light spall, cracks)
5. Slight Damage (cracking)
6. Average Crater Radius

Hc = Moderate Cracking  
Hc = Heavy Cracking  
Sp = Spall  
B = Breach  
S = Slight

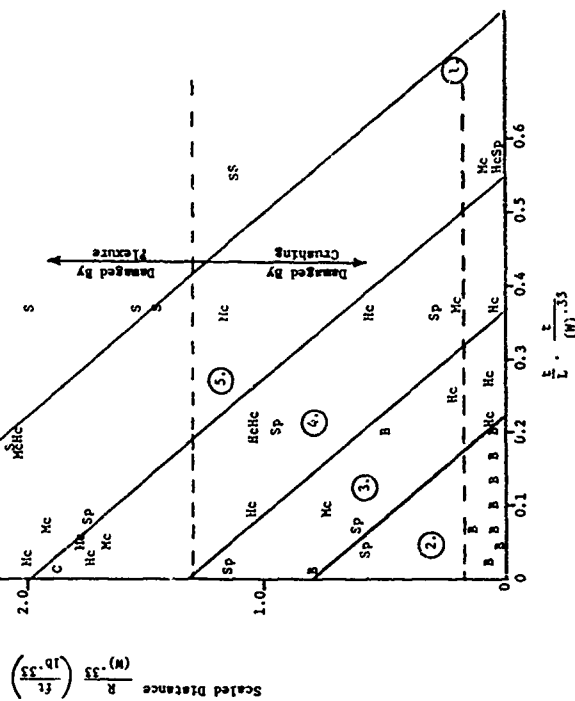


FIGURE 3

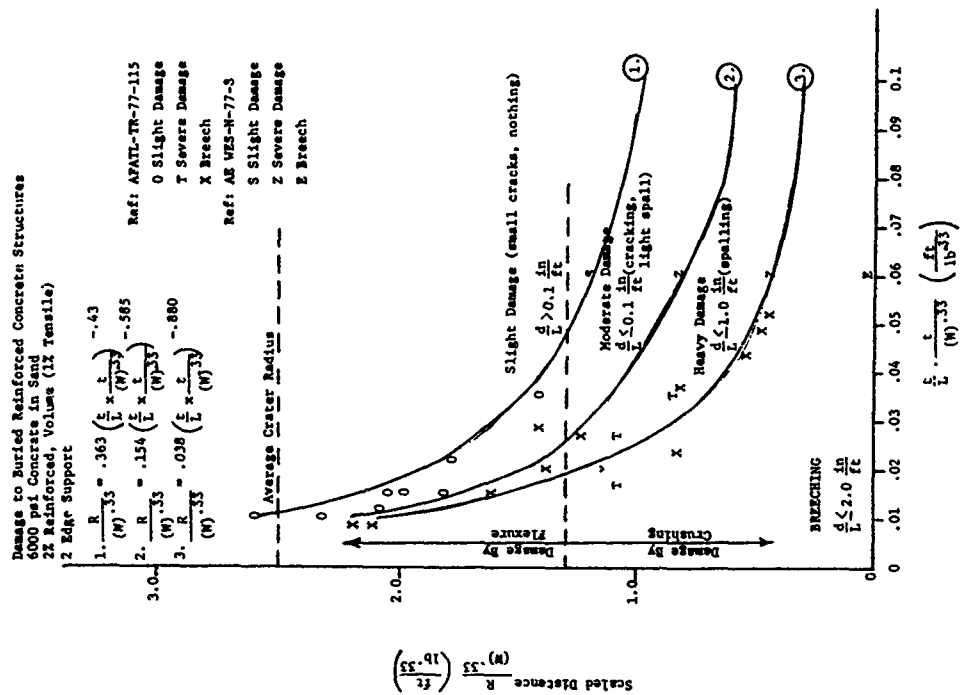


FIGURE 4

AD P 001762

# THE MEASUREMENT OF BLAST-INDUCED MOTION OF STRUCTURES USING A DOPPLER RADAR

RICHARD K. BAILEY, MARX BROOK and JAMES J. FORSTER

NEW MEXICO INSTITUTE OF MINING & TECHNOLOGY, TERA GROUP, R&D  
SOCORRO, NEW MEXICO 87801

## ABSTRACT

Measuring the motion of structures in a blast environment by photographic means is often made difficult by the presence of optical obscurants such as dust, water spray, and detonation products (fireball). The use of a CW (continuous wave) Doppler radar to make measurements of the velocities of materials within these optically opaque environments offers potential advantages. Of particular interest is the possible utilization of low-cost intrusion alarm CW radars now being mass-produced for the house/industrial security market. Preliminary results with steel, water, and concrete debris show promise of overcoming the optical limitations on visibility. Reflectivity data from various kinds of dusts and fragmented materials will be necessary to fully utilize the technique.

## THEORY

The apparent change in frequency, or wavelength, of a periodic acoustic signal caused by the motion of acoustic source relative to the observer was first explained in 1842 by the Austrian physicist Christian Johann Doppler. This phenomenon, called the Doppler effect, was later found to apply to periodic electromagnetic energy as well as to acoustic energy. The magnitude of this apparent change in frequency provides a measure of the relative radial velocity between the moving object and the observer.

In the case of a basic CW (continuous-wave) radar system, a small portion of the energy being transmitted at frequency  $f_0$  is mixed with the energy reflected back to the radar antenna from the target at frequency  $f_r$ . If the target has no radial velocity with respect to the radar antenna,  $f_r$  will equal  $f_0$  and the difference between the frequencies (i.e., the beat frequency) out of the radar receiver mixer will be zero, (i.e., only a direct current output will exist). If the target is moving radially either toward or away from the radar antenna, however, then  $f_r \neq f_0$ , and an alternating current signal will exist at the output of the radar receiver mixer circuit. The frequency of the mixer output signal ( $f_d$ ) is a direct measure of the radial velocity in accordance with the well known relationship:

$$f_d = \frac{2 v_r}{\lambda}, \text{ in consistent units; where:}$$

$f_d$  = frequency shift (Doppler frequency), Hz

$v_r$  = radial velocity, cm/sec

$\lambda$  = wavelength of transmitted signal, cm.

For example, the Doppler frequency ( $f_d$ ) for a target whose radial velocity is 150 m/sec with respect to a radar operating at a wavelength of 3.2cm would be 9,380 Hz.

It should be noted here that for the simplest possible receiver (as described later) the value of  $f_d$  will define the magnitude of  $v_r$  but will not indicate whether the target was approaching, or receding from, the radar antenna.

A number of other theoretical and practical factors must be considered when designing a CW radar system. One important factor is the wavelength to be used. The physical size of an object has a significant influence on its reflectivity at various wavelengths, i.e., an object becomes nearly invisible when its size is a small fraction of one wavelength. This fact places a powerful tool at the disposal of the designer who wishes to minimize the radar return from objects that are much smaller than the target(s) of interest in a given test. Another factor of great importance is the necessity for shock-isolating the radar antenna from the test environment long enough for the primary data to be acquired prior to shock-induced movement of the antenna. Any such movement introduces unwanted Doppler frequencies in the receiver output.

## APPLICATIONS

The application of the principles of CW radar to some types of ordnance testing activities has been well established for a number of years<sup>(1,2)</sup>. Measuring the translational velocity of projectiles and rockets is a common application, and commercial units designed to acquire and analyze such data are currently available<sup>(3)</sup>.

Problems associated with acquiring velocity information by conventional means (high-speed photography, break grids) in some test programs conducted at New Mexico Tech have given rise to a search for additional measurement techniques. These problems typically consist of a combination of optical obscurants (dust, water spray, gases) with flying debris. The use of a CW radar system appears to offer advantages in several such instances. Two ongoing programs at Tech with potential for such applications are a) survivability of shipboard ordnance stores, and (b) safety-distance studies for Ready-Service Magazines.

#### Survivability of Shipboard Ordnance Stores

One of the ongoing test programs at New Mexico Tech is a study to examine the mechanism that causes detonation of various kinds of shipboard ordnance stores when they are impacted by portions of ship structure. A common test set-up involves a large donor charge submerged in a water-filled pit. A lower deck plate in contact with the top surface of the water is accelerated upward toward palletized bombs, projectiles, or rocket motors when the donor charge is detonated. The velocity history of the deck plate prior to impacting the palletized munitions is of primary interest in this study, but water spray and other debris that surround the event, combined with the short distance the deck plate travels prior to impact, makes it difficult to obtain reliable velocity information from high-speed motion-picture film records. Pin probes and accelerometers have been used on these tests to measure plate velocity, but the results are not always satisfactory and the equipment and installation are somewhat expensive. A non-expendable CW radar has been used on plate calibration tests with promising results (see Figure 11 and the associated discussion in Review of Test Results). An expendable CW radar test unit offers attractive possibilities in terms of both performance and expense, and one such unit has been tried on one test to date. The results of this test are still being analyzed.

#### Safety-Distance Studies for Ready-Service Magazines

Upcoming tests at New Mexico Tech are designed to acquire data concerning the fragments generated by the reinforced concrete roof of a munitions storage magazine when the roof fails due to internal overpressure caused by a detonating munition. The data will consist of the size of the fragments, their initial velocity, the direction in which they go, and the distance at which they are found from their initial location. In most of these tests the roof will have a soil overburden, and the dust cloud generated by this soil during roof failure is expected to make optical measurement of the velocity of the roof fragments emerging from the dust cloud very difficult. It is hoped that the CW radar concept can be utilized here to obtain better data with less effort.

#### TECHNICAL DETAILS

A schematic diagram of the CW radar circuit currently being used at New Mexico Tech is shown in Figure 1 below:

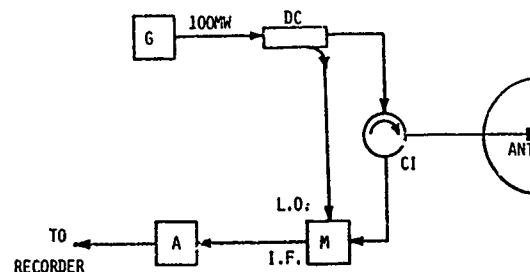


FIGURE 1. BLOCK DIAGRAM OF CW RADAR

G - Gun Diode Oscillator; DC - Directional Coupler; CI - Circulator; ANT - Parabolic Antenna; M - Mixer; A - Amplifier

This circuit represents the simplest possible configuration for a CW radar system. The microwave power output is on the order of 100 milliwatts and the frequency is 9.375 GHz ( $\lambda = 3.2\text{cm}$ ). The package in which the circuitry is assembled is mounted on the back side of the parabolic antenna used with the system. This parabolic antenna is 4 feet in diameter and produces a radiated conical beam that has a beamwidth of about 2 degrees at the half-power points (3 dB down).

The ability to analyze the complex waveform that constitutes the receiver output for a "real-world" test environment is the key to successfully utilizing the CW radar concept. In the simplest case, the output of the radar receiver would consist of a sine wave whose frequency is a function of the radial velocity between the target and the radar antenna. In practice, however, the radar typically sees more than one target and these multiple targets are likely to have a wide range of sizes, velocities, directions of travel, and distances from the radar antenna. The result of this multiplicity of targets is an output signal whose complex waveform is the sum of all the individual sine waves caused by each target. These individual sine waves are usually independent of each other in terms of frequency, magnitude, and phase (for an infinite bandwidth receiver and assuming no multiple scattering). An example of such a complex waveform observed in an actual test is shown in Figure 2.

A wealth of literature exists describing the various techniques available for analyzing the content of complex waveforms resulting from the combination of individual sine waves having unrelated frequencies, amplitude, and phase relationships<sup>(4)</sup>.



The technique chosen for the initial studies at New Mexico Tech involves first translating the analog radar output into digital form using an analog-to-digital (A/D) converter and then processing this information in a digital computer<sup>(9)</sup> utilizing a Fast Fourier Transform (FFT) program. Two special precautions must be observed during this data-reduction process:

1. The digitizing rate must be high enough to accommodate the highest frequency of interest ( $f_{\text{dig}} \geq 2f_{\text{max}}$ ) and;
2. The duration of the samples selected for analysis by the FFT program must be long enough to yield the desired velocity resolution. A record of length  $T$  sec gives a frequency resolution  $\Delta f = 1/T$ . A velocity resolution ( $\Delta v$ ) of 8 m/sec is obtained for a 2 millisecond sample using a 3.2 cm radar (assuming the radar receiver has an infinite bandwidth).

Output data from the computer is displayed in three formats. The first format consists of the analog waveform as reconstituted from the digitized data for the duration of the sample interval selected for FFT analysis. An example of this analog waveform printout (for a 2ms duration sample) is shown in Figure 2. Examination of this display provides a general feeling about the character and quality of the signal. This display permits some obvious problems to be identified, such as overdriven signals (peak clipping), noisy signals, or low-amplitude signals, thus alerting the analyst to view the subsequent data with suspicion.

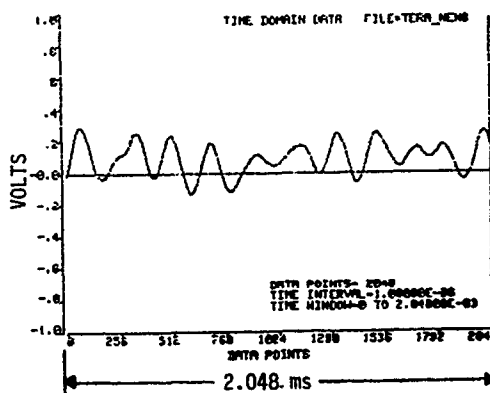


FIGURE 2. ANALOG SIGNAL FROM CW RADAR RECEIVER  
(Reconstituted from Digitized Data)

The second display format consists of a graph that shows the relative power contained in each of a number of frequency increments, normalized to the amplitude of the frequency increment within the sample that contained the greatest power level. An example of this display is shown in Figure 3. In the simplest possible case this graph would contain only one vertical bar whose horizontal location corresponded to the Doppler frequency and

whose amplitude would be 1.0. The output for a real test is typically not this simple, however, and a set of spectral lines may be expected to surround the predicted Doppler frequency, as can be seen in Figure 3. The target(s) in tests of the kind discussed here are seldom moving directly toward the radar antenna, so that the true translational velocity of a given target along its trajectory must be obtained by supplementing the radar data with other information, such as test geometry.

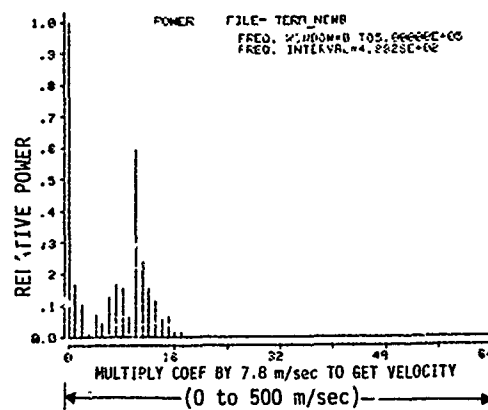


FIGURE 3. GRAPHIC DISPLAY OF POWER LEVEL  
VS. FREQUENCY (VELOCITY)

The third display format consists of a tabular printout of the same data that is displayed in the graph of Figure 3. The numerical values of the relative amplitudes of each frequency increment are more easily and accurately obtained from the table than from the graph. An example of this format is shown in Figure 4.

COEFF.	VEL. (ft/s)	FREQ. (Hz)	POWER	(P)/Max
BC				
MAX	0.0000E+00	0.0000E+00	5.5521E+02	1.0000E+00
	0.0000E+00	5.0000E+05	5.3059E+02	
1	2.5629E+01	4.8825E+02	9.2469E+01	.167
2	5.1258E+01	9.7650E+02	5.6117E+01	.101
3	7.6887E+01	1.4647E+03	1.1174E+01	.070
4	1.0252E+02	1.9531E+03	4.0385E+01	.072
5	1.2814E+02	2.4414E+03	2.4544E+01	.044
6	1.5377E+02	2.9298E+03	6.3809E+01	.120
7	1.7940E+02	3.4179E+03	9.0756E+01	.164
8	2.0503E+02	3.9062E+03	8.5328E+01	.154
9	2.3066E+02	4.3945E+03	3.4257E+01	.062
10	2.5629E+02	4.8825E+03	3.2859E+02	.592
11	2.8192E+02	5.3710E+03	1.3136E+02	.237
12	3.0755E+02	5.8592E+03	8.4625E+01	.152
13	3.3318E+02	6.3476E+03	6.2087E+01	.114
14	3.5881E+02	6.8359E+03	2.3658E+01	.053
15	3.8444E+02	7.3242E+03	3.7943E+01	.068
16	4.1007E+02	7.8125E+03	8.1984E+00	.015
17	4.3570E+02	8.3008E+03	7.3957E+00	.014
18	4.6133E+02	8.7890E+03	1.3623E+00	.002
19	4.8696E+02	9.2773E+03	3.0527E+00	.005
20	5.1258E+02	9.7656E+03	1.7542E+00	.003
21	5.3821E+02	1.0253E+04	1.7412E+00	.003
22	5.6384E+02	1.0741E+04	1.3773E+00	.004
23	5.8947E+02	1.1230E+04	1.3528E+00	.002
24	6.1510E+02	1.1718E+04	1.1663E+00	.002
25	6.4073E+02	1.2207E+04	4.1549E+01	.001
26	6.6636E+02	1.2695E+04	8.1167E+01	.001
27	6.9199E+02	1.3183E+04	3.8151E+01	.001
28	7.1762E+02	1.3671E+04	4.6879E+01	.001
29	7.4325E+02	1.4160E+04	2.1893E+01	.000
30	7.6887E+02	1.4648E+04	1.2552E+01	.000
31	7.9450E+02	1.5136E+04	7.6381E+01	.001
32	8.2013E+02	1.5625E+04	2.4695E+01	.006
33	8.4576E+02	1.6113E+04	3.2657E+01	.001
34	8.7139E+02	1.6601E+04	4.8679E+01	.009
35	8.9702E+02	1.7090E+04	2.9323E+01	.001
36	9.2265E+02	1.7578E+04	5.5626E+01	.001
37	9.4828E+02	1.8066E+04	4.8963E+01	.001
38	9.7391E+02	1.8554E+04	4.6450E+01	.001
39	9.9954E+02	1.9042E+04	4.1842E+01	.001

FIGURE 4. TABULAR PRINTOUT OF POWER  
LEVEL VS. FREQUENCY

# REVIEW OF TEST RESULTS TO DATE

New Mexico Tech has applied the CW radar technique to four test programs so far. These programs consisted of: 1) measuring the velocity of a 3-inch-diameter steel sphere fired at velocities of greater than 1500 m/sec; 2) measuring the initial velocity of a large vertical steel surface that represented the hull of a ship; 3) measuring the early velocity history of a small horizontal steel plate that was explosively launched upwards; and 4) measuring the early velocity history of a large horizontal steel surface that represented the false deck of a ship.

In the first application (measuring the velocity of a 3-inch steel sphere) the analysis program used was found to contain several "bugs." The effort expended on de-bugging this analysis program contributed to a better program for the next test series and also pointed out the desirability of expanding the output to include the three display formats discussed above. The analog radar data from this test series is still available on magnetic tape, and it is hoped that time and resources will permit a re-analysis of this data with the improved program.

The second application involved measuring the initial velocity of a large (about 4m x 6m) vertical steel wall that simulated the outside surface of a ship's hull. Detonation of a 100-lb explosive charge simulating a torpedo accident inside the ship propelled the wall. This structure is shown prior to testing in Figure 5.

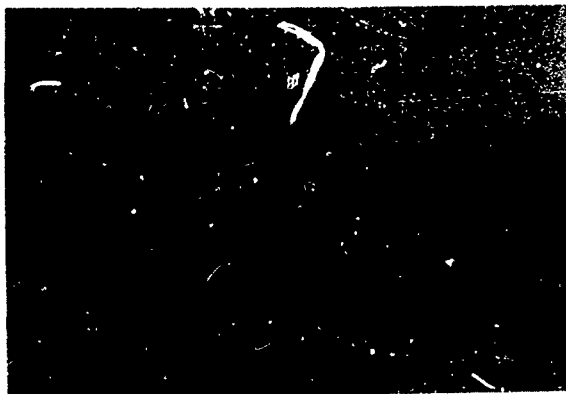


FIGURE 5. EXTERIOR VIEW OF SIMULATED SHIP HULL

The CW radar unit was located about 130m from the wall and was mounted on timber cribbing to minimize the coupling of ground shock into the radar set. A protective barrier was placed between the test wall and the radar. The radar beam was reflected to the test wall from a heavy plane reflector that was centered on a normal to the test wall. The reflector was also shock isolated on timber cribbing. The details of the reflector and radar installation can be seen in Figures 6 and 7.



FIGURE 6. CW RADAR BEHIND PROTECTIVE BARRIER

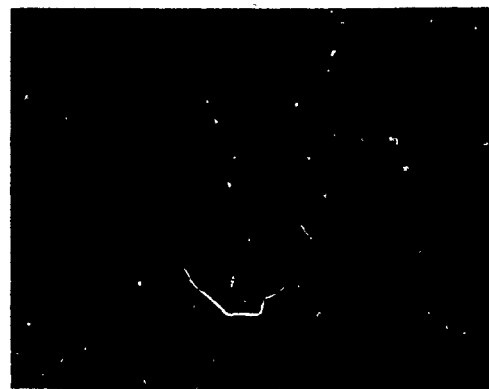


FIGURE 7. PLANE REFLECTOR USED WITH CW RADAR

The average initial velocity of the wall, as determined from high-speed photographic records, for the first 4.3 milliseconds of wall movement was 9.5 m/sec. The graphical output from the FFT analysis (shown in Figure 8) contains a relatively large power level at 10 m/sec, which is in good agreement with the photographically determined velocity.

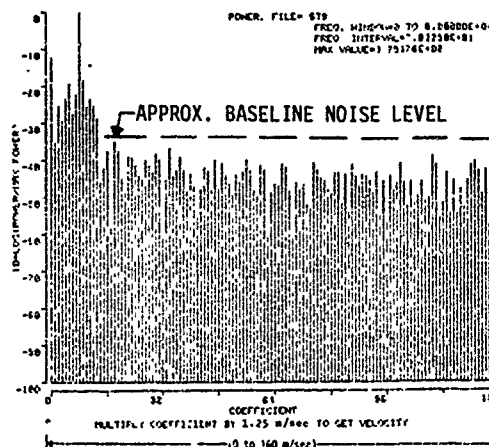


FIGURE 8. POWER LEVEL (LOGARITHMIC SCALE) VS. FREQUENCY FOR TEST OF SHIP'S HULL

The third application involved reflecting the radar beam downward toward a horizontal steel plate, as shown in Figures 9 and 10.



FIGURE 9. RADAR REFLECTOR SUSPENDED ABOVE TARGET REGION



FIGURE 10. HORIZONTAL STEEL PLATE IN POOL OF WATER

The steel plate was explosively launched upward by a charge submerged in a pool of water in which the bottom of the plate was also submerged. Velocity-pin data obtained from this test yielded an initial velocity of 91 m/sec. The graphic display of the sample of radar data shown in Figure 11 includes relatively high-level returns centered around a velocity of 78 m/sec.

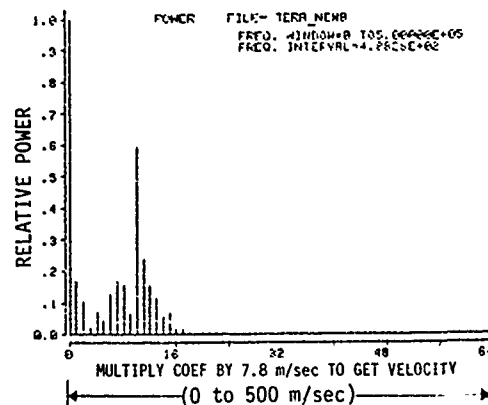


FIGURE 11. FFT GRAPHIC OUTPUT FOR TEST NO. PS0217A3, PLATE CALIBRATION

The geometry of the test setup would produce a vector velocity toward the center of the reflector of 79 m/sec for an object travelling straight up at 91 m/sec. This vector velocity is in good general agreement with the radar result.

The fourth, and most recent, application consisted of suspending an expendable CW radar transceiver<sup>(8)</sup> directly above a large horizontal steel surface and recording the transceiver output on magnetic tape as the steel deck was explosively launched upward. It is not feasible to use a non-expendable radar unit because of the severity of the test environment (the donor charge is about 1200 lbs). The analysis from this test has not yet been completed. It is hoped that the results will be favorable because there is a significant potential economic advantage in successfully measuring deck velocity in this way. Microwave CW radar units (intrusion alarms) can presently be procured for less than \$100. The cost of the pin probes and accelerometers currently being used on these tests is at least 20 times this amount. These low-cost commercial units have such a broad antenna beamwidth that it is likely that a disposable parabolic reflector will be needed to collimate the radiated microwave energy into a planar wavefront at the target plate to avoid unwanted Doppler spread.

#### FUTURE PLANS

Two general categories of application are presently anticipated for CW radar systems at New Mexico Tech. The first category involves a non-expendable radar system having longer stand-off distances, higher rf power output than used to date, narrow beam width, a more sensitive receiver, and possibly a superheterodyne receiver that would permit discrimination between approaching and receding targets. The second category involves expendable low-power radar units for use at very close ranges within very harsh test environments for measuring target movements of just a few inches.

More basic information is needed about factors that affect the performance of both the types of systems mentioned above. The primary need is for radar cross-section data for commonly encountered test materials (such as rough concrete, water spray, dust, rock, wood fragments, and plastic sabot parts). To be most useful, this data should relate the radar cross section to material parameters (such as size, roughness, and attitude) and to radar parameters (such as wavelength and power level). It is clearly desirable to have enough such information to permit sound engineering selections to be made concerning radar wavelength, power level, beam width, range, and type of receiver. The ability to make such selections will enhance the prospects of maximizing radar returns from primary target objects and of suppressing radar returns from obscurants such as dust and water spray. More complete information of this kind will also help identify test situations that are not favorable for the application of CW radar and thus avoid needless expenditures.

#### REFERENCES

1. Hoffleit, L. D., "On the Determination of Drag Coefficients from Doppler Radar Records with Specific Application to the 4.5-inch Rockets T22 and M8A3 Launched from Aircraft," BRL Memorandum Report No. 405, USA Ballistic Research Laboratories, Aberdeen Proving Ground, MD, 1945.
2. Walbert, J. N., "Projectile Motion Determination, Fourier and Numerical Methods for the Derivation of Trajectory Data from Doppler Radar", U.S. Army TECOM Final Report, Sept., 1979.
3. Lear Siegler, Inc., Astronics Div., DR810 MK11 Muzzle Velocity Radar.
4. One such source is: Brigham, E.O., "The Fast Fourier Transform, Prentice-Hall, Inc., Englewood Cliffs, New Jersey, 1974.
5. A Hewlett-Packard 9825 desk-top computer with appropriate accessories has been used thus far.
6. Solfan Model 2600 Microwave Intrusion Detector.

AD P 001768

## HIGH EXPLOSIVE TESTING OF HARDENED AIRCRAFT SHELTERS

Ronald R. Bousek  
Lt Col, USAF  
Defense Nuclear Agency  
Field Command  
Kirtland AFB, New Mexico 87115

## ABSTRACT

Two full-size, hardened, third-generation aircraft shelters of the type employed by the U.S. Air Force in Europe and by NATO countries were subjected to a series of five high explosive tests. The purpose of the tests (nicknamed DISTANT RUNNER) was to gather empirical data necessary for the Department of Defense Explosives Safety Board to reduce existing explosives quantity-distance safety standards for storage of conventional munitions in and near hardened aircraft shelters. The first two tests each used a 120-ton explosive stack of ANFO located external to the shelters. The other three tests consisted of internal detonations of AIM-9 warheads and Mark-82 bombs. As a result of these tests the ODESB has reduced certain quantity-distance safety standards. As a bonus, a large amount of structural response data was gathered which can be applied to problems involving dynamic loading of reinforced concrete structures.

## INTRODUCTION

In Europe, real estate restrictions and property constraints pose difficulties in placing aircraft shelters and munitions storage areas within U.S. Air Force and NATO aircraft bases. Overly restrictive safety criteria may compromise military operations and readiness. Under sponsorship of the Department of Defense Explosives Safety Board, the Defense Nuclear Agency conducted a series of five high explosives tests, involving two full-size aircraft shelters, with the goal of obtaining data which would allow the reduction of certain established quantity-distance (QD) safety standards. The tests were conducted at White Sands Missile Range, New Mexico, during September to November 1981.

Quantity-distance standards are expressed according to the equation,  $D = KW^{1/3}$ , where D is the safe distance from a weight, W, of mass-detonating explosives. K is the QD factor, or safe scaled distance, investigated by this test series. At the time of the tests a QD factor of 30 ft/lb<sup>1/3</sup> (16m/kg<sup>1/3</sup>) was applied to military aircraft parked in the open and in shelters. A standard of 40 ft/lb<sup>1/3</sup> (16m/kg<sup>1/3</sup>) was applied as the scaled distance required to separate explosive storage from public areas, subject to minimums required for protection against fragments. The QD factor applied to an aircraft parked within a shelter was

taken to be the same as for an aircraft parked in the open. One objective of these tests was to demonstrate that the QD factor could be decreased for sheltered aircraft due to the protection afforded by the shelter. A second objective was to show that the QD factor of 18 applied to runways could be substantially reduced. The third major objective was to assess the response of the third-generation shelter to various sizes of internal detonations in terms of airblast and fragmentation propagated outward from the shelter.

## PROCEDURE

Construction

Two full-size third generation aircraft shelters with adjoining taxiways were constructed on a remote test site on the northern part of White Sands Missile Range. The shelters were structurally identical to those constructed in Europe by the U.S. Air Force and by NATO countries except for two minor details: the electrical motors normally used to open the front doors were omitted and the shelter foundations were slightly wider to accommodate the load-bearing properties of the soil at the test site. Construction took 11 months. The quonset-shaped shelters were constructed of highly reinforced concrete and were designed to accommodate one fighter aircraft. The arched walls were approximately two feet thick with various colors of concrete to aid in identification of debris following destructive testing (Fig. 1). The two sliding front doors were one foot thick and each weighed 100 tons. An exhaust port at the rear of the shelter could be closed off by two large sliding doors.

Instrumentation

Free field instrumentation in the test area surrounding the shelters consisted of 44 air blast pressure gages and 33 triaxial accelerometers for ground motion (Fig. 2). Each shelter was instrumented with approximately 30 blast pressure gages and a dozen or so biaxial accelerometers to record the pressure environment and the resulting dynamic structural response. Passive strain measurements, to document permanent deformation of the shelters from the external explosions, were taken by measuring pretest and post-test positions of

50 punch marks on each of four arch ribs. High speed technical photography was used to document each test. Eight aerial cameras and up to 23 ground-based cameras recorded shelter motion and explosives performance. A comprehensive program for measuring debris was conducted. Following the external explosions, the density of soil ejecta which landed on the taxiways was measured. Following the destructive internal explosions, previously cleared ground sectors surrounding the shelters were surveyed for shelter fragments which were then counted and weighed. Data from gages was recorded using a Digital Encoding System installed in a bunker near the test bed. Two hundred data channels were amplified, digitized, and multiplexed in the bunker and sent via coaxial cable to the instrumentation van located one mile from the test bed where the data was recorded on magnetic tape. A calibration test consisting of 1200 lb of ammonium nitrate and fuel oil explosive was detonated prior to the main test series and verified that the instrumentation system was working properly.

#### EXTERNAL EXPLOSIONS

##### Description

The first two explosions in the DISTANT RUNNER test series each used a 120-ton stack of ANFO (a mixture of ammonium nitrate and fuel oil) as the explosive located external to the shelters. An obsolete F-101B fighter plane was positioned in each shelter. The primary objective of the test was to demonstrate that at an incident overpressure of 15 psi, leakage airblast inside the closed shelters would be less than 1.7 psi. A second objective was to test the taxiway at a scaled distance 4 ft/lb<sup>1/3</sup> from the explosion. The first test subjected shelter B to a side-on blast and shelter A to a rear-on blast, both at a nominal 15 psi. The second test, conducted a month later, subjected shelter A to a nominal 15 psi front-on while shelter B received 7 psi from an angle 27 degrees off of front-on. These tests were designated as Event 2 and Event 5. (Event 1 was rescheduled to occur between Events 4 and 5. The original designations were kept despite the resequencing.)

##### Results: Event 2 and 3

No structural damage occurred to the concrete arches or rear walls. Both rear exhaust doors were blown down (inward) on the shelter with its rear to the blast. The tail of the F-101B was damaged considerably by one of the flying doors. The front doors of this shelter were not damaged. One rear exhaust door of the shelter oriented side-on to the blast was blown down but did not strike the aircraft. Several bolts securing the roller mechanism in the front doors broke, but the doors stayed on their tracks.

Based upon free field air blast measurements the desired nominal environment of 15 psi was produced on both external tests (Fig. 3). Pressure build-up inside the shelters was measured to be less than 1.6 psi except for one location in the corner near the front door of the shelter exposed side-on to the blast. A pressure in excess of 8 psi was recorded there, but was evidently a very localized high pressure region which dissipated before reaching the next gage only 20 feet away.

#### INTERNAL EXPLOSIONS

##### Description

Following the two external tests, three internal tests were conducted. The explosives used are listed in the Table. The objectives of the internal tests were: assess blast suppression by the shelters, assess debris patterns with regards to safety criteria, and observe the failure mode of the shelter.

##### Results: Event 4

The shelter and aircraft were completely destroyed in Event 4. High speed photography showed that the arch was first lifted off its foundation and then split longitudinally along the crown. As a result the entire right half (as viewed from the front) of the arch was launched into the air and traveled 200 feet as a unit. The break-up of the left half of the arch was influenced by the personnel door entry way. Several large sections impacted at ranges of 100-200 feet. The rear of the shelter suffered extreme damage, but on the whole was displaced only several feet. The front doors were blown directly forward and traveled about 400 feet. High speed photography showed them tumbling top-over bottom. One front door came to rest against the other shelter causing only superficial gashes on its side.

TABLE  
INTERNAL EXPLOSIONS

Event 4:	12 MARK-82 bombs 2292 lb Tritonal 30 lb C-4 2 lb PETN
Event 1:	4 AIM-9 air-to-air missiles 42 lb HBX-1 6 lb C-4 .6 lb PETN
Event 5:	48 Mark-82 bombs 9168 lb Tritonal 64 lb C-4 9 lb PETN

A ground survey of debris (Fig. 4) indicates that 90% of the debris was contained in large pieces at ranges less than 250 feet from the shelter (except for the front doors). The debris with the longest range came from the metal ring beam on the front face of the arch. Beam sections were projected forward in a 180-degree fan with ranges of 1000 to 1700 feet.

Initial failure of the shelter along the arch-foundation interface and complete destruction of the shelter were consistent with pre-shot calculations. Blast pressures to the rear were attenuated slightly by the shelter, while blast pressures forward and to the sides showed no attenuation effects (Fig. 5). Consequently, a reduction in the quantity-distance factor for internal explosive storage does not appear to be indicated. The failure of the shelter to attenuate the blast laterally can be ascribed to the initial failure mode of the shelter along the foundation. By strengthening the arch-foundation connection (rebar) it should be possible to cause initial failure to occur at the crown with consequent upward (rather than lateral) venting of the blast.

#### Results: Event 1

The four AIM-9 warheads were two feet above the floor positioned as if they were on an aircraft. No aircraft was in the shelter. As a result of the explosion the two front doors were blown evenly outward about 20 feet with no major damage. The blast deflectors, which normally might have restricted this motion, had been broken off from the bottom of the doors by a previous test. The shelter suffered no structural damage. All shrapnel was contained by the shelter, although the warhead base plates punched through the rear doors and struck the rear wall of the exhaust port. The personnel door was undamaged and remained closed. Airblast was effectively suppressed.

#### Results: Event 5

Twelve bombs were positioned beneath an F-101B. Another 36 bombs were positioned near the aircraft and at the front corners of the shelter to simulate weapon storage. As expected, the shelter was completely destroyed. In general the debris pattern was similar to that from Event 4, but the fragments were smaller and had larger ranges. Sections of the front doors were scattered between 400 and 1200 feet directly forward of the shelter. The arch was fragmented into several large pieces which landed at ranges of 100-300 feet. Numerous smaller chunks had ranges up to 1200 feet. The rear of the shelter was completely demolished and leveled. Sections of the front ring beam were found at roughly the same ranges as for Event 4. They were not thrown further by the larger explosion because the greater force distorted their aerodynamic shapes causing increased drag during their flight.

Blast overpressures (Fig. 6) were slightly suppressed by the shelter to the rear and to a lesser extent to the front of the shelter. No suppression was observed in the lateral directions. Consequently, a reduction in the current airblast quantity-distance criteria for internal explosives is not expected. Debris patterns from this test and Event 4 are being carefully evaluated with regard to the other safety hazard, flying debris.

#### CONCLUSION

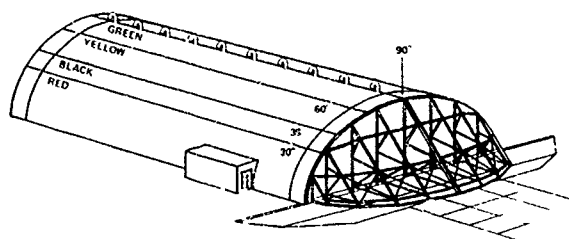
The DISTANT RUNNER test series was highly successful. The primary objective of experimentally verifying that certain quantity-distance safety standards could be reduced was met. The DOD Explosive Safety Board has reduced the QD factor from 30 ft/lb<sup>1/3</sup> to 5 for aircraft shelters near munitions storage igloos, and to 8 for aircraft shelters near open storage sites. The DDESB has also recommended these changes to NATO Subgroup AC/258. As another result of the tests, structural modifications have been identified and are under study which would increase the strength of the shelters.

A large amount of technical data which was gathered from the tests can be applied to the analysis of structural response to blast loading. The tested shelters were full size, so the problem of scaling was avoided. Companion measurements of airblast loading and the resulting dynamic structural response were made which can be used to evaluate dynamic modeling techniques (Fig. 7 & 8). Post-test measurements on permanent building deformation can be used in developing and checking methods for modeling inelastic deformations (Fig. 9). An extensive effort was expended collecting and analyzing debris fragments produced by the destructive tests. Thousands of fragments were surveyed, weighed, and measured. These data can be applied toward the study of fragment size distribution functions and ranges. The details of DISTANT RUNNER testing and a summary of technical results are presented in the References.

#### REFERENCES\*

1. "DISTANT RUNNER Test Execution Report" POR 7062, Defense Nuclear Agency, 29 Jan 1982.
2. "Proceedings of the DISTANT RUNNER Symposium" POR 7063, Defense Nuclear Agency, 2 Sep 1982.
3. "DISTANT RUNNER Test Program Final Report" Defense Nuclear Agency, In Preparation.

\*Distribution limited to U.S. Government agencies only. Other requests must be referred to the Defense Nuclear Agency, Washington, DC 20305.



NOTE: ANGLES MARK THE CHANGE IN CONCRETE DYE COLOR  
ORIGIN IS LOCATED AT BOTTOM CENTER OF FRONT DOOR

Figure 1. Third Generation Aircraft Shelter

○ BLAST PRESSURE GAGE  
△ TRIAXIAL ACCELEROMETERS

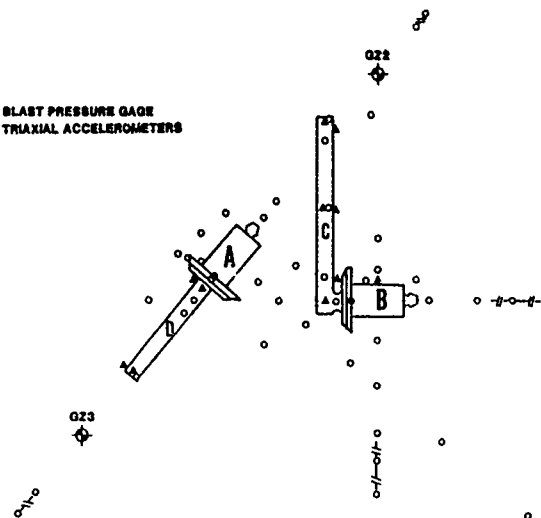


Figure 2. Free-Field Gage Locations

### DISTANT RUNNER EVENT 2 — BLAST ENVIRONMENT

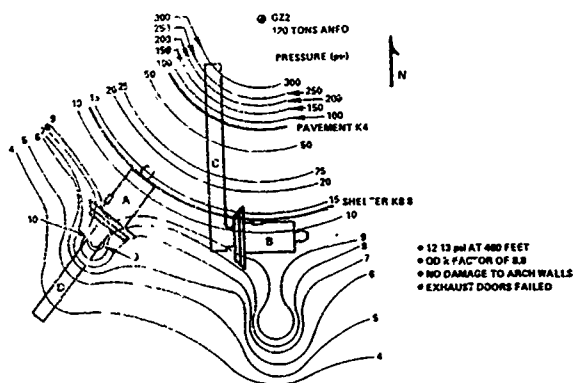


Figure 3. Event 2 Peak Pressure Contours

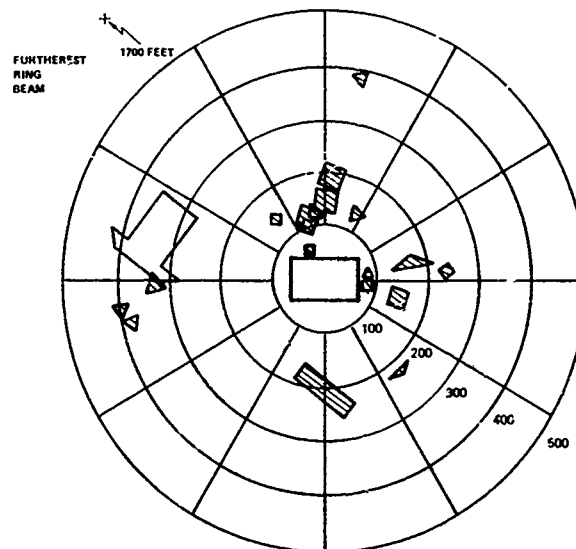


Figure 4. Event 4 Large Debris Map



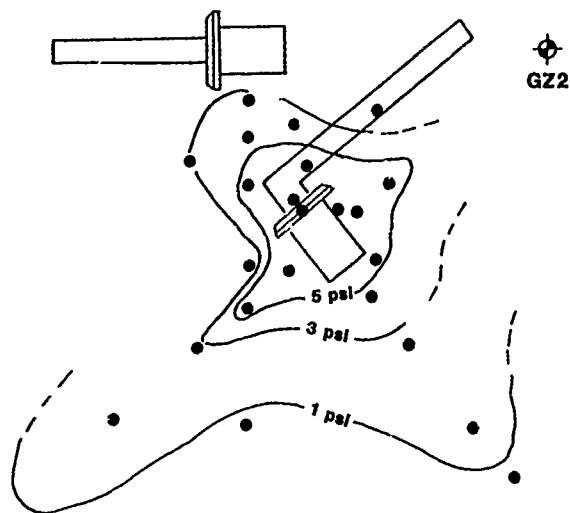


Figure 5. Event 4 Peak Pressure Contours

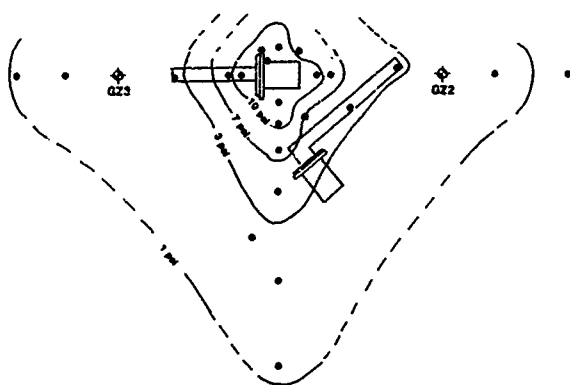


Figure 6. Event 5 Peak Pressure Contours

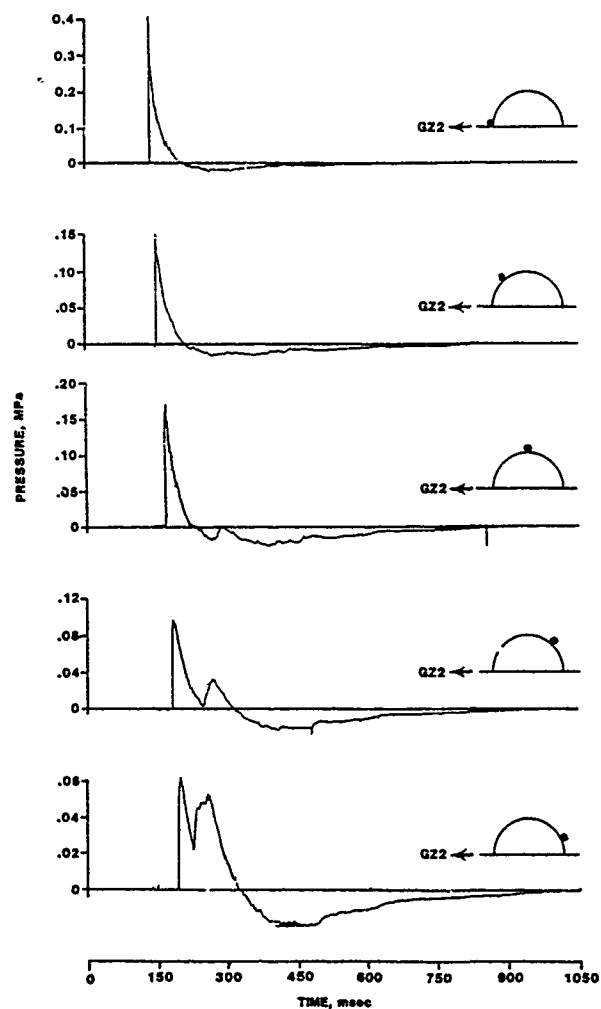


Figure 7. Event 2 - Shelter B External Pressures

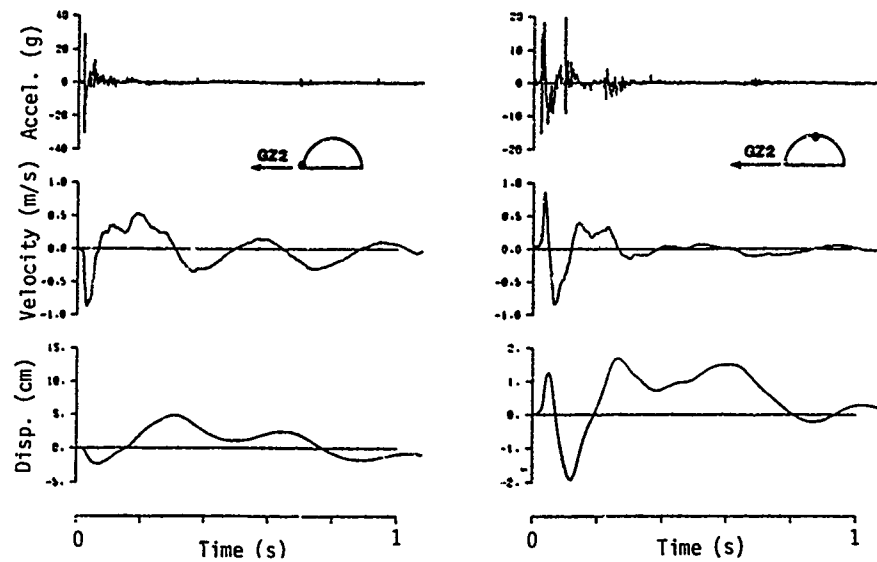


Figure 8. Event 2 - Shelter B Wall Motions

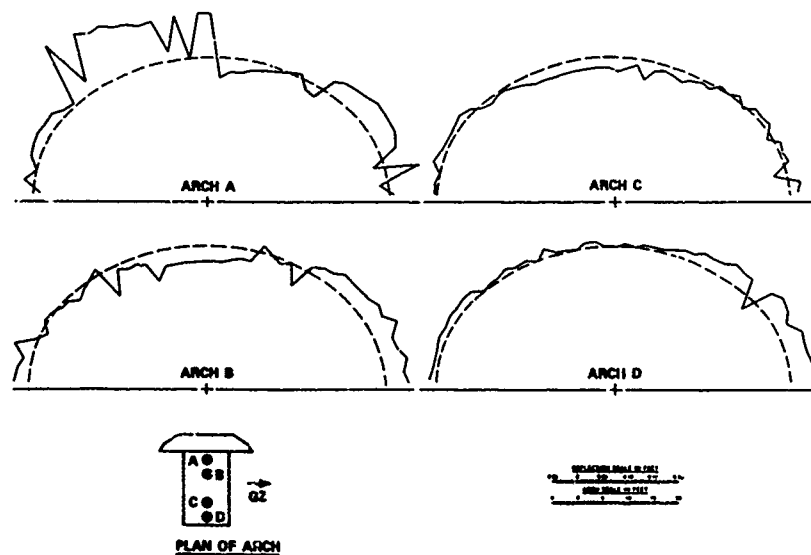


Figure 9. Event 2 - Shelter B Permanent Radial Deformation

AD P001769

# A STATISTICAL APPROACH TO CONVENTIONAL WEAPONS EXPERIMENTATION

James M. Carson

New Mexico Engineering Research Institute  
University of New Mexico  
Albuquerque, New Mexico

## ABSTRACT

A statistically based strategy of experimentation has been applied to the Air Force Weapons Laboratory's Conventional High Explosive Blast and Shock test series. The basis of this design and analysis method is reviewed. The purpose of the procedure is the measurement of the various experimental variances and the development of design curves that include confidence bands. Application of the statistical design of experiments impacts the areas of test design, cost, instrumentation layout, instrumentation performance evaluation, and data and parameter analysis.

## INTRODUCTION

A statistically based strategy of experimentation has been applied to the Air Force Weapons Laboratory's Conventional High Explosive Blast and Shock (CHEBS) test series. This paper presents an overview of statistical design procedures that are available. The procedures used for the CHEBS series will be used to illustrate the methodology and philosophy of statistical experimental design.

It should be noted that these procedures are not new, although they do not appear to be in widespread use in this community. They are in common use in the areas of process and product control, product acceptance, and quality control [1-5].

A look at a design curve from "Protection from Nonnuclear Weapons" [6] (Figure 1) illustrates a common problem. A design curve, which usually is based on experimental data, is inadequate if it is only some type of trend line for the data. Adding one standard deviation confidence bands, for example, would better represent the data and would better allow the designer to choose a design value appropriate to his application.

In addition to adopting an experimental strategy to develop more useful design curves, other motivations to adopt such a strategy exist. Properly planned experiments can help maximize the information received per dollar invested in an experimental test or test series. A trade-off exists between the number of tests and the number of instrumentation channels per test. In the CHEBS series, for example, it was determined that

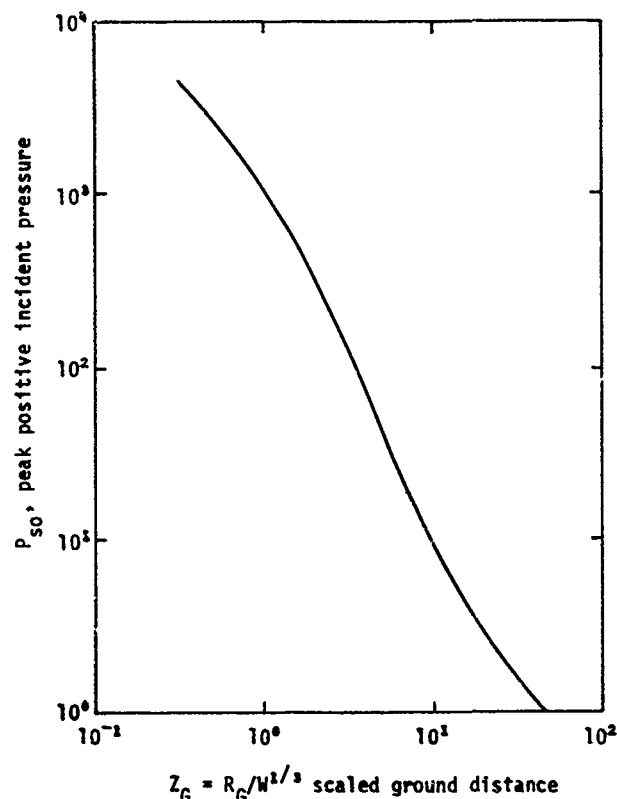


Figure 1. Peak pressure design curve.

more information could be gained from multiple tests, even though the number of channels per test was reduced. Many costs involved in fielding the first test are nonrecurring.

Often experimental data are thrown out because they do not "look right." Statistical data analysis can identify outliers and place their rejection on a more quantitative basis.

## STATISTICALLY BASED PLANS

Statistically based experimental plans have several characteristics in common, even though

they are tailored to different experimental objectives.

- Experimental error is a fact of life and must be measured if the importance of other variables is to be determined.

- All variables should be considered over a wide range. Various testing schemes, which amount to test parameter variation plans, have been developed to first crudely identify the important problem variables, and then more precisely measure the impact of the important parameters. A balance should be drawn between the costs of a test, the number of variables to be explored, and the number of tests and measurements required for adequate resolution.

- Random data acquisitions are desirable.

- A goal of an experimental test plan should be a model that will enable predictions about future similar events.

#### FACTORIAL TEST APPROACH

Figures 2 and 3 compare two experimental approaches. The classical approach varies one factor while holding the others constant. Three variables would require four test points. Each variable is compared with the origin point and only tested at one level of the other variables. No replication or repetition is present and the experimental space is one-fourth of a cube. By doubling the number of test points to eight, a basic three-dimensional, two-level factorial design is achieved. Although the number of points doubles, four times the experimental space is covered. In addition the main effect of a single variable can be determined over the range of the remaining variables. The difference between the two dotted planes determines the main effect of variable  $X_1$  in Figure 3. Diagonal planes produce the interaction response of variables. The lined planes in Figure 3 show the planes and test points that would be used for the  $X_1, X_2$  interaction. Replication is inherent in these designs since the effects are the differences of averages. Note also that each data point is used for multiple calculations.

Center points can be added to the factorial cube to produce an estimate of curvature or lack of fit to a linear model. Multiple tests at a center point can also be used to estimate experimental error.

If the number of variables or factors ( $f$ ) and/or the number of levels ( $l$ ) for each variable becomes large, the number of tests ( $n$ ) required for a full factorial design can become large since  $n = l^f$  or  $n = 2^f$  for the common two-level case of Figure 3. Various screening designs that are fractions of a full factorial design, such as the Plackett-Burman [1] and the Box-Behnken [1] have been developed to help identify the key variables. These designs are conceptually the same as the factorial approach in that they bound variable hyperspace with experimental test points. The

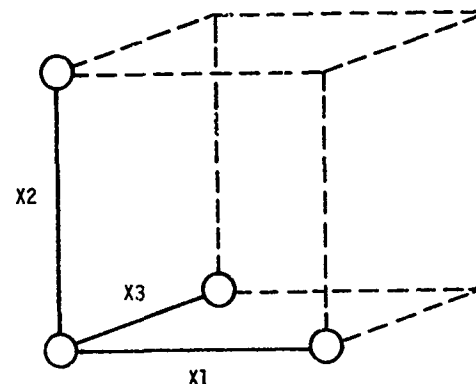


Figure 2. Classical experimental approach.

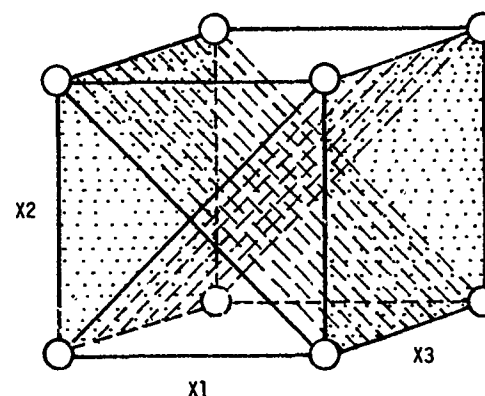


Figure 3. Factorial experimental approach.

bounded volume may change shape depending on the design used.

In planning an experimental test program some guidelines exist to help determine the number of degrees of freedom (tests and measurements) required to detect a factor effect of size  $E$ , in the presence of an experimental error having a standard deviation  $\sigma$ . The number of observations ( $n$ ) required for two-level factorial experiments is approximately

$$n = \left( \frac{8\sigma}{E} \right)^2$$

The 8 stems from the definition of the power of an experiment (2) which is the probability of making the right decision. In this case the  $\alpha$  error, the risk of saying an effect does not exist when it does, is 5 percent (95 percent confidence) and the  $\beta$  error, saying an effect exists when it does not, is 10 percent (90 percent confidence). Thus, to detect an effect twice the experimental error ( $E = 2\sigma$ ), about 16 ( $n = 4^2$ ) observations are required.

## 2<sup>2</sup> FACTORIAL EXAMPLE

Figure 4 represents a simple factorial design for two variables and two levels with four center points. The measured variable readings are listed within the circles of the figure. Table 1 is a convenient computation scheme for calculating the variable main and interaction effects and curvature. The plus and minus signs refer to the high and low levels of each variable and are a shorthand notation for the formula for the following variable effects.

$$\begin{aligned}\text{main effect } X_1 &= \frac{(D + B) - (A + C)}{2} \\ \text{main effect } X_2 &= \frac{(D + C) - (A + B)}{2} \\ \text{interaction effect } X_1X_2 &= \frac{(D - C) - (B - A)}{2}\end{aligned}$$

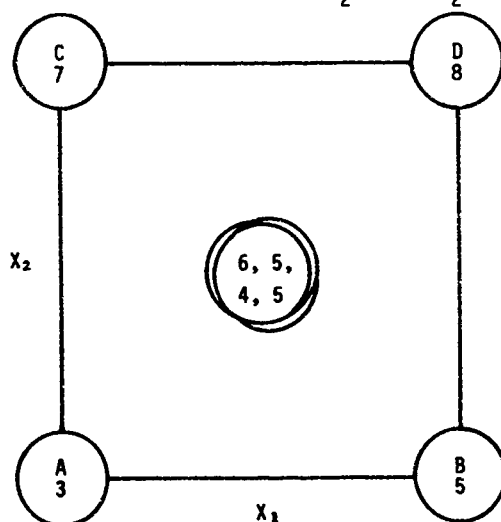


Figure 4. 2<sup>2</sup> factorial with center points.

TABLE 1. FACTOR EFFECT COMPUTATION

Measure location	Average response	Mean	X <sub>1</sub>	X <sub>2</sub>	X <sub>1</sub> X <sub>2</sub>
1 (A)	3	+	-	-	+
2 (B)	5	+	+	-	-
3 (C)	7	+	-	+	-
4 (D)	8	+	+	+	+
Sum +	23	13	15	11	
Sum -	0	10	8	12	
Sum CK	23	23	23	23	
Difference	23	3	7	1	
Effect	5.75	1.5	3.5	0.5	

$$\text{Centerpoint average} = \frac{6 + 5 + 5 + 4}{4} = 5$$

$$\text{Curvature (Mean - CTR PT)} = 5.75 - 5 = 0.75$$

$$\text{Standard deviation of error (S)} = \left[ \frac{(6-5)^2 + (5-5)^2 + (5-5)^2 + (4-5)^2}{(4-1)} \right]^{1/2} = 0.817$$

$$\text{Significant factor effect (2 DF)} \\ t_s \left( \frac{2}{DF} \right)^{1/2} = (3.182)(0.817) \left( \frac{2}{2} \right)^{1/2} = 2.60$$

$$\text{Significant curvature effect (4 DF, 4 center (C) points)} \\ t_s \left( \frac{1}{DF} + \frac{1}{C} \right)^{1/2} = (3.182)(0.817) \left( \frac{1}{4} + \frac{1}{4} \right)^{1/2} = 1.84$$

The standard deviation(s) of the experimental error is estimated from the repeated center points as 0.81. This value is used with Student's *t* value for 3 degrees of freedom (DF) and 95 percent confidence level to estimate the minimum significant factor and curvature effects. Comparing the factor effect to the effects in the table only variable *X*<sub>2</sub> is shown to have a significant effect. The calculated curvature is not significant.

The average response column in Table 1 records the average corner measurement. In this example there was no replication of corner points.

The results might have been improved by measuring each of the corner points a second time. This would have allowed more degrees of freedom and the calculation of a pooled experimental error standard deviation involving both the center and corner points.

The computed factor effects can be directly used in a simple polynomial model of the experimental space.

$$Y = b_0 + b_1X_1 + b_2X_2 + b_{12}X_1X_2$$

where *Y* is the predicted value, *b*<sub>0</sub> the mean, and *b*<sub>1</sub>, *b*<sub>2</sub>, and *b*<sub>12</sub> one-half the factor effects. Thus for the example

$$Y = 5.75 + 0.75X_1 + 1.75X_2 + 0.25X_1X_2$$

the nonsignificant effects might be deleted from this equation. Also ignored are any higher order effects not measured.

## CHEBS TEST PLAN

The first sequence of tests in the CHEBS series was designed to measure the ground level pressure waveforms produced by a general purpose 500-lb bomb (Mark 82) placed both horizontally and vertically on the ground surface (bomb center of gravity at ground level).

It was recognized that at least three components of variance were present: experimental

error ( $V_{EX}$ ); blast nonsymmetry ( $V_{SY}$ ), particularly in the horizontal orientation case; and bomb-to-bomb variation ( $V_{BB}$ ). A characteristic of variance (standard deviation squared and a measure of data dispersion) is that it is additive. Thus the total variance might be simply expressed

$$V_T = V_{EX} + V_{SY} + V_{BB}$$

It was recognized that other--it was hoped smaller--contributions exist and that they would be folded into the above components. However, by the variance analysis of various data subgroups it is possible to estimate the various components of the total variance.

The test plan evolved into the pressure gage grid placed around the bomb shown in Figure 5 and a test sequence of four horizontal and two vertical bombs. A multiple-bomb program was required to allow the measurement of  $V_{BB}$  and to allow adequate replication. The horizontal bombs were aimed in the 0, 90, 180, and 270° directions, thus effectively sweeping the higher resolution gage area (0-45°) around the bomb. The number of gages on the reusable test pad and the initial cost of the test pad were larger cost items than the cost of the bombs.

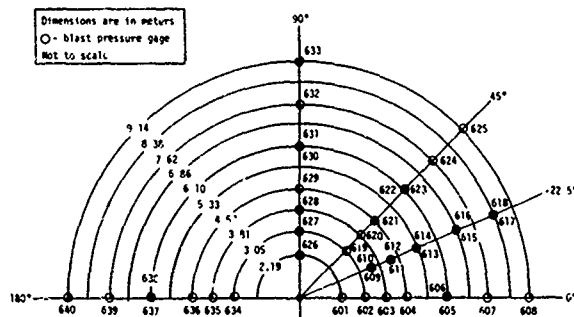


Figure 5. Test bed layout for CHEBS I-VI tests.

The basis of the gage grid, represented a little differently in Figure 6, is a series of two-dimensional factorial boxes intersecting over the region of interest. Gage spacings were based on predicted pressure levels with range. The CHEBS design incorporates a number of double gage points on the 22.5° azimuth and the 6.1-m range. The double gage locations allow the determination of experimental error and also serve as center points in the factorial box.

The center point determination of experimental error is an approximation. Normally center points are replicated by repeating the event. In this case similar gages on the same concrete pier measured the same event. This estimate of experimental variance avoids the addition of  $V_{BB}$  and

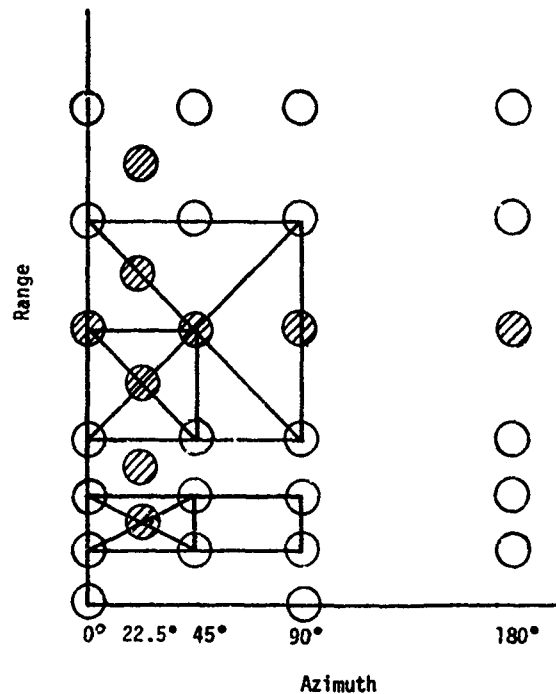


Figure 6. Factorial gage layout.

uses the technique of pooled variance, which is simply a degree of freedom weighted average of separate variances. The pooling technique assumes, however, that the population variance is about the same for all levels of range, azimuth, and so forth. This is often not the case. In cases where gage error can be approximated as a constant percentage of the actual reading some kind of normalization procedure is needed. One technique is to calculate variances on the logarithms of the numbers [3]. Another method, dividing each variance by the local mean squared, which is the same as dividing each double gage value by the local mean, was developed and used in this study.

Nonsymmetry can be detected by comparing one azimuth with another. For example, bomb nose-tail symmetry could be examined by comparing azimuth 0° and 180° for two of the horizontal bombs. Bomb-to-bomb variance can be calculated by pooling like azimuths (nose, tail, side) for all bombs and finding the total variance. Since this grouping would also include experimental error variance, which has been estimated, a subtraction produces the desired bomb-to-bomb variance.

#### CONCLUSION

The techniques and applications of the statistical design and analysis of experiments are broader than indicated by this brief overview.

The process of identifying the purpose of a test, developing an experimental plan that produces meaningful and economic tests, and, finally, having a scheme of data analysis that is both simple and powerful in the interpretation of experimental data merits consideration in every experimental test situation. The most attractive feature of the statistical design process is that the procedures have been developed and are simply waiting to be utilized.

#### REFERENCES

- [1] "Strategy of Experimentation," Applied Technology Division, E.I. duPont de Nemours and Co., Wilmington, DE, 1975.
- [2] C. Lipson and N.J. Sheth, Statistical Design and Analysis of Engineering Experiments, McGraw-Hill, New York, 1973.
- [3] W.E. Duckworth, Statistical Techniques in Technological Research, Methuen and Co., London, 1968.
- [4] E.G. Schelling, Acceptance Sampling in Quality Control, Marcel Dekker, Inc., New York, 1982.
- [5] S.L. Meyer, Data Analysis for Scientists and Engineers, John Wiley and Sons, New York, 1975.
- [6] R.E. Crawford et al., "Protection from Non-nuclear Weapons," AFWL-TR-70-127, Air Force Weapons Laboratory, Kirtland AFB, NM, Feb. 1970.

AD P001720

## BLAST RESPONSE TESTS OF REINFORCED CONCRETE BOX STRUCTURES

David R. Coltharp

U. S. Army Engineer Waterways Experiment Station  
Structures Laboratory  
Vicksburg, Mississippi

### ABSTRACT

Six explosive tests were conducted against reinforced concrete walls to determine the effect of steel reinforcement design on structural response and damage. Reinforcement percentages varying from 0.25 to 2.0 and two reinforcement designs (one with shear stirrups and one with shear dowels) were tested. Test specimens consisted of box structures with 32.5-cm-thick walls. Cased-explosive charges were detonated on the ground near one of the walls of the box. Test structures were instrumented to record blast-pressure loading, steel strains, wall deflection, in-structure acceleration, and concrete-spall velocities. Damage to the walls (similar for all tests, differing only in severity) consisted of a region near the bottom center where the concrete on the wall interior spalled and cracked coupled with a flexural-type response. The loading of the walls was more severe than predicted and the majority of the structural damage was due to spalling.

### INTRODUCTION

#### Background

The design of aboveground reinforced concrete facilities for protection from near-miss detonations of air-delivered bombs has for many years been based on conservative procedures. Recent tests (References 1 and 2) have indicated that these procedures produce overly conservative steel reinforcement designs and that lower-than-recommended steel percentages could be used. To better quantify the effect of reinforcement design on the response to nearby detonations, a series of scale-model tests were conducted. The Air Force Engineering Services Center (AFESC), Tyndall AFB, managed the program. The U. S. Army Engineer Waterways Experiment Station (WES) planned the test series and designed the test specimens and instrumentation. The test structures were constructed by the AFESC. The Air Force Weapons Laboratory (AFWL) provided instrumentation support and acted as test director. The first phase of testing (six tests) was conducted in August-September 1982 at Tyndall AFB. This paper presents the results of those tests and plans for the

second test series to be conducted in October-November 1983.

#### Objective and Approach

The objective of the first test series was to determine the effect of various reinforcement designs on the response of concrete walls to nearby surface detonations of cased explosive charges. Six tests were conducted with explosive charges detonated at a given standoff from one-half scale model structures. All tests were instrumented with active and passive gages and high-speed photography to obtain data on the loading and response of the walls.

### EXPERIMENTAL PROCEDURES

#### Test Structures

Three reinforced concrete box-type structures were constructed for use as test specimens. Each box had a floor, roof, and two test walls and was open at both ends (Figure 1). The boxes were 4 m long, 2.3 m high, and 2.3 m wide. The floor, roof, and walls were each 32.5 cm thick. The test structures represented one-half scale models of full-scale generic structures. For identification, they were labeled as Structures A, B, and C. The steel reinforcement percentages used are presented in Table 1. The main test parameters were the wall-reinforcement percentage which varied from 0.25 to 2.0 percent and the use of either shear stirrups (which provided confinement and tied the front and rear face steel together) or shear dowels (which offered resistance to direct shear). Typical reinforcement details are shown in Figure 2.



Figure 1. Placement of test specimen in reaction structure.



Box/Element	Principal Steel	Longitudinal Steel	Shear	Shear
	% Each Face	% Each Face	Stirrups %	Dowels %
A,B,C/floor, roof	0.25	0.13-0.25	0.09-0.39	--
A/2.0 wall	2.05	0.25	0.34-0.69	---
A/0.25 wall	0.25	0.25	0.20-0.39	---
B/1.0 wall	1.00	0.25	0.34-0.69	---
B/0.5 wall	0.49	0.25	0.39-0.78	---
C/0.5 wall	0.49	0.13	--	0.45
C/0.25 wall	0.25	0.13	--	0.22

Table 1. Test structure reinforcement percentages.

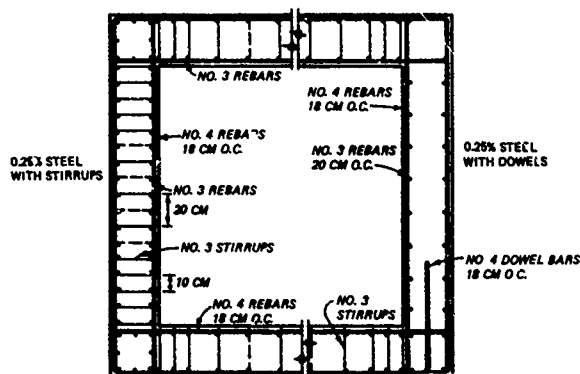


Figure 2. Typical steel reinforcement details.

#### Reaction Structure

Each of the test structures was affixed to a reaction structure prior to testing. This structure (Figure 1) served to minimize rigid-body translation and rotation of the test box and consisted of an L-shaped reinforced concrete structure and six 1.22- by 1.22- by 2.44-m concrete blocks. The L-shaped structure was attached to the blocks with long rods and was positioned so that the upper-floor surface of the box structures would be flush with the ground surface. Soil was bermed up on the rear side of the structure to further aid in reducing rigid-body motion.

#### Material and Structural Properties

The concrete mixture used for the structures was designed to give a 28-day compressive strength of 31.0 MPa. Actual data from test cylinders gave an average strength of 30.7 MPa at 28 days and 35.7 MPa at time of testing.

The reinforcement steel was specified as ASTM A615-68, Grade 60, having a design minimum yield strength of 413.8 MPa and a minimum ultimate strength of 496.6 MPa. Actual tests of a random sample of the reinforcing bars used in the structures gave an average yield strength of 517.5 MPa and an average ultimate strength of 810.1 MPa. Approximately one month after casting the structures, the walls were nondestructively tested to determine their fundamental modal frequencies and damping characteristics. The frequencies ranged from 147.6 to 157.0 Hz. Damping ranged from 2.3 to 3.8 percent critical.

#### Measurements

The gage layout for the active instrumentation used in the tests is shown in Figure 3. It was chosen and located to measure:

- Airblast load imposed on the wall and roof surface.
- Strain induced in the reinforcement steel.
- In-structure motion (acceleration, velocity, and displacement).
- Relative displacement of the test wall.

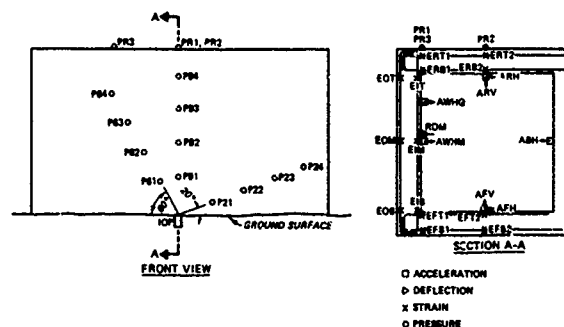


Figure 3. Gage location.

In addition to the active gages, passive scratch gages were used to measure the peak and permanent displacement of the wall.

High-speed cameras were used to record the velocities of fragments generated from the metal case surrounding the explosive charge and the velocities of concrete spall fragments. One camera viewed a fragment-witness plate located near the explosive charge to record the time of fragment impact from which metal case fragment velocities were calculated. Two other cameras were located to view the interior of the box structure and record crack formation, wall motion, and concrete spall fragment position versus time.

Pretest and posttest measurements were made of the box location to record rigid-body motion and of permanent wall deflection at various locations.

### Explosive Charges

All charges were fabricated by packing composition C-4 explosive into a cylindrical metal container. The explosive weight and type and the metal case thickness and diameter were chosen to simulate a scaled specified weapon.

### Test Procedure

Table 2 presents the order of the tests and the main test parameters. The general arrangement for each of the tests is shown in Figure 4.

Test No.	Test Structure	Wall Reinforcement
1	B	1.0% with stirrups
2	B	0.5% with stirrups
3	C	0.5% with dowels
4	C	0.25% with dowels
5	A	2.0% with stirrups
6	A	0.25% with stirrups

Table 2. Test sequence.

Prior to the start of testing, the reaction structure was positioned and assembled so that its bottom face was approximately 2 ft below the ground surface. The ground surrounding the reaction structure was then made level out to approximately 50 ft in front of the structure. Preparation for the individual tests proceeded as follows:

- The test specimen was placed in position on the reaction structure and secured with bolts.
- Instrumentation was prepared and the original measurements of structure location and wall deflections were made.
- Lighting for the cameras was installed and special concrete closures were attached to each end of the box.
- Cameras viewing the interior of the box were positioned and prepared.
- The fragment-witness plate was installed along with the high-speed camera that viewed it.
- The area in front of the box was sprayed with a special dust retardant.

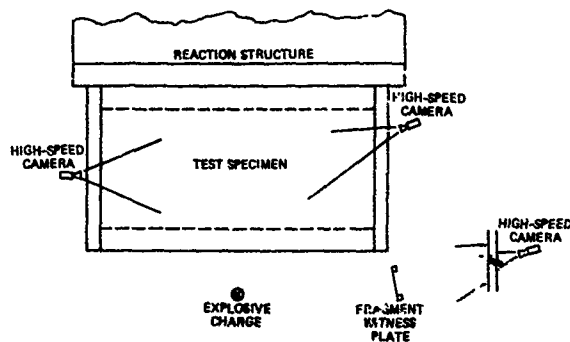


Figure 4. Typical test setup.

g. The charge was emplaced and armed.

h. Final checks were made, the final count-down began, and the charge was detonated.

After each test, the following procedure was used:

- Still photographs were taken of the undisturbed damage on the exterior of the box, i.e., the soil crater, front wall damage, roof damage, etc.
- Measurements were made of the crater dimensions.
- The cameras, end closures, lighting, and instrumentation cables were removed, and photographs were made of the interior damage.
- Measurements were made of the posttest structure location and wall deflection.
- Major cracks were marked and a drawing was made of the interior wall damage.

### TEST RESULTS

#### Pressure Data

The six-test average of the peak pressure and time-of-arrival data was used to plot the curves shown in Figures 5 and 6, respectively. Peak

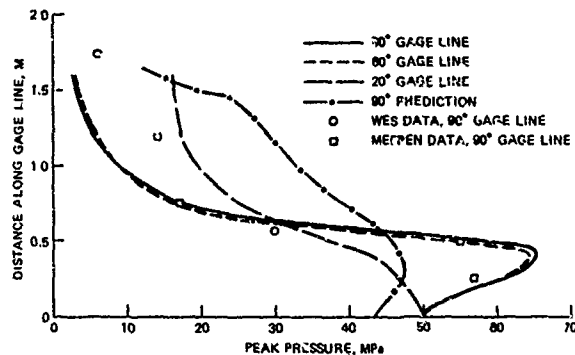


Figure 5. Peak pressure distribution along gage lines.

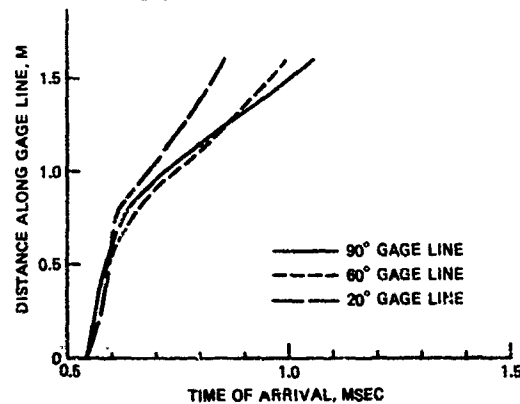


Figure 6. Blast wave arrival times.

pressure data for similar tests conducted by the WES (Reference 3) and by the German Infrastructure Staff in tests at Meppen (Reference 4) are also plotted in Figure 5. A predicted pressure distribution is shown for the 90-deg gage line. This distribution was determined from Reference 5, assuming a hemispherical surface burst. The plots of Figure 5 were used to estimate the isobars shown in Figure 7. To determine the spatial distribution (Figure 8) of the blast load on the wall at various times, data from each test were analyzed and averaged.

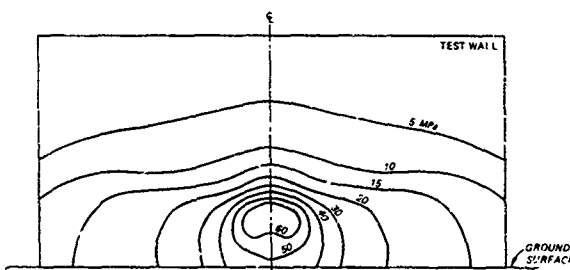


Figure 7. Peak-pressure distribution on wall.

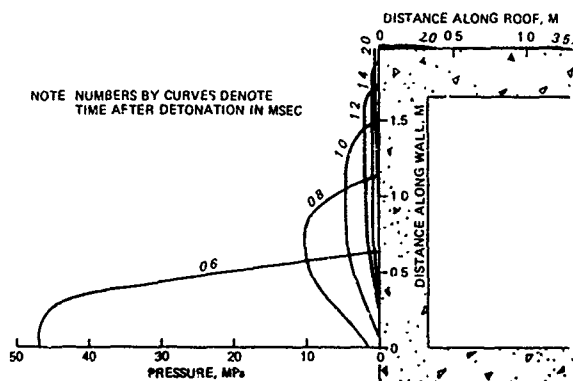


Figure 8. Typical pressure distribution on wall for various times along 90-deg gage line.

#### Acceleration Data

Peak accelerations for the various gage locations are presented in Table 3. Analysis of the acceleration records for velocity and displacement is not yet complete. Preliminary analysis of the records indicate that the high frequency, early time acceleration is due to the transmission of the shock through the concrete. Later time acceleration is due to wall motion. From the arrival time of the acceleration pulse, it was estimated that the longitudinal sound velocity of the concrete was approximately 3735 m/s. It was also noted that the stress wave transmitted through the concrete was the major contributor to the acceleration recorded by gages on the floor, roof, and back wall (gages AFH, AFV, ARH, ARV, and ABH).

Test No.	Gage						
	AWHQ	AWHM	ARH	ARV	AFH	AFV	ABH
1	6500	11,000	580	750	-1250	*	*
2	3500	6,250	800	-450	*	*	-325
3	4500	8,000	1400	650	*	*	*
4	6500	10,000	400	1100	*	*	200
5	3000	--	900	1800	*	*	*
6	3500	15,000	800	600	*	*	400

\* Data invalid.

Table 3. Peak acceleration data (g's).

#### Deflection Data

The peak deflections, as measured from the active displacement and scratch gage located at the midspan of the structure, are presented in Table 4. Plots of deflection versus time are shown in Figure 9. The record for test 5 was invalid and is not shown. The gages located at the lower quarter-span point failed to function due to the heavy spalling of the concrete in this region.

Test No.	Gage	
	RDM Maximum/Permanent	Scratch Maximum/Permanent
1	15.5/4	16/4
2	23/8	23/8
3	76/*	74/*
4	57/35	62/40
5	*	*
6	37/13	40/17

\* Data invalid.

Table 4. Wall deflection data (mm) at midspan.

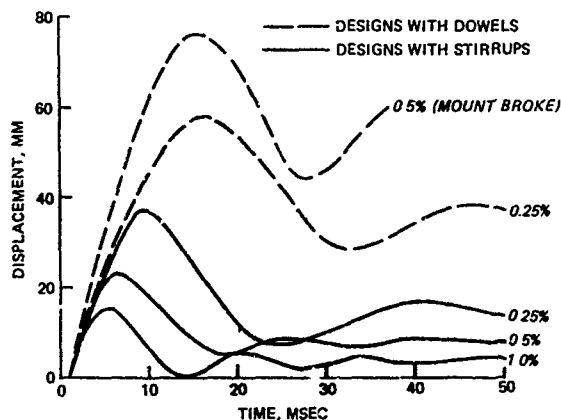


Figure 9. Deflection versus time data from displacement gage RDM.

#### Fragmentation Data

Peak fragment velocities calculated from the time-of-arrival of the fragments at the steel-witness plate ranged from 2613 m/s to 2706 m/s.

Judging from the location of the perforations of the witness plate, it appeared that the majority of the fragments were traveling downward at an angle of 4 to 6 deg below horizontal. Fragment impacts on the test walls were concentrated in the lower one-third of the span and maximum fragment penetration into the concrete ranged from 5 to 6 cm (Figure 10).



Figure 10. Typical damage to exterior of test wall showing numerous fragment impact.

#### Spallation

Spalling of the lower portion of the interior of the wall occurred in all tests. Camera records indicated peak spall velocities of from 15.8 to 28.0 m/s. (There was no apparent correlation between steel percentage and spall velocity.) The spalling occurred early in time (within 2 msec after detonation) and spall fragments varied in size from dust and aggregate size particles to larger pieces on the order of 20 to 30 cm long. The maximum measured depth of the spall was on the order of 6 cm. However, it appeared that the reinforcing mat retained some of the spalled concrete so that the true spall depth may have been greater. Figure 11 shows a typical spalled area and crack pattern for one of the walls. The spall region was generally 60 to 80 cm high and 200 to 230 cm wide.

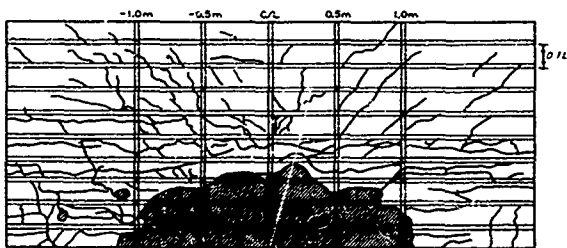


Figure 11. Cracks and spall region for test 1.

#### Structural Damage

Figures 12 and 13 show typical damage to the interior of the test wall. As shown, structural damage to the walls was localized in the region of the spall. None of the tests resulted in a breach of the structure. However, the concrete was cracked and loosened to such an extent in test 4 (0.25 percent steel, shear dowels, no stirrups) that it was fairly easy to manually poke a rod all the way through the wall.

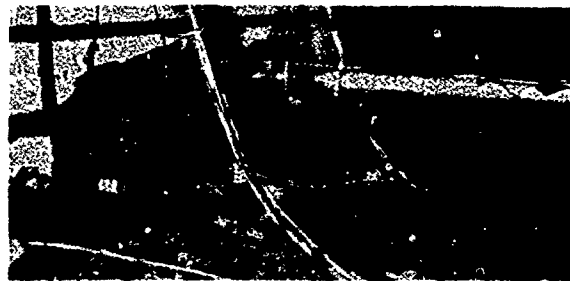


Figure 12. Damage to interior of wall for test 1.



Figure 13. Damage to interior of wall for test 3.

Both radial and longitudinal (horizontal) cracking was evident on the interior of the walls. In addition, tests 1, 2, 3, and 5 resulted in a noticeable longitudinal crack in the roof at the wall support (Figure 14), indicating rotation of the wall relative to the roof. The crack location was due to the larger stiffness of the wall when compared to the roof. Where both the roof and wall had 0.25 percent reinforcing and approximately the same stiffness (tests 4 and 6), cracks were not noticed.

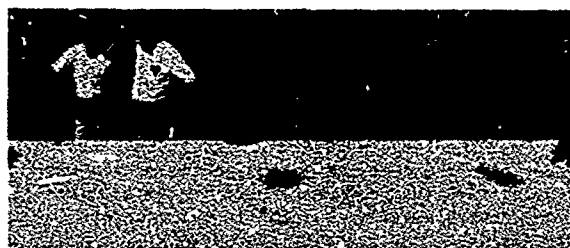


Figure 14. Crack in roof from test 2.

Tests 1 and 5 with 1 and 2 percent reinforcing showed no significant structural damage other than loss of the concrete cover in the region of the spall and fragment impact. In tests 2 (0.5 percent) and 6 (0.25 percent), the concrete was noticeably cracked behind the interior reinforcing steel and several of the stirrups began to unbend in the region of the spall.

Tests 3 and 4 (0.5 and 0.25 percent, respectively, with dowels) gave the largest deflections of the test series and resulted in the most structural damage. The concrete in the wall was heavily cracked and loosened. For test 4, breach of the wall was judged imminent.

## CONCLUSIONS

### Loading

The blast-pressure loading recorded on the exterior face of the wall showed that the charge's cylindrical geometry had a large effect on the pressure distribution. The peak pressures are higher on the lower portion of the wall and lower on the upper portion than those predicted using current spherical charge data curves. Also, the pressure distribution is highly transient being concentrated near the bottom of the wall in early time and then spreading to a lower magnitude, almost uniform load later in time.

The test results indicated that the fragment impact on the lower portion of the wall adds to the blast-pressure loading in that region. Data showed that the fragments impacted the wall at or near the time of arrival of the blast wave.

### Spallation

The results indicated that the occurrence of spalling depends primarily on the transmission of the blast-induced stress wave in the wall and not on the walls' structural response (or steel percentage). Spall velocities (calculated from one-dimensional, unattenuated stress-wave propagation through the wall, using the pressure data for gage P91 as input) were on the order of 15 m/s. Recorded velocities were generally higher and could be due to the added stress waves generated from fragment impact.

### Structural Response

In all the tests, the response of the walls was similar differing only in severity. It consisted of a local region of damage near the bottom center of the wall coupled with an overall flexural response, typical of a one-way slab under uniform loading. This type of damage is consistent with previous similar tests. The response mechanism appears to be as follows:

- a. The large magnitude, highly concentrated blast pressure near the bottom center of the wall, coupled with the fragment impact in the same region, causes a spall to occur in the concrete on the inside of the interior face steel.
- b. The spalled concrete that is not contained by the rebars breaks loose and flies off the wall into the interior of the structure.
- c. The part of the spall behind the interior face steel begins to place a load on these rebars.
- d. The interior steel tries to contain the spall and responds to it in what appears to be a membrane mode. In principle, for those walls with stirrups, some of the spall load on the interior steel is transferred to the exterior face steel through the stirrups. In the actual tests, some of these stirrups began to unbend (due to their design), thereby negating their effect. However, it was clear from the tests that the stirrups

significantly reduced the wall deflection (by transferring some of the load to the exterior face steel and/or confinement of the concrete).

- e. At some time during this localized response, the wall undergoes a more uniform blast loading and begins a flexural response typical of a one-way slab.

## SECOND TEST SERIES

A second test series will be conducted at Tyndall AFB in October-November 1983 to evaluate: (a) Methods of reducing or eliminating spallation of the wall by using thicker walls or spall plates, (b) A more conventional shear-stirrup design (closed-rectangular loop versus the single-open stirrups used in the first test series), and (c) Effect of aboveground detonation (e.g., center of gravity of charge at midheight of wall) on spalling and structural response.

This series will consist of eight tests (Table 5) on box structures similar to those used in the first series.

Test No.	Steel %	Wall Thickness cm	Spall Plate	Stirrup Design
1	0.5	32.5	X	Single
2	0.25	32.5	X	Single
3	0.5	32.5	X	Closed
4	0.25	32.5	X	Closed
5	0.17	40		Closed
6	0.09	55		Closed
7	0.5	32.5	X	Closed
8*	0.5	32.5	X	Closed

\* Charge located aboveground at midspan of wall for this test only.

Table 5. Test parameters for second test series.

## REFERENCES

- Pahl, H. and Kropatscheck, M., "Explosive Tests on Reinforced Concrete Elements Performed by Test Site 91 of the Federal Armed Forces at Meppen," Infrastrukturstab der Bundeswehr, WWTB-80-17, Summer 1980.
- Loos, G. and Pahl, H., "Explosive Tests on Underreinforced Model Structures in Incirlik (Republic of Turkey) and Meppen (Federal Republic of Germany)," Infrastrukturstab der Bundeswehr, TB-82-01, January 1982.
- Coltharp, D. R., "Preliminary Data Report: Explosive Tests on Reinforced Concrete Walls at Camp Shelby, Mississippi," unpublished.
- Kropatscheck, M., "Explosive Tests on Underreinforced Model Structures at Proving Ground 91 of the Federal Armed Forces of Germany at Meppen," Infrastrukturstab der Bundeswehr, WW-TB-82, January 1983.
- Department of the Army, TM 5-1300, "Structures to Resist the Effects of Accidental Explosions," June 1969.

AD P001271

## CONCRETE BRIDGES SUBJECTED TO IMPULSIVE LOADING FROM FUEL-AIR EXPLOSIVES

BRIAN HOBBS

University of Sheffield, Department of Civil and Structural Engineering, Mappin Street, Sheffield, S1 3JD, U.K.

## ABSTRACT

This paper is concerned with an analytical study of the effect of distributed impulsive loading on a range of concrete bridge types. The principal area of interest is collapse behaviour and the establishment of criteria for effective demolition by means of fuel-air explosives. The basis of a simplified analytical approach developed for this work is outlined. Existing data from tests on small scale metal beams is used to assess the accuracy of the analytical method and it is shown that the agreement is good for levels of loading which produce significant permanent deformations. The application of this analysis to reinforced and prestressed concrete bridges is discussed and a sample of nine representative bridges is selected for detailed consideration. Analytical results relating the expected permanent midspan deflection to the total impulse delivered by the explosion are presented. Criteria for effective demolition are discussed and the calculated critical impulse loadings required to cause bridge collapse are shown to range from 18 kNsec/m<sup>2</sup> to 46 kNsec/m<sup>2</sup>. These results are compared with those of a previous investigation concerned only with steel bridges.

## 1. INTRODUCTION

The work described in this paper was carried out as part of a research and development programme funded by the U.K. Ministry of Defence and aimed at improving the bridge demolition techniques employed by the British Army. It was known that mixtures of some common fuel vapours with air may be detonated when the proportions are within certain limits. The resulting explosion produces a high intensity, short duration pressure pulse on any surface with which the vapour cloud is in contact. It was suggested that such fuel-air explosives might be used as a rapid bridge demolition technique, the aim being to produce an overall pressure overload on the top surface of the bridge deck.

Little information was available on the response of bridges to this type of loading and none related to concrete bridges. In order to assess the order of magnitude of the impulsive loadings required to effect demolition, an analytical study of the response of beam structures to impulsive loading was undertaken. There is a considerable amount of uncertainty about the response of large concrete structures to heavy dynamic loads and the use of suitable approximate methods of analysis is thus frequently appropriate. The development of such methods was pioneered by Newmark [1], and their appli-

cation to a range of problems has been described by Biggs [2]. For the present study, it was decided that this basic approach should be developed to take into account the important effect of material strain rate sensitivity. The analytical procedure developed was then applied to a range of simply supported reinforced and prestressed concrete bridge types.

## 2. DEVELOPMENT OF METHOD OF ANALYSIS

## 2.1 Idealization of the Loading

The pressure-time curve for the loading produced by fuel-air explosions usually exhibits an essentially instantaneous rise to the peak pressure followed by an approximately exponential decay. It has been shown by Symonds [3] and by Abrahamson and Lindberg [4] that if the peak pressure of a short duration impulse of this form exceeds 10 times the static collapse pressure of the loaded beam then the loading may be treated as an ideal impulse. This means that only the magnitude of the impulse, i.e. the area under the pressure-time curve, is significant. The precise magnitudes of the peak pressure and the duration of loading need not be considered. The static collapse pressure for most bridge decks is of the order of 50-100 kN/m<sup>2</sup> and the peak pressure produced by a fuel-air explosion is generally in the range 2000 to 3000 kN/m<sup>2</sup>. Also the natural period of vibration of most bridge decks is of the order of 50-200 msec whereas the duration of the positive phase of the pressure-time curve is usually of the order of 1-5 msec. Thus the impulsive loading on bridge decks due to fuel-air explosive may be treated as an ideal impulse for the purposes of calculating the overall response.

## 2.2 Material Behaviour

Most structural materials exhibit strain-rate sensitivity in their behaviour under dynamic loading, i.e. their yield or failure stress increases as the rate of deformation increases. For metals the relationship governing this behaviour is usually taken as:-

$$\frac{f_{yd}}{f_y} = 1 + \frac{\dot{\epsilon}}{D}^{1/p} \quad \dots (1)$$

where  $f_{yd}$  and  $f_y$  are the dynamic and static yield stresses,  $\dot{\epsilon}$  is the strain rate, and  $D$  and  $p$  are constants. For mild steel the values of these constants giving the best representation of the available test data are  $D = 40$  and  $p = 5$  [5].

Concrete also exhibits strain-rate sensitivity but the available test results contain a great deal of scatter and no investigation has yet covered the

same wide range of strain-rates over which data is available for mild steel. Mainstone[6] summarised the results obtained up to 1975 and it is evident that both the compressive strength and the modulus of elasticity are affected by the rate of straining. The effects tend to reduce somewhat as the strength of the concrete increases, and may be influenced by factors such as the precise mix proportions and the type of aggregate used. For high strength concretes (40-60 N/mm<sup>2</sup> static cube strength) it appears that, at the strain rates relevant to this investigation (10<sup>-1</sup> to 10 per sec.), both the elastic modulus and the compressive strength may be expected to increase by between 30% and 50%. More recently published work by Hughes and Watson [7], however, indicates no effect of strain rates below about 8 per sec. and average increases in strength of 10% and 25% at 10 per sec. and 14 per sec. respectively. There is thus, as yet, no generally accepted relationship for concrete equivalent to equation(1). It does appear, however, that strain-rate effects in concrete may be rather smaller than in mild steel.

In developing a method of analysis for impulsively loaded beams, it has been assumed that strain-rate effects may be accounted for by the incorporation of a relationship of the type given in equation(1). The effects of strain hardening at large deformations have been ignored since it has been shown that its effects are not significant at high rates of straining[5]. The significance of these assumptions in applying the method to bridge decks is discussed in section 3.2

### 2.3 Mode of Deformation

The primary mode of deformation has been assumed to be flexure and the collapse mechanism considered is shown in Figure 1.

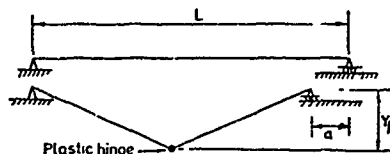


FIGURE 1. Assumed Collapse Mechanism

The use of such mode approximations involving stationary displacement fields allows the structure to be represented by an equivalent single degree of freedom system having the same displacement-time history. This technique greatly simplifies the analysis and has been employed in various investigations of structural response to blast waves[1,2] and has also been used by Kaliszky[8] in the analysis of concrete pressure vessels and other structures under the influence of impulsive loading. It is thus a well established procedure and is thought to be capable of giving reasonably accurate results, despite the great simplifications of the real structural behaviour that are involved.

### 2.4 Basis of the Analysis

The analysis is based on an energy approach similar to that proposed by Newmark[1] for dealing with blast loading. The method has been adapted to cater for the ideal impulse loading, with effectively zero

duration, as opposed to the very much longer duration blast loading. The permanent deflection of the structure is computed on the assumption that all of the initial kinetic energy imparted by the impulsive loading is absorbed by the work done in plastic rotation of the central hinge. This has been shown to be valid in rigid-plastic analyses provided that the duration of loading is short compared with the natural period of the structure and that the input energy is significantly greater than the elastic strain energy capacity of the system[9, 10]. It has already been shown that the first condition is satisfied for the loading from fuel-air explosions and, since damage to bridge decks will only become significant when the deflection is considerably greater than the maximum elastic deformation, the second condition must be satisfied for impulses of interest to this investigation.

It is assumed that the moment/rotation characteristic for the central hinge is bi-linear in form, as shown in Figure 2.

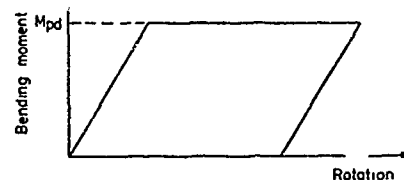


FIGURE 2. Moment/Rotation Characteristics

The impulsive load is applied at the beginning of the elastic phase of the motion and the kinetic energy imparted has therefore been computed using the elastic properties of the structure. It is in this respect that the analysis differs from the simple rigid-plastic mode approximation techniques. Although the actual behaviour of beams will vary somewhat from the idealized form shown in Figure 2 the effect of these differences on the calculated central deflection will be very small[1,2]. It has been shown by Bodner[10] and Perrone[11] that the effects of strain rate sensitivity may be accounted for with sufficient accuracy by the use of a single overall correction factor for the yield or failure stress of the material. This is because the form of equation (1) is such that it is only necessary for the strain rate,  $\dot{\epsilon}$  to be of the correct order of magnitude for the dynamic yield stress,  $f_{yd}$ , to be accurate to within a few per cent. For the purposes of these calculations the strain rate,  $\dot{\epsilon}$ , has been taken as the average strain rate over the initial elastic portion of the moment/rotation characteristic. Due to the idealized bi-linear nature of the moment/rotation characteristic, this procedure is not rigorous, but it gives strain rates of the correct order of magnitude and therefore provides a simple and sufficiently accurate method of taking into account the effects of strain rate sensitivity.

Clearly no permanent deflection of the bridge deck will be produced unless the energy imparted by the impulse loading is greater than the maximum elastic strain energy that can be absorbed by the system. Thus there is a critical impulse,  $i_c$ , below which no permanent deformation of the bridge deck will occur, the only effect of the fuel-air explosion

being to start vibrations of the bridge deck which will slowly die away due to the natural dumping of the system.

The detailed derivation of equations for the strain rate, the mid-span permanent deflection  $y_p$  and the elastic critical impulse  $i_c$  has been presented elsewhere [12].

## 2.5 Comparison with Test Data

The results of an extensive test programme on small scale beams subjected to uniformly distributed impulsive loading have been reported by Florence and Firth [13]. The tests were conducted using small scale rectangular beams and sheet explosive was used to provide the impulsive loading. Approximately half the beams tested were made from aluminium and the remainder were made from CR1018 steel. Most of the steel beams were tested on the untreated condition with a yield strength of 580 N/mm<sup>2</sup>, but five of the simply supported beams were annealed to give a yield strength of 296 N/mm<sup>2</sup>. The method of analysis developed herein is specifically intended for strain rate sensitive, elasto-plastic beams and is not therefore suitable, in its present form, for application to the aluminium beams. The application of the method depends upon a knowledge of the constants in equation (1). The annealed test beam might be expected to correspond closely to mild steel, for which the values  $D = 40$  and  $p = 5$  are appropriate. A comparison between these test results and the results calculated using the procedure outlined herein, is shown in Figure 3. In the absence of any better information for untreated CR1018 steel, the same constants have been used to obtain the calculated results for these beams and these are also shown in Figure 3.

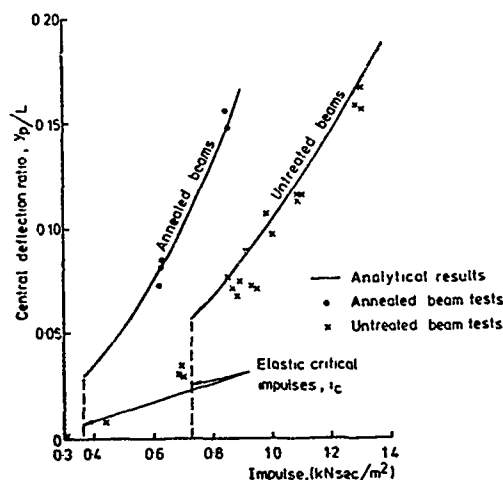


FIGURE 3. Comparison with Test Results of Florence and Firth [13]

There is considerable scatter in the test data but it is seen that there is good agreement between the calculated and test results for the annealed beams, and for the untreated beams when the impulse is significantly greater than  $i_c$ . The calculated effect of the strain rates in these tests is to

increase the yield stress by between 45% and 60%. This highlights the importance of accounting for this effect when interpreting data from model tests, since the strain rates experienced by large massive structures, such as concrete bridges, may differ considerably from the very high rates present in small scale structures.

The execution of experimental work of this type is very difficult and the results may be affected by many factors. The differences between the predictions of the proposed analysis and the experimental results at low impulse values may be partly due to elastic vibrations in the beams, and this has been discussed in detail by Symonds [9]. In addition the assumption of a sudden change from purely elastic to purely plastic behaviour as the motion passes the limiting elastic displacement is obviously a gross simplification. For beams of solid rectangular section the first yield moment is only 2/3 of the fully plastic moment and the threshold impulse, at which some permanent deformation first takes place, might be more accurately assessed on this basis. This would reduce the relevant values of  $i_c$  to approximately 0.24 kN sec/m<sup>2</sup> and 0.43 kN sec/m<sup>2</sup>. This effect would be less serious in actual bridge structures since the yield moment is generally rather closer to the plastic moment. This investigation is concerned, however, with larger impulses which cause substantial permanent deflections. This was therefore considered to be of sufficient accuracy over the relevant range of impulsive loadings.

## 3. APPLICATION TO CONCRETE BRIDGE DECKS

### 3.1 General

The method has been applied to a sample of bridge designs selected so as to represent a wide range of span lengths and construction types, details are given in Table 1.

Reference No.	Type of Construction	Span (m)
RS2	Reinforced concrete slab	5.5
RS10		9.7
RS13		14.1
RB3	Reinforced concrete beam-and-slab	9.1
RB14		15.7
RB16		22.3
PS18	Pre-tensioned I beam with in-situ top slab	23.0
PS22	Pre-tensioned inverted T beam with in-situ top slab	25.0

TABLE 1. Bridge details

In order to give results which are on the same basis as the demolition requirements derived for other techniques [14], the probable variations in the properties of the materials in bridge decks have been allowed for by assuming upper bound material strength values. These strengths were estimated from a statistical analysis of various test data for bridge concrete, reinforcing bars and prestressing tendons. The upper bounds were taken as the strength values above which only 5% of the results



would be likely to fall. In addition an allowance was made for long term ageing effects in concrete. The resulting upper bound strengths were  $65 \text{ N/mm}^2$  and  $84 \text{ N/mm}^2$  for concrete in reinforced and prestressed concrete bridges respectively,  $350 \text{ N/mm}^2$  and  $520 \text{ N/mm}^2$  for mild and high yield steel reinforcing bars and  $2000 \text{ N/mm}^2$  for prestressing strand. This means that for most bridges the actual deformation due to impulsive loading may be greater than that calculated herein, but this approach puts these calculations on the same conservative basis as the previous demolition damage calculations. Another slightly conservative approximation that was made throughout is that the effect of the bending moment due to self weight of the bridge deck has been ignored. The influence of this on the calculated results will be small, however, since the self weight moment is generally small in relation to the dynamic collapse moment.

### 3.2 Reinforced Concrete Bridges

The stiffness in the initial elastic range is based on the gross concrete section. The modulus of elasticity used was estimated from the values given in BS 5400[15]. This value was then increased by 40% in order to allow for strain rate effects, yielding a dynamic modulus of  $51 \text{ kN/mm}^2$  for a cube strength of  $65 \text{ N/mm}^2$ . The value of  $M_{pd}$  for the idealized moment rotation characteristic has been based on the value of ultimate moment of resistance,  $M_u$ , calculated according to BS 5400. Since RC bridge decks are always under-reinforced, the value of  $M_u$  is governed primarily by the yield force in the tension reinforcement. It has therefore been assumed that the value of  $M_{pd}$  is directly proportional to the dynamic yield stress of the reinforcement and, in the absence of any better information, the values of  $D$  and  $p$  for mild steel have been applied to both mild and high yield steel reinforcement. The strain rate was calculated using the static modulus of elasticity of the steel ( $200 \text{ kN/mm}^2$ ).

### 3.3 Prestressed Concrete Bridges

The initial elastic stage has been treated in the same way as RC bridges, using a dynamic modulus of elasticity of  $57 \text{ kN/mm}^2$ . At ultimate moment, however, these bridges usually fail in the over-reinforced mode and the value of  $M_u$  is thus not directly dependant upon the yield stress of the tendons. In addition, there appears to be no data available on the behaviour of prestressing tendons at high rates of strain, but it is known that treatment of steels to give a high static yield strength may reduce the effects of strain rate[6]. It therefore seems likely that the ultimate moment of a PSC section will be far less sensitive to strain rate effects than that of an RC section. It has been concluded by Bate[16] that use of energy absorption of PSC beams under static loading conditions to predict deflections due to impact loading gives results that are in reasonable agreement with the available test data. The strain rates under impact loading conditions are likely to be smaller than those under the impulsive loading considered here but, since no data is available for these higher strain rates, it has been assumed that PSC bridge

decks will be relatively insensitive to strain rate effects. The unmodified static upper bound value of  $M_u$  has therefore been used as the dynamic plastic moment,  $M_{pd}$ .

## 4. ANALYTICAL RESULTS

### 4.1 Response of Bridge Decks to Impulsive Loading

The values of the permanent central deflection ratio  $y_p/L$ , corresponding to a range of values of impulsive loading have been calculated for each bridge and the results are plotted in Figure 4. Due to the limitations outlined in section 2.5, the results for low impulses can only be regarded as tentative estimates. The area of real concern to this investigation is, however, at the higher impulse loads, where the results may be expected to be more reliable.

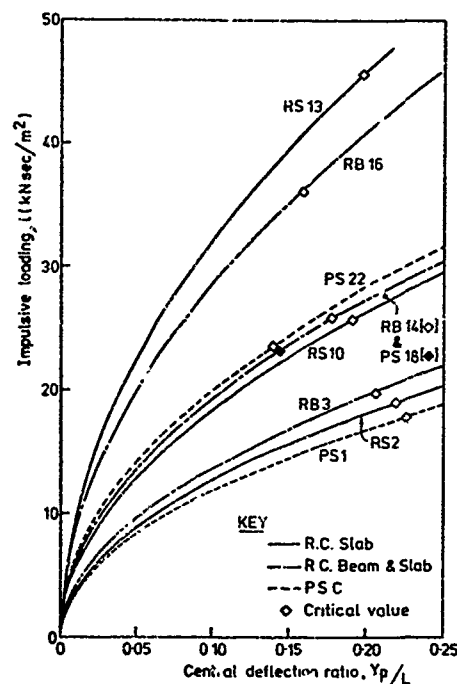


FIGURE 4. Results for Concrete Bridges

It can be seen from Figure 4 that there is a considerable variation in the value of the impulse required to produce a given value of  $y_p/L$ . The results depend both upon the span of the bridge and the form of construction. For a given span the lightest form of construction, PSC, requires a considerably smaller impulse than the heaviest form RC slab, with the RC beam-and-slab form being intermediate between these two.

### 4.2 Criterion for Critical Damage

Various possible criteria for effective demolition were considered but it was decided that passage of vehicles and personnel across a bridge could only be effectively prevented if the bridge collapsed from its supporting abutments. The critical condition for overall collapse of the bridge span

therefore occurs when the end of the bridge deck moves inwards sufficiently for it to drop from its support. Details of the typical support arrangement considered are given in Figure 5.

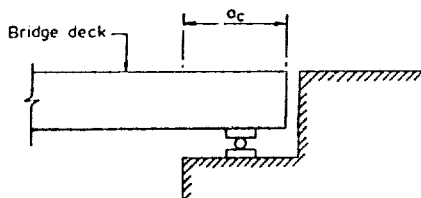


FIGURE 5. Support Details

From the geometry of the collapse mechanism shown in Figure 1, the following relationship may be derived:-

$$\frac{Y}{L} = \sqrt{\frac{a}{2L} - \left(\frac{a}{2L}\right)^2} \quad \dots (2)$$

and by substituting the appropriate values of  $a_c$  for  $a$ , the critical central deflection ratios may be obtained. In practice there will be spreading of the central "hinge" and this will lead to a central "plastic zone". For a given central deflection, however, this would lead to a slight increase in the horizontal movement,  $a$ , and the critical deflection ratios may therefore be slightly conservative. These critical values are indicated in Figure 4 and from them the value of the impulse required for effective demolition may be obtained. These critical impulse values range from 18 kNsec/m<sup>2</sup> for the shortest span PSC bridge to 46 kN sec/m<sup>2</sup> for the longest span RC slab.

## 5. COMPARISON WITH PREVIOUS WORK

### 5.1 Method of Analysis

The only available published work in this field was that due to Sliter and Abrahamson[17]. Their approach was to use a rigid-plastic analysis based on that developed by Florence and Firth[13]. This approach allows for the formation of travelling plastic hinges but no account is taken of either the initial elastic phase of the deformation of any strain-rate effects. They compared their theoretical results with the test results of Florence and Firth, but the agreement was poor and they found if necessary to introduce a correction factor of 0.5, by which all of their theoretical deflection values were multiplied. The agreement was less good than that obtained in Figure 3.

### 5.2 Bridge Deck Calculations

The only bridges analysed were U.S. Army "Line of Communication" (LOC) bridges. These are military equipment bridges designed for rapid erection and only temporary use. They consist of steel beams or plate girders supporting timber or metal grid flooring, and are thus rather unrepresentative of normal civil bridges. The analysis of these bridges was based on their design yield stress (276 N/mm<sup>2</sup>) and on a critical central deflection ratio of 0.20. No attempt was made to relate this deflection ratio to the horizontal movements of the ends of the bridge and precise details of the supporting abutments were not given. From the diagrams in the report, however, it appears that

the value of  $a_c$ , should be not greater than 1m. and this value has therefore been assumed in applying the present analytical procedure.

In order to provide a basis for comparison between the two analytical methods, three of these LOC bridges, covering the full span range available, have been selected and analysed by the method used herein. The analysis has been carried out using the yield stress and deflection ratio values used by Sliter and Abrahamson, and using an upper-bound yield stress and the criterion for critical damage proposed herein. The upper bound yield stress was estimated using the same procedure as that used for reinforcing bars. This gave a value of approximately 380 N/mm<sup>2</sup>. The results are presented in Table 2.

Bridge type	span, L (m)	Calculated impulse required to cause collapse (kNsec/m <sup>2</sup> )			
		a	b	c	d
7 plate girders	12	37.5	26.2	26.2	30.6
11/36WF150 beams	20	20.7	13.5	12.1	14.3
7 plate girders	39	21.0	13.2	10.0	11.7

Key. a. Figures given by Sliter & Abrahamson[17]  
( $f_y = 276 \text{ N/mm}^2$  and  $y_p/L = 0.2$ )

b. Calculated by method proposed herein  
( $f_y = 276 \text{ N/mm}^2$  and  $y_p/L = 0.2$ )

c. Calculated by method proposed herein  
( $f_y = 276 \text{ N/mm}^2$  and  $a_c = 1.0\text{m}$ )

d. Calculated by method proposed herein  
( $f_y = 380 \text{ N/mm}^2$  and  $a_c = 1.0\text{m}$ )

TABLE 2. Comparison of results for LOC Bridges

The results in columns a. and b. provide a direct comparison between the two analytical approaches and show that the Sliter and Abrahamson method yields results between 40% and 60% higher than the present method. It seems likely that the principal reason for this will be their use of a single overall connection factor and consequent neglect of strain rate effects. The effect of strain rate calculated according to the present method is to raise the yield stress of these bridges by between 32% and 60%. A comparison between columns b. and c. shows that the effect of the differences in assumed critical damage levels varies between 0 and 32%. The differences between columns c. and d. illustrate the influence of the different assumed yield stress values, the effect of the conservative value proposal herein being to raise the required impulse by approximately 18% in all three cases. Finally, the results in columns a. and d. provide a comparison between the overall procedure proposed herein and that due to Sliter and Abrahamson. For the short span bridge their approach yields a 20% higher impulse requirement, but for the largest span, it predicts an 80% greater impulse requirement, even though the calculations are based on the design yield strength of the steel and should therefore be non-conservative. For this particular bridge the value of  $y_p/L$  corresponding to  $a_c = 1.0\text{m}$  is only 0.12 and the strain rate effect on the yield stress is only 30%. These two factors combine to

yield the very large difference in the results. The importance of allowing for strain rate effects is highlighted by this comparison, since the calculated strain rate in the Florence and Firth test beams is approximately 30 times as great as the strain rate in this LOC bridge at the same value of  $\dot{\gamma}_p/L$ .

#### 6. CONCLUSIONS

The conclusions from this analytical study may be summarised as follows:-

- (i) Material strain-rate sensitivity can have a major influence on the calculated permanent deformations of beam structures subjected to large impulsive loads. Strain rates experienced by large bridge structures may be very much lower than those present in small scale tests and due account must therefore be taken of strain rate effects when using model test data to predict the response of large scale structures.
- (ii) The simplified method of analysis used herein gives results which are in quite close agreement with model test data and is therefore considered sufficiently accurate for predicting the likely flexural response of bridge decks.
- (iii) Fuel-air explosives may provide an effective means of demolition for a wide range of bridge structures provided that impulsive loadings of the order of 50kN sec/m<sup>2</sup> can be generated. Loadings of 25kN sec/m<sup>2</sup> are likely to be effective for all but short span bridges of fairly heavy construction.

#### 7. ACKNOWLEDGEMENT

The work described in this paper was carried out with the support of the Procurement Executive, Ministry of Defence.

#### 8. REFERENCES

1. NEWMARK, N.M. 'An engineering approach to blast resistant design', Transactions A.S.C.E. V120, 1955, pp.45-61.
2. BIGGS, J.M. 'Introduction to Structural Dynamics', McGraw Hill, New York, 1964.
3. SYMONDS P.S. 'Plastic shear deformation in dynamic load problems', Engineering Plasticity. Eds. J. Heyman and F.A. Leckie, Cambridge University Press, 1968, pp.647-664.
4. ABRAHAMSON G.R. and LINDBERG H.E. 'Peak load - impulse characterization of critical pulse loads in structural dynamics', Dynamic Response of Structures, Eds. G. Hermann and N. Perrone, Pergamon N.Y. 1972, pp.31-53.
5. JONES N. 'Response of structures to dynamic loading', Mechanical Properties at High Rates of Strain, Ed. J. Harding, Institute of Physics, London, 1980 pp.254-276.
6. MAINSTONE R.J. 'Properties of materials at high rates of straining or loading', Materials and structures, V8, No.44, 1975. pp.102-115.
7. HUGHES B.P and WATSON A.J. 'Compressive strength and ultimate strain of concrete under impact loading', Magazine of Concrete Research, V30, No.105, 1978, pp.189-199.
8. KALISZKY S. 'Plastic deformation of thick-walled concrete tubes under dynamic internal pressure', Archives of Mechanics, V24, 1972, pp.1013-1021.
9. SYMONDS P.S. 'Survey of methods of analysis for plastic deformation of structures under dynamic loadings', Report BU/NSRDC/1-67, Brown University, 1967.
10. BODNER S.R. 'Strain-rate effects in dynamic loading of structures', Behaviour of Materials under Dynamic Loading, Ed. N.J. Huffington, P.S.M.E., N.Y. 1965, pp.106-124.
11. PERRONE N. 'On a simplified method for solving impulsively loaded structures of rate sensitive materials', J. of Applied Mechanics, V32, 1965, pp.489-492.
12. HOBBS B. 'Allowing for strain-rate sensitivity in impulsively loaded structures', Design for Dynamic Loads, Eds. G.S.T. Armer and F.K. Garas, Construction Press, London, 1982, pp.234-240.
13. FLORENCE A.L. and FIRTH R.D. 'Rigid-plastic beams under uniformly distributed impulses', J. of Applied Mechanics, V32, 1965, pp.481-498.
14. RAWLINGS B, JOINER J.H. and HOBBS B, 'Behaviour of bridges under dynamic overload', Research Report SUS 14, Dept. of Civil and Structural Engineering, University of Sheffield, August 1974, pp.57.
15. BRITISH STANDARDS INSTITUTION 'BS 5400, Steel, concrete and composite bridges - Part 4', B.S.I. London 1978.
16. BATE S.C.C. 'The strength of concrete members under dynamic loading', Proc. of Symposium on the Strength of Concrete Structures, Cement and Concrete Association, London 1958.
17. SLITER G.E. and ABRAHAMSON G.R. 'Bridge damage from fuel-air explosions', Report SRI-74-936, Stanford Research Institute, 1974.

AD P001722

# THE AFWL CHEBS (CONVENTIONAL HIGH EXPLOSIVE BLAST AND SHOCK) TEST SERIES

Dennis Morrison

New Mexico Engineering Research Institute  
University of New Mexico  
Albuquerque, New Mexico

## ABSTRACT

The objectives of the CHEBS test series are to develop a data base for the blast and shock environments created by conventional high explosive weapons and subsequently to develop appropriate analytical techniques. Both efforts are aimed at producing reliable protective structure design criteria. This paper presents results of this test series. In particular the free-field "close-in" blast and shock environment, bomb-to-bomb variation, and experimental error are examined. Brief results of a statistical analysis are presented.

## INTRODUCTION

The design of protective structures to resist the blast effects of conventional general purpose bombs has typically used empirically derived curves that specify parameters of the airblast waveform [1]. These parameters (i.e., peak pressure, time of arrival, positive-phase duration, and positive-phase impulse) have been determined from uncased hemispherical surface bursts of various yields. Cube root scaling of the yield is used to normalize the data so that each parameter can be represented by a single curve rather than a family of yield-dependent curves [2, 3]. Conventional general purpose bombs, however, are not hemispherical and the effects of the case and the shape of the explosive on the airblast waveform, are of concern to the protective design community. Of particular interest are scaled ranges of less than  $1 \text{ m/kg}^{1/3}$ .

The data near the hemispherical bursts are limited and have a lot of scatter. It is therefore not satisfactory to represent the data as a single curve through an estimated mean of the data. It is desirable to represent the data not only by their mean but also by some description of the distribution. The Conventional High Explosives Blast and Shock (CHEBS) test series is being conducted jointly by the Air Force Weapons Laboratory and the New Mexico Engineering Research Institute to produce such a representation.

The test series covers several general purpose bombs. The blast parameters are measured at scaled ranges from  $\sim 0.5$  to  $2.0 \text{ m/kg}^{1/3}$ . The test

design and layout have used a statistically based approach that allows evaluation of the airblast parameters in comparison to experimental error, blast symmetry, bomb-to-bomb differences, and bomb orientation. A complete description of the statistical approach used is included in the presentation entitled "A Statistical Approach to Conventional Weapons Experimentation," in this conference.

## TEST BED DESCRIPTION AND LAYOUT

The test bed configuration is shown in Figure 1. The dual gages at the various locations are part of the statistically based approach. Six tests with a specific general purpose bomb have been conducted to date on this test bed. The nose of the bomb has been pointed along each of the  $90^\circ$  axes for four of the tests and nose down for the remaining two tests. The center of gravity of the bomb has been placed at the surface. The tests were conducted using available piezoelectric pressure transducers to measure the airblast pressure history. In the farther scaled ranges (greater than  $1.5 \text{ m/kg}^{1/3}$ ) the range of the gage used was probably unreasonably large compared to the peak pressure measured. However, the data do not appear to have significant noise problems.

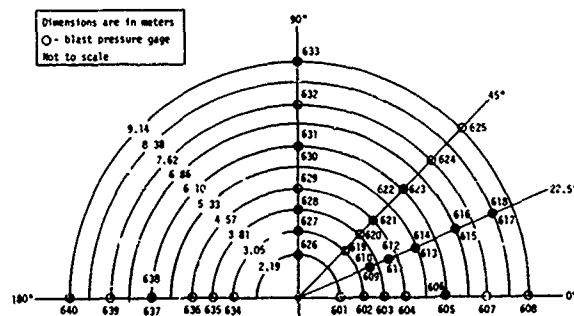


Figure 1. Test bed configuration.

## TEST RESULTS AND ANALYSIS

Only peak pressures from the two vertical bombs are presented in this report. Figure 2 shows all of the peak pressure data plotted with range. The data scatter is probably not surprising, but it is desirable to know in quantifiable terms how much of the scatter is random experimental error and how much is related to some system parameter such as bomb-to-bomb variation. Other parameters such as symmetry and bomb orientation variation could and will eventually be considered.

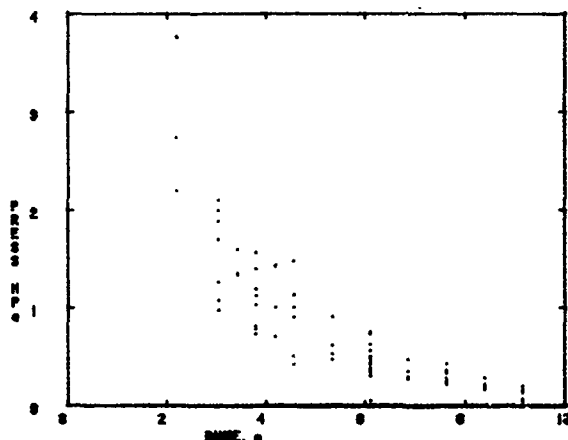


Figure 2. Peak pressure versus range for vertical MKB2 general purpose bomb.

Shown in Table 1 is the computation of the pooled variance of corresponding range data from both of the vertical bomb tests. This variance contains both the effects of experimental error and bomb-to-bomb variation. Also shown are the computations for the pooled variance of the pairs of gages from each test. This represents the experimental error for each test. The ratio for the variances for the two tests is compared with the associated F-statistic, and it appears that the experimental error from the two tests comes from the same family of data and are then combined. The experimental error then can be subtracted from the total variance, leaving the bomb-to-bomb variance. The magnitude of bomb-to-bomb standard deviation illustrates that single tests may not be adequate for protective design verification.

A variance that contains not only the bomb-to-bomb variation and the experimental error but also includes symmetrical variation can be obtained by grouping the same data in a different way. All data from both tests at a given range are grouped for this combined variance. Since the bomb-to-bomb variance and the experimental error variance are available, the symmetrical variance can be computed. The total variance is 0.1112.

TABLE 1. COMPUTATION OF NORMALIZED VARIANCE FOR VERTICAL BOMBS

TEST	DEGREES OF FREEDOM	NORMALIZED <sup>a</sup> VARIANCE	RATIO	F(95)	POOLED VARIANCE	NOTE
ALL CHEBS V & VI Data	42				0.0806	1
CHEBS V (constant angle)	5	0.0431	1.66	9.02	0.0367	2
CHEBS V (constant range)	3	0.0260				
CHEBS VI (constant angle)	4	0.0318	1.54	6.39	0.0262	3
CHEBS VI (constant range)	4	0.0269				
CHEBS V	8	0.0367	1.40	3.44	0.0315	4
CHEBS VI	8	0.0262				

<sup>a</sup>Normalized by mean square of the data.

### Notes:

1. Contains combined bomb-to-bomb variation and experimental error.
2. Experimental error in CHEBS V.
3. Experimental error in CHEBS VI.
4. Combined experimental error.

Bomb-to-bomb normalized variance =  $0.0806 - 0.0315 = 0.0491$   
Bomb-to-bomb normalized standard deviation = 0.2218

Then

$$\text{symmetrical variance} = 0.1112 - 0.0491 - 0.0315 \\ = 0.0306$$

Thus the total variance is composed of somewhat equal parts of the bomb-to-bomb variance, the symmetrical variance, and the experimental error. A structure could be subjected to peak pressure that could have variance that includes both symmetry and bomb-to-bomb differences. The sum would be a measure of the expected variance of peak pressure. That is

$$0.0306 + 0.0491 = 0.0797$$

which can be interpreted as having a standard deviation of  $\sqrt{0.0797}$  or 28.2 percent of the mean peak pressure.

It should be noted here that there may be other effects but they are assumed to be small compared to the effects examined.

## CONCLUSION

It is possible to perform conventional weapon testing in such a way as to separate factors that cause scatter in the data so that both the analyst and the designer are informed as to reasonable variations of airblast parameters about their mean values.

#### REFERENCES

- [1] Crawford, Robert E., et al., **Protection from Nonnuclear Weapons**, AFWL-TR-70-127, Air Force Weapons Laboratory, Kirtland Air Force Base, New Mexico 1971.
- [2] Kingery, C. N., **Airblast Parameters Versus Distance for Hemispherical TNT Surface Bursts**, BRL Report Number 1344, Ballistic Research Laboratories, Aberdeen Proving Ground, Maryland.
- [3] Guirke, G., Scheklinski-Gluck, G., Detterer, M., and Mehlin, H. P., **Blast Parameters from Cylindrical Charges Detonated on the Ground**, E6/82, Ernst-Mach I Institute, March 1982.

F

AD P001773

## THE BEHAVIOR OF MOUNDED HORIZONTAL CYLINDERS IN A CONVENTIONAL-WEAPON ENVIRONMENT

Stephen R. Whitehouse

Air Force Weapons Laboratory  
Civil Engineering Research Division  
Kirtland Air Force Base, New Mexico

### ABSTRACT

This paper discusses the behavior of a mounded horizontal cylinder exposed to conventional-weapon blast and shock effects. This discussion is based on data obtained in the Horizontal Cylinder Test (HCT) series conducted by the Air Force Weapons Laboratory at Kirtland AFB, NM [1]. This paper provides a summary of some of the HCT data, and examines the data to identify the important load and response mechanisms and possible failure modes for this configuration in a conventional-weapon environment.

### TEST CONFIGURATION

The test article used in the HCT series was a ribbed cylinder constructed of fiber-reinforced concrete covered by a soil overburden (Fig. 1). Light bulbs and a pipe with a 0.15-m (6-in) diameter were installed to determine the effect of conventional-weapon blast and shock on simple items of equipment (Fig. 2).

Blast and shock environments were produced by 227-kg (500-lb) Mk 82 bombs detonated outside the soil overburden. Although four tests were conducted in the HCT series, only results from HCT-1 and HCT-3 are discussed in this paper.

In HCT-1, the longitudinal axis of the bomb was parallel to the longitudinal axis of the test article. In HCT-3, the longitudinal axis of the bomb was parallel to the vertical axis with the nose of the bomb pointing downward. In both tests, the bombs were half buried so that their centers of gravity were at ground level.

Data were obtained from blast pressure gages, free-field accelerometers, interface pressure gages, a soil stress gage, and structural accelerometers (Fig. 3).

### DATA REVIEW

The data recorded during HCT-1 are presented in Figure 4. Data obtained from two gages in

HCT-3 are shown in Figure 5. The sequence of events which occurred in these two tests is summarized below.

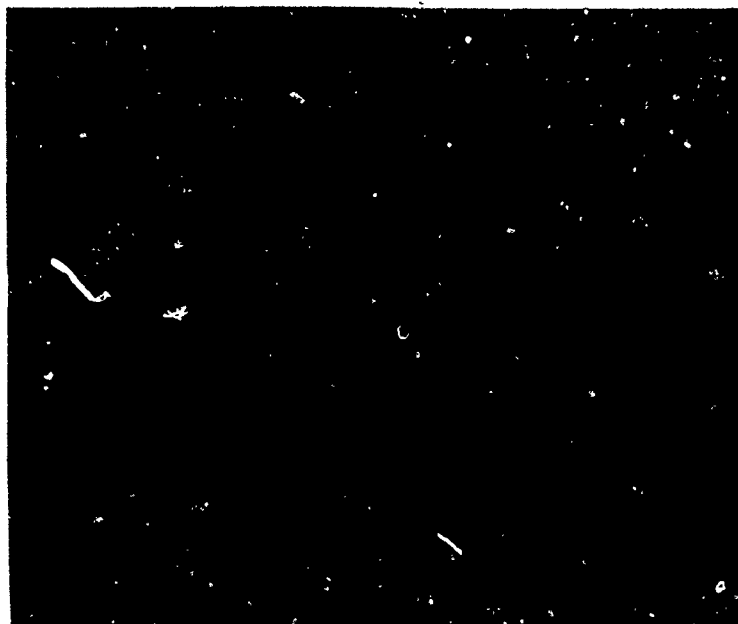
1. The airblast produced by the detonation of the bomb engulfed the soil overburden. As can be seen in Figures 4a and b, the airblast was reflected as it traveled up the upstream slope of the overburden, which produced pressures at the location of gages 0701 and 0702 which were higher than the corresponding free-field pressures. However, the upstream slope directed the airblast away from the top of the overburden, causing pressures at gage 0703 which were less than the corresponding free-field pressures (Fig. 4c).

2. The airblast which acted on the overburden induced vertical and horizontal ground shock in the soil. The vertical velocity-time history recorded by gage 1301 (Fig. 4d) is a classic waveform for airblast-induced soil motion, indicating initial downward motion was followed by soil recovery. The initial velocity pulse seen in Figure 4e is also typical of airblast-induced ground shock. The second pulse in this waveform is discussed in the following paragraph. The smoothness of the vertical and horizontal-motion waveforms reveals that the soil filtered the multiple peaks seen in the airblast data.

3. Energy from the bomb's detonation was coupled directly into the ground, causing a mechanism called upstream-induced ground shock. This ground shock, which propagated from the location of the bomb, produced the second pulse seen in the horizontal soil motion waveform (Fig. 4e).

4. Vertical airblast-induced ground shock arrived at the crown of the cylinder first. The pressure associated with this ground shock must have been increased by reflections at the soil-structure interface, since the peak interface pressure seen in Figure 4f is higher than the peak airblast pressure observed in Figure 4c.

5. The loading at the crown caused the structure to respond in a flexural mode called ovaling. The ovaling response pushed the springlines into the surrounding soil, which caused passive pressures at these locations.



(a) Unburied test article.

#### Cylinder Dimensions

Length = 5.95m  
 Outer diameter = 2.41m  
 Thickness  
   At rib = 0.207m  
   Between ribs = 0.127m  
 Rib width = 0.270m  
 Rib spacing = 0.495m



(b) Soil overburden.

#### Overburden Dimensions

Length  
   At foot = 10.83m  
   At top = 5.95m  
 Width  
   At foot = 7.32m  
   At top = 2.44m  
 Height = 2.44m

Note: 1-to-1 slopes used  
 throughout overburden

Figure 1. Test article and overburden configuration.





Figure 2. Interior of test article.

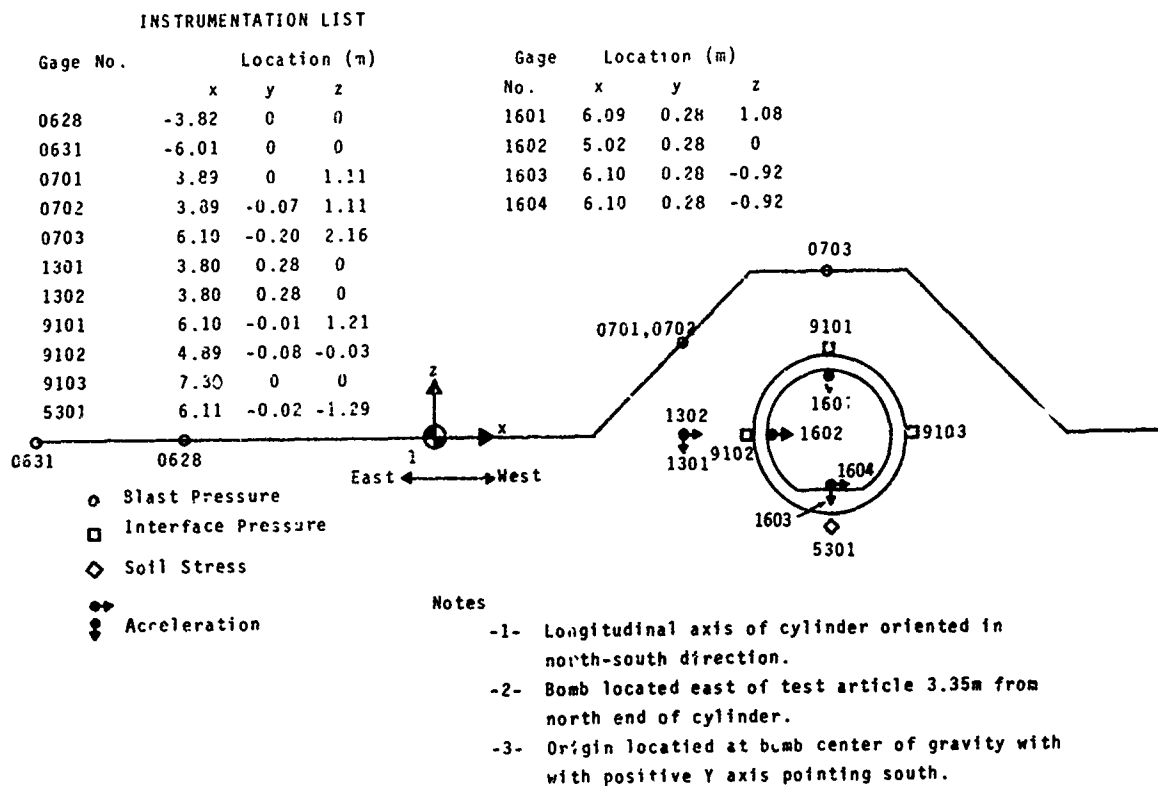
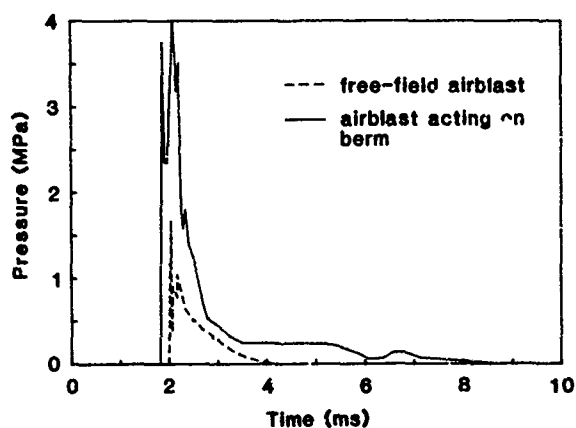
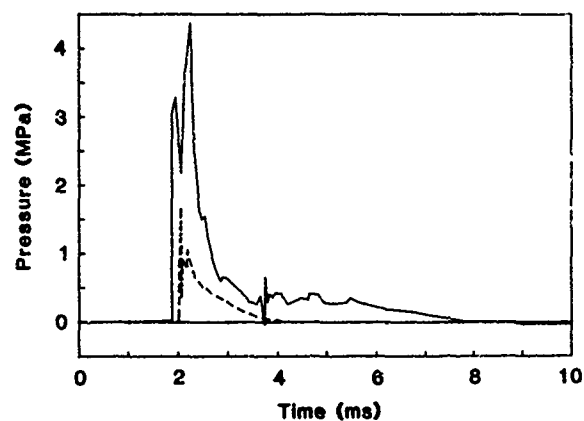


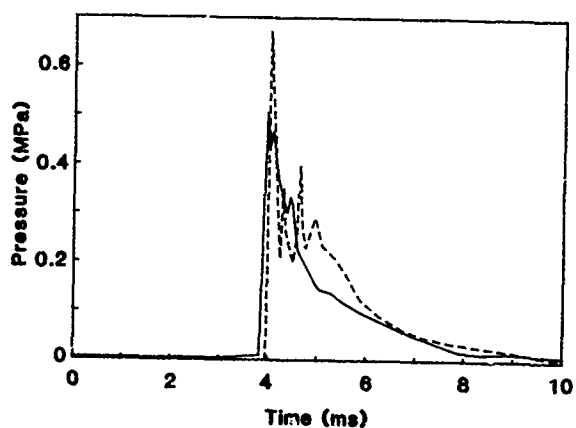
Figure 3. HCT instrumentation.



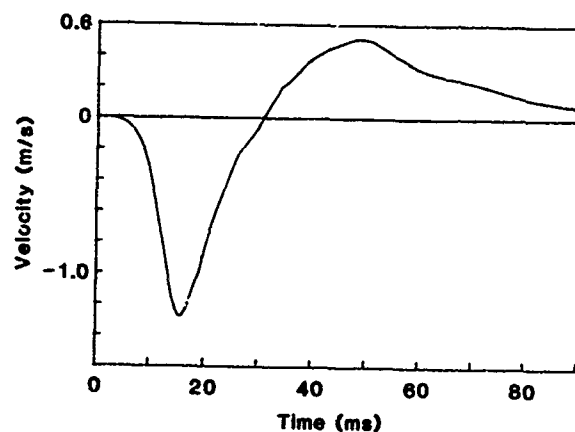
(a) Gage 0628 (free-field) and gage 0701 (berm).



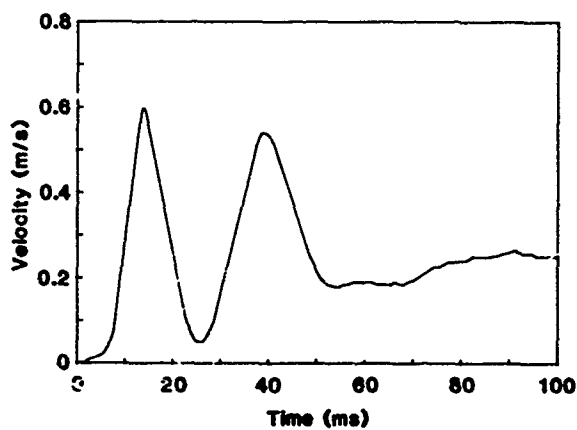
(b) Gage 0628 (free-field) and gage 0702 (berm).



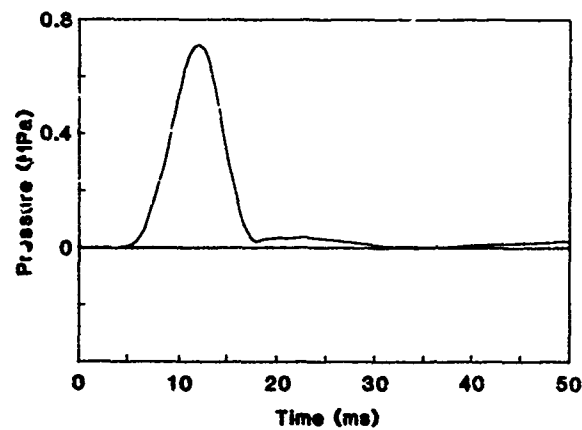
(c) Gage 0631 (free-field) and gage 0703 (berm).



(d) Gage 1301.

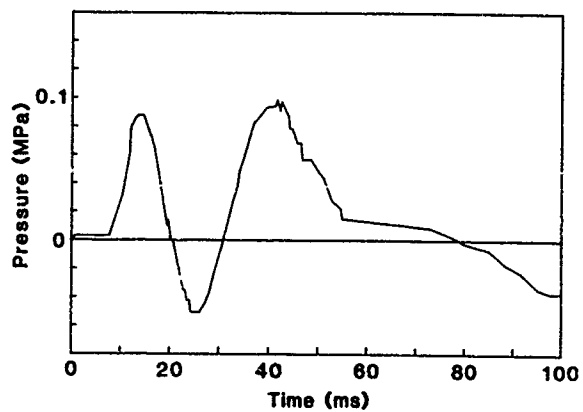


(e) Gage 1302.

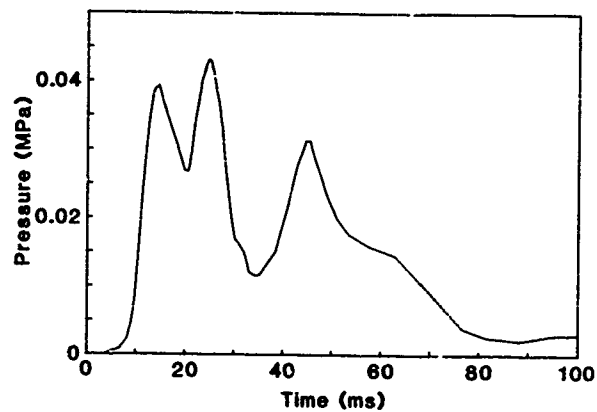


(f) Gage 9101.

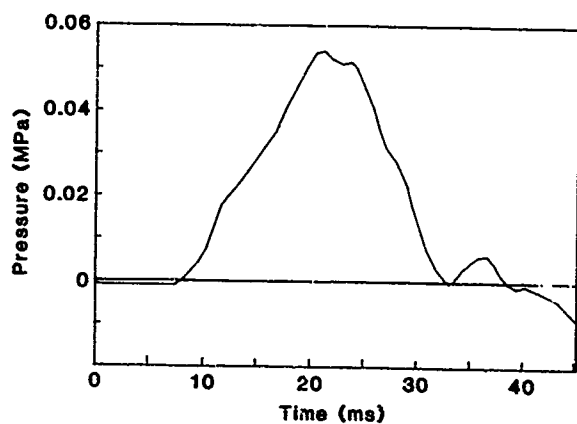
Figure 4. HCT -1 data.



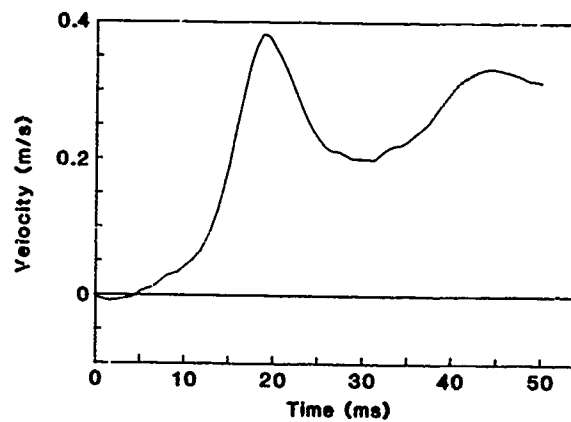
(g) Gage 9102.



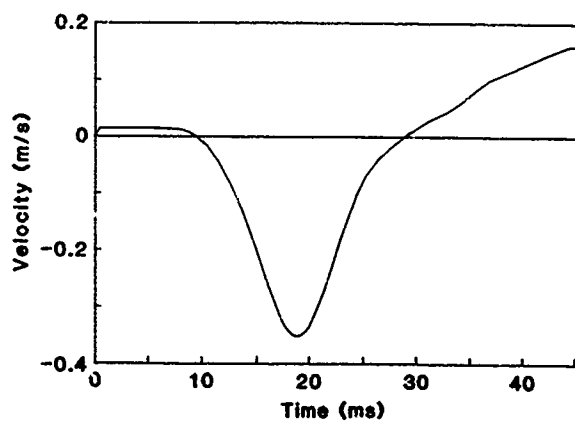
(h) Gage 7103.



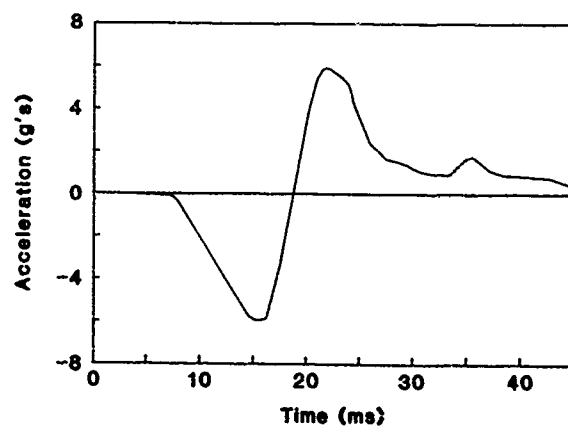
(i) Gage 5301.



(j) Gage 1602.

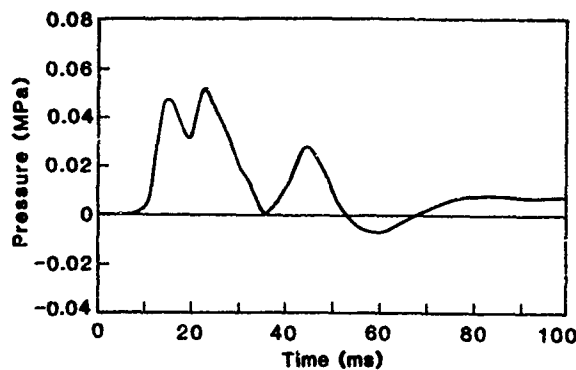


(k) Gage 1603 (velocity).

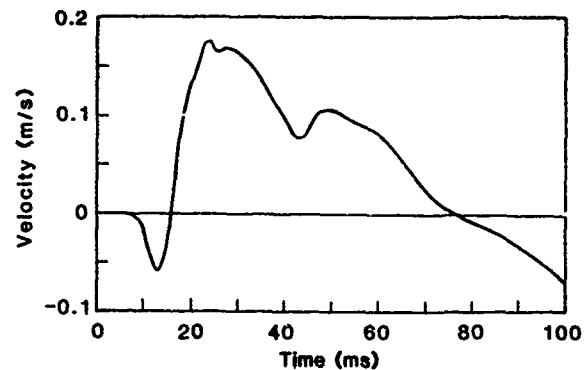


(l) Gage 1603 (acceleration).

Figure 4. Concluded.



(a) Gage 9102.



(b) Gage 1602.

Figure 5. HCT-3 data.

This event accounts for the fact that initial loading at both springlines started simultaneously in HCT-1 (Fig. 4g and h), and explains the upstream motion of the upstream springline which accompanied the initial loading at this location in HCT-3 (Fig. 5). The minor upstream motion at this location apparent in HCT-1 data prior to 5 ms (Fig. 4j) is considered to be an error, since it indicates motion occurred before the airblast-induced effects arrived at the structure. Therefore, no upstream motion can be clearly seen in the HCT-1 data. The absence of this motion in HCT-1 is explained in the following paragraph.

6. Horizontal airblast-induced ground shock arrived at the upstream springline. In HCT-1 this loading was concurrent with the passive loading associated with ovaling of the cylinder. Therefore, only one peak is seen in the loading prior to 30 ms (Fig. 4g) and no upstream motion at this location is apparent in the HCT-1 data. The concurrence of the passive and active loading at this springline also explains why the initial peak interface pressure at the upstream springline was about two times the initial peak experienced at the downstream springline (Fig. 4g and h). Since the active loading arrived later in HCT-3, two distinct peaks are present in the early-time interface pressure data recorded at the upstream springline (Fig. 5a). This delay also allowed upstream motion of this springline as the structure ovaled (Fig. 5b).

7. The cylinder moved downward (Fig. 4k) and downstream (Fig. 4j and 5b) in rigid-body motion as vertical and horizontal airblast-induced ground shock engulfed the structure. In addition to the vertical motion data, the information obtained from gage 5301 (Fig. 4i) provides evidence that the structure underwent rigid-body

motion in the vertical direction. The slow rise and decay seen in the initial pulse of the waveform obtained from gage 5301 are indicative of passive pressure produced by rigid-body motion. The downstream motion recorded by gage 1602 in both tests is attributed to rigid-body motion since no evidence of ovaling can be found in load and motion data obtained at other locations. The second interface pressure peak recorded at the downstream springline appears to be either passive loading associated with horizontal rigid-body motion or active loading produced as airblast-induced ground shock engulfed the structure.

8. The upstream-induced ground shock arrived at the upstream springline as airblast-induced effects decayed. This ground shock produced late-time active loading at the upstream springline (Fig. 4g and 5a) and late-time rigid-body motion downstream (Fig. 4j and 5b). The third peak seen in the waveform obtained from gage 9103 (Fig. 4h) is attributed to the passive loading associated with this rigid-body motion.

9. Finally, reflected ground shock arrived at the invert producing active loading at late time (Fig. 4i) accompanied by an upward acceleration (Fig. 4l).

#### LOAD AND RESPONSE MECHANISMS

Several load and response mechanisms for a mounded horizontal cylinder in a conventional-weapon environment are apparent in the data presented above. The first major loading mechanism evident is airblast-induced ground shock. This mechanism induces ovaling and rigid-body motion in the vertical and horizontal directions. Upstream-induced ground shock, the second major

load mechanism seen in the data, produces additional horizontal rigid-body motion. The final load mechanism apparent in the HCT data is reflected ground shock which produces loading and localized response at the invert. Since this mechanism produced minor loading and response in the HCT series, it is not considered a major load mechanism.

The ovaling experienced by the test article in the HCT events produced only hairline cracks in the structure. Also, the pipe and light bulbs were not damaged by the motions of the structure. This lack of damage is attributed to the rapid reduction of conventional-weapon airblast over short distances and to the attenuation of conventional-weapon ground shock by the soil.

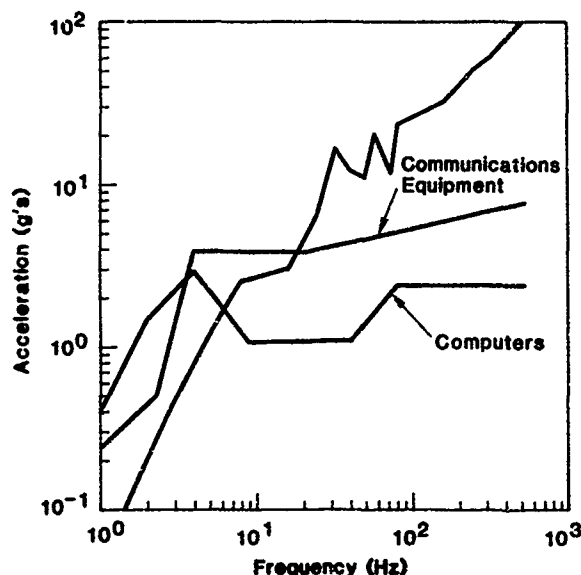
The data from gages 0628 and 0631 indicate how rapidly the airblast decays with distance (Fig. 4a and c). The data from gages 0701, 0702, and 9102 are evidence that soil can be very effective in attenuating airblast-induced ground shock (Fig. 4a,b, and g). Such a drastic attenuation is not seen in the data from gages 0703 and 9101 (Fig. 4c and f). This difference is attributed to the fact that the duration of the loading recorded by gage 0703 was longer than the duration of the loading measured by gages 0701 and 0702. Since this longer-duration loading had a lower frequency content than the reflected airblast pressure, the soil was able to transmit more of the lower-frequency loading.

#### POSSIBLE FAILURE MODES

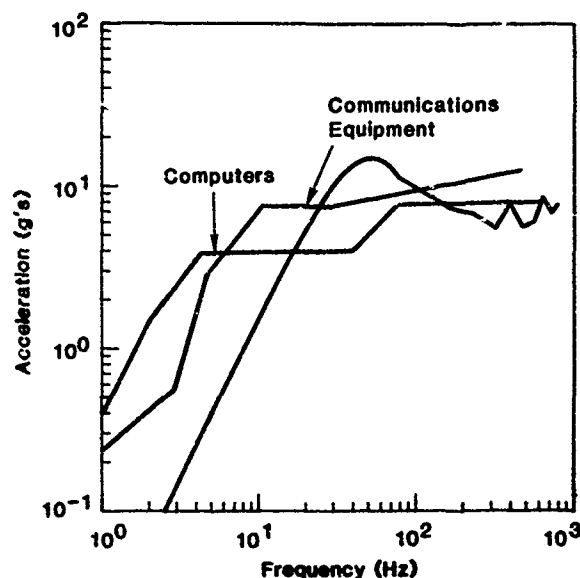
Although no failures occurred in the HCT series, failures may be produced in severer environments associated with larger weapons or smaller ranges, or if more delicate equipment is used in horizontal-cylinder structures.

Since the effects of conventional-weapon loading mechanisms attenuate rapidly, severe loading around an entire cylinder is not expected. Therefore, the flexural, or ovaling, failure associated with a fairly uniform load distribution is not anticipated. However, shear failures caused by severe localized loads are quite possible.

Figure 6 compares the shock tolerance spectra for communication equipment and computers with the response spectrum associated with the motions recorded by gages 1602 and 1603. This comparison indicates that more delicate equipment hardmounted to the structure may fail when exposed to the structural motions which occurred in the HCT series, since the response spectrum exceeds the tolerance spectra at some frequencies. The fact that equipment failures may occur in environments which are not destructive to the structure is evidence that the survivability of mounded horizontal cylinders in a conventional-weapon environment may be limited by the fragility of internal equipment rather than by the strength of the structure. The vulner-



(a) Gage 1602.



(b) Gage 1603.

Figure 6. Equipment fragility analysis.

ability of internal equipment may be enhanced if the timing of the airblast-induced and upstream-induced loading excites natural frequencies in the equipment.

#### CONCLUSIONS

The data obtained from the HCT series have increased the understanding of the behavior of a mounded horizontal cylinder in a conventional-weapon environment. The major loading mechanisms for this configuration when exposed to a surface burst are airblast-induced and upstream-induced ground shock. Ovaling as well as horizontal and vertical rigid-body motion are caused by airblast-induced loading; upstream-induced effects produce horizontal rigid-body response. The environments generated in the HCT series did not cause failure of the structure or the internal equipment. However, severer environments may cause shear failure in the cylinder or mechanical failures in the equipment. In addition, more delicate equipment may fail at shock levels experienced in the HCT series.

#### REFERENCE

1. Whitehouse, S.R., Wong, M.K.W., First Horizontal Cylinder Test, HCT-1, Draft Technical Note, Air Force Weapons Laboratory, Kirtland AFB, NM, 17 September, 1982.